Atomic Force Microscope-Based Methods for the Nano-Mechanical Characterisation of Hydrogels and other Viscoelastic Polymeric Materials for Biomedical Applications



Alba Rosa Piacenti

Wolfson College

University of Oxford

Supervisor: Prof. Sonia Contera

A thesis submitted for the degree of

Doctor of Philosophy

Michaelmas 2020

Abstract

Hydrogels, porous hydrated polymeric materials, are being increasingly used in biomedical applications. The mechanical properties of hydrogels play an important role in the success of many of these applications (e.g. tissue engineering and drug delivery), and can be modulated by external stimuli and/or by changing hydrogel structure and composition. Therefore, it is important to measure and understand these mechanical properties at cellular length scales (nano/micro-scale) to improve the efficacy of hydrogels in biomedical applications.

Hydrogels are often studied in terms of their elasticity. In this thesis, elastic properties of hydrogels were studied in terms of their elasticity via Atomic Force Microscopy (AFM) quasi-static micro-indentations. It is important to consider that hydrogels are not just elastic, but exhibit viscoelasticity, a time-dependent mechanical behaviour typical of hydrogels and polymeric materials in general. In this thesis, a novel AFM-based technique was developed to measure nano/micro-scale viscoelasticity.

First, changes in the local elastic properties of chitosan (a biopolymer) hydrogels in response to an external magnetic field were measured, demonstrating magneto-mechanical coupling. Second, this coupling was further explored by incorporating magnetic nanowires into the hydrogels. Both experiments suggest this coupling could be exploited to control hydrogel mechanics. Third, elasticity of hydrogels based on fullerenes was measured, and depended on the size of the fullerene used. Hydrogel elasticity

in all three experiments matched that of biological tissues, suggesting biomechanical compatibility. The possibility of controlling hydrogel properties either by external stimuli or by composition, opens the door for all three of these materials to be used for therapeutic applications. Lastly, a novel technique based on photothermal excitation of the AFM cantilever was developed and proved to quantify viscoelasticity of polymeric materials over a frequency range up to five orders of magnitude (0.2 Hz to 20 200 Hz), in good agreement with macroscopic data, revealing a promising tool for the viscoelastic characterisation of hydrogels.

Acknowledgements

I would specially like to thank my supervisor, Prof. Sonia Contera for her constant support, guidance, and enthusiasm during my DPhil. I am truly grateful to have met her in my career.

A special thanks goes to all the people that I have met at the Contera lab: Dr. Ileana Andrea Bonilla Brunner, for all the hours spent on the endless chitosan project, for helping me with sample preparation and modification of cantilevers for AFM experiments, for all the drinks, and lunches at the market; Dr. Jacob Seifert (in Kienast) for the long discussions on polymer physics, all his help with Python coding and with the Cypher AFM, and the countless beer pints; Casey Adam, for her constant support, her help in the lab, her enthusiasm in science, and the trips together in Durham and Rome that cross-linked our friendship. I would also like to thank Aleksander Zagajewski, Dr. Zeinab Al-Rekabi, Dr. Chih-Yao (Thomas) Chui (former DPhil student in the Department of Engineering Science, University of Oxford) and the masters and visiting students that have passed by Contera lab for the discussions on materials, physics, and biology.

I would like to acknowledge Dr. Ilija Rašović (former DPhil student in the Department of Materials, University of Oxford), for the beautiful collaboration of the fullerene-based hydrogels.

I would like to thank Nicholas Hawkins (Department of Engineering Science, University of Oxford), for the priceless and essential help with the

DMA experiments, all the discussions on polymers and rheology, and all the coffees that we had together. Thanks also to Dr. Marzena Tkaczyk (Department of Engineering Science, University of Oxford) for her help with the equipment in the Department of Engineering Science (University of Oxford).

I also acknowledge Dr. Jason Brown (Department of Physics, University of Oxford) for his help with SEM, and Dr. Shiv Jee Singh (Department of Physics, University of Oxford) for his help with VSM.

I would like to thank people from Oxford Instruments Asylum Research who helped me with the AFM nano-DMA project, including Dr. Roger Proksch, Dr. Ryan Wagner (former postdoc), Dr. Yukinori Taniguchi, Dr. Aleks Labuda, Dr. Marta Kocun, Dr. Mario Viani, Dr. Anil Gannepalli. A particular thanks to Dr. Proksch, Dr. Wagner, and Dr. Taniguchi for the extensive discussions on the AFM nano-DMA technique. Additional thanks to the entire Oxford Instruments Asylum Research crew for their warm welcome during my stay in Santa Barbara. I would like to acknowledge Dr. Jonathan Moffat and Dr. Chris Mulcahy for their help with the equipment in Oxford.

I would like to address my gratitude to Prof. Stephen Duncan (Department of Engineering Science, University of Oxford) for the time he took to help me with Fourier transform and signal processing.

A great thanks to the Physics Department of the University of Oxford for welcoming me, and giving me the chance of improving myself. A particular thanks to the Clarendon mechanical workshop and to the Clarendon store.

Thank you also to Wolfson College and its awesome staff. Thank you for always making me feel safe, especially during the lockdown.

Thank you to all the members of my family, that supported me in every occasion. I would also like to thank Marco Molteni, for his constant support. Thank you to all my friends that accompanied me in this amazing experience, including my college friends, the OUVC, my flatmates, and my friends from Italy.

I would also like to acknowledge Prof. Antoine Jérusalem (Department of Engineering Science, University of Oxford) and Dr. Charles Clifford (National Physical Laboratory, UK), for taking the time to help me improve my thesis.

I would also like to express my gratitude to Prof. Anna Tramontano, that I met during my studies at the Sapienza University of Rome, for her invaluable support when I applied for this DPhil position.

I am grateful to all the institutions that funded my DPhil: the EPSRC, the Sidney Perry foundation, the Blanceflor Boncompagni Ludovisi née Built foundation, the Sapienza University of Rome for the Borsa di Perfezionamento all'Estero, the Angelo Della Riccia foundation, and, of course, my mother. Thank you also to Wolfson College and the Royal Microscopical Society for their travel grants to attend conferences.

Contents

1 Introduction **1**

1.1 Polymeric materials in biomedical applications 2

1.2 Mechanical properties of polymeric materials: elasticity, viscosity and viscoelasticity 10

1.2.1 Static and dynamic experiments 11

1.2.2 Time-temperature superposition principle 14

1.3 Existing techniques to measure viscoelasticity 17

1.3.1 Macroscale techniques 18

1.3.2 Micro and nano-scale techniques 19

1.4 Aims 21

2 Introduction to Experimental Techniques **23**

2.1 Introduction 23

2.2 Atomic force microscopy (AFM) 24

2.2.1 Indirect versus direct cantilever excitation: photothermal (PT) actuation 25

2.2.2 AFM for elastic measurements: quasi-static force indentation curves 27

2.2.2.1 Hertz and Sneddon contact models 28

2.2.2.2 Contact models for adhesive contacts 29

2.2.3 AFM for viscoelastic measurements 35

2.2.4 Chirp signals for broad and continuous AFM viscoelastic spectra 39
2.3 Electron microscopy (EM) 42
2.3.1 Scanning electron microscopy (SEM) 42
2.3.2 Energy-dispersive X-ray spectroscopy (EDS) 43
2.4 Vibrating sample magnetometry (VSM) 43
2.5 Dynamic mechanical analysis (DMA) 43
3 Materials and Methods 46
3.1 Introduction 46
3.2 Materials 46
3.2.1 Chitosan-based hydrogels 46
3.2.2 PNIPAAm-based hydrogels 47
3.2.3 PDMS elastomer 48
3.2.4 Fullerene-based hydrogels 48
3.2.5 Styrene-butadiene rubber 49
3.2.6 Poly(HEMA) hydrogels 49
3.3 Methods 50
3.3.1 SEM and EDS 50
3.3.2 VSM 50
3.3.3 AFM 51
3.3.3.1 AFM quasi-static force indentation curves 52
3.3.3.2 AFM stress relaxation 55
3.3.3.3 AFM nano-DMA 55
3.3.4 Simulations 58
3.3.5 DMA 59
3.4 Contributions 60

4 Effect of an Applied Magnetic Field on the Mechanical Properties of Hydrogels **62**

4.1 Introduction 62

4.2 Results 65

4.2.1 Morphological, chemical, and magnetic characterisation 65

4.2.2 Mechanical characterisation 65

4.3 Discussion 76

4.3.1 Morphological, chemical, and magnetic characterisation 76

4.3.2 Mechanical characterisation 76

4.4 Conclusions 79

5 Composite Hydrogels **80**

5.1 Introduction 80

5.2 Chitosan composite hydrogels with Fe_3O_4 nanowires 81

5.2.1 Results 83

5.2.1.1 Morphological and chemical characterisation 83

5.2.1.2 Magnetic characterisation 84

5.2.1.3 Mechanical characterisation 84

5.2.2 Discussion 88

5.2.2.1 Morphological and chemical characterisation 88

5.2.2.2 Magnetic characterisation 89

5.2.2.3 Mechanical characterisation 89

5.2.3 Conclusions 90

5.3 Fullerene-based hydrogels 92

5.3.1 Results 93

5.3.1.1 Morphological characterisation 93

5.3.1.2 Mechanical characterisation 96

5.3.2 Discussion 96
5.3.2.1 Morphological characterisation 96
5.3.2.2 Mechanical characterisation 98
5.3.3 Conclusions 99

6 Development of an AFM nano-DMA technique based on PT excitation of the AFM cantilever 101

6.1 Introduction 101
6.2 DMA experiments 102
6.3 Contact stiffness simulations 105
6.4 Stress relaxation experiments 108
6.5 PT-AFM nano-DMA experiments 110
6.5.1 Effects of altering the position of the PT excitation laser . . . 115
6.5.2 Effects of PT excitation laser spot displacements during cantilever movements 118
6.5.3 Determination of the optimal tip-sample distance for the reference measurement 123
6.5.4 Effect of the PT excitation laser power 125
6.5.5 Effect of the PT excitation laser drive amplitude 127
6.5.6 Effect of the indentation depth 131
6.5.7 Effect of the cantilever approach and withdraw velocity 134
6.5.8 Effect of the cantilever: choosing the correct stiffness 134
6.6 Direct versus indirect cantilever actuation 137
6.7 Calculation of the dynamic modulus 141
6.8 Quasi-static force indentation curves 151
6.9 Viscoelastic mapping 156
6.10 Conclusions 158

7 Conclusions and future work **161**

7.1 Hydrogels for biomedical applications 161

7.1.1 Changes in the local elastic properties of chitosan-based hydrogels due to magneto-mechanical coupling 162

7.1.2 Local elastic properties of hydrogels based on C_{60}, C_{84}, and C_{90-92} fullerenes 164

7.2 PT-AFM nano-DMA for viscoelastic measurements at the local scale 165

7.3 Implications of the findings in this thesis 170

Appendices **171**

A Mechanical models for viscoelastic materials 171

B Lock-in and time signals 173

C Linear versus logarithmic chirp signals 175

D Control of the effect of an applied magnetic field on AFM measurements 175

E Heterogeneity in the effect of an applied magnetic field on plain polymeric materials 176

F Heterogeneity in the effect of an applied magnetic field on chitosan composite hydrogels with Fe_3O_4 nanowires 182

G Error calculation for the dynamic modulus 183

Bibliography **185**

List of Figures

1.1 Schematic representation of cross-linked polymer chains and hydrogel. 4

1.2 Viscoelastic response to an oscillatory stimulus 12

1.3 Schematic representation of storage modulus versus frequency of an amorphous polymeric material 17

2.1 AFM indentation and the Hertz model 29

2.2 Indenters with different geometries 30

2.3 Quasi-static force indentation curve and "special points" for an adhesive sample 31

2.4 PT versus PE AFM cantilever excitation 36

2.5 Comparison between linear and logarithmic chirp signals 41

3.1 Freezing process for chitosan composite hydrogels 48

3.2 AFM set up for the magnetic indentation experiments 53

3.3 Setup for indirect actuation by means of a piezo actuator 59

4.1 SEM and EDS on chitosan 66

4.2 VSM on chitosan 66

4.3 SEM on PNIPAAm and PDMS 67

4.4 AFM force indentation curves on chitosan in water 69

4.5 Change in $\tilde{E}$ with B for chitosan in water 70

4.6 Distribution of changes in $\tilde{E}$ with B for chitosan 72

4.7 Changes in $\tilde{E}$ with B for PNIPAAm and PDMS in water 73
4.8 Change in $\tilde{E}$ with B for chitosan in PBS 75

5.1 SEM of chitosan with randomly oriented Fe_3O_4 nanowires 83
5.2 SEM and EDS of chitosan with horizontally oriented Fe_3O_4 nanowires 85
5.3 VSM on chitosan composite with Fe_3O_4 nanowires 86
5.4 Change in $\tilde{E}$ with B for chitosan composite in PBS 87
5.5 $\overline{\tilde{E}}_B$ for plain chitosan and chitosan composite 88
5.6 C_{60} fullerene hydrogel 94
5.7 SEM of fullerene-based hydrogels 95
5.8 AFM mechanical characterisation of fullerene-based hydrogels 97

6.1 TTS principle applied to DMA of a SBR sample 103
6.2 Master curves of the viscoelastic quantities of the SBR sample 104
6.3 Contact stiffness simulations for small spherical and conical indenters 106
6.4 Contact stiffness simulations for large spherical indenters 107
6.5 Stress relaxation of a SBR sample 109
6.6 Response of an AC160TSA-R3 cantilever to a chirped PT excitation . 112
6.7 Dynamic stiffness and loss tangent of a SBR sample obtained by the PT-AFM nano-DMA technique 113
6.8 PT-ELS positions on the cantilever 116
6.9 Amplitude and phase for different PT-ELS positions 117
6.10 Loss tangent calculated for different PT-ELS positions 119
6.11 Reference measurements from rising and lowering the cantilever . . . 120
6.12 Sample measurements from rising and lowering the cantilever 121
6.13 Loss tangent uncertainty 123
6.14 Cantilever reference signals at different distances from the sample . . 124

6.15 Loss tangent calculated with references at different distances from the sample. 125
6.16 Effect of laser power 126
6.17 Artefacts in the deflection signal caused by failure to be in the PT-EL operating range 127
6.18 Reference and sample amplitudes for different drive amplitudes 128
6.19 Linear relationship between the reference and sample amplitudes . . . 129
6.20 Loss tangent calculated from signals at different drive amplitudes . . 130
6.21 Reference and sample amplitudes for different drive amplitudes in a second AFM system 131
6.22 Loss tangent calculated from signals at different drive amplitudes in a second AFM system 132
6.23 Viscoelastic quantities for different trigger points 133
6.24 Loss tangent calculated for different cantilever approach velocities . . 134
6.25 Viscoelastic quantities for different AFM cantilevers 136
6.26 Amplitude and phase signals obtained via direct (PT) and indirect (PE) actuation 139
6.27 Loss tangent calculated for direct (PT) and indirect (PE) actuation . 140
6.28 Force versus indentation of a PT-AFM nano-DMA experiment 142
6.29 Force versus indentation of PT-AFM nano-DMA experiments for different chirp regimes 144
6.30 PT-AFM nano-DMA storage and loss moduli calculated for a spherical indenter with JKR and flat punch stiffness 145
6.31 Comparison between PT-AFM nano-DMA storage and loss moduli calculated with spherical, conical, and hyperboloidal contact models with flat punch stiffness 146

6.32 Force versus indentation curves of PT-AFM nano-DMA experiments obtained with different cantilevers for different chirp frequency regimes 147
6.33 Comparison of PT-AFM nano-DMA storage and loss moduli for different cantilevers 148
6.34 Comparison between storage and loss moduli for PT and PE AFM nano-DMA. 150
6.35 Quasi-static force indentation curves obtained with and without the PT-EL focused on the cantilever 151
6.36 Comparison of PT-AFM nano-DMA storage and loss moduli for different velocities. 152
6.37 Comparison between PT-AFM nano-DMA and quasi-static indentation curves 154
6.38 PT-AFM nano-DMA, PT AM-FM AFM, and DMA on a SBR sample 157

7.1 Loss tangent of poly(HEMA) hydrogels measured by PT-AFM nano-DMA 169
A.1 Mechanical models for viscoelastic materials 172
A.2 Storage and loss moduli for the SLS model 172
B.1 Comparison between PT-AFM nano-DMA signals obtained with TS and LI 174
C.1 Comparison between the response of a cantilever from a linear and a logarithmic chirp drive signals 175
D.1 Effects of B on an AFM cantilever 176
E.1 Distribution of change in $\tilde{E}$ with B for PNIPAAm 178
E.2 Distribution of change in $\tilde{E}$ with B for PDMS 179
E.3 Changes of $|\Delta\bar{\tilde{E}}|$ for chitosan and PNIPAAm 180
E.4 Changes in $|\Delta\bar{\tilde{E}}|$ for PDMS 181

E.5 $\overline{\tilde{E}}_B$ for chitosan, PNIPAAm, and PDMS 182

F.1 Distribution of change in $\tilde{E}$ with B for chitosan composites in PBS . 183

G.1 Contact radius calculated at the "special point" "1" for different tip dimensions 185

Acronyms

2D two-dimensional.

3D three-dimensional.

AC alternating current.

AFM atomic force microscopy.

AM-FM amplitude modulation-frequency modulation.

CR contact resonance.

DC direct current.

DMA dynamic mechanical analysis.

DMT Derjaguin-Muller-Toporov.

DNA deoxyribonucleic acid.

ECM extracellular matrix.

EDS energy-dispersive X-ray spectroscopy.

EM electron microscopy.

FFT fast Fourier transform.

FIV force-indentation variation.

HEPES 4-(2-hydroxyethyl)piperazine-1-ethanesulfonic acid.

HPF high-pass filter.

IPR isolated pentagon rule.

JKR Johnson-Kendall-Robertson.

KFM Kelvin force microscopy.

KV Kelvin-Voigt.

LI lock-in.

LIA lock-in amplifier.

LPF low-pass filter.

MEE monoethyl ether.

MNPs magnetic nanoparticles.

MRI magnetic resonance imaging.

MSCs mesenchymal stem cells.

MW Maxwell.

NIR near-infrared.

OLS optical lever sensitivity.

PBS phosphate buffered saline.

PDMS polydimethylsiloxane.

PE piezoelectric.

PEGDA poly(ethylene glycol) diacrylate.

PEO poly(ethylene oxide).

PNIPAAm poly(N-isopropylacrylamide).

poly(HEMA) poly(2-hydroxyethyl methacrylate).

PSD position sensitive detector.

PT photothermal.

PT-ELS photothermal excitation laser spot.

PT-EL photothermal excitation laser.

SBR styrene-butadiene rubber.

SEM scanning electron microscopy.

SLS standard linear solid.

SPMs scanning probe microscopies.

TEG triethylene glycol.

TS time signals.

TTS time-temperature superposition.

UV ultraviolet.

VSM vibrating sample magnetometry.

WLF Williams-Landel-Ferry.

List of Symbols

Symbol	Description	Units
A	Amplitude	m
a	Contact radius	m
a_T	Horizontal shift factor	$-$
B	External magnetic field	T
b_T	Vertical shift factor	$-$
d	Indentation	m
E	Young's modulus	Pa
$\bar{E}$	Average of E measured on a single spot on the sample	Pa
$\tilde{E}$	Reduced Young's modulus	Pa
$\bar{\tilde{E}}$	Average of $\tilde{E}$ measured on a single spot on the sample	Pa
$\overline{\bar{\tilde{E}}}$	Average of $\bar{\tilde{E}}$ measured on several spots on the sample	Pa
E^*	Dynamic modulus	Pa
E'	Storage modulus	Pa
E''	Loss modulus	Pa
F	Force	N
f	Frequency	Hz
G	Shear modulus	Pa
h	Thickness	m
k_B	Boltzmann constant	$\mathrm{J\,K^{-1}}$
k	Stiffness	$\mathrm{N\,m^{-1}}$
k^*	Dynamic stiffness	$\mathrm{N\,m^{-1}}$
k'	Storage stiffness	$\mathrm{N\,m^{-1}}$
k''	Loss stiffness	$\mathrm{N\,m^{-1}}$
K	$= \frac{4}{3}\tilde{E}$	Pa

L	Length	m
n	Number of molecules per unit volume	m^{-3}
OLS	Optical lever sensitivity	$\mathrm{V\,m}^{-1}$
R	Radius	m
$\tilde{R}$	Reduced radius	m
$\tan\delta$	Loss tangent	–
t	Time	s
T	Temperature	°C (or K)
T_0	Reference temperature	°C
T_g	Glass transition temperature	°C
W	Width	m
w	Energy of adhesion	$\mathrm{J\,m}^{-2}$
z_0	Interatomic equilibrium separation	m
z	Deflection	m
Z_P	Position of Z-piezo	m
α	Semi-vertical angle	°
δ	Phase shift between stress and strain	°
ϵ	Strain	–
ξ	Friction coefficient	$\mathrm{kg\,s}^{-1}$
η	Viscosity	$\mathrm{N\,m}^{-1}\,\mathrm{s}$ (or Pa s in stress-strain notation)
μ	Tabor parameter	–
ν	Poisson's ratio	–
ρ	Density	$\mathrm{kg\,m}^{-3}$
σ	Stress	Pa
ϕ	Phase	°
τ	Relaxation time	s
ω	Angular frequency	$\mathrm{rad\,s}^{-1}$

Subscripts: $_c$ for "cantilever", $_I$ for "indenter", $_R$ for "reference", $_S$ for "sample".

Chapter 1

Introduction

Polymeric materials are widely used in people's everyday life. Thanks to the broad spectrum of their composition, chemical and physical properties, and the possibility of being structured in various and complex forms, polymeric materials are employed in a large range of applications, including packaging [1], automobile and aircraft components [2], insulation [3], and electronics [4]. Thanks to their versatility, polymeric materials, often in the form of hydrogels, are also extensively used in biomedical applications [5–10]: they are useful materials for wound healing as dressings or gels [11], for drug delivery as drug carriers [12], for tissue engineering as structures to reproduce the biological environment of cells [13], and for vaccine delivery as carriers and implants [14, 15].

Depending on the application, polymeric materials need to exhibit specific properties. For biomedical applications, they need to be biocompatible, non-toxic, chemically stable or degradable, and have structural properties that depend on their application [8, 16]. The importance of the mechanical properties of polymeric materials has been long known for applications such as wound healing, for example for the elasticity of the dressing used. Lately, the mechanical properties of polymeric materials have been found to be a key component for the efficiency of other applications including tissue

engineering [17] and drug delivery [18].

This thesis aims to contribute to the measurement of the mechanical properties of polymeric materials at the nano and micro-scale, in order to improve our understanding of these properties for the design and development of novel materials for biomedical applications. To achieve this aim, the experiments presented in Chapters 4 and 5 measure the elasticity of hydrogels in order to examine their feasibility for biomedical applications in terms of their mechanical properties. Nevertheless, polymeric materials are not only elastic, but they display a time-dependent mechanical behaviour called viscoelasticity [19]. Therefore, measuring the viscoelastic properties of hydrogels could provide additional knowledge on the behaviour of hydrogels that could lead to more effective materials for therapeutic applications. For this reason, I developed a novel technique, tested in Chapter 6, that enables quantification of the viscoelastic properties of materials at the nano and micro-scale, in order to take into account the time-dependent mechanical behaviour of polymeric materials.

This chapter provides the relevant background for the work in this thesis in terms of polymeric materials and their mechanical properties. First, I introduce polymeric materials (especially hydrogels) and their role in biomedical applications (Section 1.1). Second, I describe the mechanical properties that characterise polymeric materials, with particular attention to their viscoelastic behaviour (Section 1.2). Third, I review the most relevant techniques in use to measure viscoelasticity (Section 1.3). Lastly, I give an overview of the contents of this thesis (Section 1.4).

1.1 Polymeric materials in biomedical applications

Polymeric materials provide an important platform for biomedical applications [5–10]. Polymers are molecules composed of many repeating units (monomers) bonded together by covalent bonds, through a process called polymerisation, that form poly-

mer chains [20]. Polymers can be found in both liquid and solid state. Polymer liquids can be distinguished in two categories: (i) polymer melts (polymers above their glass transition and melting temperature), and (ii) polymer solutions, (polymers dissolved in solvents) [20]. By decreasing the temperature, a polymer melt can turn into a semi-crystalline material (molecular arrangement that alternates between ordered and random patterns), or into an amorphous solid [20]. If the temperature is lowered below the glass transition temperature (T_g) of the amorphous phase, only local rearrangements of the polymer chains are permitted hence the polymer becomes hard and glassy [19, 21].

Chains in a polymer melt can be cross-linked (bonded together, see Fig. 1.1 (a)). Chain cross-linking results in a polymer network that maintains its shape in time without flowing [20, 22]. For example, rubbers (or elastomers) are cross-linked amorphous polymer networks above their T_g [20–22]. The properties of polymeric materials can be tuned by changing the concentration of cross-links (the number of bonds that hold polymer chains together, see Fig. 1.1 (a)), for example by increasing the concentration of cross-linking agents, or by incorporating different polymers or other molecules into the network [23]. When swollen in solvents, polymer networks are called gels [20, 22]. In particular, hydrogels are hydrophilic polymer networks that absorb large quantities of aqueous solutions and swell [7, 21] (see Fig. 1.1 (b)).

Thanks to their versatility, polymeric materials are a functional class of materials for biomedical applications [5], including implantable medical devices [24], drug delivery [12], tissue engineering [13], wound healing [11], and contact lenses [25]. Smart polymeric materials, whose properties can be modulated by external stimuli (e.g. light, pH, temperature, magnetic and electric fields, etc.), are attractive materials for applications ranging from medicine to microelectronics [26–30], including artificial muscles [31], microrobots [32], biosensors [33], actuators [34], membranes [35], and drug delivery [36].

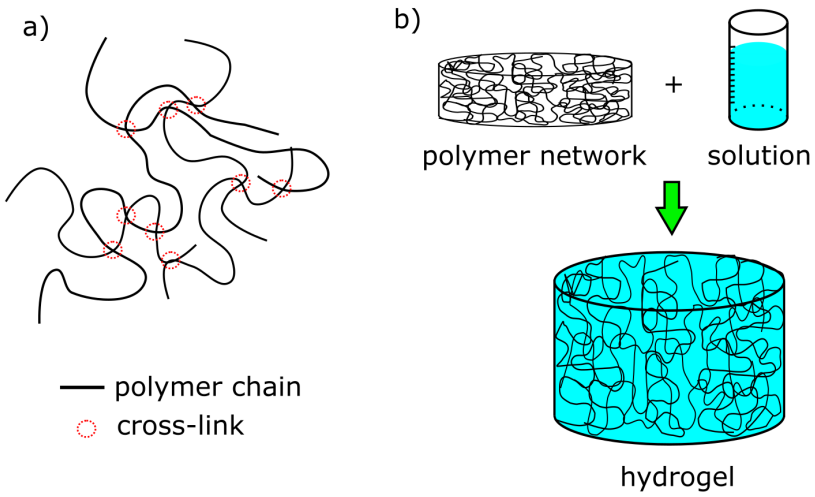


Figure 1.1: Schematic representation of (a) cross-linked polymer chains, and (b) a hydrogel. Note the volume increase of the polymeric material when the solution is added, due to gel swelling. The high solution content within the polymer network and swelling is characteristic of hydrogels.

Hydrogels are particularly important polymeric materials in biomedicine [6–9], and are already being applied in wound healing, contact lenses, drug delivery and tissue engineering [10]. Hydrogels can be designed in a wide range of shapes and sizes, and designed to exhibit specific physical properties. For example the porosity, mechanical, and chemical properties of hydrogels can be modulated by altering their composition (e.g. by changing cross-linking agent concentration and/or the reagents used during their synthesis) [7–9]. Hydrogels can be based on both biopolymers (polymers produced by living organisms) and synthetic polymers and can be engineered to be stable or degradable [7–9]. Hydrogels made from biopolymers (e.g. collagen, chitin, alginate) are particularly useful in biomedical applications due to their biodegradability and low toxicity [37–39]. Hydrogels can be highly biocompatible, and have the ability to encapsulate drugs, cells, and/or biological factors (e.g. growth factors), specific to the desired application/therapy [7–9]. All these properties, together with their high water content that resembles that of biological tissues, make hydrogels widely applicable to a broad range of biomedical applications including contact lenses [8,

10], wound healing [8, 10], vaccine delivery [15], drug delivery [9, 10, 40], and tissue engineering [10, 41].

Conventionally administered drugs (e.g. by oral or intravenous administration) often suffer from inefficient targeting and/or short circulation times, therefore requiring the use of high drug concentrations, which can cause unwanted effects [40, 42]. Novel systems for controlled targeting and release of drugs usually employ elements such as nanoparticles and/or polymeric materials as drug carriers to protect and deliver the drugs [40, 42]. The tunable porosity, the water compatibility, and the possibility of being designed to respond to external stimuli, makes hydrogels appealing for the loading and controlled releasing of drugs [10, 12, 40].

For example, hydrogels that respond to changes in pH by swelling are promising for the controlled release of drugs in cancer tissues that have a different pH compared to healthy tissues [43, 44]. Another strategy is to combine the delivery of drugs with other therapies. For example, chemo-photothermal therapy can be used in cancer treatment to eradicate tumor cells more efficiently [28]. In such treatments, smart hydrogels which generate heat in response to light could be used to produce a dual effect (drug release plus heat) in killing cancer cells at the tumour site [28, 45]. Carbon nanomaterials, thanks to their high near-infrared (NIR) light absorption and heat conversion, in conjunction with anticancer drugs have proved to be promising for chemo-photothermal cancer treatment [45–47].

The drug delivery process involves a number of crucial steps to obtain the desired effect of the drug, including: the response of the immune system, blood circulation, targeting, and cell uptake. Recent studies have highlighted how these steps can be influenced by the mechanical properties of the hydrogel-based nanoparticles used as drug carriers [18, 48, 49], therefore implying that care must be taken in the mechanical characterisation of drug carriers to improve their efficiency.

The properties of hydrogels also make them suitable materials for tissue engineer-

ing purposes [10]. Tissue engineering is an interdisciplinary field that focuses on the design and the development of artificial materials that mimic the *in vivo* conditions of healthy tissues and organs. Engineered tissues can replace those that have been impaired by disease or trauma, or be used for drug testing as an alternative to animal/human testing. In tissue engineering, hydrogels' role is to provide a three-dimensional (3D) "scaffold" for the containment and sustainment of cells and/or regulating biomolecules, such as growth factors, to mimic the biological environment of cells: the extracellular matrix (ECM) [7, 41, 50, 51].

The ECM is a hydrated heterogeneous 3D polymer network in which cells are distributed. The ECM is made of fibrous proteins (i.e. collagen and elastin), polysaccharides, and many other molecules secreted by cells. The exact composition and properties are tissue specific [52, 53]. The ECM has several roles besides the physical support for cells. Indeed, the ECM provides chemical and mechanical stimuli that regulate cell behaviour, survival, morphogenesis, differentiation, homeostasis, proliferation, and migration [52–54]. In turn, cells remodel and organise the ECM [55, 56]. Dysregulation of the ECM composition and properties is often linked to diseases, for example its stiffening is often connected to fibrosis or tumors [55–57].

The mechanical properties of the environment affect resident cells' growth [58], apoptosis [58], motility [59, 60], and differentiation [61–63]. For example, mesenchymal stem cells (MSCs) (stem cells that can differentiate into various cell types), in the same media conditions, were proved to commit to a specific type based on the elasticity of their substrate [61]. By matching the elastic (Young's) modulus (E) of MSCs substrates to that of the brain, muscles, and collagenous bones ($E \approx 0.1\,\text{kPa}$ to $1\,\text{kPa}$, $8\,\text{kPa}$ to $17\,\text{kPa}$, and $25\,\text{kPa}$ to $40\,\text{kPa}$, respectively [61]), the substrates proved to be neurogenic, myogenic, and osteogenic, respectively [61].

One promising tissue engineering strategy is the combination of artificial scaffolds with stem cells, such as MSCs [64, 65]. The mechanical properties of cell seeded poly-

meric scaffolds for tissue engineering are of primary importance for the well-being of cells and tissues, including cell differentiation to the desired cell type [17]. Often, hydrogels are integrated with the incorporation of nanostructures within their polymeric matrices (hydrogel composites) to attribute new, or enhanced, properties to the scaffolds [66]. For example, the integration of carbon nanomaterials into hydrogels can lead to composite structures with enhanced properties, such as electrical conductivity and mechanical stability, that are important for the design of hydrogels for tissue engineering [67, 68].

Smart hydrogels are promising scaffold materials for tissue engineering [69]. In particular, magnetic hydrogels can provide the ability of stimulating cells with mechanical cues using external magnetic fields [70] to, for example, direct their differentiation [71–73]. Magnetic hydrogels are useful in such applications because the stimulus used to control the gel, the magnetic field, is biocompatible, non-invasive, and easy to control spatially and temporally [29]. These characteristics make magnetic fields appealing in biomedical applications [29], including hyperthermia cancer treatment [74], magnetic resonance imaging (MRI) [75], drug delivery [76], and tissue engineering [71].

The field of magnetic hydrogels for biomedical applications has seen significant development in recent years [77]. Usually, smart magnetic hydrogels are formed by incorporating magnetic micro and/or nanoparticles into the structure of a hydrogel to induce a magnetic behaviour [29, 77, 78]. However, the possibility of working with plain hydrogels (hydrogels without the incorporation of magnetic particles) that respond to external magnetic fields would eliminate the risk of toxicity introduced by the incorporation of magnetic particles [79].

Given how the mechanical properties of polymeric materials play a crucial role in determining their biological function (e.g. drug delivery efficiency, cell differentiation for tissue engineering, etc.), it is important to study and control the mechanical prop-

erties of hydrogels used in biomedical applications. Although most studies usually focus on the elasticity of materials (and do not take into account time-dependent mechanical behaviour of the material (see Section 1.2)) [17, 18, 48, 49, 58–63, 80, 81], the role of viscoelasticity in biology and biomedical applications has recently been recognised [82–84]. Indeed, biological systems are viscoelastic [82–84], which suggests that this time-dependent mechanical response should not be ignored for biomedical applications [82–84].

As discussed above, materials used for biomedical applications are often polymer-based. Polymeric materials are viscoelastic, which is important to consider for the interactions with cells [17, 82–84]. Biological timescales are varied, ranging from the nanosecond (for molecular dynamics) to years (for process such as organism growth) [85]. The timescales for cellular and subcellular processes typically range from nanoseconds to hours or days [85, 86]. For example, the process of cell migration spans all these timescales [87]. Cells migrate by: (i) probing their substrate, (ii) regulating adhesion with the substrate, (iii) rearranging their cytoskeleton, and (iv) altering cell shape [60, 88]. Biological processes such as molecular dynamics and cytoskeleton reorganisation involved in (i-iii) can happen at very short timescales (subsecond) [85, 86, 89]. These processes regulate cellular adhesion to the substrate (ii), which can last for ten of seconds to tens of minutes [90]. Cells have also been proved to probe their substrate (i) with podosomes (adhesion complexes that cells use to adhere to the ECM [91]) with oscillatory forces with period of approximately 40 s [92]. Cell movement, instead, can take minutes to days, depending on how far the cell moves [86, 87].

Cells can also sense the time-dependent response of their environment, and adjust their behaviour accordingly. For example, a previous study has revealed how the osteogenic differentiation of MSCs is affected by the viscoelastic properties of alginate hydrogels [93] (alginate is an algae derived biopolymer promising for several

biomedical applications [94]). In this study, the viscoelastic properties of such alginate hydrogels were modulated by tuning cross-linking density in the gel, altering the molecular weight of the alginate, and adding another short polymer during the hydrogel synthesis [93]. Hydrogels with the same initial elastic modulus but different relaxation times (the material's characteristic time to relax when deformed, see Section 1.2 and Appendix A), altered cell osteogenic differentiation and collagen matrix deposition [93]. Hydrogels with shorter relaxation times enhanced osteogenic differentiation and matrix deposition [93]. Therefore, this study highlights the importance of controlling the viscoelastic properties of hydrogels in order to direct cell behaviours for tissue engineering purposes [93].

Nevertheless, many of the studies that examine the effect of viscoelasticity of on cells are performed by measuring viscoelasticity at the macroscale (typically millimetre scale) [93, 95–98], even though a local characterisation at the nano/micro-scale is more appropriate to understand the cells' interaction with the material [82, 99].

Probing the viscoelasticity of polymeric materials is therefore crucial for biomedical applications to understand how their mechanical properties affect the efficiency of the therapy. Time-dependent mechanical properties of materials are usually measured at the macroscale. Techniques that enable the characterisation of viscoelasticity at the micron and submicron scale, the length scale relevant to cells, are required for a comprehensive understanding of the effect that the viscoelasticity of materials has on cells. This understanding will introduce the possibility of perfecting polymeric material properties, for example by tuning their compositions, in order to achieve and improve the desired drug carrier or engineered scaffold for a therapeutic application.

1.2 Mechanical properties of polymeric materials: elasticity, viscosity and viscoelasticity

In this section the mechanical properties of materials, in particular elasticity, viscosity and viscoelasticity, are discussed.

When a material is subjected to a certain normal force F, the material in question is compressed/elongated of a certain amount $\Delta x = x - x_0$ where x and x_0 are the initial and final dimensions of the sample, respectively.

For perfectly elastic materials, Hooke's law establishes a linear relationship between F and Δx that describes the instantaneous response of the material:

$$F = k\Delta x \tag{1.1}$$

where k is a proportional coefficient called spring constant (or stiffness). For Newtonian viscous fluids, the response to an applied force is described with Newton's law:

$$F = \eta\dot{x} \tag{1.2}$$

where η is called viscosity and $\dot{x} = \dfrac{dx}{dt}$ is the deformation rate.

By dividing F to the cross-section area A to which F is applied, the stress $\sigma = F/A$ can be defined. The strain of the material can be defined as $\epsilon = \Delta x/x_0$. It is possible to rewrite Eqs. (1.1) and (1.2) in terms of σ and ϵ as follows:

$$\sigma = E\epsilon \quad \text{for elastic materials} \tag{1.3}$$

$$\sigma = \eta\dot{\epsilon} \quad \text{for viscous materials} \tag{1.4}$$

In the stress-strain notation η units are Pa s.

If dealing with a shear stress σ_{shear} applied to the top face of a material, the shear

deformation is $\gamma = \Delta y/h$, where Δy is the displacement along the direction of the shear stress and h the thickness of the material. The shear equations are analogous to Eqs. (1.3) and (1.4) but the elastic constant is called the shear modulus G. The Poisson's ratio of a material (ν) is a measure of how the dimensions normal to the applied load change, $\nu_{ij} = -\epsilon_j/\epsilon_i$ with i being the direction of the load and j a normal direction. For isotropic materials, ν is a constant and E and G can be linked by ν as $E = 2(1 + \nu)G$. For incompressible materials, $\nu = 0.5$ which leads to $E = 3G$.

Polymeric materials are viscoelastic systems that exhibit a behaviour that is in between the elastic and the viscous responses of Eqs. (1.3) and (1.4). When a stimulus is applied to a viscoelastic material, part of the energy is "stored" and the material can partially recover its original conditions after the stimulus is lifted, and some is "dissipated" as heat due to molecular rearrangements [19, 23]. For small strains, the viscoelastic behaviour of materials can be described with linear differential equations with constant coefficients (linear viscoelastic behaviour) [19]. Some of the most used mechanical models to describe the linear viscoelastic behaviour of materials are illustrated in Appendix A.

It is also worth mentioning that hydrogels might also present time-dependent behaviour due to poroelasticity (fluid flowing through a porous material when the material is deformed) [100]. In this thesis, the time-dependent behaviour of polymeric materials in Chapter 6 is analysed on non-porous samples, thereby excluding poroelastic effects.

1.2.1 Static and dynamic experiments

To characterise the viscoelastic behaviour of materials two main types of experiments can be performed: static and dynamic [19, 21, 23, 101].

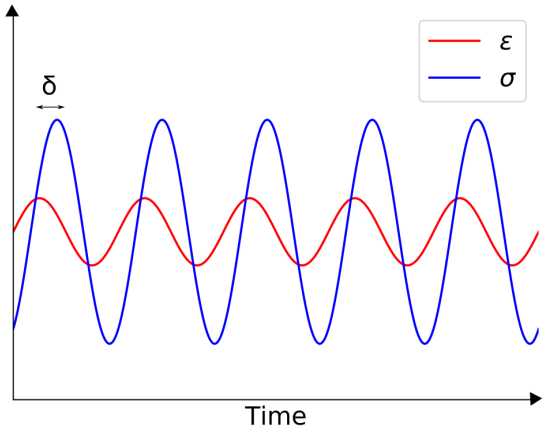


Figure 1.2: Viscoelastic response to an oscillatory stimulus. Schematic representation of the response of a viscoelastic material when subjected to a periodic stimulus: the stress σ and the strain ϵ have a phase shift δ.

Static experiments: creep and stress relaxation

Static experiments consist of exposing the material to a constant stimulus and studying its response. In a creep experiment, a constant stress is applied to the sample leading to a time-dependent strain. In a stress relaxation experiment, the sample is subjected to a constant strain that results in a time-dependent stress. The time-dependence of the response of a viscoelastic material to a stimulus reflects in the modulus of the sample that therefore shows a time dependency.

Dynamic experiments

In dynamic experiments the stimulus applied is periodic. For example, a periodic strain with angular frequency ω can be written as follows:

$$\epsilon(t) = \epsilon_0 \sin(\omega t) \tag{1.5}$$

For a perfectly elastic material, the response to this stress is exactly in phase with the stimulus: $\sigma \propto \epsilon \propto \sin(\omega t)$. For a viscous liquid, instead, the response is 90° out of phase: $\sigma \propto \dot{\epsilon} \propto \cos(\omega t)$. For a viscoelastic material, the phase shift δ between

the stimulus and the response of the material is between 0° and 90°. In Fig. 1.2, a schematic representation of the phase shift between σ and ϵ is presented. The viscoelastic response to the excitation of Eq. (1.5) can be then written as [19, 20, 23]:

$$\sigma(t) = \sigma_0 \sin(\omega t + \delta) \tag{1.6}$$

$$= \sigma_0 \cos(\delta) \sin(\omega t) + \sigma_0 \sin(\delta) \cos(\omega t) \tag{1.7}$$

where the first term is in phase with the applied strain, while the second one is out of phase. It is possible to introduce a complex quantity called the dynamic modulus $E^* = E' + iE''$. The real part E' is called storage modulus, and represents the energy stored elastically by the material during the process. The imaginary part E'' is called loss modulus and represents the energy that is dissipated into the medium, causing the phase shift. Eq. (1.7) can now be rewritten as [19, 20, 23]:

$$\sigma(t) = \epsilon_0 \left[E' \sin(\omega t) + E'' \cos(\omega t) \right] \tag{1.8}$$

where $E' = \frac{\sigma_0}{\epsilon_0} \cos\delta$ and $E'' = \frac{\sigma_0}{\epsilon_0} \sin\delta$.

The loss tangent is defined as the ratio between the loss and the storage components [19, 20, 23]:

$$\tan\delta = \frac{E''}{E'} \tag{1.9}$$

Importantly, being the ratio of E'' and E', $\tan\delta$ does not depend on the geometry of the system [23]. Also, both E' and E'' (and therefore $\tan\delta$) depend on the frequency of the excitation.

Sometimes, it is also useful to express the periodic signals in their complex form therefore write $E^* = \frac{\sigma^*}{\epsilon^*}$ [19, 101].

A more detailed description of polymer viscoelasticity can be found in refs. [19, 21, 23, 101].

1.2.2 Time-temperature superposition principle

When a constant strain is applied to a polymeric material, its chains are displaced from their equilibrium conformation. For the duration of the strain, the polymer chains can rearrange themselves reducing the stress. The Rouse model is one of the most important models to describe polymer dynamics [19, 20, 22]. Briefly, for a polymer chain of N monomers, there are N relaxation modes associated with the coherent movement of sections of the polymer chain with a fraction of monomer N/p, with p being the mode index ($p = 1, 2, ..., N$) [20]. A relaxation time τ_p is associated to each relaxation mode p and has the following form [20]:

$$\tau_p \propto \frac{\xi}{T}\left(\frac{N}{p}\right)^2 \tag{1.10}$$

where T is the temperature and ξ is the monomeric friction coefficient. For modes involving a smaller number of monomers (high p), the respective relaxation times are smaller [20]. In the Rouse model, the shear relaxation modulus $G(t)$ has the following form [19, 20]:

$$G(t) = nk_BT\sum_{p=1}^{N} e^{-t/\tau_p} \tag{1.11}$$

where k_B is the Boltzmann constant, and n is the number of polymer molecules per unit volume. More details on the Rouse model can be found in refs. [19, 20, 22].

The same temperature dependence of Eqs. (1.10) and (1.11) can be used to describe polymers in general with $\tau_p \propto \xi/T$ for the relaxation times, and with $G \propto \rho T$ for the relaxation modulus, with ρ being the density of the polymer [19, 20] (e.g. for undiluted polymers $n = \rho N_A/M_W$, with N_A being the Avogadro's number and M_W the molecular weight of the polymer [19]). Since all τ_p have the same dependence on T, and given the temperature contribution to $G(t, T)$, it follows that $G(t, T)$ measured at a certain T can be shifted and superimposed to $G(t, T_0)$ calculated at another temperature T_0 (reference temperature) [19, 20, 23]. This is commonly called the

"time-temperature superposition (TTS) principle". The TTS principle is an empirical rule and allows extension of the viscoelastic properties of many polymeric materials in the time (or frequency) domain to several order of magnitudes. In practice, the sample is measured in a certain time (or frequency) interval at several temperatures. The data obtained at the different temperatures are then superimposed to the curve obtained at an arbitrarily chosen reference temperature T_0, generating a so-called master curve. The TTS principle is particularly important because it widens the measured time (or frequency) range of the viscoelastic quantities of interest, and therefore overcomes the limitations of many experimental techniques that are able to operate only in restricted range of frequencies (see Sections 1.3 and 2.5).

The TTS principle can be expressed as follows [19, 20]:

$$G(t, T_0) = b_T G(t/a_T, T) \tag{1.12}$$

where a_T and b_T are the horizontal and the vertical shift factors, respectively. a_T is the horizontal factor that is needed to shift G on the time axis [19, 20]:

$$a_T(T, T_0) = \frac{\tau(T)}{\tau(T_0)} = \frac{\xi T_0}{\xi_0 T} \tag{1.13}$$

where ξ_0 is the friction coefficient at $T = T_0$. $a_T < 1$ for $T > T_0$, and $a_T > 1$ for $T < T_0$ [19]. b_T has the following form [19, 20]:

$$b_T(T, T_0) = \frac{\rho_0 T_0}{\rho T} \tag{1.14}$$

where ρ_0 is the density at $T = T_0$.

For oscillatory measurements, the TTS principle can be expressed as [19, 20]:

$$G^*(\omega, T_0) = b_T G^*(\omega_0, T) \tag{1.15}$$

where $\omega_0 = \omega\ a(T, T_0)$ is the shifted frequency for a reference temperature T_0. To shift the master curve to another reference temperature T_0', it is easy to show that:

$$G^*(\omega, T_0') = b_T' G^*(\omega_0', T_0) \tag{1.16}$$

where $\omega_0' = \omega / a_T(T_0', T_0)$ and $b_T' = 1/b(T_0', T_0)$.

In practice, the shift factors are calculated experimentally by superimposing the curves at different temperatures to the curve at T_0. Once a_T is calculated, its temperature dependence can be compared with theoretical $a_T(T)$ models that are commonly used to describe the behaviours of polymeric materials. The Williams-Landel-Ferry (WLF) model has been proved experimentally to describe well the temperature dependence of a_T of many polymeric materials and has the following form [19, 23]:

$$\log(a_T) = -\frac{c_1(T - T_0)}{c_2 + T - T_0} \tag{1.17}$$

where c_1 and c_2 are constants that depend on T_0. For many polymeric materials it has experimentally been found that $c_1 = 8$ and $c_2 = 101.6\,^{\circ}\mathrm{C}$ when T_0 is chosen so that $T_0 = T_g + 50\,^{\circ}\mathrm{C}$ [19]. More details about the TTS principle can be found in refs. [19, 20].

The above description of the TTS principle was given in terms of $G(t)$, but its application is also valid for $E(t)$ [19, 23]. Indeed, $G(t)$ and $E(t)$ are related, and for isotropic incompressible materials ($\nu = 0.5$) the relationship between $G(t)$ and $E(t)$ is $E(t) = 3G(t)$ [19].

As mentioned before, the TTS principle makes it possible to study a very wide time (or frequency) range of the viscoelastic spectra that would be otherwise unreachable by the limitations of commercially available instrumentation (see Sections 1.3 and 2.5).

A simplified sketch of $E'(\omega)$ obtainable with the TTS principle is shown in Fig. 1.3

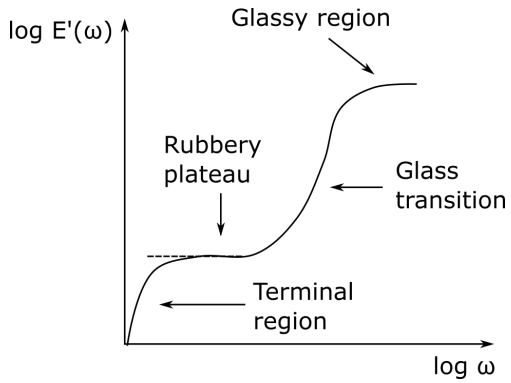


Figure 1.3: Schematic representation of the storage modulus (E') versus angular frequency (ω) for an amorphous polymeric material in a log-log plot.

for a certain T_0. When a polymeric material is subjected to a high frequency stimulus, the polymer chains do not have time to relax during the oscillation and only local molecular motions can occur (glassy region) [19]. For lower frequencies, longer sections of the polymer chains have time to relax and E' drops substantially (glass transition) [19]. For even lower frequencies, E' of cross-linked polymeric materials reaches a plateau (rubbery plateau), while for uncross-linked polymeric materials polymer chains are allowed to slip through each other and flow (terminal region) [19]. For lower T_0 the master curve is shifted to lower frequencies, while for higher T_0 the master curve is shifted to higher frequencies.

1.3 Existing techniques to measure viscoelasticity

The branch of science that studies the deformation of solid and liquid materials is called rheology. The study of the rheological properties of materials is extremely important in several fields, for example the tyre industry. Indeed, car tyres are subjected to a wide range of frequencies and temperatures and must ensure gripping to the road at all times [21]. Therefore, it is important that their composition assures that in their working range they are far from their glassy region, where the polymer chains are not able to relax, and avoid skidding. Rheological studies on the mechanical

behaviour of tyres depending on their composition can therefore be used to enhance their performance [21].

Analogously, viscoelastic studies on materials for biomedical applications and biological samples can be used to develop adequate materials for the desired application.

In this section, I give a brief overlook of some of the most used experimental techniques that enable the study of the viscoelastic properties of materials.

1.3.1 Macroscale techniques

The first commercial instruments to study oscillatory deformations of matter appeared in the 1950-60s [23]. Depending on the modulus of the material, several geometries can be employed to apply torsional or axial stimuli to the sample. Rheometers are commonly used to measure the shear of liquids, melts, or soft polymeric materials (modulus $<10^7$ Pa) and include geometries where the shear stimulus is applied by fixtures such as two parallel plates or a cone and a plate [19, 23]. Dynamic mechanical analysis (DMA) is commonly used for harder samples (modulus $>10^7$ Pa) and include geometries for compression, bending, tension, and shear experiments that can be chosen depending on the characteristics of the material [19, 23].

The above mentioned instruments can usually work in a $10^{-6}-10^{-3}$ Hz to $10^{1}-10^{2}$ Hz frequency range and in a 10^{-2} °C to 10^{2} °C temperature range, depending on the instrument. Therefore, they can employ the TTS principle to extend the frequency range studied.

Clearly, macroscopic techniques are not suitable to study material inhomogeneities at the micron and nanometre scale. Techniques that allow quantification of the mechanical properties of materials at the nano/micro-scale might be more appropriate to study materials useful for biomedical applications, to replicate the length scales at which cells interact with their surroundings [17, 82].

1.3.2 Micro and nano-scale techniques

Micro-rheology techniques can be divided into passive and active, depending on whether the quantification of the viscoelastic properties is done by studying the thermal fluctuation of the probe or by applying an external force to the probe, respectively [102, 103]. Passive micro-rheology techniques track the thermal fluctuation of a probe immersed in the sample and are usually limited to the study of soft matter (moduli below $10^3 - 10^4$ Pa) [102, 103]. Passive micro-rheology techniques include particle tracking, dynamic light scattering, and diffusive wave spectroscopy [102, 103]. Active micro-rhelogy techniques enable measurements of higher moduli and include optical and magnetic tweezers, and atomic force microscopy (AFM) [102, 103].

Among the nano/micro-rheology techniques, AFM has several advantages that makes it a very important tool for the study of materials at the nano/micro-scale, especially for biomaterials [104]. AFM provides a large range of forces that can be applied to the sample (from pN to µN), and the possibility of probing a wide spectrum of length scales (from nm to tens and hundreds µm) by using sharp tips or colloidal tips [104, 105]. AFM also allows quantitative mapping of the mechanical properties of materials with very high spatial resolution [104]. Furthermore, AFM does not require the application of external fields (e.g. magnetic) that could potentially modify the properties of materials (e.g. magnetic materials). AFM can also work in liquid, and at different temperatures [105].

Some AFM methods have been developed to map the viscoelastic properties of materials around the cantilever eigenmode frequencies. For example, in contact resonance (CR)-AFM the changes in the resonance of the cantilever when in contact with the sample can be used to calculate the viscoelastic properties of the sample [106–110]. Multifrequency AFM is another method used to map the mechanical properties of materials [111, 112]. Multifrequency AFM consists of the excitation and/or the detection of the cantilever's motion at multiple frequencies, either at higher harmonics

of the oscillations or resonances of the cantilever [111, 112]. In bimodal AFM, the cantilever is simultaneously driven at two of its eigenmodes, typically the first and the second [111–113]. One of the most used bimodal AFM methods is called amplitude modulation-frequency modulation (AM-FM) AFM. AM-FM AFM enables quantitative mapping of both the topography of the sample and its mechanical properties at the two frequencies [113–116].

In recent years, off-resonance AFM nano/micro-rheology (sometimes called differently, e.g. "AFM-based nano-DMA" [117], "AFM-nDMA" [118]) studies have provided a new and powerful tool to study the viscoelastic behaviour of many materials including cells [119–123], single cell nuclei [124], cartilage [125–129], polymer gels [119, 130], and rubbers [117, 118, 131–134]. One limitation of AFM rheology studies is often the limited accessible frequency range due piezoelectric (PE) actuation to oscillate the cantilever (or the sample), generally used in AFM. Indeed, one of the drawbacks of using PE cantilever actuation in AFM is the presence of spurious peaks in the cantilever spectrum [135–137] that usually limits the working frequency range, especially in liquid environments. Overcoming this frequency limitation is important. For example, it has been found that the high-frequency viscoelastic behaviour of cells can be an indicator for their metastatic state [122].

Of the above mentioned off-resonance studies, only some exceed the 10^4 Hz frequency range [117, 118, 122, 123, 131–134]. To overcome the frequency limitation, these studies had to either adapt a high-frequency piezo actuator to the AFM [118, 122, 131, 132] or compensate for the resonances [123].

Another solution to the frequency limitations can be the usage of the TTS principle to widen the working frequency range. The TTS principle has recently been proved to work for AFM studies on rubbers leading to a frequency range up to $10^5\,\mathrm{Hz}-10^6\,\mathrm{Hz}$ [117, 133, 134], and on fluorinated ethylene propylene up to 10^{17} Hz [118]. Nevertheless, the advantage of having an instrument that enables the study of viscoelasticity

in a broad frequency range without the usage of the TTS principle eliminates the risk of compromising the material (e.g. biological matter) due to changes in temperature (e.g. denaturation of proteins). Also, TTS may not be applicable in highly inhomogeneous biological systems. It is then important to achieve a high frequency range without recurring to the TTS principle.

Another solution could be to use a different cantilever excitation method that leads to a clean cantilever spectrum without spurious resonances. One option is to use magnetic actuation [130, 138], even though the presence of magnetic fields might affect the sample, for example magneto-active materials. The other option is to use photothermal (PT) actuation, that is discussed in detail in Section 2.2.1.

1.4 Aims

The goal of this thesis is the mechanical characterisation of materials that can be used for biomedical applications and the development of a novel technique that allows study of the viscoelastic behaviour of materials at the nano/micro-scale over a wide range of frequencies using AFM.

In Chapter 2, the experimental techniques used in this thesis are described, with focus on the quantification of elastic and viscoelastic properties of materials by means of the AFM. In Chapter 3, I present the materials and methods used in this thesis. Experiments and results are then presented in Chapter 4 through Chapter 6.

The experiments in Chapter 4 examine whether smart magnetic hydrogels can be constructed without incorporating magnetic particles into the gel, and whether the local elastic properties of these hydrogels can be modified and controlled with the application of an external magnetic field. Specifically, Chapter 4 focuses on the effect of an applied external magnetic field on the local elastic properties of hydrogels made of chitosan, an appealing biopolymer for several biomedical applications [139, 140].

The experiments in Chapter 5 study composite hydrogels. In Section 5.2, the study of smart magnetic chitosan hydrogels is continued. Experiments in Section 5.2 test whether control over hydrogel local elasticity by an applied magnetic field can be enhanced by incorporating magnetic nanowires into the chitosan matrix. In Section 5.3, the local elastic properties of hydrogels based on fullerenes (nanostructured carbon materials [141]) are quantified. Three hydrogels, each based on fullerenes with a different number of Carbon atoms (C_{60}, C_{84}, and C_{90-92}), are characterised. Differences in their elastic properties could reveal a new class of hydrogels based on carbon nanomaterials that could be employed in different biomedical applications depending on the fullerene used.

Nevertheless, as discussed in the previous sections, hydrogels are not only elastic, instead they present a viscoelastic behaviour. Better understanding of the local viscoelastic properties of hydrogels is essential to the development of new and more efficient disease treatments and tissue constructs. It is therefore important to introduce new strategies to encourage a transition from the measurement of elastic properties to that of viscoelasticity. For this reason, I developed a novel AFM nano/micro-rheology technique based on PT cantilever excitation. The goal of this technique is to provide a tool for the viscoelastic characterisation of materials over a broad and continuous frequency range. The advantages of using PT excitation of the AFM cantilever, rather than PE and magnetic excitation (cfr. Section 2.2.1), widen the application of AFM nano/micro-rheology, especially in liquid environments. Thereby, this novel PT-AFM nano/micro-rheology technique could increase the ease of quantifying the viscoelasticity of hydrogels and biological matter at the local scale. Experiments in Chapter 6 validate this novel technique.

Outcomes of the experiments in this thesis are summarised in Chapter 7, together with suggestions of some experiments that could be conducted in the future to further develop the findings of this work.

Chapter 2

Introduction to Experimental Techniques

2.1 Introduction

In this chapter, I introduce the experimental techniques used in this thesis by describing their working principles. The experimental details used for the experiments in this thesis are described in Chapter 3 for each technique.

In Section 2.2, I describe AFM with particular attention to its usage for the mechanical characterisation of materials. In Section 2.2.2, I describe theoretical contact models that can be use to extract the elastic properties of materials from AFM quasi-static force indentation curves. In Sections 2.2.1, 2.2.3 and 2.2.4, I present the tools and the theory that I have used to develop an AFM nano/micro-rheology method for the quantification of a sample's viscoelastic properties. These tools include: (i) direct actuation of the AFM cantilever via PT excitation (Section 2.2.1), (ii) the use of chirp signals to obtain a wide and continuous frequency spectrum of the viscoelastic properties of materials from AFM observables (Section 2.2.4), and (iii) the models used to calculate the sample's viscoelastic quantities (Section 2.2.3).

In Section 2.3, I describe electron microscopy (EM) for the study of both the topography (by means of scanning electron microscopy (SEM)) and the chemical composition (by means of energy-dispersive X-ray spectroscopy (EDS)) of materials. In Section 2.4, I present vibrating sample magnetometry (VSM) as a tool to study the magnetic properties of materials. Lastly, in Section 2.5, I introduce DMA for the quantification of the macroscopic viscoelastic properties of materials.

2.2 Atomic force microscopy (AFM)

The AFM belongs to the family of scanning probe microscopies (SPMs), and was invented by Binning *et al.* [142] in 1986. The probe of an AFM consists of a cantilever with a tip at the end. The physical principle of AFM relies on the interaction force acting between the tip and the sample when they are brought in proximity of each other. The interaction force causes the bending of the cantilever, and can be expressed with Hooke's law $F = k_c z_c$, where k_c and z_c are the spring constant and the deflection of the cantilever, respectively [105]. The deflection of the cantilever is usually measured by focusing a detection laser on the back of the cantilever at its free end, which then reflects the laser into a position sensitive detector (PSD) [105]. The voltage measured by the PSD (V_{PSD}) can be converted in the z_c with the optical lever sensitivity (OLS) as follow: z_c (m) $= OLS^{-1}$ (m V^{-1}) $*V_{PSD}$ (V) (see Section 2.2.2) [105]. The fixed end of the cantilever is often connected to a piezoelectric element that allows vertical movements of the cantilever (Z-piezo) [105].

To study the topography of a sample, the cantilever is scanned very close to the material surface [143, 144]. In contact mode AFM, the height of the cantilever is adjusted by a feedback loop to keep the cantilever force (deflection) constant to a certain value, called a setpoint, during the scan [111, 143, 144]. The other commonly used mode is called amplitude modulation AFM, where the cantilever is driven at its

free resonance frequency and the feedback loop is used to keep the amplitude of the oscillations constant [111, 143, 144].

As mentioned in Section 1.3, the AFM cantilever can be excited indirectly, using piezoelectric elements to oscillate the cantilever, or directly, with either magnetic or PT excitation. As explained in Section 2.2.1, direct excitation, and in particular PT excitation, is advantageous compared to indirect actuation, because direct actuation avoids introducing mechanical resonance due to PE excitation that affect the cantilever's motion [135–137].

AFM is also a tool to measure the mechanical properties of materials at the nano/micro-scale, again by studying the deflection of the cantilever during the measurements [104, 105]. A description of how these measurements can be achieved is presented Sections 2.2.2 and 2.2.3.

In this thesis, AFM was used to study the mechanical properties of materials in Chapter 4 through Chapter 7.

2.2.1 Indirect versus direct cantilever excitation: photothermal (PT) actuation

The most common way to excite the AFM cantilever is via indirect actuation by means of piezoelectric elements placed either at the base of the cantilever or underneath the sample [105]. However, one of the main drawbacks of piezolectric (PE) actuation is that, especially in liquids, the coupling of the thermal spectrum of the cantilever with internal resonances of the instrument and the movement of the fluid results in the so called "*forest of peaks*" [135] in the cantilever's spectra [135–137]. The presence of spurious peaks in the cantilever spectra might limit the range of application of AFM nano/micro-rheology to a restricted frequency range.

Direct actuation of the cantilever can be adopted to avoid the presence of spurious peaks from PE excitation in the cantilever's spectra. Developed in the early 1990s,

magnetic actuation introduced a way to directly drive the cantilever [145–148]. The magnetic actuation was achieved by attaching a magnetic bead to the cantilever [145–147] or coating the back of cantilever with a magnetic coat [148], then using a sinusoidal magnetic field to excite the modified cantilever.

Also introduced in the 90s, photothermal (PT) excitation is another means of direct cantilever actuation [149, 150]. In PT excitation, a laser is focused on the back of the cantilever and drives the cantilever's movement via changes in temperature due to the laser's modulation. PT excitation works on metal-coated cantilevers by employing the bimorph bending effect caused by the difference of the thermal expansion coefficient between the thin metallic layer (e.g. gold) and the body of the cantilever (e.g. silicon, silicon nitride) [150–152]. PT is widely usable, because most cantilevers are covered with metallic coats to enhance their reflectivity for the detection system in the AFM. Furthermore, PT actuation also works, albeit with lower efficiency, on uncoated cantilevers, due to the thermal gradient that it generates along the thickness of the cantilever body [153, 154].

Theoretical investigations have highlighted the fact that cantilever magnetic actuation is more efficient than PT actuation for exciting high modes of a soft ($k_c = 0.1\,\mathrm{N\,m^{-1}}$) cantilever [155]. However, PT actuation is more efficient for exciting the cantilever for frequencies below the cantilever's first mode [155].

Furthermore, PT excitation works on both metallic coated cantilevers [150, 151] and with uncoated cantilevers [153, 154]. Only a few commercial magnetic cantilevers, with a limited range of features, are available. Thus, PT actuation works for a broader range of cantilevers than magnetic actuation.

PT excitation has been employed in bimodal AM-FM AFM [115], and in CR AFM [156] to accurately quantify the mechanical properties of materials with a large range of moduli by driving the cantilever at its eigenmodes (on-resonance). PT excitation has also shown promise in quantifying the mechanical properties of a sample

off-resonance [157, 158], although only the stiffness of the material was measured in these studies.

For the reasons described here, I decided to use PT actuation for the development of a novel AFM nano/micro-rheology technique that is applied in Chapter 6.

2.2.2 AFM for elastic measurements: quasi-static force indentation curves

In a AFM quasi-static force indentation experiment (often referred to as "force-indentation curve", "force curve", or "indentation curve") the cantilever approaches the sample and contacts the material, thus applying a force (F) and causing a indentation (d) of the material. The cantilever keeps indenting the sample until a certain value of either force or indentation (called a "trigger point") is reached (red line in Fig. 2.1(a)). When the trigger point is reached, the cantilever retracts from the sample until it is not in contact with the sample any more (blue line in Fig. 2.1(a)). If there are adhesion forces acting between the tip and the sample, more force is required to retract the cantilever away from the sample surface (see Section 2.2.2.2). The raw signals obtained for an AFM force curve are V_{PSD} and the position of the Z-piezo (Z_P) [105]. The OLS of a cantilever (with a non-deformable tip) can be measured by doing a force curve measurement on a very hard material (non deformable) [105]. The slope of the contact part of the V_{PSD}-Z_P curve corresponds to the OLS and can be used to calculate z_c [105]. Once the OLS is known, both $F = k_c z_c$ and $d = Z_P - z_c$ can be calculated [105]. It is important to consider k_c with respect to the sample stiffness k_S. In fact, if $k_c << k_S$ the force curve reproduces the cantilever bending more than the sample indentation [105]. It is therefore recommended to use a cantilever with $k_c \geq k_S$. A more detailed description of AFM force curves can be found in ref. [105]. From quasi-static force indentation curves, the elastic properties of materials can be calculated using contact mechanics models to describe the system.

2.2.2.1 Hertz and Sneddon contact models

The most general and most used contact mechanics model is the Hertz model. It is based on a model proposed in 1882 by Hertz [159] and describes the deformation of spherical elastic bodies as one exerts force against the other [159, 160]. Hertz's theory is valid for two homogeneous elastic bodies with continuous and smooth surfaces, which are subjected to small deformations compared to their dimensions, in absence of adhesion forces [159, 160]. He found that for two elastic spheres of radii R_I and R_S, the contact radius a can be calculated as [159, 160]:

$$a^3 = \frac{3}{4}\tilde{E}\tilde{R}F \tag{2.1}$$

where $\tilde{E}$ is the reduced Young's modulus defined as:

$$\frac{1}{\tilde{E}} = \frac{1-\nu_S^2}{E_S} + \frac{1-\nu_I^2}{E_I} \tag{2.2}$$

where the subscripts S and I indicate the quantities of the sample and the indenter, respectively. If $E_I >> E_S$, than $\tilde{E} \approx \frac{E_S}{1-\nu_S^2}$. $\tilde{R} = \frac{R_I R_S}{R_I + R_S}$ is the reduced radius. $\tilde{R}$ can be approximated with the radius of the smallest sphere if the two spheres have very different sizes. For example, for an indenter with a very small tip compared to the size of the sample (often the case in AFM experiments) $\tilde{R} \approx R_I$, that represents the case of a spherical indenter deforming a half-space (see Fig. 2.1(b)). The relation between F and d can be expressed as [159, 160]:

$$F = \frac{4}{3}\tilde{E}\sqrt{\tilde{R}}d^{\frac{3}{2}} \tag{2.3}$$

In 1965, Sneddon extended the study of elastic contacts, to include indenters with a solid of revolution geometry [161]. The separation profile $\tilde{z}$ between an elastic homogeneous half-space and an indenter with a solid of revolution geometry can be

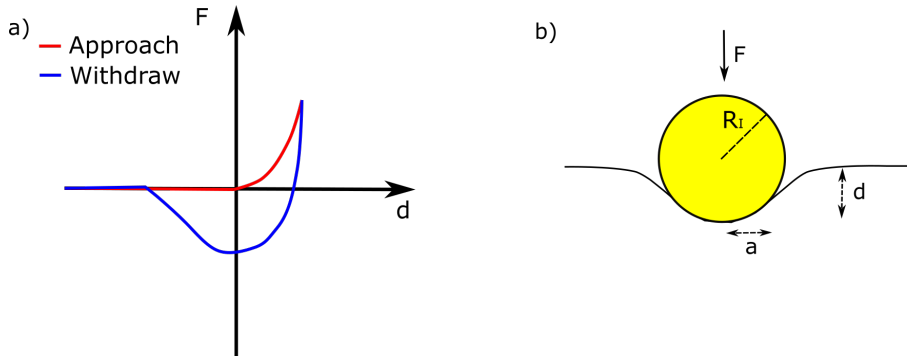


Figure 2.1: AFM indentation technique and the Hertz model. (a) Diagram of an AFM quasi-static force indentation curve: the cantilever approaches the sample until the tip is in contact with it, applying a force (F) on the sample and deforming (indentation, d) it to a certain extent (red line). Then, the cantilever is withdrawn from the sample (blue line). (b) Schematic representation of a spherical indenter of radius R_I deforming a half-space. a is the contact radius between the indenter and the half-space (the Hertz model).

expressed as a function of the polar radius coordinate describing the contact (r) as $\tilde{z} = f(r)$ [161]. A simple relation to describe F and d applied to an elastic half-space that is valid for some of the most common indenter shapes can be derived from the Sneddon model [161]:

$$F = G\tilde{E}d^{\gamma} \tag{2.4}$$

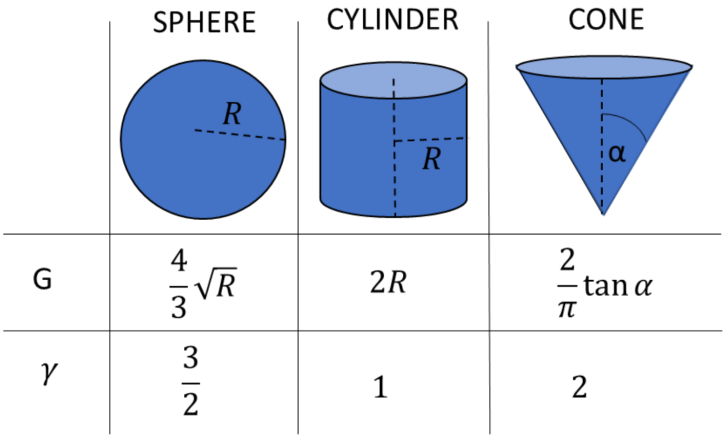
where G and γ are factors that depend on the geometry of the indenter (see Fig. 2.2).

The contact stiffness (k_S) is the derivative of the load applied by the indenter inducing the sample deformation ($k_S = \frac{dF}{dd}$) [105, 162]. k_S and $\tilde{E}$ can be linked by a as follows [105, 162]:

$$k_S = 2\tilde{E}a \tag{2.5}$$

2.2.2.2 Contact models for adhesive contacts

In the presence of adhesion forces equations are different. Two of the most used models to describe the adhesive contact between two bodies are the Derjaguin-Muller-Toporov (DMT) [163] and the Johnson-Kendall-Robertson (JKR) [164] models. The DMT model assumes that the adhesion forces act outside the contact area (long-range



	SPHERE	CYLINDER	CONE
G	$\frac{4}{3}\sqrt{R}$	$2R$	$\frac{2}{\pi}\tan\alpha$
γ	$\frac{3}{2}$	1	2

Figure 2.2: Indenters with different geometries and the geometrical factors used in Eq. (2.4) for spherical (Hertz) [159, 160], cylindrical, and conical indenters [161].

forces), while the JKR model assumes that adhesion force act inside the contact area (short-range forces). These two models are the limits of a single adhesive contact model [165–167]. The correct model to chose can be determined with the help of a dimensionless parameter μ introduced by Tabor [165] (Tabor parameter) that compares the height of the adhesive "*neck*" [165] between the two bodies outside the contact zone and the interatomic equilibrium separation z_0 [165]:

$$\mu = \left(\frac{R_I w^2}{\tilde{E}^2 z_0^3}\right)^{1/3} \tag{2.6}$$

where w is the energy of adhesion per unit contact area. For heights smaller than z_0 ($\mu < 1$) the DMT limit is valid, whereas for heights much larger than z_0 ($\mu \gg 1$) the JKR limit applies [166, 167].

In this work $\mu \gg 1$ (see Chapter 6), therefore the JKR model applies.

JKR extended the Hertz model in the presence of adhesion forces and demonstrated how a is larger compared to that of the Hertz model (cfr.Eq. (2.1)) [164]:

$$a^3 = \frac{\tilde{R}}{K}\left(F + 3\pi\tilde{R}w + \sqrt{6\pi w\tilde{R}F + (3\pi w\tilde{R})^2}\right) \tag{2.7}$$

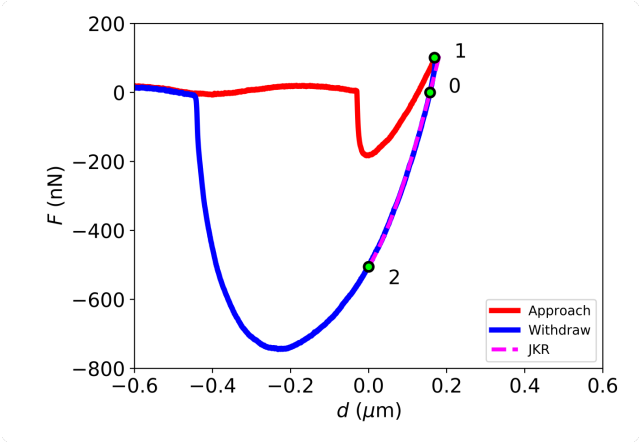


Figure 2.3: Quasi-static force indentation curve and "special points" for an adhesive sample. Typical force (F) versus indentation (d) curve obtained on a SBR sample using a biosphere$^{\text{TM}}$-NT_B2000_v0010 cantilever and a trigger point of 100 nN. The cantilever approach is showed in red, and the withdraw in blue. Point "1" is where the withdraw starts. Point "0" is where the load on the cantilever is zero. Point "2" is where the deformation of the sample is zero. The pink dashed lines represent the theoretical JKR curve by calculating a_0, K, and w with Eqs. (2.9) to (2.11) from the experimental data as explained in the text.

where $K = \frac{4}{3}\tilde{E}$.

For a spherical intender in the presence of adhesion forces, a can be calculated for the JKR model with Eq. (2.7). The quantities K and w can be obtained by using the *"two-points method"* [168], introduced by Sun *et al.* [168]. This method uses two "special points" of the withdraw curve to obtain K and w [168], needed to calculate a. Fig. 2.3 displays a force curve obtained on a styrene-butadiene rubber (SBR), and illustrates some of the key features of the withdraw curve. The first point of the curve "1", the point of zero load "0", and the point of zero deformation "2" are labelled on the withdraw curve.

Other useful JKR relationships used in the two-points method are [164, 168]:

$$d = \frac{a^2}{\tilde{R}}\left[1 - \frac{2}{3}\left(\frac{a_0}{a}\right)^{3/2}\right] \tag{2.8}$$

$$a_0^3 = \frac{6w\pi\tilde{R}^2}{K} \tag{2.9}$$

By using the point "2" and point "0", K is found as [168]:

$$K = \frac{-F_2}{2}\frac{3}{\sqrt{d_0\tilde{R}}} \tag{2.10}$$

a_0 can be calculated using Eq. (2.8) [168]:

$$a_0 = \sqrt{3d_0\tilde{R}} \tag{2.11}$$

w can now be calculated by combining Eq. (2.10) and Eq. (2.11) with Eq. (2.9). It is now possible to obtain a via Eq. (2.7). The theoretical JKR curve is plotted in Fig. 2.3 from point "1" to point "2" with a pink dashed line and overlaps well with the experimental data. As said before, the JKR equations are derived from the Hertz model and hence are valid in the approximation of a small contact radius compared to the radius of the spherical indenter.

For indenters with different geometries, the presence of adhesion can be included with the following simple relations [169]:

$$d(a) = d_{NA} - \sqrt{\frac{2\pi wa}{\tilde{E}}} \tag{2.12}$$

$$F(a) = F_{NA} - \sqrt{8\pi wa\tilde{E}} \tag{2.13}$$

where d_{NA} and F_{NA} are the deformation and the force in the non-adhesive case (i.e. Hertz [159, 160] and Sneddon's solutions [161]). For a Hertzian spherical ($f(r) = r/(2R)$) and a conical ($f(r) = r\cot(\alpha)$) indenters [169], one finds the results originally obtained by JKR [164] and by Maugis and Barquins [170], respectively.

Sun *et al.* [168] proposed a model to describe an indenter with a hyperboloidal shape ($f(r) = R_I(\cot\alpha)^2\left[\sqrt{r/(R_I\cot\alpha)^2+1}-1\right]$). Equations for the deformation and

load of a hyperboloidal indenter in the presence of adhesion are [168]:

$$d = \frac{aA}{2R_I}\left[\frac{\pi}{2} + \arcsin\left(\frac{(a/A)^2 - 1}{(a/A)^2 + 1}\right)\right] - \sqrt{\frac{2\pi w a}{\tilde{E}}} \tag{2.14}$$

$$\begin{aligned} F = {} & \frac{2\tilde{E}A}{2R_I}\left[aA + \frac{a^2 - A^2}{2}\left(\frac{\pi}{2} + \arcsin\left(\frac{(a/A)^2 - 1}{(a/A)^2 + 1}\right)\right)\right] \\ & - \sqrt{8\pi w a \tilde{E}} \end{aligned} \tag{2.15}$$

where $A = R_I \cot\alpha$, with α being the tip semi-vertical angle.

For my analysis, I have introduced the following approximation in order to simplify the calculations. For $a >> A$:

$$\begin{aligned} \arcsin\left(\frac{(a/A)^2 - 1}{(a/A)^2 + 1}\right) &\approx \arcsin(1) \\ &= \frac{\pi}{2} \end{aligned} \tag{2.16}$$

Therefore, Eqs. (2.14) and (2.15) simplify to:

$$d = \frac{aA\pi}{2R_I} - \sqrt{\frac{2\pi w a}{\tilde{E}}} \tag{2.17}$$

$$F = \frac{\tilde{E}A}{R_I}\left[aA + \frac{a^2 - A^2}{2}\pi\right] - \sqrt{8\pi w a \tilde{E}} \tag{2.18}$$

Using the two-points method it is possible to calculate a for an indenter with hyperboloidal shape [168]. For point "0", Eq. (2.17) becomes:

$$\begin{aligned} d_0 &= \frac{a_0 A}{2R_I}\pi - \sqrt{\frac{2a_0 w\pi}{\tilde{E}}} \\ \sqrt{\frac{2a_0 w\pi}{\tilde{E}}} &= \frac{a_0 A}{2R_I}\pi - d_0 \end{aligned} \tag{2.19}$$

From which:

$$\frac{w}{\tilde{E}} = \frac{\left(\frac{a_0 A}{2R_I}\pi - d_0\right)^2}{2a_0\pi} \tag{2.20}$$

From Eq. (2.18):

$$F_0 = 0 = \frac{A}{2R_I}\left(a_0 A + \frac{a_0^2 - A^2}{2}\pi\right) - a_0\sqrt{\frac{2\pi a_0 w}{\tilde{E}}} \tag{2.21}$$

Using Eq. (2.19), Eq. (2.21) becomes:

$$\frac{A}{2R_I}\left(a_0 A + \frac{a_0^2 - A^2}{2}\pi\right) - a_0\left(\frac{a_0 A}{2R_I}\pi - d_0\right) = 0 \tag{2.22}$$

From which a_0 can be calculated. Once having a_0, $w/\tilde{E}$ can be calculated from Eq. (2.20).

For point "1", Eq. (2.17) becomes:

$$d_1 = \frac{a_1 A}{2R_I}\pi - \sqrt{2a_1\pi}\sqrt{\frac{w}{\tilde{E}}} \tag{2.23}$$

from which a_1 can be calculated. From Eq. (2.18):

$$F_1 = 2\tilde{E}\left[\frac{A}{2R_I}\left[a_1 A + \frac{a_1^2 - A^2}{2}\pi\right]\right] - \left[a_1\sqrt{2a_1\pi}\sqrt{\frac{w}{\tilde{E}}}\right] \tag{2.24}$$

By rearranging the terms, the expression to calculate $\tilde{E}$ can be written as follows:

$$\tilde{E} = \frac{F_1}{2\left[\frac{A}{2R_I}\left[a_1 A + \frac{a_1^2 - A^2}{2}\pi\right]\right] - \left[a_1\sqrt{2a_1\pi}\sqrt{\frac{w}{\tilde{E}}}\right]} \tag{2.25}$$

w can be obtained now from Eq. (2.20).

The same procedure can be applied for a conical indenter using Eqs. (2.12) and (2.13) (with $d_{NA} = \frac{\pi}{2} a \cot\alpha$, $F_{NA} = \frac{\pi}{2} a^2 \tilde{E} \cot\alpha$ [161]).

All the models described above only consider elastic bodies and thus are not appropriate to describe polymeric materials that are, instead, viscoelastic.

2.2.3 AFM for viscoelastic measurements

AFM can be also used to probe the viscoelasticity of materials by applying static or dynamic stimuli (see Section 1.2.1) to the sample with the cantilever [104]. As mentioned in Section 1.3, AFM can probe the viscoelastic properties of materials by oscillating the cantilever either on-resonance or off-resonance.

In off-resonance AFM nano/micro-rheology, the cantilever is excited with frequencies well below the cantilever's first resonance frequency [157], providing a way to obtain the viscoelastic spectrum of materials in a potentially large range of frequencies.

From the amplitude and phase of the cantilever's oscillations, it is possible to calculate the viscoelastic properties of the material by the introduction of complex quantities such as the dynamic stiffness $k^* = k' + ik''$ [130, 131]. The real and the imaginary components of k^* are called storage (k') and loss (k'') stiffness, and represent the elastic and viscous component of the material's response, respectively.

As Nalam *et al.* [130] described in their work, the system of a sinusoidally directly actuated cantilever and a sample can be described by equating the force acting on the cantilever when it is out of contact, with the force needed to deform the sample and bend the cantilever during the contact [130]:

$$k_c A_R e^{i(\omega t+\phi_R)} = (k_c + k^*) A_S e^{i(\omega t+\phi_S)} \tag{2.26}$$

where A_R and ϕ_R are the amplitude and the phase of the cantilever when it is out of contact with the sample (reference measurement, see Fig. 2.4 (a)). Similarly, A_S and ϕ_S are the amplitude and the phase of the cantilever when it is in contact with the sample (see Fig. 2.4 (b)). As shown in Fig. 2.4 (a,b) for AFM PT excitation, the PT laser excites the cantilever with a sinusoidal signal.

By rearranging the terms of Eq. (2.26) [130]:

$$k^* = k_c \left[\bar{A}(\cos\Phi + i\sin\Phi) - 1\right] \tag{2.27}$$

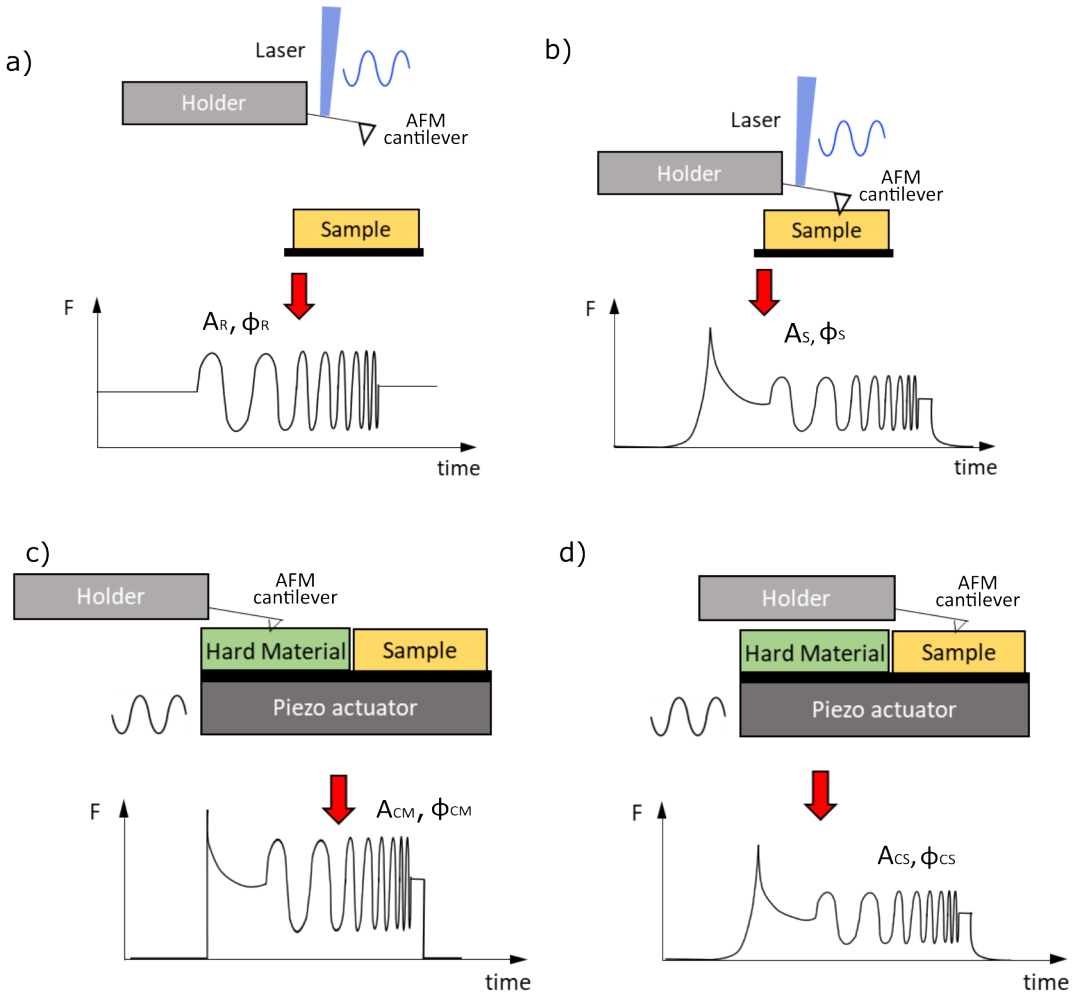


Figure 2.4: PT versus PE AFM cantilever excitation. Schematic diagram of cantilever actuation by PT (via sample modulation) and PE. The respective forces acting on the cantilever are also schematically presented. Panels (a,b) show schematic diagrams, and the respective forces, of a cantilever excited by means of PT actuation when the cantilever is (a) not in contact with the sample (reference measurement, subscript R), and (b) in contact with the sample (subscript S). Panels (c,d) show schematic diagrams, and the respective forces, of a cantilever excited by means of PE actuation (via sample modulation) when the cantilever is (c) in contact with a hard sample (reference measurement, subscript CM), and (d) in contact with the sample (subscript CS). For both PT and PE excitation, the amplitude (A) and phase (ϕ) of the cantilever's response are different between the reference measurement and the measurement on the sample.

where $\bar{A} = A_R/A_S$ and $\Phi = \phi_R - \phi_S$. k' and k'' can be determined as the real and the imaginary component of k^*, respectively, [130]:

$$\begin{aligned} k' &= k_c \left[\bar{A}\cos\Phi - 1\right] \\ k'' &= k_c \bar{A}\sin\Phi \end{aligned} \tag{2.28}$$

Igarashi *et al.* [131] proposed the following method to calculate k^* of a viscoelastic sample measured with the cantilever excited with PE actuation. This method relies on comparing signals obtained with the cantilever on the sample (subscript CS) and on a hard substrate (subscript CM) [131]. A schematic representation of the PE actuation is presented in Fig. 2.4 (c,d). The oscillatory deformation of the sample d is given by [131]:

$$\begin{aligned} d &= z_{CM} - z_{CS} \\ &= A_{CM}\ \cos(\omega t + \phi_{CM}) - A_{CS}\ \cos(\omega t + \phi_{CS}) \\ &= A_S\ \cos(\omega t + \phi_S) \end{aligned} \tag{2.29}$$

where A_{CS} (A_{CM}) and ϕ_{CS} (ϕ_{CM}) are the amplitude and the phase of the cantilever oscillations on the sample (on the hard substrate), respectively. A_S and ϕ_S are the amplitude and phase of the sample's deformation and can be calculated as follows [131]:

$$A_S = \sqrt{A_{CM}^2 + A_{CS}^2 - 2A_{CM}A_{CS}\ \cos(\phi_{CS} - \phi_{CM})} \tag{2.30}$$

$$\phi_S = \arctan\left(\frac{A_{CM}\ \sin(\phi_{CM}) - A_{CS}\ \sin(\phi_{CS})}{A_{CM}\ \cos(\phi_{CM}) - A_{CS}\ \cos(\phi_{CS})}\right) \tag{2.31}$$

For an oscillating signal, k^* can be expressed as [131]:

$$\begin{aligned} k^* &= \frac{k_c z_{CS}}{d} \\ &= \frac{k_c A_{CS} e^{i(\omega t + \phi_{CS})}}{A_S e^{i(\omega t + \phi_S)}} \\ &= k_c \frac{A_{CS}}{A_S} e^{i(\phi_{CS} - \phi_S)} \end{aligned} \tag{2.32}$$

from which [131]:

$$\begin{aligned} k' &= k_c \frac{A_{CS}}{A_S} \cos(\phi_{CS} - \phi_S) \\ k'' &= k_c \frac{A_{CS}}{A_S} \sin(\phi_{CS} - \phi_S) \end{aligned} \tag{2.33}$$

$\tan\delta$ can be calculated as [131]:

$$\tan\delta = \frac{k''}{k'} \tag{2.34}$$

As said in Section 1.2, $\tan\delta$ does not depend on the geometry of the system [23], since the geometrical contributions implicit in k' and k'' are cancelled.

Igarashi *et al.* in their studies of rubbery materials [131] used the following expressions to convert k^* in E^*:

$$\begin{aligned} E' &= \frac{1-\nu_S^2}{2a_1} k' \\ E'' &= \frac{1-\nu_S^2}{2a_1} k'' \end{aligned} \tag{2.35}$$

$$\begin{aligned} E' &= \frac{1-\nu_S^2}{2a_1} k' \frac{1 - 1/6(a_0/a_1)^{3/2}}{1-(a_0/a_1)^{3/2}} \\ E'' &= \frac{1-\nu_S^2}{2a_1} k'' \frac{1 - 1/6(a_0/a_1)^{3/2}}{1-(a_0/a_1)^{3/2}} \end{aligned} \tag{2.36}$$

where Eq. (2.35) was obtained for a Hertzian contact and Eq. (2.36) for a JKR contact [131]. a_0 and a_1 correspond to the contact radii of two particular points of a force curve, as illustrated in Fig. 2.3.

The presence of adhesion complicates the equations, as it can be observed from Eqs. (2.35) and (2.36). Nevertheless, studies have shown that for dynamic experi-

ments on viscoelastic materials in the presence of adhesion forces, if the frequency of the oscillations is high enough, a might remain constant during the oscillations [171, 172]. Viscoelastic effects can therefore make indenters of different shapes, although subjected to adhesion forces, behave like a flat cylindrical punch (i.e. constant contact radius during the oscillations) [171, 172]. In this case, the relationship between E^* and k^* can be simply expressed as $\tilde{E}^* = k^*/(2a)$ (referred as flat punch stiffness from now onwards), similarly to Eq. (2.35), even in the presence of adhesion [171, 172].

To convert k^* values into E^* values is then necessary to calculate a, which can be achieved with the models described in Sections 2.2.2.1 and 2.2.2.2, depending on the presence of adhesion forces.

2.2.4 Chirp signals for broad and continuous AFM viscoelastic spectra

Most studies use single frequency sinusoidal signals to excite the cantilever, which results in a discontinuous viscoelastic spectrum [117–122, 124, 130–134]. However, a few studies use chirp signals in place of single frequency sinusoids to measure the viscoelastic spectrum of a material [123, 125, 126, 173]. Chirp signals have already been employed for PE-AFM rheology to provide continuous and wide frequency range spectra up to 10 kHz [126, 173] or 30 kHz [123].

Chirp signals are frequency modulated signals, where the frequency varies with time. A chirp signal can be described in terms of the instantaneous phase (Ω) at a given time (t) as follows [174–176]:

$$x(t) = A\sin(\Omega(t)) \tag{2.37}$$

where A is the chirp signal amplitude. $\Omega(t) = \omega t + \phi$, with $\omega(t) = \dfrac{d\Omega(t)}{dt}$ being the instantaneous angular frequency, and ϕ a static phase. The instantaneous frequency is $f(t) = \omega(t)/(2\pi)$.

For linear chirp signals, the instantaneous frequency increases (chirp up) or decreases (chirp down) linearly with time [174–176]:

$$f(t) = f_0 + c_1 t \tag{2.38}$$

where $c_1 = (f_f - f_0)/T$, with T being the interval of time to go from the starting frequency f_0 to the final frequency f_f.

For logarithmic chirp signals (also called exponential), the instantaneous frequency varies as follows [176]:

$$f(t) = f_0 c_2^t \tag{2.39}$$

with $c_2 = (f_f/f_0)^{1/T}$.

A linear and a logarithmic chirp signals (with an initial frequency $f_0 = 1\,\text{Hz}$, final frequency $f_f = 100\,\text{Hz}$, and chirp duration $T = 30\,\text{s}$) are compared in Fig. 2.5. Panel (a) shows the two chirp signals in the time domain. A zoomed in portion of the first few seconds of the signals is plotted in the inset. Clearly, the logarithmic chirp sweeps more slowly through the low frequencies compared to the linear chirp. The fast Fourier transform (FFT) magnitude of the signals is presented in Fig. 2.5 (b). The spectrum is continuous through the entire frequency range for both the linear and the logarithmic chirp. The lobes typical of chirp signal FFT [174–176] are evident especially at the edges of the frequency range. Nevertheless, chirp signals provide a useful tool to excite the cantilever over a broad and continuous range of frequencies. The frequency modulation over time of the linear and logarithmic chirp signals is shown in Fig. 2.5 (c,d).

The advantage of having broad and continuous spectra over discrete spectra, make

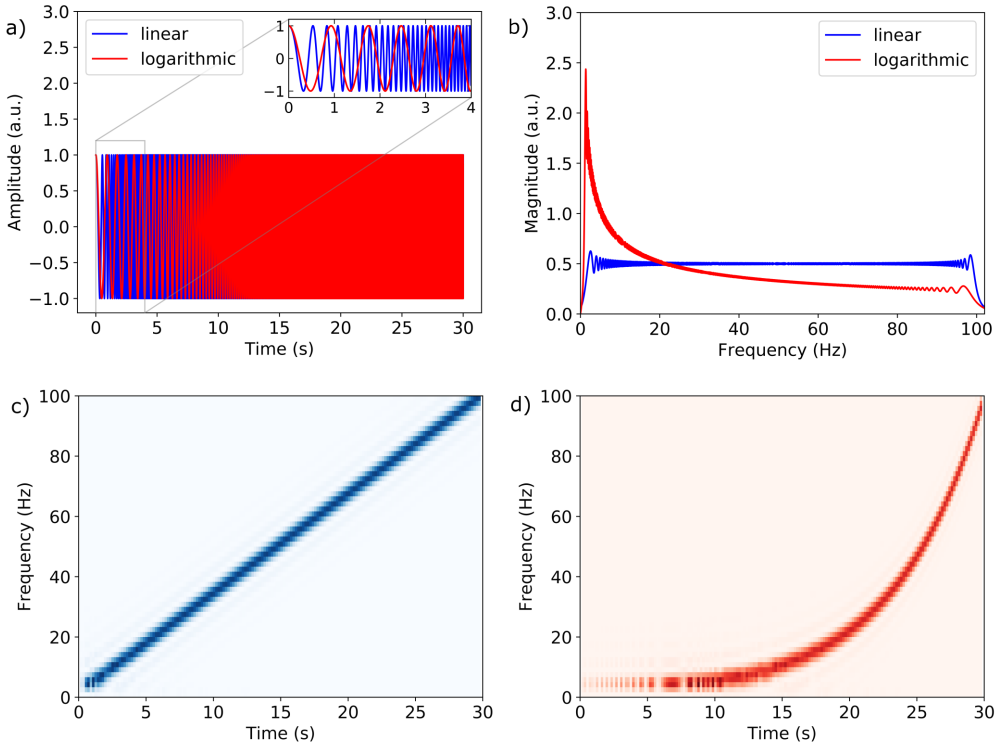


Figure 2.5: Comparison between linear (blue line) and logarithmic (red line) chirp signals. Panel (a) compares chirp signals (with an initial frequency $f_0 = 1\,\text{Hz}$, final frequency $f_f = 100\,\text{Hz}$, and chirp duration $T = 30\,\text{s}$) in the time domain. A zoomed in portion of the first few seconds of the signals is shown in the inset. Panel (b) shows the FFT magnitude of these signals. Panel (c) shows the frequency over time for the linear chirp, while (d) shows the same for the logarithmic chirp.

chirp signals an ideal choice for exciting the cantilever for the PT-AFM nano/micro-rheology technique (see Chapter 6).

2.3 Electron microscopy (EM)

EM uses a beam of electrons of energy in the keV range as a source to study the topography and the composition of materials. The electron beam is focused on the sample and scanned through a portion of the sample. The different electron-matter interactions that occur when electrons pass through a material are used to characterise the morphology and the composition of the specimen [177, 178]. In Chapters 4 and 5, SEM and EDS were used to study the topography and the chemical composition of materials, respectively.

2.3.1 Scanning electron microscopy (SEM)

SEM can be used to study the topography of materials with a resolution down to the nanometre scale [177, 178]. SEM takes advantage of backscattered and secondary electrons produced when an electron beam interacts with the sample. The operating principle is the following: an electron beam is focused and scanned onto the sample, where the interactions between the specimen and the electrons leads to the emission of electrons. Backscattered electrons are produced by the elastic scattering of the primary electrons of the beam with the sample. Secondary electrons are, instead, due to inelastic scattering of the primary electron with the sample. These secondary electrons have a much lower energy than the backscattering electrons (smaller than tens of keV) and are representative of the most superficial atoms of the sample. Usually detectors with different sensitivity are used to measure backscattered and secondary electrons. From the detector, the signals are digitalised and converted into an image.

2.3.2 Energy-dispersive X-ray spectroscopy (EDS)

The chemical composition of a specimen can be studied with EDS [177, 178]. An electron bombarding an atom in the sample can cause the atom's ionisation via the removal of an electron from an inner shell, creating a hole. An electron from an outer level can transit from its original shell to the vacancy emitting photons with energy equal to the difference in energy of the two shells (X-rays). The emitted X-rays are measured by a spectrometer forming a spectrum. The peaks in the spectrum correspond to the energy of the electron transitions that are typical for each atom and can therefore be used to study the specimen's composition.

2.4 Vibrating sample magnetometry (VSM)

VSM allows measurements of the magnetic moment of samples [179, 180]. It works by oscillating the sample at a certain frequency in a constant external magnetic field perpedicular to the motion of the sample. The external magnetic fields induces magnetisation in the sample. The oscillating magnetic field produced by the movement of the magnetised sample induces a voltage in the detection coils, used as detectors. The voltage in the detection coils is proportional to the magnetic moment of the specimen [179, 180]. By varying the magnitude of the external magnetic field, the magnetisation of the sample can be studied and, for example, the hysteresis curve of ferromagnetic materials can be obtained. In this thesis, VSM was used to study the magnetic properties of materials in Chapters 4 and 5.

2.5 Dynamic mechanical analysis (DMA)

DMA has become the "standard" to study the response of solid macroscopic materials to an oscillatory stimulus and calculate the macroscopic viscoelastic properties of the

sample [19, 23]. As explained in Section 1.2.1, when a sinusoidal stress is applied to a viscoelastic material, the material responds with a deformation that has the same frequency as the excitation, but with its phase shifted (lag). DMA instruments measure the sinusoidal force and the displacement experienced by a specimen, allowing calculation of viscoelastic parameters such as E', E'', and $\tan\delta$. They normally operate at relatively low frequencies (0.01 Hz to 200 Hz) but have a wide temperature range of measurement (−150 °C to 400 °C). By performing isothermal sweeps over a range of isothermal temperatures, viscoelastic behaviour of a material can be extended to considerably higher (and lower) frequencies using the TTS principle, as explained in Section 1.2.2. Depending on the measuring geometry of the DMA analyser, it is possible to apply a bending, axial, or shearing stimulus to calculate the dynamic modulus E^* or the dynamic shear modulus G^* of a sample [19, 23]. In this study an axial geometry was chosen to calculate E^*: DMA in tension mode was employed, because of its suitability to study E^* of viscoelastic solids [19, 23].

In DMA tension mode, the macroscopic sample is clamped at both ends: one end is kept fixed, while the other one is stretched sinusoidally by the clamp. The sinusoidal force F and sample displacement x are measured. For a sample with rectangular geometry with stimulus applied across the sample's length (L), E' and E'' can be calculated as follows [19, 23]:

$$E' = \frac{F_0}{bx_0}\cos\delta \tag{2.40}$$

$$E'' = \frac{F_0}{bx_0}\sin\delta \tag{2.41}$$

where F_0 and x_0 are the force and the displacement amplitude of the two sinusoidal signals, respectively, δ is the phase angle between F and x, and $b = Wh/L$, with h and W being the thickness and width of the sample, respectively. With DMA in tension mode it is possible to use long thin samples, so that b is small [19]. For high-

moduli samples ($> 10^8$ Pa), small b keeps the stiffness of the sample below that of the experimental apparatus [19]. Also, since DMA in tension mode applies a lengthwise stimulus to the sample, it can accommodate changes in sample length due to thermal expansion when T is altered during the experiment. In this thesis, DMA was used to study the macroscopic viscoelastic properties of materials in Chapter 6.

Chapter 3

Materials and Methods

3.1 Introduction

In this chapter, the experimental details of the materials (Section 3.2) and the methods (Section 3.3) used for the experiments in Chapter 4 through Chapter 7 are described. Section 3.4 lists collaborator contributions to the work in this thesis. Most data analysis and visualisation in this thesis were done using Python [181] with home-built codes. My Python home-built codes made use of the Csv [182], ForceMetric [183], Glob [184], Io [185], Matplotlib [186], NumPy [187], Os [188], Pandas [189], PIL [190], SciPy [191], Seaborn [192], Si_prefix [193], and SymPy [194] Python libraries/modules/packages.

3.2 Materials

3.2.1 Chitosan-based hydrogels

Chitosan hydrogels used in Chapter 4 were prepared by dissolving 0.5 % weight over volume (w/v) chitosan (Sigma-Aldrich, 448877, molecular formula $C_{56}H_{103}N_9O_{39}$) in 50 mM acetic acid by magnetic stirring for 6 h. Undissolved chitosan was removed

by centrifugation for 10 min. 0.23 M genipin (Challenge Bioproducts Co., molecular formula $C_{11}H_{14}O_5$) was added to the chitosan solution. The solution was then magnetically stirred for 1 h. Afterwards, the solution was poured in circular moulds 1.3 cm in diameter, frozen at −80 °C for 30 min, and freeze dried (SP Industries VirTis Benchtop 2K) at −75 °C in a range of 0.1 mtorr to 10 mtorr until completely dried (at least 30 h). Lastly, samples were cured at 37 °C for 24 h [195]. After this procedure, the resulting chitosan samples were cylindrical, with a diameter of approximately 1.3 cm, and a thickness of approximately 0.5 cm.

Chitosan composite hydrogels used in Section 5.2 were prepared following the same protocol described above, with the addition of 0.1 % w/v Fe_3O_4 nanowires to the chitosan solution, followed by a water sonication bath and vortexing for a few seconds to homogenise the solution. After pouring the solution into 1.3 cm diameter moulds, sample were frozen at −80 °C. Samples were frozen in the presence of a 180 mT external magnetic field to give a horizontal orientation to the nanowires (see Fig. 3.1). Chitosan composite hydrogels with randomly oriented wires were frozen without an external magnetic field.

The Fe_3O_4 nanowires used for these chitosan composite samples were synthesised by Dr. Ileana Andrea Bonilla Brunner (former DPhil student in Prof. Contera lab, Department of Physics, University of Oxford) and are described in refs. [196, 197].

3.2.2 PNIPAAm-based hydrogels

1 % w/v poly(N-isopropylacrylamide) (PNIPAAm) hydrogels used in Chapter 4 were synthesised via ultraviolet (UV) irradiation [198]. PNIPAAm samples were prepared mixing 1 % w/v NIPAAm (Sigma-Aldrich, 415324), 5 % w/v poly(ethylene glycol) diacrylate (PEGDA) (Sigma-Aldrich, 455008), and 2.5 % w/v H_2O_2 (Sigma-Aldrich, 18304) in ultrapure (Milli-Q) water and magnetically stirred for 10 min. Afterwards, the solution was poured into 1.3 cm diameter molds and frozen at −80 °C

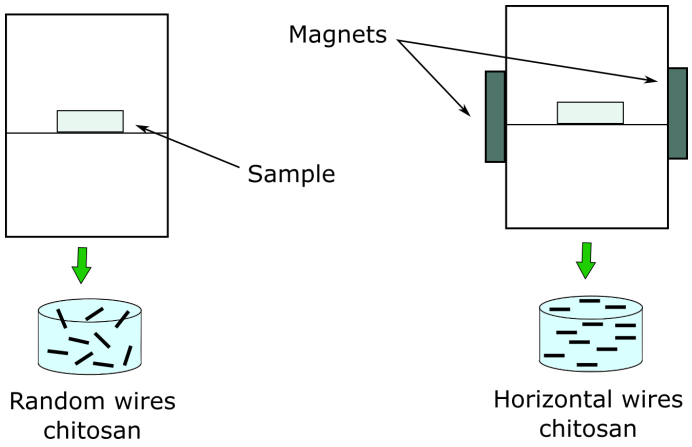


Figure 3.1: Schematic representation of the freezing process for chitosan composite hydrogels. No external magnetic field was used to create chitosan composite hydrogels with randomly oriented wires. An external magnetic field was used to create chitosan composite hydrogels with horizontally oriented wires.

for 30 min. The frozen samples were then crosslinked by UV irradiation at 302 nm (UVP UV/White Transilluminator) for 5 min.

3.2.3 PDMS elastomer

Polydimethylsiloxane (PDMS) (Sylgard® 184 Dow-Corning) elastomer used in Chapter 4 was synthesised using a mixing ratio of 10 : 1 for base and curing agent [199], and was manually stirred. The solution was poured into aluminium foil moulds, and desiccated for 30 min to remove air bubbles within the polymeric matrix to obtain a homogeneous sample. Lastly, samples were cured at 110 °C for 6 hour [199]. Samples were then cut in squares of about 1 cm(L)×1 cm(W)×0.4 cm(h).

3.2.4 Fullerene-based hydrogels

Fullerene-based hydrogels used in Section 5.3, were synthesised by Dr. Ilija Rašović (former DPhil student in the Department of Materials, University of Oxford), as detailed in ref. [200].

Briefly, C_{60}, C_{84}, or C_{90-92} fullerene cages were isolated, dissolved in toluene, and

sonicated for 10 min. triethylene glycol (TEG)-monoethyl ether (MEE) and an NaOH pellet were then added, after which the solution was magnetically stirred for 21 h at room temperature. Next, ethyl acetate was added to the solution. A precipitate of TEGylated fullerenes was then formed by leaving the solution overnight at 2 °C. The precipitate was filtered and vacuum dried, resulting in a brown powder. The powder was then diluted with deionised water and stored in sealed vials in a dark cupboard for up to six months to allow spontaneous hydrogel formation. The resulting hydrogels (of organised C_{60}, C_{84}, and C_{90-92} fullerenes) were a few millimetres in size. For brevity, hydrogels will be named after the fullerene cage used (i.e. C_{60}, C_{84}, and C_{90-92} hydrogels).

3.2.5 Styrene-butadiene rubber

A random copolymer made of styrene and butadiene (SBR) with a glass transition temperature around −13 °C was used as a test material in Chapter 6. SBR was chosen because it is a commonly used material for AFM mechanical measurements [117, 131–134]. This is a useful sample for nano/micro-rheology AFM experiments thanks to its glass transition that at room temperature occurs in the kHz frequency range [131–134]. Therefore SBR is convenient for AFM nano/micro-rheology measurements because this frequency range is achievable with the AFM used in this study.

3.2.6 Poly(HEMA) hydrogels

Poly(2-hydroxyethyl methacrylate) (poly(HEMA)) hydrogels used in Section 7.2 were synthesised and prepared for the experiments by Ms. Casey Adam (Prof. Contera lab, University of Oxford). Sample were synthesised following the procedure described in ref. [201]. Briefly, poly(HEMA) (Sigma-Aldrich, P3932) was dissolved in ethanol, deposited on a coverslip to dry, and lastly poly(HEMA) hydrogels were left 30 min in liquid (4-(2-hydroxyethyl)piperazine-1-ethanesulfonic acid (HEPES) buffered phos-

phate buffered saline (PBS)) to swell before the experiments. Poly(HEMA) hydrogels were synthesised at two different concentrations per unit surface area of the sample: 1.14 mg of poly(HEMA) per cm^2, and 11.4 mg of poly(HEMA) per cm^2.

3.3 Methods

3.3.1 SEM and EDS

FEI Quanta 600 FEG was used to perform SEM and EDS studies on chitosan-based dry hydrogels used in Chapter 4 and Section 5.2. Dry samples were fixed to the SEM pin stub with carbon tape and their topography was imaged by SEM. EDS was performed on the chitosan sample to study its chemical composition. EDS data visualisation was performed in Python [181] with a home-built code.

3.3.2 VSM

A VSM (PPMS VSM, Quantum Design) was used for the magnetic characterisation of the chitosan-based samples used in Chapter 4 and Section 5.2. A dry plain chitosan hydrogel (6.5 mg mass) and a dry chitosan composite hydrogel (6.9 g mass) were used for VSM experiments. Each sample was pushed into a capsule and the rest of the capsule was filled with cotton, to avoid sample movements during the measurements. The capsule was then inserted in a plastic straw and placed in the VSM. The background magnetic moment was measured using a capsule filled only with cotton and subtracted during the data analysis. The magnetic field was varied from -50 kOe to 50 kOe at 300 K. To be noted is that any original alignment of the Fe_3O_4 nanowires within the composite hydrogel is lost because of the way the sample is pushed and compressed into the capsule for VSM experiments. The sample used was therefore a dry chitosan composite hydrogel that originally had randomly oriented wires. Data analysis and visualisation were performed in Python [181] with a home-built code.

3.3.3 AFM

Samples in Chapters 4 and 5 were probed with quasi-static force indentation curves in liquid performed using a commercial MFP-3D AFM (Oxford Instruments Asylum Research) using modified AC240 cantilevers (Olympus, nominal spring constant $2\,\mathrm{N\,m^{-1}}$, resonance frequency 70 kHz).

In Chapter 6 and Section 7.2, a Cypher ES AFM (Oxford Instruments Aslylum Research) was used to perform AFM experiments.

In Chapter 6, two different Cypher AFM chassis and scanners were used for the experiments, depending on their availability. AC160TSA-R3 (Olympus, nominal spring constant $42\,\mathrm{N\,m^{-1}}$, resonance frequency 300 kHz, tip radius 7 nm, tetrahedral tip shape) cantilevers were used unless otherwise specified. All experiments were conducted in air. The ambient temperature of the Cypher ES AFM is measured from the software at the base of the chassis and it was around 31 °C for the experiments conducted for this thesis. The SBR sample dimensions measured in Chapter 6 were approximately $3\,\mathrm{mm}(L)\times3\,\mathrm{mm}(W)\times3\,\mathrm{mm}(h)$, and $2\,\mathrm{mm}(L)\times2\,\mathrm{mm}(W)\times3\,\mu\mathrm{m}(h)$.

Each cantilever used for AFM experiments was calibrated indenting a hard substrate to calculate the OLS (see Section 2.2), and using the thermal noise method to calibrate the cantilever stiffness [202].

Cantilever calibration and data acquisition were done using the Oxford Instruments Asylum Research software based on Igor Pro. Data analysis and visualisation were performed in Python [181] with home-built codes. The contact point for each curve was obtained using the force-indentation variation (FIV) method [203, 204] developed by Dr. Jacob Seifert (in Kienast) (former DPhil student in the Department of Plant Sciences/Physics Department, University of Oxford) at Prof. Contera lab (University of Oxford). My Python scripts for the AFM data analysis used for this thesis included the Python library ForceMetric [183], developed by Dr. Seifert, for AFM data loading, contact point determination, and calculation of the Young's modulus

with the Hertz model and Sneddon model for conical indenter (Section 2.2.2.1) in Chapters 4 and 5. Given the difficulty in isolating the contact radius in the equation for hyperboloidal (Eq. (2.17)) and conical (Eq. (2.12)) indenters, the Python SymPy library [194] was used to calculate the contact radius from Eqs. (2.12) and (2.17).

3.3.3.1 AFM quasi-static force indentation curves

Dry chitosan hydrogels used in Chapter 4 were fixed in 5.5 cm diameter plastic petri dishes with epoxy (Double Bubble Loctite) on top of double-sided tape stuck to the petri dish. The double-sided tape was used for moving the sample, if needed, without breaking it, by peeling the tape from the petri dish. Once the adhesive dried, samples were rinsed at least three times with ultrapure (Milli-Q) water. Hydrogels were left equilibrating in ultrapure (Milli-Q) water for at least one week. The week of equilibration was necessary because force indentation experiments of chitosan hydrogels before this equilibration time was experimentally more challenging, likely because the hydrogels had not reached their swelling equilibrium [204].

PDMS was plasma cleaned (Harrick Plasma PDC-002 (230V)) for 1 min to make it more hydrophilic [205] before sticking it.

A (49.21 ± 0.72) µm glass microsphere (Whitehouse Scientific) was attached to the cantilever with glue (Flex+Bond, Weicon) by dipping the cantilever's free end in the glue then the glue-coated tip into a glass bead immediately thereafter. The modified cantilevers were left to dry overnight.

In order to assess the effect of an external magnetic field on the samples, initially a permanent magnet was manually placed and removed from a hole in the AFM stage underneath the sample. This procedure increased the risk of breaking the cantilever and could inadvertently cause accidental movements of the sample while manoeuvring the magnet. To resolve these issues for later experiments, an electromagnet (First4magnets) was fitted underneath the sample and switched on and off, providing

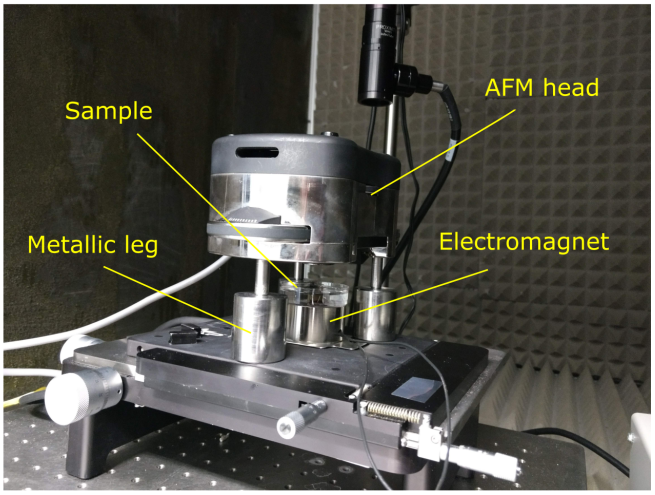


Figure 3.2: AFM set up for the magnetic indentation experiments: an electromagnet was placed underneath the sample and switched on and off. The AFM head was raised with the help of metallic legs.

an external magnetic field (B) perpendicular to the surface of the sample. The field strength was 45 mT at the sample height (≈0.5 cm), measured with a gaussmeter. The sample petri dish was fixed on the electromagnet with double-sided tape. The AFM head was raised above the electromagnet with the help of custom-made 10 cm high metallic legs. The AFM set-up used for the magnetic experiments is shown in Fig. 3.2. Only quasi-static force indentation experiments (not imaging) were feasible with this set-up.

For each sample several positions were indented with ($B \neq 0$)and without ($B = 0$) B. For each position, quasi-static force curves were obtained at three different cantilever approach (and withdraw) velocities of 10 µm s^{-1}, 25 µm s^{-1} and 50 µm s^{-1}. A force trigger point (point of maximum force) of 100 nN was used. 15 force curves were obtained for each configuration (velocity and magnetic field on/off). To avoid heating of the electromagnet, experiments were periodically interrupted to let the system cool down.

Experiments were conducted at room temperature both in ultrapure (Milli-Q) water and in a salt solution (PBS) (1xPBS, Sigma-Aldrich, P3813, 136.9 mM NaCl, 2.7 mM

KCl, 1.6 mM KH_2PO_4, 8.1 mM Na_2HPO_4, pH 7.4) filling the petri dishes above the height of the sample.

Glass slides layered to reach approximately the same height as the above mentioned polymeric materials were used as a control for the experiments in ultrapure (Milli-Q) water and 1xPBS.

For the chitosan composite hydrogels used in Section 5.2, the same AFM setup described above was used. AFM quasi-static force indentation experiments were performed in 1xPBS at $50\,\mu m\,s^{-1}$. For each sample, several positions were tested. On each position, 100 force curves were performed for each configuration ($B = 0$, $B \neq 0$).

Fullerene-based hydrogels used in Section 5.3 were glued (with either medical adhesive (Hollister) or epoxy (Double Bubble Loctite)) on top of double-sided tape and stuck to plastic containers. After the adhesive dried, samples were immersed in ultrapure (Milli-Q) water. The cantilever was modified with a $(20.0 \pm 0.3)\,\mu m$ diameter polystyrene bead (Sigma-Aldrich, 74491) glued to the tip as described above. Indentations were performed in ultrapure (Milli-Q) water at room temperature, using a trigger point of 70 nN. High indentation velocities ($40\,\mu m\,s^{-1}$) were used to reduce the time-dependent behaviour of the hydrogels [204, 206]. At least 5 positions were tested on each sample. For each position, 100 force curves were recorded.

The elastic properties of materials studied in Chapters 4 and 5 were quantified by fitting the approach curves between 30 nN to 45 nN with the Hertz model (see Section 2.2.2.1). The choice of the Hertz model was based on the fact that the indenters used for experiments in Chapters 4 and 5 were spherical with radii much larger than the indentations applied to the samples (hundreds of nanometres up to few microns), thus satisfying the Hertz assumption (see Section 2.2.2.1).

In AFM quasi-static force indentation curves used in Chapter 6, the following parameters were used. The force trigger point was set to 100 nN, with a withdraw distance of 3 µm. Some curves were shifted manually when the FIV method [203, 204] failed

to recover the right contact point. To compare quasi-static force indentation curves obtained with and without the photothermal excitation laser (PT-EL) focused on the back of the cantilever the cantilever approach (and withdraw) velocity was set to $1\,\mu m\,s^{-1}$, and a direct current (DC) voltage of 4 V was applied to the PT-EL and was switched on/off for the measurements. To compare force curves with different cantilever approach (and withdraw) velocities, the cantilever's velocities used were $0.1\,\mu m\,s^{-1}$, $1\,\mu m\,s^{-1}$, $10\,\mu m\,s^{-1}$, $50\,\mu m\,s^{-1}$ and $100\,\mu m\,s^{-1}$, and the PT-EL was focused on the cantilever with a DC voltage of 4 V.

Paired t-tests in this thesis were performed in Python [181] using the SciPy library [191].

3.3.3.2 AFM stress relaxation

AFM stress relaxation experiments in Chapter 6 were performed setting the AFM feedback loop on the Z-piezo, in order to maintain a constant deformation (see Section 6.4) during the dwell time (the time that the AFM cantilever spends in contact with the sample after the trigger point is reached and before the cantilever starts retracting from the sample). A force trigger point of 100 nN was used, with cantilever approach and withdraw velocity of $1\,\mu m\,s^{-1}$. A withdraw distance of 3 µm was used. The dwell time was set to 60 s. A voltage of 4 V was applied to the PT-EL for the duration of the measurements.

3.3.3.3 AFM nano-DMA

This section describes the experimental parameters used in Chapter 6 to perform AFM nano/micro-rheology, called AFM nano-DMA from now onwards. AFM nano-DMA was achieved by exciting the AFM cantilever with chirp signals after indenting the sample.

The following parameters were used for the initial indentation unless specified oth-

erwise. The force trigger point was set to 100 nN. The approach time was set to 5 s. The approach time includes the cantilever's approach to the sample and a pause (lasting a few seconds) to allow the sample to relax before the oscillations begin [125]. The cantilever approach and withdraw velocity from the sample was set to 1 µm s^{-1}. The oscillating chirped excitation signal was applied to the cantilever after the approach time. The position of the Z-piezo at the back of the cantilever was kept constant via the AFM feedback loop (with feedback on the Z sensor) after the desired trigger point was reached. Data were acquired both by recording the signals in the time domain (called time signals (TS) from now onwards) and by a lock-in amplifier (LIA) (see Appendix B for more details).

The final, broad frequency range of the AFM nano-DMA data was achieved by "sewing" together several logarithmic chirp signals of different frequency ranges (cfr. Appendix C for the choice of logarithmic chirp signals). The entire, broad frequency range was not performed in a single chirp in order to avoid software crashes caused by processing large amounts of data. Three main frequency ranges were used for the AFM nano-DMA chirps: 0.1 Hz to 10.1 Hz, 1 Hz to 1001 Hz, and 200 Hz to 20 200 Hz, with sweep times of 180 s, 30 s and 1 s, respectively. For each frequency range, the sampling rate was set accordingly by the highest frequency. For the three main frequency ranges, the sampling rates were respectively 1000 Hz, 10 000 Hz and 500 000 Hz for the TS, and $27.\bar{7}$ Hz, $166.\bar{6}$ Hz and 5000 Hz for the LIA measurements. The LIA low-pass filter (LPF) time constant was chosen based on the lowest frequency of the frequency range (0.05 Hz, 0.5 Hz and 100 Hz, for the above mentioned ranges, respectively).

After the end of the sweep time, the tip was withdrawn from the sample. The withdraw distance was set to 3 µm.

AFM nano-DMA experiments were performed with both PT and PE actuation.

For the data analysis, some curves were shifted manually when the FIV method [203,

204] failed to recover the right contact point.

PT-AFM nano-DMA

For PT-AFM nano-DMA experiments, the blueDrive^{TM} of the Cypher ES AFM (blueDrive^{TM}, Oxford Instruments Asylum Research, 405 nm), consisting in a blue laser, was used as the PT-EL. The PT-EL was focused at the base of the AFM cantilever (see Fig. 2.4 and Section 6.5.1 for more details) and its power was modulated to achieve the desired excitation signal features (e.g. frequency, amplitude). The PT-EL power was modulated using the "filter cubes" available for the Cypher AFM. The number associated with the filter cube represents the gain factor of the cube, e.g. a 1 x filter cube represents no reduction in the PT-EL power, a 0.1 x filter cube reduces the PT-EL power to 10 %, etc..

In Chapter 6, a 1 x filter cube was used unless otherwise specified. The DC voltage applied to the PT-EL photodiode was chosen accordingly from the PT-EL operating range. In most of the experiments the DC voltage was set to 4 V. The alternating current (AC) voltage applied to the PT-EL was 1 V unless otherwise specified. Reference measurements were taken at approximately 500 µm or higher above the sample. Preliminary PT-AFM nano-DMA data in liquid shown in Section 7.2, were obtained using an AC240TSA-R3 cantilever (Olympus, nominal spring constant 2 N m^{-1}, resonance frequency 70 kHz, tip radius 7 nm, tetrahedral tip shape). The setpoint was kept below 20 nN, the approach time was set to 5 s, the cantilever approach (and withdraw) velocity to 1 µm s^{-1}. The frequency ranges used for the chirps were 1 Hz to 1001 Hz and 1000 Hz to 11 000 Hz, with sweep times of 30 s and 1 s, sampling rates of 10 000 Hz and 500 000 Hz (TS) and 166.$\bar{6}$ Hz and 5000 Hz (LIA), LIA LPF time constants of 0.5 Hz and 500 Hz, respectively. The DC voltage applied to the PT-EL photodiode was set to 5 V, the filter cubes and drive amplitudes where chosen to keep similar amplitudes for the reference signals.

PE-AFM nano-DMA

For experiments in Chapter 6, PE-AFM nano-DMA was performed by placing an external piezo actuator (PL088.31 PICMA® Chip Actuators, Physik Instrumente Ltd, $10\,\mathrm{mm}(L)\times10\,\mathrm{mm}(W)\times2\,\mathrm{mm}$ (h)) underneath the sample, similarly to other studies [118, 122, 131, 132].

The sample was prepared in the following way: the piezo actuator was fixed to a magnetic metallic disk with double-sided tape. The SBR sample (size approximately $2\,\mathrm{mm}(L)\times2\,\mathrm{mm}(W)\times3\,\mu\mathrm{m}(h)$) and a thin glass slide (for reference measurements) were secured in close proximity to one another, on another metallic disk. The disk containing the sample and the glass was then fixed with double-sided tape on top of the piezo actuator. The choice of using double-sided tape instead of a stronger glue was made in order to be able to reuse the piezo actuator, which would be non reusable otherwise. The thin glass slide was chosen as reference instead of the metallic disk in order to avoid the possibility of the metal's roughness affecting the measurements. A schematic diagram of this configuration is shown in Fig. 3.3 (a).

The piezo actuator was connected to the AFM electronics via a BNC cable with crocodile clips, as shown in Fig. 3.3 (b), in order to control the piezo actuator motion from the AFM software. The crocodile clips were covered with aluminium foil to avoid damaging the piezo actuator wires. The AC voltage applied to the piezo actuator was 1 V.

For this experiment, a Cypher VRS AFM scanner (Oxford Instruments Aslylum Research) was used. For this experiment, it was possible to measure the temperature at the sample stage which was $\approx 33\,^{\circ}\mathrm{C}$.

3.3.4 Simulations

Simulations in Section 6.3 were performed in Python [181] with a home-built code.

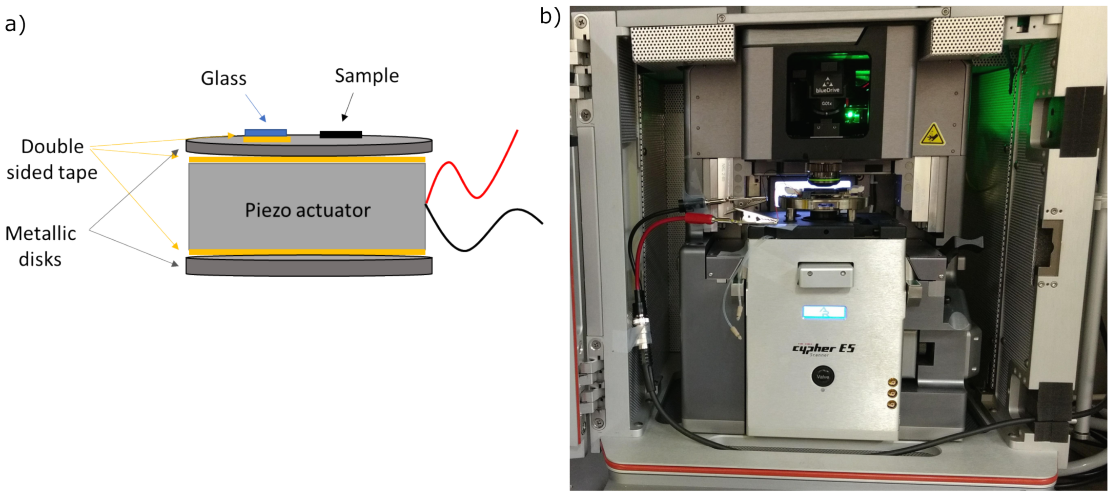


Figure 3.3: Setup for indirect actuation by means of a piezo actuator. (a) Schematic drawing of the sample preparation for piezo actuation. (b) AFM set-up for piezo actuation. The piezo actuator wires are connected to the AFM via crocodile clips.

3.3.5 DMA

For DMA experiments in Chapter 6, a dynamic mechanical analyser (DMA Q800, TA Instruments) was configured with the tension clamps (see Section 2.5) to measure the macroscopic viscoelastic properties of a SBR sample. The sample dimensions were 11.95 mm(L)×4.70 mm(W)×1.30 mm(h). The sample was cooled at −50 °C and held isothermally at this temperature for 20 min. It was then clamped tight at −50 °C (glassy phase) in order to avoid slippage of the sample during deformation. Frequency sweeps at 0.1 Hz, 0.3 Hz, 1 Hz, 3 Hz and 10 Hz were then performed at 2 °C steps from −50 °C to 70 °C. Prior to measurement at each isothermal step, the sample was held for 5 min to ensure thermal equilibrium of the sample. Measurements at all temperatures and frequencies were performed using a tensile strain of 0.1 % to ensure that deformation was within the linear viscoelastic region of the sample. A preload force of 0.01 N was used to measure the initial sample length automatically. Force track was set to 107 %. This ensures that the sample remains flat for the duration of the experiment and is not buckled during deformation.

The shift factors applied for the generation of the TTS master curve were calculated

by means of the TA Instruments Rheology Advantage Data Analysis Software (TA Instruments). The $\tan\delta$ curves obtained from frequency sweeps at the isothermal temperatures were shifted and superimposed to generate the master curve.
Data analysis and visualisation were performed in Python [181] with home-built codes.

3.4 Contributions

Part of study of the magneto-mechanical coupling of plain and composite hydrogels (Chapter 4 and Section 5.2) was done in collaboration with Dr. Ileana Andrea Bonilla Brunner [196]. Together we decided the materials to test, worked together on their synthesis (Sections 3.2.1 to 3.2.3), arranged the AFM set-up for magnetic experiments (Section 3.3.3.1), collected some of the SEM images together, and performed the AFM experiments on the chitosan composite hydrogels (Section 5.2) [196]. Dr. Bonilla Brunner synthesised the magnetic nanowires used in the chitosan composite hydrogels (Section 3.2.1) [196, 197]. The mechanical workshop of the Physics Department of the University of Oxford built the metallic legs for the magnetic AFM apparatus described in Section 3.3.3.1.
SEM and EDS experiments described in Section 3.3.1 were done with the technical support of Dr. Jason Brown (Facility Manager, Physics Department, University of Oxford). VSM experiments described in Section 3.3.2 were done with the help of Dr. Shiv Jee Singh (Physics Department, University of Oxford).
The fullerene-based hydrogel project described in Section 5.3 was done in collaboration with Dr. Ilija Rašović [200]. Dr. Rašović synthesised the samples described in Section 3.2.4, provided the sample images in Figs. 5.6 and 5.7, and quantified the pore/fibre size values of the samples [200] used in Section 5.3.
For the data presented in Chapter 6, DMA experiments described in Section 3.3.5 were done in collaboration with Mr. Nicholas Hawkins who runs the DMA facility

at the Department of Engineering Science (University of Oxford). Dr. Ryan Wagner (former postdoc at Oxford Instruments Asylum Research) worked on the final Igor Pro software version that I used for the data acquisition of AFM nano-DMA measurements in this thesis (Section 3.3.3.3). He used my input to develop this version, and I had worked on previous versions. The comparison between AM-FM AFM and PT-AFM nano-DMA (Section 6.9) was done in collaboration with Ms. Casey Adam. The AM-FM AFM images, and $\tan\delta$ and E' values in Fig. 6.38 were provided by Ms. Adam. Dr. Jacob Seifert (in Kienast) helped with the adaptation of a very preliminary Igor Pro procedure existing in Prof. Contera lab that I used as the starting point for the development of the AFM nano-DMA with the Cypher AFM. Discussions with Dr. Wagner, Dr. Yukinori Taniguchi (Oxford Instruments Asylum Research), and Dr. Roger Proksch (Oxford Instruments Asylum Research) on the theoretical and experimental framework of the AFM nano-DMA are acknowledged.

Preliminary experiments with PT-AFM nano-DMA on poly(HEMA) hydrogels in liquid presented in Section 7.2 were performed in collaboration with Ms. Adam. Ms. Adam synthesised the samples and prepared them for the experiments (Section 3.2.6).

Chapter 4

Effect of an Applied Magnetic Field on the Mechanical Properties of Hydrogels

4.1 Introduction

Smart magnetic hydrogels are promising materials for biomedical applications as described in Section 1.1. Typically, smart magnetic hydrogels are made by incorporating magnetic nano/micro-particles into the hydrogel [29, 77, 78]. The possibility of having plain hydrogels responding to external magnetic fields would supply a new type of magnetic responsive materials for biomedical applications, without the need of introducing magnetic particles that can increase the risk of toxicity and non-biocompatibility of the material [79].

Biological tissues and biopolymers, such as collagen (the main protein component of the ECM), deoxyribonucleic acid (DNA), cellulose, and chitosan, are electroactive, and are piezoelectric [207–211]. This piezoelectricity increases the potential of such molecules for the construction of smart hydrogels in biomedical applications [210,

211], and raises the possibility that biopolymers could also be smart hydrogels for other stimuli such as a magnetic field.

Among biopolymers, chitosan has several characteristics which make it appealing for biomedical applications [139, 140]. First, chitosan is a biopolymer derived by the deacetylation of chitin, the most abundant biopolymer in nature after cellulose [212]. Production of chitosan is sustainable and inexpensive as chitin is found in fungi, fish scales, and the exoskeleton of insects and crustaceans, and can be therefore recycled from food industry waste [213]. Second, the amino groups in the polymeric chains of chitosan can be protonated in acidic conditions, allowing chitosan interactions with mucin, and with the negatively charged phospholipid heads in the cell's plasma membrane [214]. Third, the biocompatibility, biodegradability, and non-toxicity of chitosan make it an appealing material for a wide number of applications, including cosmetics [215], treatment of waste water [216], wound healing [217], drug delivery [218] and tissue engineering [214]. Fourth, as mentioned before, chitosan has already been shown to be electrically responsive by exhibiting piezoelectric behaviour [219–221], thereby making chitosan hydrogels smart, electroactive hydrogels.

Chitosan piezoelectricity makes chitosan hydrogels even more useful for constructing artificial muscles and tissues, since collagen, the main component of the ECM, is also piezoelectric [210, 211]. Being piezoelectric, chitosan is a promising smart material to use for the stimulation of cells with mechanical or electrical cues [31, 210], or the controlled release of drugs from the hydrogel [36]. However, the application of external electrical fields can be problematic, especially in aqueous solutions, because they can cause electrochemical reactions and even damage cells [222, 223]. The possibility of using an external magnetic field as an alternative cue to control the mechanical properties of plain chitosan hydrogels, to the best of my knowledge, has not been tested.

Therefore, the aim of the experiments in this chapter is to test whether chitosan hy-

drogels exhibit magneto-mechanical coupling by testing the local elastic properties of chitosan hydrogels with/without B. As control experiments, the magneto-mechanical coupling of two synthetic polymeric materials, PNIPAAm and PDMS, is also studied. In this chapter I demonstrate that an external magnetic field alters the local elastic properties of chitosan hydrogels, and therefore that such hydrogels exhibit magneto-mechanical coupling. The observations of the magneto-mechanical coupling in chitosan hydrogels open the possibility of creating smart chitosan-based hydrogels which local elastic properties can be remotely modified and controlled with an external magnetic field without the incorporation of magnetic particles.

The chitosan hydrogels for the experiments in this thesis were cross-linked. Chitosan is frequently cross-linked to obtain stable hydrogels for biomedical applications [224]. In this work, chitosan hydrogels were cross-linked using genipin. Genipin is a naturally occurring compound that is extracted from the fruits of *Gardenia Jasminoides Ellis*, that has been long used in traditional oriental medicine [225]. Genipin has a reduced cytotoxicity compared to other synthetic cross-linking agents used for chitosan, such as glutaraldehyde, which makes genipin more suitable for biomedical applications [225].

Even though I have stressed the importance of studying the viscoelastic properties of polymeric materials, further discussed in Section 6.8, this chapter focuses solely on probing the elasticity of these hydrogels. Elasticity is the focus of this chapter (and Chapter 5) because, as discussed in Section 1.1, it is still one of the most used parameters to mechanically characterise polymeric materials for biomedical and biological applications.

4.2 Results

4.2.1 Morphological, chemical, and magnetic characterisation

SEM was used to study the topography of dry chitosan hydrogels. In Fig. 4.1 (a-c), images at three different magnetisations show the porous structure of the polymeric network revealing an inhomogeneous material. EDS was used to study the chemical composition of the chitosan samples. In Fig. 4.1 (d) the EDS spectrum of the material shows the typical C and O peaks at 0.277 keV and 0.525 keV, respectively. C and O are the main components of the chitosan hydrogels (see Section 3.2.1). Possibly, N (typical peak at 0.392 keV) is not evident because of its much lower concentration in the chitosan hydrogels compared to C and O that makes the N peak unresolved. Indeed, EDS cannot detect elements with concentration below 0.1 weight (wt) % [178, 226]. The EDS results here found are similar to results obtained elsewhere on chitosan films [227]. The absence of other peaks excludes the presence of impurities.

VSM was used to characterise the magnetic properties of chitosan. VSM results are shown in Fig. 4.2: the lack of a net magnetisation when the magnetic field increases excludes the presence of undesired magnetic impurities in the sample.

SEM was also employed to characterise the morphology of two other polymeric materials. Dry PNIPAAm hydrogels also presented a porous structure (see Fig. 4.3 (a,b)), with elongated pores alternating with flat regions. PDMS presented a homogeneous structure, without pores (Fig. 4.3 (c)).

4.2.2 Mechanical characterisation

The mechanical properties of chitosan hydrogels were probed by means of AFM quasi-static force indentation curves. Experiments were performed in the presence/absence of B. Assuming the presence of electrical charges when the polymeric material is de-

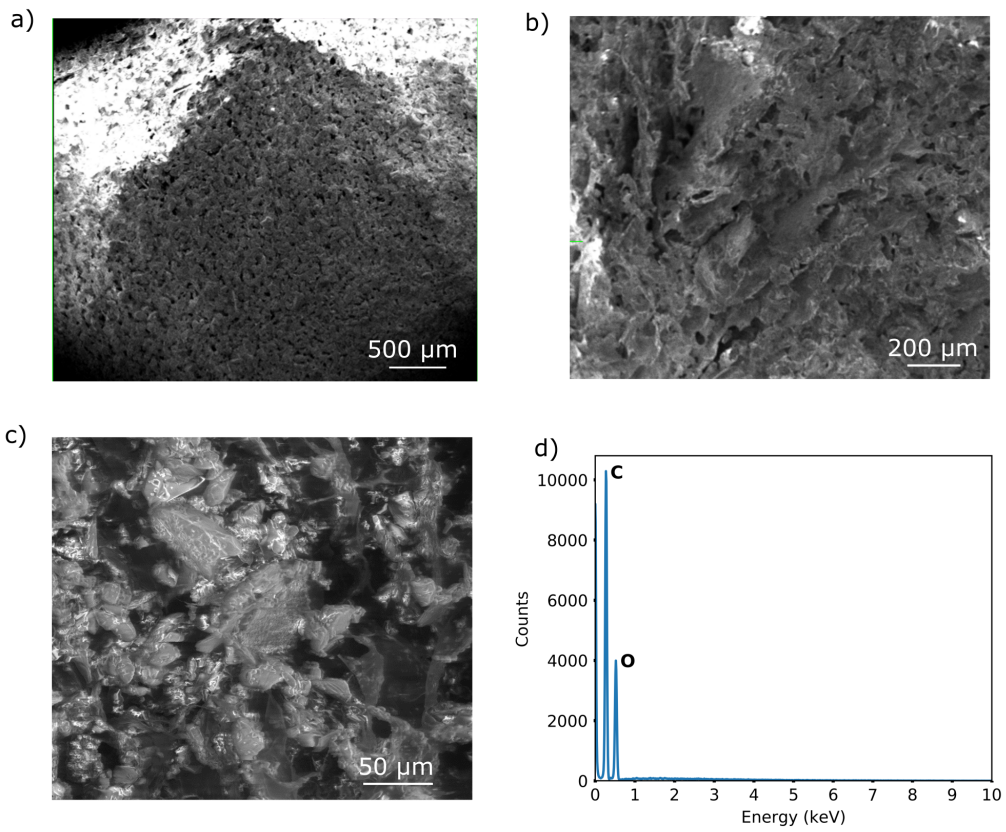


Figure 4.1: SEM and EDS on chitosan. (a-c) SEM images of dry chitosan samples at different magnifications as indicated by the scale bars. (d) EDS analysis of dry chitosan hydrogel.

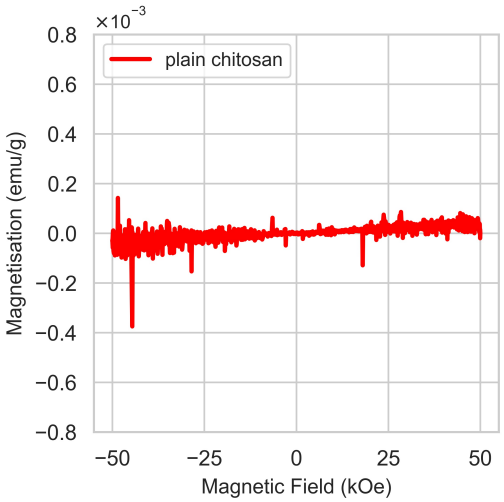


Figure 4.2: VSM on chitosan. Magnetisation curve of a dry chitosan hydrogel at 300 K.

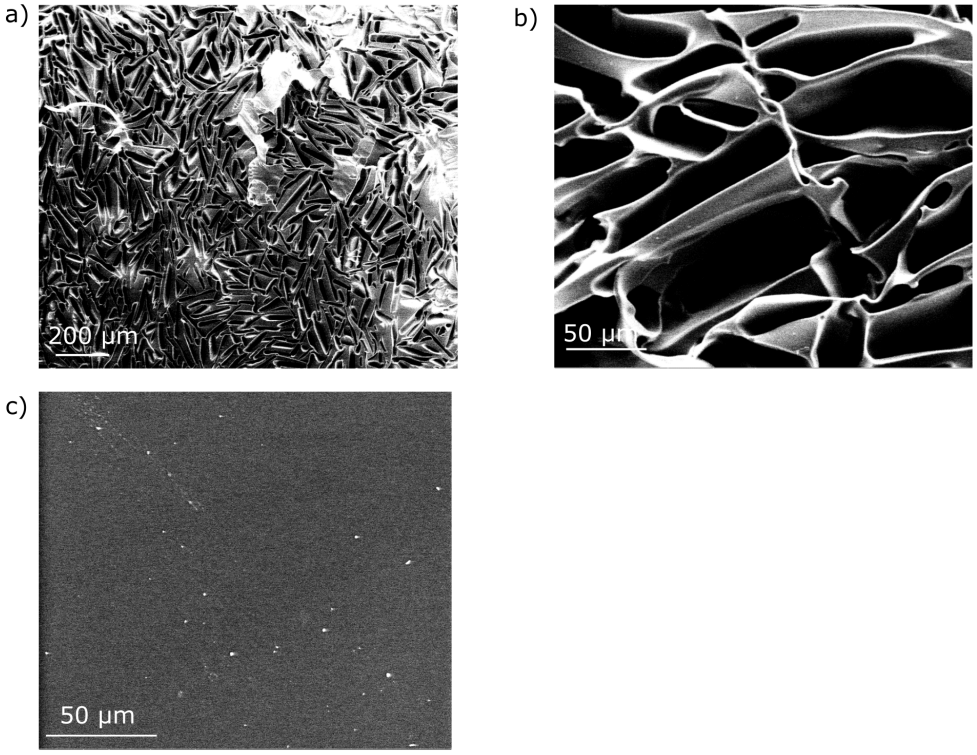


Figure 4.3: SEM on PNIPAAm and PDMS. SEM images of a dry PNIPAAm hydrogel at low (a), and high (b) magnification. (c) SEM images of a PDMS elastomer.

formed (for example because of the chitosan piezoelectric behaviour [219–221]), the displacement of these charges in B might lead to different results depending on the velocity at which the charges are being displaced (Lorentz force). For this reason, three different cantilever approach (and withdraw) velocities ($10\,\mu m\,s^{-1}$, $25\,\mu m\,s^{-1}$ and $50\,\mu m\,s^{-1}$) were tested.

In Fig. 4.4 (a) a typical quasi-static force (F) indentation (d) curve obtained at high velocity ($50\,\mu m\,s^{-1}$) in ultrapure water is shown. The red curve shows the approach of the cantilever to the sample until the trigger point is reached, while the blue curve represents the cantilever's withdraw from the sample. Typical force curves on chitosan showed a smooth approach, while withdraw curves presented many "jumps" (see Fig. 4.4 (a)). These "jumps" were probably caused by some polymeric chains sticking to the AFM cantilever bead, and being released as the cantilever retracted from the sample. Therefore, to minimise error caused by chain sticking, the approach part of the force curve was used to extract the mechanical properties of the samples. To analyse the mechanical behaviour of chitosan in the presence of B perpendicular to the surface of the sample, the sample was indented when B was applied ($B \neq 0$, red line) and turned off ($B = 0$, black line), as shown in Fig. 4.4 (b) for measurements with cantilever approach velocity of $10\,\mu m\,s^{-1}$ in ultrapure water. The reproducibility of the results when this process was repeated in the same spot (dashed lines in Fig. 4.4 (b)) shows that differences in the mechanical behaviour were not caused by plastic deformations produced by the indentation. Results obtained on a hard substrate (glass) used as a control (see Appendix D) excluded the possibility that B was affecting the AFM. Hence, the following results are due to the sample's response, not experimental artefacts from plastic deformation or alterations in the AFM, indicating a magneto-mechanical coupling.

To quantify the difference in the mechanical properties of chitosan caused by B, the Hertz model was used to calculate $\tilde{E}$ (see Section 2.2.2) for each curve. The

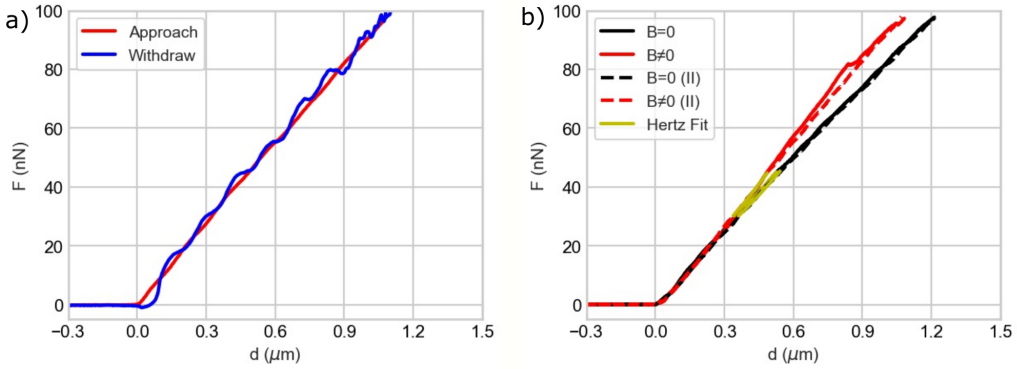


Figure 4.4: AFM force (F) vs. indentation (d) curves on a chitosan hydrogel in ultrapure water. (a) Force curve at $50\,\mu m\,s^{-1}$. (b) Effect of external magnetic field (B) on force curves at $10\,\mu m\,s^{-1}$. Measurements were done switching the electromagnet off ($B = 0$, black line) and on ($B \neq 0$, red line) underneath the sample. Measurements were repeated in the same spot of the sample to test reproducibility, and exclude the possibility of plastic deformations ((II), dashed lines). The force curves were fit with the Hertz model (yellow line).

yellow lines in Fig. 4.4 (b) show the good agreement between the Hertz fit and the experimental data.

For each configuration in Fig. 4.4 (b) (i.e. $B = 0$, $B \neq 0$, $B = 0(II)$, $B \neq 0(II)$ with II indicating the repetition) fifteen curves were acquired. Quantification of $\tilde{E}$ for all the force curves collected in a single spot (that is, all curves like Fig. 4.4 (b)) is shown in Fig. 4.5 (a) (filled markers; black for $B = 0$, red for $B \neq 0$, grey for $B = 0(II)$).

In Fig. 4.5 (a), each box represents the distribution of $\tilde{E}$. Each box shows the mean of $\tilde{E}$ calculated over the fifteen curves for the different B configurations ($\bar{\tilde{E}}_B$, blue unfilled circles), and the quartiles of the $\tilde{E}_B$ distribution. Different colours in Fig. 4.5 (a) represent the different B configurations during the measurements: black for $B = 0$, red for $B \neq 0$, grey for $B = 0(II)$.

From $\bar{\tilde{E}}_{B=0} = (13.1 \pm 0.4)\,kPa$, $\bar{\tilde{E}}_{B\neq0}$ increased to $(16.0 \pm 0.8)\,kPa$. When repeated, $\bar{\tilde{E}}_{B=0(II)}$ decreased back to lower values $(12.4 \pm 0.3)\,kPa$, and $\bar{\tilde{E}}_{B\neq0(II)}$ increased to $(15.6 \pm 0.4)\,kPa$ (not shown in Fig. 4.5 (a)).

Paired t-tests between $\tilde{E}_{B=0}$ and $\tilde{E}_{B\neq0}$, and between $\tilde{E}_{B=0(II)}$ and $\tilde{E}_{B\neq0}$ had p values

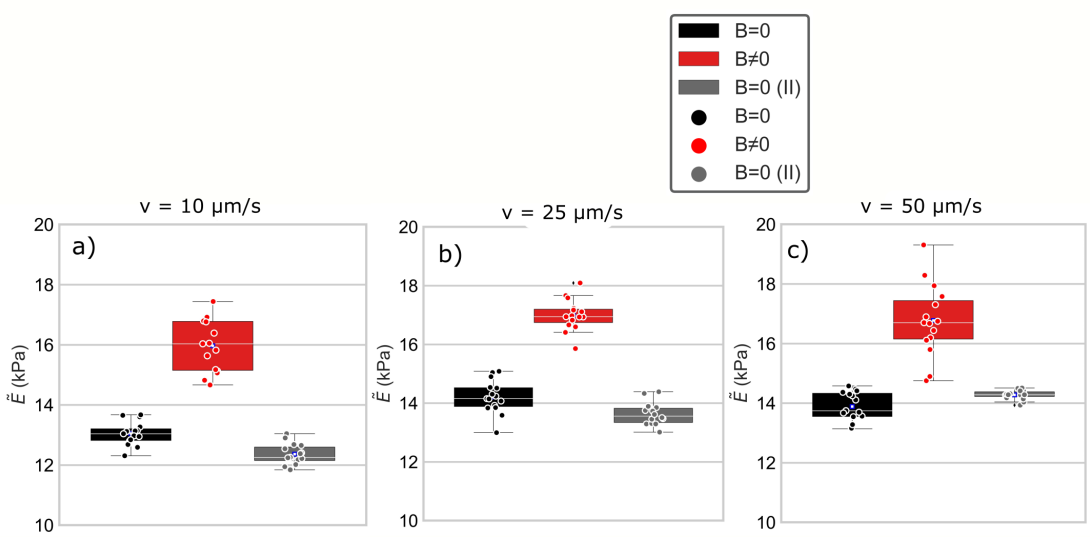


Figure 4.5: Change in the reduced Young's modulus ($\tilde{E}$) with an external magnetic field (B) for a chitosan hydrogel in ultrapure water: boxplot representing $\tilde{E}$ obtained on chitosan hydrogel with B off ($B = 0$, black), on ($B \neq 0$, red), and off again ($B = 0(II)$, grey), at different AFM approach velocities, in ultrapure water. Filled markers represent $\tilde{E}$ calculated for each of the fifteen individual force curves. Data obtained at (a) $10\,\mu m\,s^{-1}$, (b) $25\,\mu m\,s^{-1}$, and (c) $50\,\mu m\,s^{-1}$ cantilever approach velocities.

< 0.05. Therefore, chitosan's mechanical properties in the presence and absence of B are significantly different. Similar results were obtained at higher cantilever approach velocities (i.e. $25\,\mu m\,s^{-1}$ and $50\,\mu m\,s^{-1}$) as shown in Fig. 4.5 (b,c).

Fifteen positions were measured over the surface of the chitosan sample immersed in ultrapure water (with 15×4 force curves collected for each spot). For each velocity, positions where $\bar{\tilde{E}}_B$ was much larger (three times higher or more) than the average of $\tilde{E}$ calculated over all the measured positions were considered outliers, and discarded for the analysis. Fig. 4.6 (a) shows changes in $\tilde{E}$ with/without B across the several positions tested. In Fig. 4.6 (a), red asterisks mark positions where the following conditions were satisfied:

$$
\begin{aligned}
&(a)\ |\bar{\tilde{E}}_{B=0} - \bar{\tilde{E}}_{B=0(II)}| < ((\bar{\tilde{E}}_{B=0} + \bar{\tilde{E}}_{B=0(II)})/2)/3 \\
&(b)\ |\bar{\tilde{E}}_{B\neq 0} - \bar{\tilde{E}}_{B=0}| > |\bar{\tilde{E}}_{B=0(II)} - \bar{\tilde{E}}_{B=0}| \\
&(c)\ p < 0.05 \text{ for } \tilde{E}_{B\neq 0} \text{ and } \tilde{E}_{B=0} \\
&(d)\ p < 0.05 \text{ for } \tilde{E}_{B\neq 0} \text{ and } \tilde{E}_{B=0(II)}
\end{aligned}
\tag{4.1}
$$

where Eq. (4.1) (a,b) were introduced to discount positions where plastic deformations likely occurred. In Eq. (4.1) (c,d) the p values of paired t-tests were used to identify positions where the local elastic properties statistically changed between $\tilde{E}$ calculated with/without B. In particular, Eq. (4.1) (a) ensures that the difference between $\bar{\tilde{E}}$ calculated without B before and after the application of B is smaller than 1/3 of the average of the two. This condition ensures that positions where plastic deformation likely occurred (that is positions where $\bar{\tilde{E}}$ without B before and after the application of B are very different from each other) are discarded from the analysis. Eq. (4.1) (b) ensures that the difference between $\bar{\tilde{E}}$ calculated with and without B is larger than the difference between $\bar{\tilde{E}}$ calculated without B before and after the application of B. This condition allows discarding of positions where a significant change in $\tilde{E}$ with B (Eq. (4.1) (c)) occurred due to plastic deformations.

Several positions probed on the chitosan hydrogel satisfy Eq. (4.1) (a-d) (see Fig. 4.6 (a)), indicating a significant change in $\tilde{E}$ due to the application of B. Interestingly, the nature of the change in $\tilde{E}$ between $B = 0$ and $B \neq 0$ varied across spots.

As mentioned in Section 4.1, chitosan is piezoelectric [219–221], which could be related to its magneto-mechanical coupling. To test whether the piezoelectric nature of chitosan was related to its magneto-mechanical coupling, two other polymeric materials were examined: PNIPAAm, a porous synthetic hydrogel (see Fig. 4.3 (a,b)) used for biomedical applications [228] that, to the best of my knowledge, is not piezo-

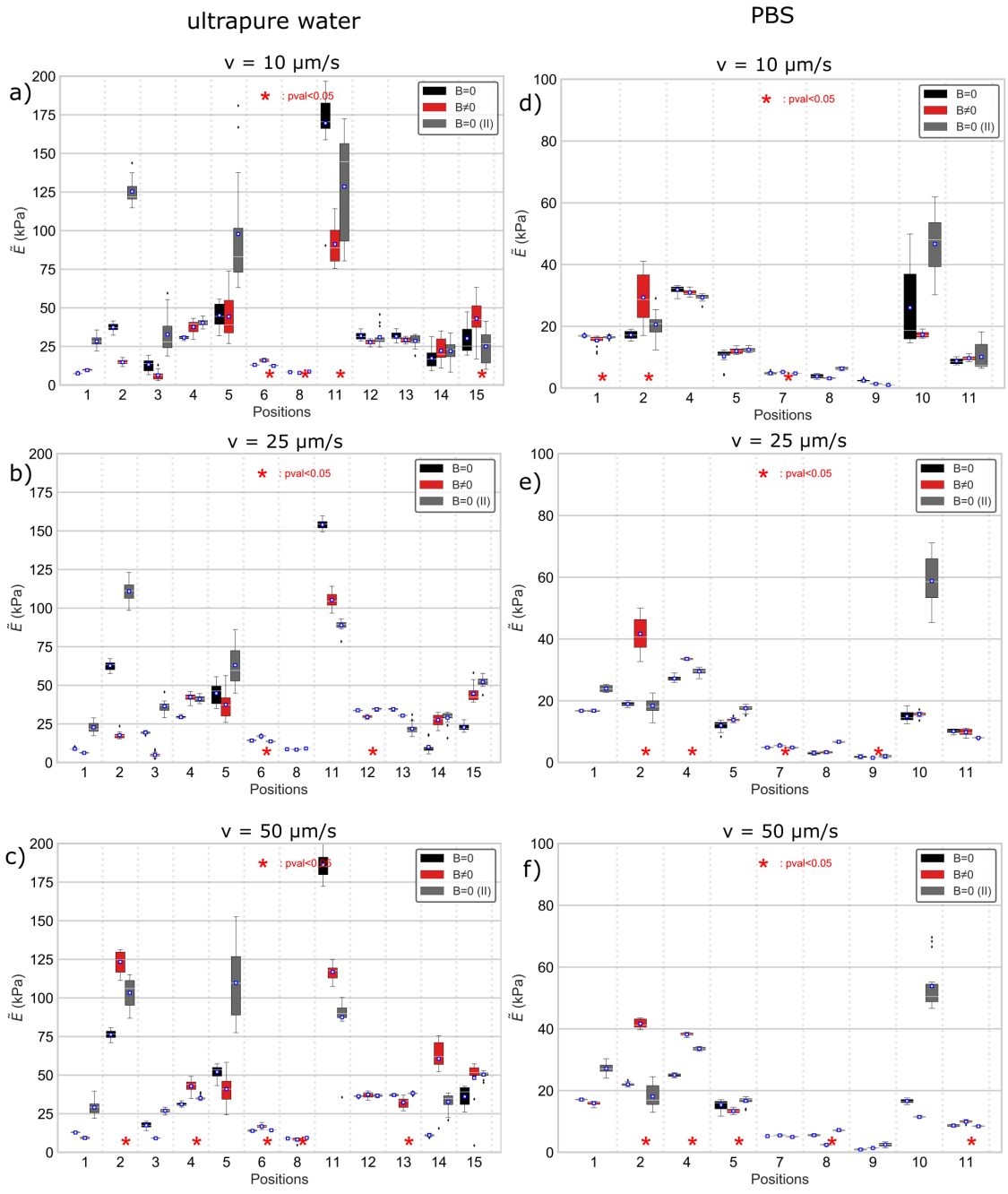


Figure 4.6: Distribution of change in reduced Young modulus ($\tilde{E}$) with an external magnetic field (B) for a chitosan hydrogel: $\tilde{E}$ calculated in several positions on chitosan hydrogel in ultrapure water from indentations at (a) $10\,\mu m\,s^{-1}$, (b) $25\,\mu m\,s^{-1}$, and (c) $50\,\mu m\,s^{-1}$, and in PBS at (d) $10\,\mu m\,s^{-1}$, (e) $25\,\mu m\,s^{-1}$, and (f) $50\,\mu m\,s^{-1}$ approach velocities.

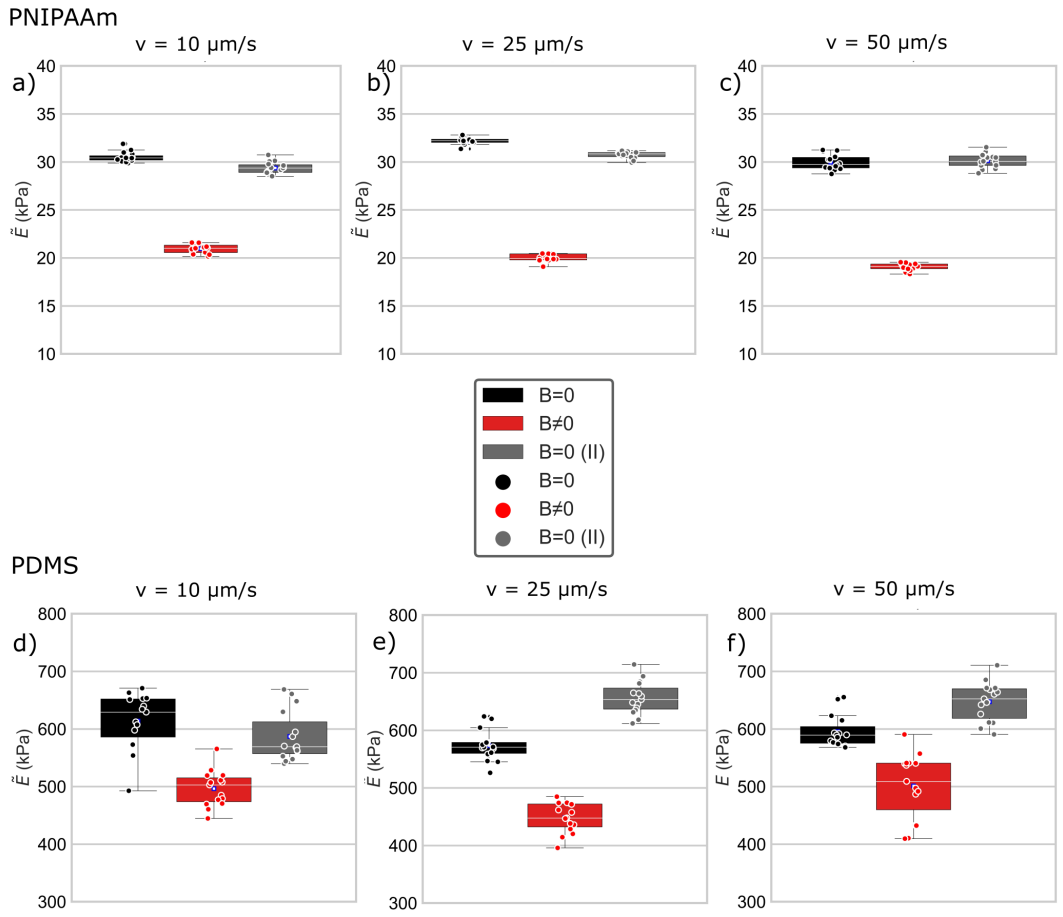


Figure 4.7: Changes in the reduced Young's modulus ($\tilde{E}$) with an external magnetic field (B) for PNIPAAm and PDMS in ultrapure water: boxplots representing $\tilde{E}$ obtained on PNIPAAm and PDMS polymeric materials with B off ($B = 0$, black), on ($B \neq 0$, red), and off again ($B = 0(II)$, grey), at different AFM approach velocities, in ultrapure water. Filled markers represent $\tilde{E}$ calculated for each of the fifteen individual force curves. Data from each approach velocity on PNIPAAm are shown in panel (a) $10\,\mu m\,s^{-1}$, (b) $25\,\mu m\,s^{-1}$, and (c) $50\,\mu m\,s^{-1}$, and on PDMS in panel (d) $10\,\mu m\,s^{-1}$, (e) $25\,\mu m\,s^{-1}$, and (f) $50\,\mu m\,s^{-1}$.

electric; and PDMS, a homogeneous silicon based elastomer (see Fig. 4.3 (c)), that, to the best of my knowledge, does not exhibit piezoelectricity unless microstructured and subjected to high electric fields [229, 230] (not the case in this thesis).

Using the same procedure on PNIPAAm and PDMS samples, I found several positions on the samples with a significant mechanical change with/without B (see Appendix E for the distribution of $\tilde{E}_B$ across the different tested positions). In Fig. 4.7, an example of significant change in $\tilde{E}_B$ is plotted for both PNIPAAm ((a) $10\,\mu m\,s^{-1}$, (b) $25\,\mu m\,s^{-1}$, (c) $50\,\mu m\,s^{-1}$ approach velocities), and PDMS ((d) $10\,\mu m\,s^{-1}$, (e) $25\,\mu m\,s^{-1}$, (f) $50\,\mu m\,s^{-1}$ approach velocities). Therefore, the observed magneto-mechanical coupling does not stem (only) from piezoelectricity.

For all the measured positions, both chitosan and PNIPAAm hydrogels presented $\bar{\tilde{E}}$ values below 200 kPa, independently of the application of B (see Figs. E.1 and 4.6). Changes in $\bar{\tilde{E}}$ with and without B for the three polymeric materials were not significantly different between approach velocities (e.g. a larger change with increasing velocity), as shown in Appendix E.

While changes in the mechanical properties with/without B were observed locally, the global elastic behaviour of the three polymeric materials with/without B did not show a significant change (see Appendix E). The global elastic behaviour ($\overline{\tilde{E}}$) was measured for each B configuration ($B \neq$ and $B = 0$) by averaging $\bar{\tilde{E}}$ over all the positions that did not present plastic deformations (i.e. satisfied Eq. (4.1) (a,b)), for each approach velocity. For example, $\overline{\bar{\tilde{E}}}_{B=0}$ of chitosan hydrogels with an approach velocity of $10\,\mu m\,s^{-1}$ was (41.5 ± 48.6) kPa. When the magnetic field was turned on $\overline{\bar{\tilde{E}}}_{B\neq 0}$ was (34.7 ± 27.5) kPa. Similar results were obtained for $25\,\mu m\,s^{-1}$ and $50\,\mu m\,s^{-1}$.

As shown in Figs. E.1, E.2 and 4.6, the nature of the local changes in $\tilde{E}$ varied across spots, thereby demonstrating a heterogeneous nature of the polymeric materials. This heterogeneity of the mechanical response to B of the sample led to a non-significant change in the global $\overline{\tilde{E}}$ with/without B (see Fig. E.5). Only by probing small length

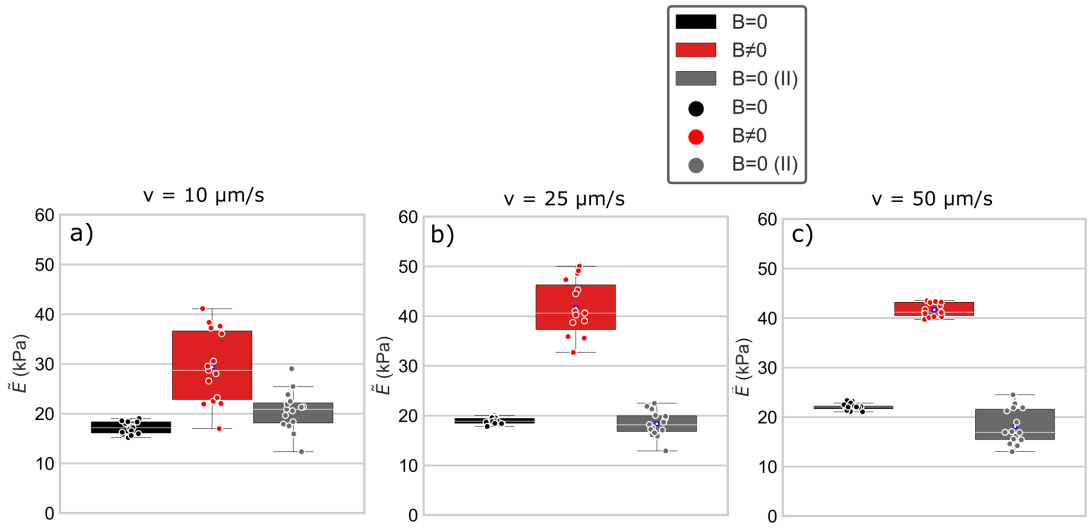


Figure 4.8: Changes in the reduced Young's modulus ($\tilde{E}$) with an external magnetic field (B) for a chitosan hydrogel in PBS: boxplots representing $\tilde{E}$ obtained on chitosan hydrogels with B off ($B = 0$, black), on ($B \neq 0$, red), and off again ($B = 0(II)$, grey), at different AFM approach velocities, in PBS. Filled markers represent $\tilde{E}$ calculated for each of the fifteen individual force curves. Data are shown for approach velocities of (a) $10\,\mu m\,s^{-1}$, (b) $25\,\mu m\,s^{-1}$, and (c) $50\,\mu m\,s^{-1}$.

scales relevant to cell the magneto-mechanical coupling of these polymeric materials can be observed.

To mimic physiological conditions, the same experiments for chitosan, PNIPAAm, and PDMS samples were conducted in PBS instead of ultrapure water. PBS is a salt solution commonly used in cell culture that mimics physiological extracellular ion concentrations.

As in ultrapure water, significant changes in $\tilde{E}_B$ for chitosan hydrogels were found. Fig. 4.8 and Fig. 4.6 (b) show an example of these changes for chitosan hydrogels in PBS. Also in PBS, for the three polymeric materials, no effect of $\overline{\tilde{E}}$ with B could be noticed (see Appendix E).

4.3 Discussion

4.3.1 Morphological, chemical, and magnetic characterisation

SEM enabled the morphological characterisation of the three dry polymeric materials. SEM and VSM were employed to characterise the chemical composition and the magnetic properties of the dry chitosan hydrogels, respectively.

From Fig. 4.1 (a-c), the chitosan sample was found to be a heterogeneous material, with flat regions alternating with pores. The chemical analysis conducted with EDS shows the presence of O and C in the chitosan sample (Fig. 4.1 (d)), as expected [227]. The EDS and the VSM results (Fig. 4.1 (d) and Fig. 4.2) indicate that magnetic impurities were not present in the samples.

Fig. 4.3, shows that PNIPAAm hydrogel presented a polymeric network with elongated pores, while PDMS elastomer had a homogeneous structure.

4.3.2 Mechanical characterisation

AFM quasi-static force indentation curves enabled the characterisation of the local elastic properties of three polymeric materials in the presence/absence of B.

As shown in Fig. 4.4 (b), the presence of B clearly affected the way chitosan hydrogels responded to the deformation applied by the AFM probe, suggesting a magneto-mechanical coupling in the polymeric matrix. This change in the mechanical properties due to B was quantified by using the Hertz model to calculate $\tilde{E}$.

For the different configurations ($B = 0$, $B \neq 0$, and $B = 0(II)$), a significant change of $\tilde{E}$ depending on the presence of B occurred (Fig. 4.5). Differences between $\bar{\tilde{E}}_{B=0}$ and $\bar{\tilde{E}}_{B=0(II)}$ were attributed to small plastic deformations of the sample. Similar results were obtained for all cantilever approach velocities ($10\,\mu m\,s^{-1}$, $25\,\mu m\,s^{-1}$ and $50\,\mu m\,s^{-1}$). The slight increase of $\bar{\tilde{E}}$ with velocity is attributed to the time-dependent

mechanical behaviour of polymeric materials.

Several positions were tested over the surface of the chitosan hydrogel, some of which showed a significant change in $\tilde{E}$ depending on B (Fig. 4.6). Different positions showed a variety of effects that B had on $\tilde{E}$. Similar results were obtained both in ultrapure water and PBS (Figs. 4.5, 4.6 and 4.8), at the three different cantilever approach velocities used ($10\,\mu m\,s^{-1}$, $25\,\mu m\,s^{-1}$ and $50\,\mu m\,s^{-1}$).

Similar results were also found in another porous hydrogel, PNIPAAm, and in a homogeneous non-porous PDMS elastomer (Fig. 4.7 and Appendix E).

No clear trend to describe the change in $\bar{\tilde{E}}$ in the presence of B with increasing/decreasing cantilever velocity was observed (Appendix E). It is possible that small plastic deformations of the polymeric materials during the deformation hid the effect of velocity on the measurements.

The global elastic behaviour measured by $\overline{\tilde{E}}$ for $B \neq$ and $B = 0$, for all three polymeric materials (see Appendix E), was not significantly different. This behaviour can be attributed to the heterogeneity in the response of $\tilde{E}$ with/without B over the different positions. At small scales relevant to cells, the three polymeric materials show a variety of responses ($\bar{\tilde{E}}$) which combine into a neutral response when averaged ($\overline{\bar{\tilde{E}}}$), showing no significant difference in their global elastic behaviour (see Appendix E and Fig. E.5).

Both chitosan and PNIPAAm hydrogels showed $\bar{\tilde{E}}$ from few kPa up to 200 kPa, quantitatively comparable with muscle and bone elasticity (E muscles ≈ 10 kPa, and bones $>$ tens of kPa) [17, 57, 61, 231]. In particular, $\bar{\tilde{E}}$ of the chitosan hydrogels in this study were found to be in the elastic range of cross-linked porous chitosan hydrogels used for chondrocyte cell cultures [232]. The elastic properties of chitosan and PNIPAAm hydrogels are also similar to those of nano/micro particles used in drug delivery [18].

In order to explain the magneto-mechanical coupling observed in these polymeric ma-

terials several hypothesis were considered. The hypothesis of magnetohydrodynamic effects (effects produced by a magnetic field on a flowing conducting fluid [233]) affecting the changes in $\tilde{E}$ in response to B was discarded. If magnetohydrodynamic effects were to blame, $\tilde{E}$ of the non-porous PDMS elastomer, where liquid cannot flow through pores during the deformation, should not have changed in response to B. Changes of $\tilde{E}$ with B in the PDMS sample (see Fig. E.2) therefore exclude magnetohydrodynamic effects as the cause of this magneto-mechanical coupling.

One hypothesis to explain the magneto-mechanical effect seen in the chitosan sample could be made in analogy to its piezoelectric properties: the change in the local mechanical properties of chitosan in the presence of B could be due to the effect of B on electric dipoles forming in the chitosan hydrogel during the deformation caused by the AFM probe. Although it is not possible to exclude that piezoelectricity in chitosan hydrogels could affect their magneto-mechanical coupling, similar changes in $\bar{\bar{\tilde{E}}}$ with B were observed in non-piezoelectric samples (PNIPAAm and PDMS, as mentioned in Section 4.2.2). This suggests that something else caused the local magneto-mechanical effect.

It has been shown that neutral polymeric materials can present regions at the nano/micro-scale where electrical charge gets localised giving rise to an *"electric mosaic"* [234]. It is probable that such an electric structure could form in the samples used in these experiments. Therefore the observed magneto-mechanical coupling could be attributed to the displacement of the localised electrical charges within the polymeric matrices during the indentation, and that can be affected by the application of B (i.e. by Lorentz force). The presence of localised charged regions on the polymeric matrix could also explain the heterogeneity in the change of $\tilde{E}$ with the presence of B (i.e. softening or stiffening of the sample) on different regions of the specimen.

4.4 Conclusions

In this study, I showed that a 45 mT B significantly altered the local elastic properties of polymeric materials (chitosan, PNIPAAm, and PDMS) in aqueous solutions. Moreover, both chitosan and PNIPAAm hydrogels showed elastic properties in the range of those of biological tissues such as muscles and bones [17, 57, 61, 231], thereby showing promise for tissue engineering. They also fall in the range of particle elasticity used for drug delivery applications [18].

In both ultrapure water and PBS, porous hydrogels, namely chitosan and PNIPAAm, and a homogeneous non-porous elastomer, PDMS, displayed a significant change in their local elastic properties when B was applied. This effect can be attributed to the presence of localised electrical charges on the matrices of the three polymeric materials. The displacement of these localised charges during the indentation could be affected by the presence of a magnetic field causing, in turn, a change in the mechanical properties of the material. To the best of my knowledge, this is the first time that a change in the local elastic properties ($\tilde{E}$) of plain chitosan hydrogels due to the application of B is observed, suggesting a magneto-mechanical coupling in these hydrogels. This observation could inspire the development of new smart chitosan-based scaffolds for tissue engineering that, without the incorporation of magnetic particles, could influence cell activities by modulating the mechanical properties of the hydrogels with external magnetic fields.

Chapter 5

Composite Hydrogels

5.1 Introduction

The introduction of nanostructures in polymeric matrices not only can improve their chemical and physical properties, but also confers them electrical or magnetic behaviours that can be employed for biomedical applications such as imaging, cancer treatment, drug delivery, and many others [28]. In this chapter, I analyse the possibility of modulating the local elasticity of composite hydrogels to test their suitability for biomedical applications in terms of their mechanical properties (cfr. Section 1.1). In Chapter 4, I showed that the mechanical properties of plain chitosan hydrogels are altered by the presence of magnetic fields. To further explore the mechanism behind this finding, Section 5.2 investigates whether incorporation of magnetic nanowires into chitosan hydrogels would lead to a more homogeneous elastic response of the composite hydrogels to magnetic fields, and thereby enhance the gel's controllability. In Section 5.2, chitosan hydrogels with embedded Fe_3O_4 nanowires are described, and their local elastic behaviour with an external magnetic field is presented.

In Section 5.3, the local elastic properties of composite hydrogels based on carbon nanostructures are researched. In particular, the elastic behaviour of hydrogels syn-

thesised from fullerenes of different size is measured. If the elastic properties of hydrogels synthesised from different fullerenes are different, it could be possible to control their mechanical properties and tailor fullerene-based hydrogels to specific applications by synthesising the gels from different fullerenes. Additionally, knowledge of the elastic properties of fullerene-based hydrogels could indicate whether such hydrogels are suitable for biomedical applications in terms of their mechanical properties, and if so, for which biomedical application they show the most promise.

5.2 Chitosan composite hydrogels with Fe_3O_4 nanowires

Magneto-responsive hydrogels are attractive for biomedical applications. Encapsulation of micro or nanoparticles into polymeric materials supplies a way to enhance their response to magnetic stimuli [29, 77, 78]. Magnetic nanoparticles (MNPs) are particles with at least one dimension in the nanometre scale ($\leq 100\,\text{nm}$) that can be manipulated with external magnetic fields [235, 236].

Thanks to the development of nanotechnology, MNPs can be designed in a wide variety of shapes and sizes, providing them with different properties. For example, MNPs smaller than a certain critical size (typically below 15 nm) display a superparamagnetic behaviour [236, 237]. Similarly to paramagnetic materials, superparamagnetic nanoparticles in the presence of an external magnetic field align with the field. When the field is removed, superparamagnetic MNPs present no remanent magnetisation (residual magnetisation when the external magnetic field is removed) which reduces the likelihood of their aggregation [238].

The possibility of being remotely detected and manipulated with external magnetic fields, makes MNPs extremely attractive for biomedical applications [236–239], including tissue engineering [69], MRI [75], controlled release of drugs [76], cancer treatment

[74], and biosensing [240]. In tissue engineering, composites with MNPs are appealing as scaffolds for cell culture thanks to the MNPs ability of responding to magnetic field by applying physical cues to stimulate cells [70], and affect cell differentiation [71–73]. In particular, MNPs with geometrical anisotropy, such as nanowires, have shown a great potential in biomedicine. Indeed, thanks to their anisotropy, they experience higher magnetic torques when a magnetic field is applied compared to spherical MNPs [223]. The advantage of anisotropic particles allows generation of higher mechanical stresses and frictional losses, and has a wide range of applications including hyperthermia cancer treatment [241], drug delivery [242], cell manipulation [243], targeted cell therapy [244, 245], and in substrates for cell stimulation [246].

MNPs made of magnetite (Fe_3O_4) are some of the most researched for biomedical applications, because they have lower toxicity compared to MNPs based on other elements, such as Co and Ni [236, 237]. In particular, Fe_3O_4 MNPs have found use in applications related to hyperthermia [247], drug delivery [248], MRI [249], and biosensors [240]. Fe_3O_4 MNPs are usually stabilised with coatings, such as biocompatible polymers, to prevent their agglomeration [250]. Studies on composite cell culture scaffolds of chitosan and Fe_3O_4 MNPs have shown these scaffolds to be biocompatible [251]. Therefore, such composites have good potential for tissue engineering applications [251, 252].

In this study, Fe_3O_4 nanowires are embedded into a chitosan matrix (see Section 3.2.1), therefore combining the flexibility and biocompatibility of chitosan with the magnetic properties of the Fe_3O_4 nanowires. In this section, the morphological, chemical, magnetic, and mechanical characterisation of the composite hydrogels are described. In particular, the mechanical response of these hydrogels in the presence of external magnetic fields is studied. Modulating the mechanical properties of these hydrogels by means of an external magnetic field could provide the possibility of using these hydrogels for cell stimulation in the development of artificial tissues or in the

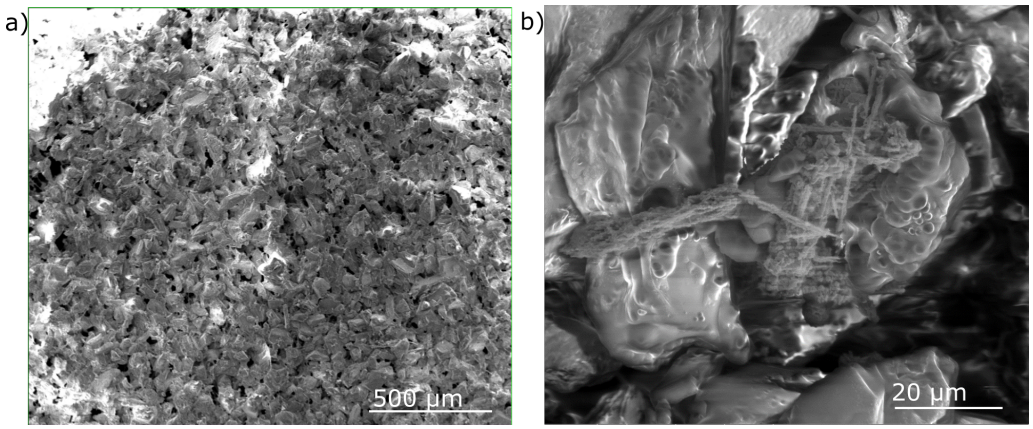


Figure 5.1: SEM images of a dry chitosan composite hydrogel with randomly oriented Fe_3O_4 nanowires at (a) low and (b) high magnification as indicated by the scale bars.

controlled load and release of drugs.

5.2.1 Results

5.2.1.1 Morphological and chemical characterisation

SEM was used to study the topography of dry chitosan composite hydrogels. In Fig. 5.1, SEM images of a chitosan composite with randomly oriented wires are shown at low (a), and high (b) magnification. Fig. 5.1 (b) shows an example of a large agglomerate of structures that could be found throughout the sample. EDS was used to study the chemical composition of the dry chitosan composite hydrogels. EDS analysis shows that regions including these agglomerated structures have a higher concentration of Fe (not shown).

Fig. 5.2 shows SEM images and EDS analysis obtained on a chitosan composite hydrogel with horizontally oriented Fe_3O_4 nanowires. Coherently aligned structures were found within the composite's surface (highlighted with red ovals in Fig. 5.2 (a,b)), possibly due to the Fe_3O_4 nanowires. A zoomed image of one of these aligned structures is presented in Fig. 5.2 (c). A zoomed image of a different region of the composite with no aligned structure is shown in Fig. 5.2 (d).

EDS analysis of the regions in Fig. 5.2 (c,d) is shown in Fig. 5.2 (e). Fe peaks at 0.705 keV and 6.405 keV are visible in addition to the C (at 0.277 keV) and O (at 0.525 keV) peaks typical of chitosan (cfr. Fig. 4.1 (e)). The EDS analysis in Fig. 5.2 (e) indicates a higher concentration of Fe in Fig. 5.2 (c) compared to Fig. 5.2 (d).

5.2.1.2 Magnetic characterisation

VSM was used to analyse the magnetic behaviour of the dry chitosan composite hydrogels. The magnetisation curve of the dry chitosan composite hydrogel with embedded Fe_3O_4 nanowires obtained at 300 K is shown in Fig. 5.3. The inset zooms in on the hysteresis loop at low magnetic field, showing the remanent magnetisation, typical of ferromagnetic materials.

5.2.1.3 Mechanical characterisation

The mechanical properties of the chitosan composite hydrogels immersed in PBS were probed with AFM quasi-static force indentation curves. Experiments were performed in the presence and absence of B, using a cantilever approach velocity of $50\,\mu m\,s^{-1}$. Several positions were tested over the surface of the hydrogels. Indentation depths ranged from hundreds of nanometres to a few microns depending on the position tested (not shown). $\tilde{E}$ was quantified using the Hertz model (see Section 2.2.2). $\tilde{E}_B$ was calculated for each configuration (magnetic field off ($B = 0$), and on ($B \neq 0$)) in several positions on the composite hydrogels (see Appendix F). Given the ferromagnetic nature of the chitosan composite hydrogels, no repetitions ($B = 0(II)$, see Section 4.2.2) were performed (the remanent magnetisation of the nanowires could affect $\tilde{E}_{B=0(II)}$).

Fig. 5.4 shows the mechanical response of chitosan with horizontally (a,b), and randomly (c,d) oriented wires in different positions where $\tilde{E}_B$ had a significant change when B was applied (i.e. p value of paired t-test between $\tilde{E}_{B=0}$ and $\tilde{E}_{B\neq0}$ smaller

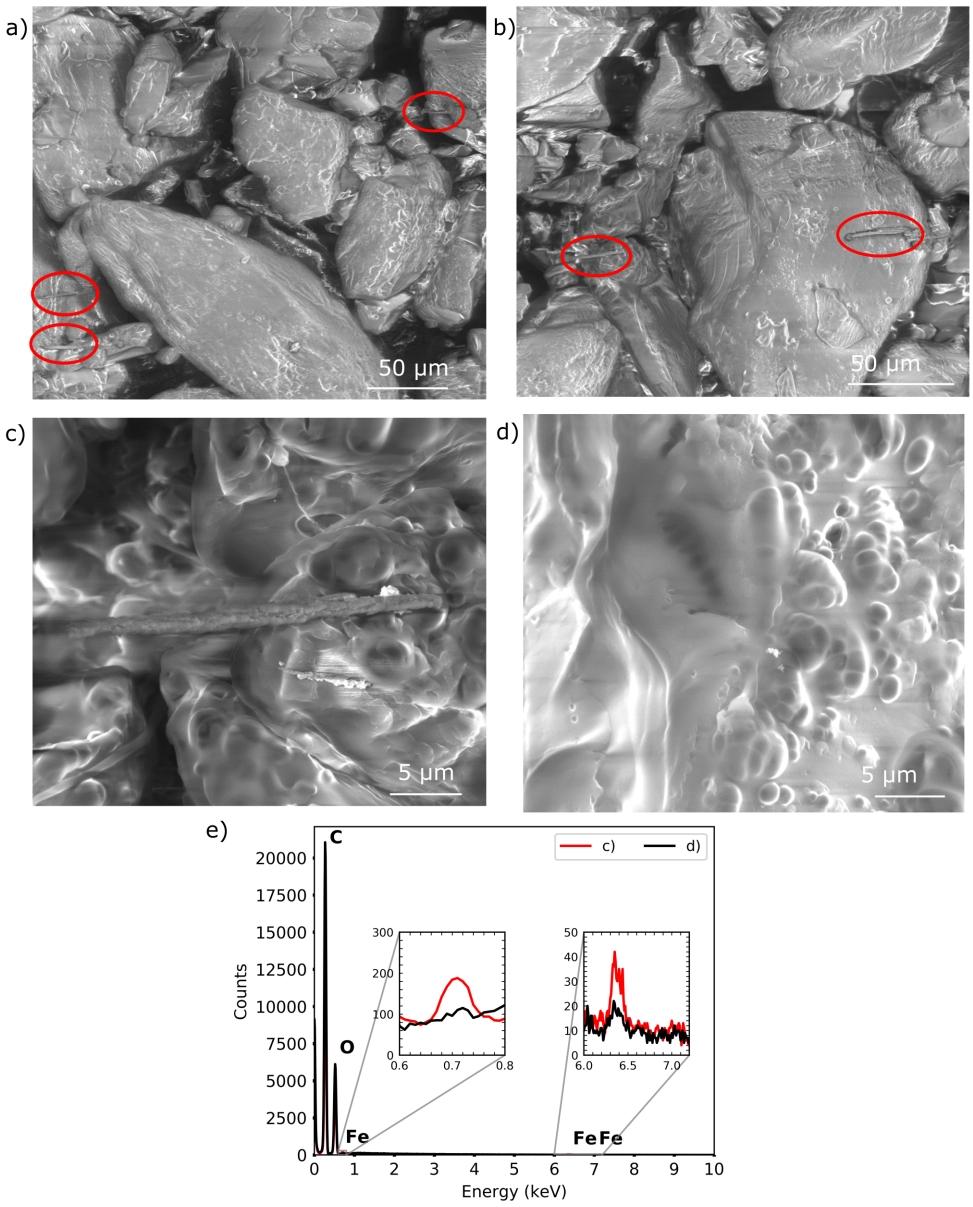


Figure 5.2: SEM and EDS results on a dry chitosan composite hydrogel with horizontally oriented Fe_3O_4 nanowires. (a,b) Low, and (c,d) high magnification SEM images as indicated by the scale bars. Red ovals in panels (a,b) highlight the presence of aligned structures within the sample's surface. (e) EDS analysis of (c,d).

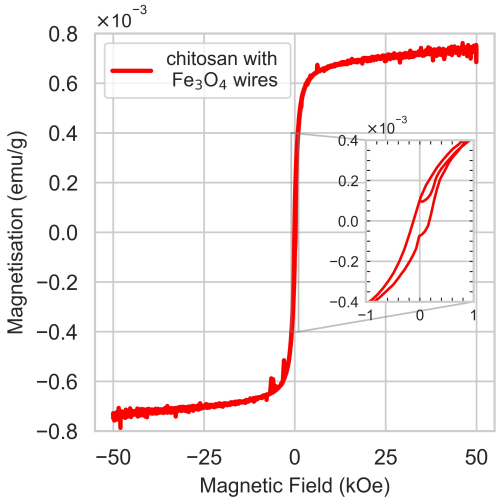


Figure 5.3: Magnetisation curve of a dry chitosan composite hydrogel with Fe_3O_4 nanowires at 300 K obtained by means of VSM. The inset enlarges the magnetisation at low magnetic fields in order to show the remanent magnetisation.

than 0.05).

The global elastic behaviour ($\overline{\tilde{E}}$) of plain chitosan hydrogels was calculated as explained in Chapter 4 and Appendix E. $\overline{\tilde{E}}$ of chitosan composite hydrogels was calculated over all the measured positions. $\overline{\tilde{E}}$ values are plotted in Fig. 5.5 for $B \neq 0$ (red) and $B = 0$ (black). The results in Fig. 5.5 are for the three chitosan-based hydrogels indented in PBS at $50\,\mu m\,s^{-1}$.

As shown in Fig. 5.5, composite hydrogels have a higher $\overline{\tilde{E}}$ than the hydrogels without nanowires. Composite hydrogels also have a greater heterogeneity in their mechanical properties. This heterogeneity is reflected by the fact that the standard deviation of $\overline{\tilde{E}}$ is larger for chitosan composite hydrogels than that of plain hydrogels. Most likely, regions with higher concentrations of nanowires had different mechanical properties compared to the others, which resulted in a large distribution of $\overline{\tilde{E}}$.

For all the three chitosan-based hydrogels, no significant change in $\overline{\tilde{E}}$ in the presence of B was observed. $\overline{\tilde{E}}$ of chitosan hydrogel with randomly oriented wires was slightly lower when $B = 0$ compared to that of $B \neq 0$. This is due to a large change in $\tilde{E}$ in response to B of certain positions (i.e. positions 2 and 22 in Fig. F.1 (b)). These large

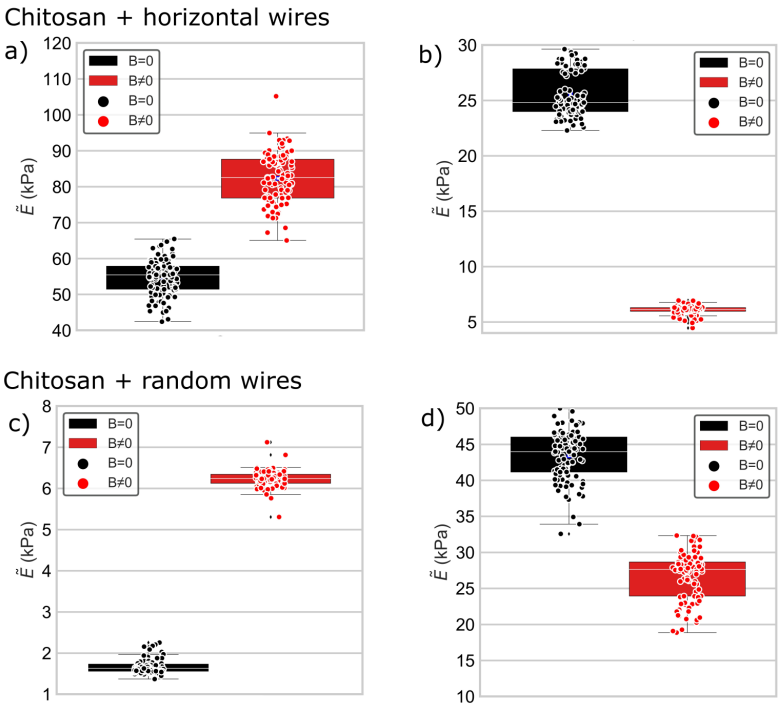


Figure 5.4: Change in the reduced Young's modulus ($\tilde{E}$) with magnetic field (B) for chitosan hydrogels with embedded Fe_3O_4 nanowires: boxplots representing $\tilde{E}$ obtained on chitosan composite hydrogels with B off ($B = 0$, black), and on ($B \neq 0$, red), from force curves with a $50\,\mu m\,s^{-1}$ cantilever approach velocity. Filled markers represent $\tilde{E}$ calculated for each force indentation curve. (a,b) $\tilde{E}$ calculated for chitosan hydrogels with horizontally oriented nanowires in two different positions. (c,d) $\tilde{E}$ calculated for chitosan hydrogels with randomly oriented nanowires in two different positions.

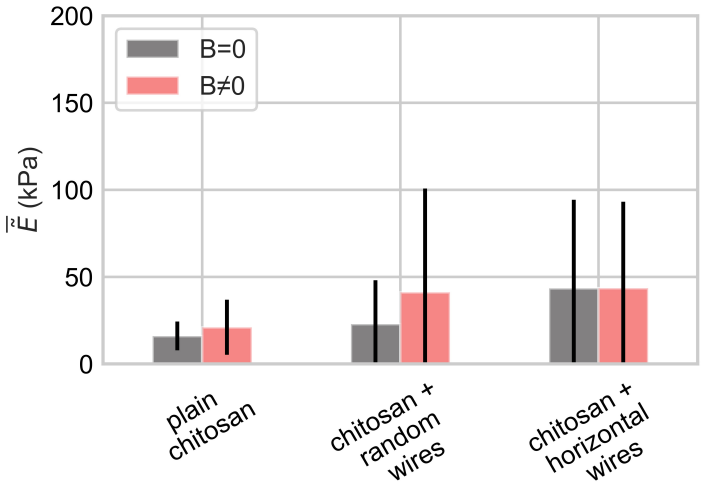


Figure 5.5: Average of reduced Young's modulus ($\overline{\tilde{E}}$), calculated as described in the text, for plain chitosan hydrogels, and for chitosan composite hydrogels with randomly and horizontally oriented nanowires. Values of $\overline{\tilde{E}}$ were calculated for $B \neq 0$ (red) and $B = 0$ (black). Hydrogels were measured in PBS, via indentation curves with a cantilever approach velocity of $50\,\mu\mathrm{m\,s^{-1}}$. Error bars correspond to the standard deviation.

changes could be due to indentations occurring closer to the nanowire aggregates (see Fig. 5.1), which could enhance the effects of B.

5.2.2 Discussion

5.2.2.1 Morphological and chemical characterisation

The morphology of dry chitosan composite hydrogels was studied by means of SEM. Chitosan composites had a different morphology (see Figs. 5.1 and 5.2) compared to the plain chitosan samples (see Section 4.2.1). These morphological differences were likely due to the interaction between chitosan and Fe_3O_4 nanowires.

The presence of agglomerated structures on the chitosan composite samples is attributed to a clustering of Fe_3O_4 nanowires. This clustering is confirmed by EDS analysis, which shows a higher concentration of Fe in regions presenting these agglomerates (see Fig. 5.2 (c,e)). In regions without these agglomerates ("nanowire-

free" zones) Fe is barely detected (see Fig. 5.2 (d,e)). In the case of chitosan with horizontally oriented nanowires (aligned during the freezing process with an external magnetic field, see Section 3.2.1 and Fig. 3.1), these nanowire agglomerates formed microstructures that aligned coherently (see Fig. 5.2 (a,b)).

5.2.2.2 Magnetic characterisation

The magnetic behaviour of dry chitosan composite hydrogels was analysed by means of VSM. VSM results on the chitosan composites (Fig. 5.3) show magnetisation typical of ferromagnetic materials. The magnetic characterisation of the plain chitosan samples did not present ferromagnetic magnetisation (cfr. Fig. 4.2), suggesting that the ferromagnetic response of the chitosan composites is given by the presence of the Fe_3O_4 nanowires. The coercivity (the external magnetic field intensity required to demagnetise the sample, H_C) is approximately 120 Oe, similar to values obtained for other Fe_3O_4 nanowires with diameters of 60 nm to 200 nm [253, 254]. The low magnetisation of the chitosan composites is attributed to the small concentration of Fe_3O_4 nanowires in the hydrogels, and to screening of the magnetic nanowires by the surrounding chitosan matrix [255]. It is also possible that the random alignment of the nanowires with respect to the applied magnetic field (see Section 3.3.2) might also have a contribution to the low magnetisation [253].

5.2.2.3 Mechanical characterisation

AFM quasi-static force indentation curves were employed to study the local elastic behaviour of chitosan composite hydrogels. $\tilde{E}$ in the presence/absence of B was quantified using the Hertz model (see Section 2.2.2).

Fig. 5.4 clearly shows that $\tilde{E}$ changed significantly when B was applied to the composite hydrogels, with both horizontally and randomly oriented nanowires (Fig. 5.4). However, there was no specific trend in the nature of these changes (see Appendix F).

These results are similar to those of chitosan hydrogels without nanowires (see Section 4.2.2). It is likely that the formation of nanowire clusters within the composite hydrogels, and thereby by the scarcity of magnetic nanowires in other regions of the polymeric matrix (see Section 5.2.2.1), could be responsible for the heterogeneous mechanical response of the composite hydrogels to B. It is reasonable that "nanowire-free" regions of the composite hydrogel would behave similarly to the plain chitosan hydrogels. Additionally, it is important to note that B might be affecting the mechanical properties of the hydrogels by deforming the polymer chains as a result of magnetic torque of the nanowires due to B. Therefore, the presence of nanowire agglomerates is likely to increase the heterogeneity of the elastic response of the composite hydrogels, compared to that of plain samples.

The presence of nanowires in chitosan composites increased the global elastic value $\overline{\tilde{E}}$ compared to that of plain hydrogels (Fig. 5.5). Similarly to plain hydrogels (cfr. Section 4.2.2), chitosan composites did not present a significant change in $\overline{\tilde{E}}$. Therefore, the hydrogels show a significant magneto-mechanical coupling at the length scale relevant to cells, but not on a global level. Regardless, the observed elastic properties of chitosan composite hydrogels fall in the range of those of biological tissues and drug carriers [17, 18, 57, 61, 231]. These observations make these hydrogels promising materials for tissue engineering and drug delivery. Indeed, these results suggest the possibility of tuning the elastic properties of these hydrogels via B, which could be used for cell stimulation in artificial constructs in order to modulate cell activities. The impact that the magneto-mechanical coupling of these hydrogels could have on cells merits future investigation.

5.2.3 Conclusions

In this study, Fe_3O_4 nanowires were incorporated into a chitosan matrix in order to enhance the controllability of the hydrogel's mechanical properties with B. The result-

ing hydrogels were heterogeneous materials, with nanowire aggregates surrounded by "nanowire-free" zones. In the case of pre-aligned (horizontal) nanowires these agglomerates were found to be coherently aligned within the hydrogel surface, in contrast to hydrogels with randomly oriented wires where no coherent aligning was found. Composite hydrogels presented ferromagnetic behaviour with very low magnetisation.

The local mechanical behaviour of the composite hydrogels changed in response to B. However, heterogeneity in these changes resulted in a lack of global response of the hydrogels to B. The heterogeneity in the magneto-mechanical response of these composite hydrogels is attributed to a non-homogeneous distribution of the nanowires within the chitosan matrix. Indeed, the presence of nanowire aggregates as well as nanowire-free zones is likely to introduce a different mechanical behaviour across the hydrogel composite when B is applied. For example, polymeric chains in proximity to nanowire aggregates could be deformed by the magnetic torque exerted on the wires when B is applied, thereby displaying a change in the local elastic properties with/without B. This effect is expected to be less relevant to nanowire-free zones, which most likely behave similarly to the plain chitosan hydrogels. A more sophisticated way of synthesising the material is needed to achieve a homogeneous local response. Indeed, it is likely that the non uniform distribution of nanowires in the chitosan matrix is preventing the control on the mechanical properties with B.

Importantly, the measured elastic properties of these hydrogels suggest their biomechanical compatibility for tissue engineering and drug delivery purposes. The magneto-mechanical behaviour of these hydrogels with B could potentially be exploited in engineered tissues for modulating cell behaviour remotely. The impact that the local mechanical alterations of these chitosan composite hydrogels with B could have on cells would be an interesting avenue of future research. For example, it would be worth testing the possibility of applying sinusoidal strains to the hydrogels to direct cell alignment, proliferation, and differentiation [256] by using alternating

magnetic fields to take advantage of both the magneto-mechanical coupling and the magnetic torque experienced by the nanowires in the chitosan composite hydrogels.

5.3 Fullerene-based hydrogels

Carbon is one of the most abundant elements on Earth and the foundation of life as we know it. Nanoscale carbon structures such as graphene (a single atom thick sheet), carbon nanotubes (cylindrical hollow structures made of rolled graphene sheets) and fullerenes (carbon atoms connected to form a hollow cage) have unique chemical and physical properties that have attracted interest in a wide range of material science and biomedical applications. In biomedical applications, carbon nanostructures have been used for tissue engineering [257], biosensing [258], and drug delivery [258]; moreover, they have also shown antimicrobial activity [259].

The surface of carbon nanomaterials can be functionalised to enhance their biocompatibility by increasing their water-solubility and reducing their aggregation [260, 261]. Carbon nanomaterials can also be loaded with drugs for drug delivery applications [262], or used to enhance the electrical conductivity and mechanical stability of hydrogels for tissue engineering [67, 68]. Additionally, the combination of carbon nanostructures and polymeric materials can result in supramolecular hydrogels (hydrogels held together by non-covalent bonds [263]), with interesting properties such as self-healing (gels repair themselves spontaneously when they are damaged [263]) [263, 264].

Fullerenes are particularly useful carbon materials for biomedical applications, because of their unique cage-like structure. This cage-like structure allows encapsulation of small molecules inside their cage [265], in addition to functionalisation of the cage's surface. Therefore, fullerene cages are attractive candidates in medical applications including drug delivery, cancer treatment, and diagnostics [266–270]. Furthermore,

they have also shown antiviral, antibacterial and antioxidant activity [267–270].

Stable fullerene cages are made of carbon pentagons and hexagons arranged in a corannulene structure (where every carbon pentagon is surrounded by five carbon hexagons) [271]. This corannulene geometry is often referred as the isolated pentagon rule (IPR) [141, 271]. The smallest and most abundant fullerene which obeys the IPR contains 60 carbon atoms (C_{60}) that form a truncated icosahedron [141]. Fullerenes with a higher number of carbon atoms can be found in different structures (isomers) with different symmetries [141]. While some work has been done on supramolecular structures with C_{60} [272–274], not much is known about fullerenes higher than C_{70}.

In this section, the local elastic properties of novel fullerene-based hydrogels synthesised from one of three fullerenes (C_{60}, C_{84}, and C_{90-92}) and functionalised with hydrophilic polymer chains named TEG-MEE (samples provided by Dr. Rašović, see Section 3.2.4) are studied. The characterisation of the local elasticity of these novel hydrogels is important to test their suitability for biomedical applications in terms of mechanical properties (see Section 1.1).

5.3.1 Results

5.3.1.1 Morphological characterisation

In this section the morphology of the fullerene-based hydrogels is described. The hydrated behaviour of the fullerene-based hydrogels can be observed from Fig. 5.6. Fig. 5.6 (a) shows that the C_{60} hydrogel was manipulable at the macroscopic scale by tweezers, and (b) that the gel released large amounts of water upon removal from aqueous solution, thus displaying characteristic hydrogel behaviour.

SEM was employed to study the morphology of the dry fullerene-based hydrogels. Fig. 5.7 shows SEM images of the freeze-dried fullerene hydrogels. The C_{60} sample (Fig. 5.7 (a)) was revealed to be a porous network of fibres. Typical fibre widths were

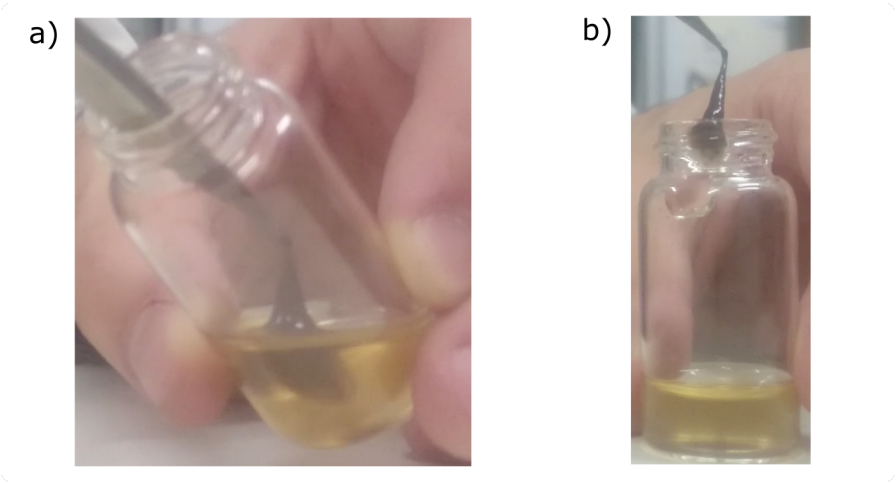


Figure 5.6: A C_{60} hydrogel after six months of spontaneous formation (a) being removed from solution with tweezers, and (b) releasing water after removal from solution. Images provided by Dr. Rašović [200] and printed with his permission.

approximately 2 µm, and the average network pore size was (60 ± 15) µm. Higher magnification (Fig. 5.7 (b)) reveals that smaller, hollow fibres with an inner diameter of approximately 900 nm, hierarchically assembled to form the larger (2 µm diameter) fibres.

The C_{84} sample (Fig. 5.7 (c)) presented a porous network of hollow fibres distributed over flat, homogeneous regions. These fibres had a 1 µm to 2 µm outer diameter, and an inner diameter ranging from 0.6 µm to 0.9 µm (data not shown). These fibres arranged themselves forming the porous network with average pore size (19 ± 5) µm, smaller than that of C_{60} samples.

The C_{90-92} sample (Fig. 5.7 (d)) presented a similar structure to the other two hydrogels, but with more flat, sheet-like regions. The average fibre size was approximately 5 µm, and the average pore size of the fibrous network was (26 ± 11) µm.

(Images in Figs. 5.6 and 5.7, and pore/fibre quantification used in Section 5.3 were provided by Dr. Rašović, further details can be found in ref. [200].)

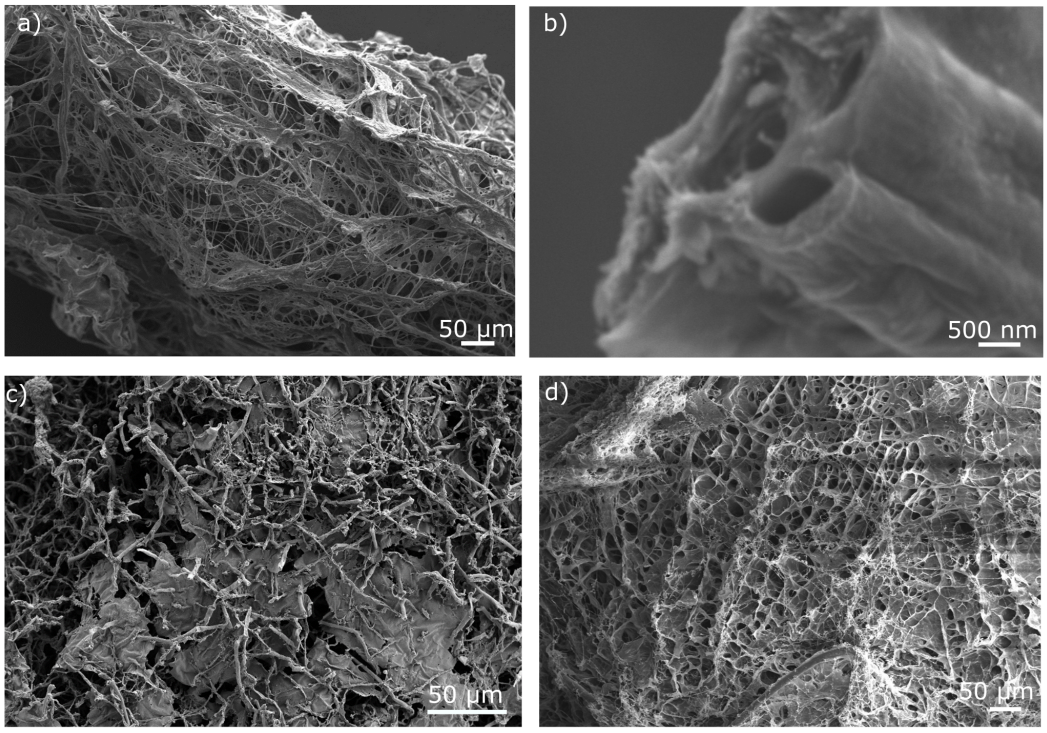


Figure 5.7: SEM images of the C_{60} (a,b), C_{84} (c), and C_{90-92} (d) freeze-dried hydrogels. SEM images at (a) low, and (b) high magnification are shown for the C_{60} sample. Images provided by Dr. Rašović [200] and printed with his permission.

5.3.1.2 Mechanical characterisation

The elasticity of the fullerene-based hydrogels in ultrapure water was quantified by calculating $\tilde{E}$ from AFM quasi-static force indentation curves. Indentations were performed by a modified AC240 cantilever with a 20 µm diameter bead attached to the tip, in order to quantify $\tilde{E}$ at the micron scale. For each sample, the several positions measured on the surface were indented one hundred times each.

An example of force indentation curve on the C_{84} hydrogel is plotted in Fig. 5.8 (a). The red curve represents the cantilever's approach towards the sample. The measured force gradually increases until the trigger point is reached. Once the trigger point is reached, the cantilever is withdrawn from the sample (blue curve in Fig. 5.8 (a)) until it is no longer in contact.

From Fig. 5.8 (a), the cantilever's approach is smooth. The withdraw curve presents some "jumps" that are likely due to polymeric chains detaching from the bead as the cantilever retracted from the sample. The Hertz model was used to calculate $\tilde{E}$ (see Section 2.2.2) from the approach of each indentation curve. Withdraw curves were not fit in order to minimise any error caused by chain sticking. In Fig. 5.8 (a), the Hertz model (yellow line) fits the experimental data well, meaning that it was the appropriate model to quantify $\tilde{E}$.

$\bar{\tilde{E}}$ was calculated over the one hundred curves at every position. The values of $\bar{\tilde{E}}$ were then averaged over all positions ($\overline{\bar{\tilde{E}}}$). The resulting averages ($\overline{\bar{\tilde{E}}}_{C_{60}} = (8.2 \pm 6.2)\,\text{kPa}$, $\overline{\bar{\tilde{E}}}_{C_{84}} = (183 \pm 29)\,\text{kPa}$, and $\overline{\bar{\tilde{E}}}_{C_{90-92}} = (432 \pm 286)\,\text{kPa}$) are plotted in Fig. 5.8 (b).

5.3.2 Discussion

5.3.2.1 Morphological characterisation

Fig. 5.6 demonstrates that the fullerene hydrogels were manipulable at the macroscale, and exhibited water retention typical of hydrogels.

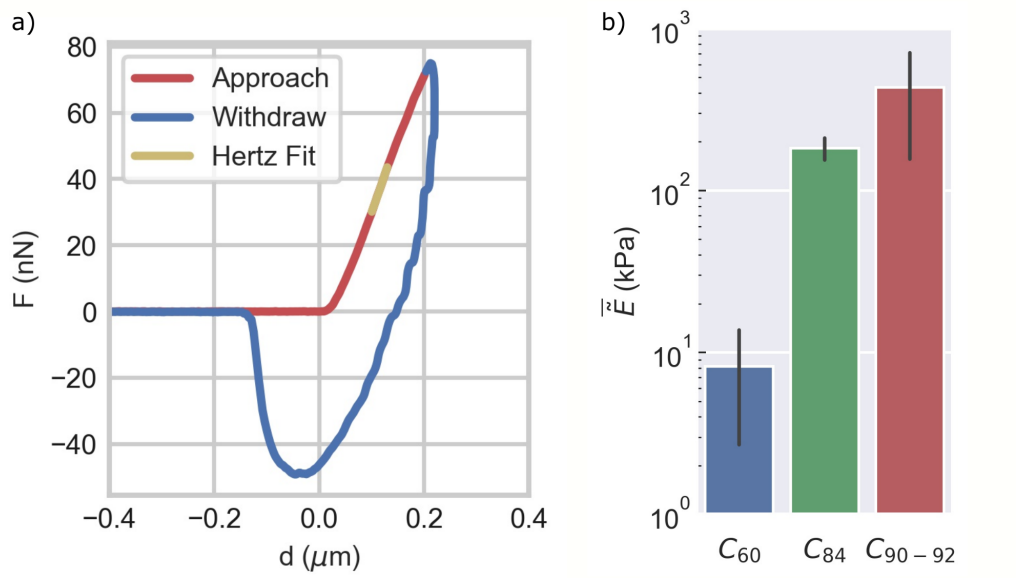


Figure 5.8: Mechanical characterisation of fullerene-based hydrogels with AFM. (a) An example of force (F) vs indentation (d) curve on a C_{84} hydrogel. The Hertz fit is plotted in yellow. (b) Averaged reduced Young's modulus calculated over all the measured positions ($\overline{\tilde{E}}$) of C_{60}, C_{84}, and C_{90-92} hydrogels. Error bars correspond to the standard deviation.

SEM allowed the morphological characterisation of the porous structures of the freeze-dried fullerene-based hydrogels. Fig. 5.7 (a,b) reveal that the structure of the C_{60} hydrogel was made of a porous fibrillar network, and that small hollow fibres hierarchically assembled to form larger fibres. In other studies, structures based on C_{60} were much smaller [272, 273].

The C_{60} hydrogels were made possible by the TEGylation of the fullerenes, which resulted in the formation of a self-assembled hydrogel. This possibility of forming clusters made of fullerenes functionalised with poly(ethylene oxide) (PEO), in aqueous solutions, had already been predicted by molecular dynamic simulations [275, 276]. From these studies, it is known that non-covalent interactions between PEO-C_{60} fullerenes, including the short-range attraction between the hydrophobic fullerene cages and the "wrapping" of PEO chains around adjacent fullerenes, lead to the formation of supramolecular chainlike clusters [275, 276]. The non covalent interactions

between the TEGylated C_{60} resulted in the formation of a self-assembled C_{60} hydrogel which can therefore be defined a supramolecular hydrogel [263].

Most likely, some parts of the lower symmetry fullerene cages were not functionalised during the synthesis, leaving some hydrophobic regions of the cages uncovered. Additionally, the formation of the C_{84} hydrogel, like in the C_{60} hydrogel, was due to non-covalent interactions between higher symmetry C_{84} cages (higher symmetry cages are the most stable and abundant C_{84} isomers [277]) and the TEG-MEE chains, which led to the formation of tubular structures. The flaky regions (Fig. 5.7 (c)), can potentially be attributed to less symmetrical isomers of C_{84} fullerenes. It is possible that for non spherical cages, the TEG-MEE chains "wrapped" the cages leaving some hydrophobic regions free. These hydrophobic regions are attracted to each other in the aqueous environment and formed a two-dimensional (2D) structure.

It is likely that the C_{90-92} hydrogel formed through a similar mechanism to the C_{84} hydrogel. Again, the heterogeneous morphology (Fig. 5.7 (d)) of the hydrogel can likely be attributed to the different symmetries of the C_{90-92} isomers [141].

Therefore, Fig. 5.7 reveals the possibility of tuning the macroscopic structure of fullerene-based hydrogels depending on the symmetry of the constituent fullerene cage.

5.3.2.2 Mechanical characterisation

The inhomogeneities in porosity and morphology of the hydrogels is reflected by the large standard deviation of the calculated $\overline{\tilde{E}}$ (Fig. 5.8 (b)). It is possible that the presence of flat regions in C_{84} and C_{90-92} hydrogels increased their resistance to deformations thereby resulting in higher $\overline{\tilde{E}}$.

The value of $\overline{\tilde{E}}$ calculated for C_{60} hydrogels is more than one order of magnitude smaller than those of the higher fullerene hydrogels (Fig. 5.8 (b)). The calculated $\overline{\tilde{E}}_{C_{60}}$ is comparable to that of muscle [17, 57, 61, 231], and to that of carbon nan-

otube composite hydrogels for engineered cardiac tissue [67]. The calculated $\overline{\tilde{E}}_{C_{84}}$ and $\overline{\tilde{E}}_{C_{90-92}}$ are comparable to that of skeletal muscle and pre-calcified bone [17, 57, 61, 231]. Being in the range of biological tissues, the elastic properties of these fullerene-based hydrogels suggest that they could be promising scaffold material for tissue engineering. Additionally, $\overline{\tilde{E}}$ of all three fullerene hydrogels fell in the range of those of drug carriers used for drug delivery [18].

This is not the first time that differences in morphological and mechanical properties were found between supramolecular hydrogels built on carbon nanomaterials with different geometries [264]. This fact supports the hypothesis that the geometry of the fullerene cage used to build the hydrogels is linked the structure and elasticity of the resulting network.

5.3.3 Conclusions

In this section, the local elasticity of novel supramolecular macroporous self-assembled hydrogels based on TEGylated fullerenes was explored. Structural differences between hydrogels can be attributed to the geometry of the fullerene cages used as a primary material. C_{60} possessed a porous structure of interconnected hollow fibres that resulted from non-covalent bonds between the TEGylated fullerene cages and the TEG-MEE chains of neighbouring TEGylated fullerenes. C_{84} and C_{90-92} hydrogels possessed a similar porous structure, with the addition of flat regions that can be attributed to the lower symmetry of their cages.

Study of the mechanical properties of fullerene-based hydrogels synthesised from different fullerene cages revealed that the elasticity of these hydrogels is in the range of biological tissues, and that it is possible to tune hydrogel elasticity by changing the primary component (i.e. the fullerene cage used) of the hydrogel. Additionally, the porous structure, high water content, and elastic properties of these fullerene-based hydrogels suggest promising biomedical applications in tissue engineering.

$\overline{\tilde{E}}$ of C_{60} hydrogels was in the range of those of muscle tissues [17, 57, 61, 231], suggesting the possibility of using C_{60} hydrogels for muscle tissue engineering. Additionally, as mentioned earlier, incorporating carbon nanostructures into hydrogels can improve the electric conductivity of the hydrogels [67, 68] which is necessary for some types of tissue engineering, such as cardiac tissue engineering [67]. Therefore, C_{60} hydrogels could potentially be used to engineer artificial heart tissue. C_{84} and C_{90-92} hydrogels had higher $\overline{\tilde{E}}$, similar to those of harder tissues [17, 57, 61, 231], and therefore could be promising materials for bone tissue engineering.

In addition to tissue engineering applications, as discussed in Section 1.1, carbon-based nanomaterials can also be used for chemo-photothermal therapies [45–47]. It is possible to combine fullerenes with anticancer drugs [278–280], and the $\overline{\tilde{E}}$ of the fullerene-based hydrogels studied in this thesis is in the range of other drug carriers [18]. Therefore, these fullerene-based hydrogels are also promising candidates for chemo-photothermal therapies.

Chapter 6

Development of an AFM nano-DMA technique based on PT excitation of the AFM cantilever

6.1 Introduction

In Chapters 4 and 5 the local elastic properties of hydrogels were probed to test their feasibility for biomedical applications in terms of their mechanical properties. In reality, hydrogels mechanics can be more appropriately described by viscoelasticity, as explained in Chapter 1. In order to provide a new tool to quantify the viscoelastic properties of hydrogels, I developed a novel nano/micro-rheology technique based on PT actuation of the AFM cantilever, which will be called PT-AFM nano-DMA from now onwards, that I present in this chapter. PT-AFM nano-DMA takes advantage of AFM, PT excitation (see Section 2.2.1), chirp signals (see Section 2.2.4), and theoretical models for the calculation of the viscoelastic properties of the material (see Sections 2.2.2 and 2.2.3). PT-AFM nano-DMA allowed the investigation of the viscoelastic properties of a SBR, used as a test material, at the nano- (and micro-)

scale in a continuous frequency range spanning up to five orders of magnitude (0.2 Hz to 20 200 Hz). To the best of my knowledge, this is the first time that PT actuation is used for AFM nano/micro-rheological measurements to calculate the viscoelastic properties of polymeric materials ($\tan\delta$, k', k'', E', and E'') and reproduce results from macroscopic DMA over such a broad and continuous frequency range.

In this chapter, I describe the tools and strategies used to test the PT-AFM nano-DMA for the quantification of the viscoelastic properties of materials. First, I show the results obtained with macroscopic DMA that I later use as a comparison for the PT-AFM nano-DMA. Second, I present simulations useful for the choice of the cantilever for PT-AFM nano-DMA experiments. Third, the PT-AFM nano-DMA results are presented, initially in terms of the $\tan\delta$ and k^* of the material. The final part of this chapter is focused on choosing the correct contact model to calculate the material E^*. Additionally, I compare results obtained with PT-AFM nano-DMA to that of quasi-static force indentation curves, and to results obtained with a bimodal AFM method to map viscoelastic properties of materials.

6.2 DMA experiments

The macroscopic viscoelastic behaviour of the SBR sample was studied with DMA in tension mode (see Section 2.5). In Fig. 6.1 (a) $\tan\delta$ is shown for a T range of 30 °C to 50 °C measured at 0.1 Hz, 0.3 Hz, 1 Hz, 3 Hz and 10 Hz. As explained in Section 1.2.2, it is possible to obtain a master curve by shifting the curve at a certain T with respect to a fixed curve at $T = T_0$ (TTS principle). It is worth noting in Fig. 6.1 (a) how the $\tan\delta$ of the SBR changes between the measured frequencies for isothermal sweeps, and between the T in the measured frequency range, typical behaviour for most viscoelastic materials. Fig. 6.1 (b) shows the TTS shifted data for $\tan\delta$ of Fig. 6.1 (a) with $T_0 = 40$ °C.

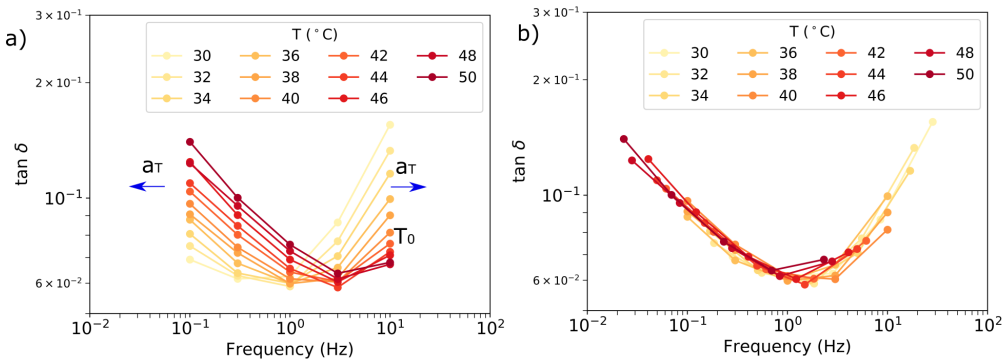


Figure 6.1: The TTS principle applied to DMA measurements of a SBR sample. TTS widens the frequency range in which the viscoelastic properties of the SBR can be studied by applying a shift factor (a_T). (a) Loss tangent ($\tan\delta$) obtained at different temperatures (T) between 30 °C and 50 °C at frequencies 0.1 Hz, 0.3 Hz, 1 Hz, 3 Hz and 10 Hz. (b) $\tan\delta$ obtained shifting the curves in (a) relative to the reference temperature (T_0) of 40 °C.

The complete master curves for $\tan\delta$, E', and E'' moduli at 40 °C (T_0) are shown in Fig. 6.2. Master curves were constructed from TTS of the data from the entire T range from −50 °C to 70 °C.

In Fig. 6.2 (a), $\tan\delta$ at 40 °C identifies the SBR glass transition at 10^5 Hz ($\tan\delta$ peak position). The low frequency resonance between 10^{-2}−10^{-3} Hz is attributed to the relaxation of physical entanglements between the polymer chains, a phenomenon which has been reported for SBR previously [19, 281]. The inset in Fig. 6.2 (a) shows the logarithm of the horizontal shift factors (a_T) plotted and fit with the WLF model (see Section 1.2.2, Eq. (1.17)). The two constants c_1 and c_2 were determined as 5.04 ± 0.16 and 91.80 ± 1.24, very close to the one expected for $T_0 = T_g + 50$ °C (see Section 1.2.2). The WLF curve is in good agreement with the experimental data for $T > -20$ °C.

The lack of adherence to the WLF model for $T < -20$ °C is attributed to sample's contraction at very low T causing the sample to slip from the clamps, thereby affecting the measurements. Nevertheless, $T < -20$ °C correspond to frequencies >

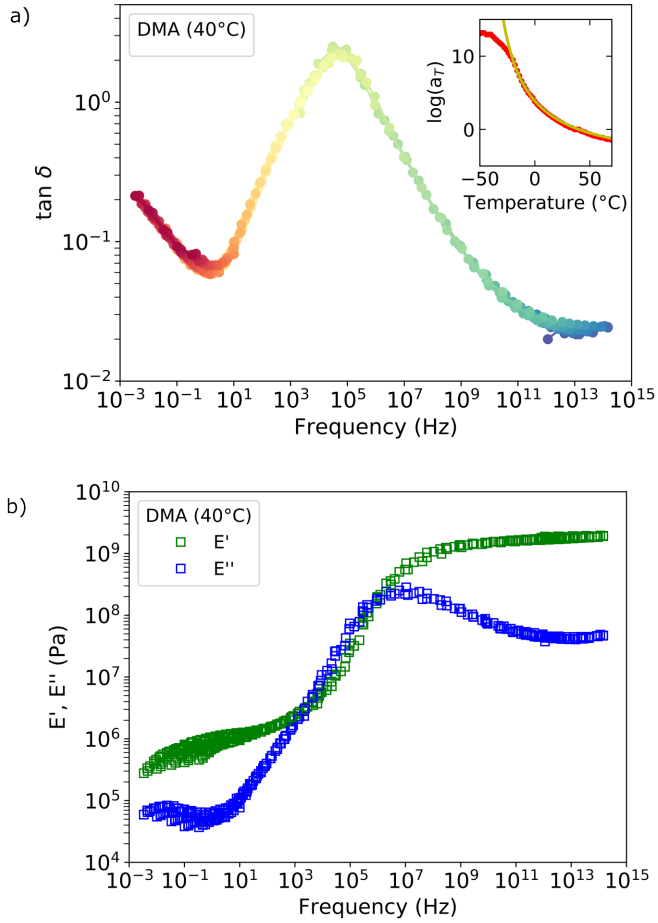


Figure 6.2: Master curves of the viscoelastic quantities of a SBR sample. Panel (a) shows the loss tangent ($\tan\delta$) at 40 °C obtained by applying the TTS principle to data collected at temperatures T ranging from −50 °C (blue circles) to 70 °C (dark red circles). T within this range are plotted in shades from blue to red. In the inset, the horizontal shift factors (a_T) for the reference temperature $T_0 = 40$ °C are plotted for each T (red markers) and fit with the WLF model (yellow curve). Panel (b) shows the master curves for the storage (E', green unfilled squares) and loss (E'', blue unfilled squares) moduli at 40 °C.

10^9 Hz in the master curve in Fig. 6.2. These frequencies are much higher than the resonance frequencies of the cantilevers used in this study, and therefore irrelevant for the comparison to the AFM nano-DMA results.

In Fig. 6.2 (b), E' and E'' are plotted in green and blue, respectively. As expected in the glass transition region both E' and E'' increase by several orders of magnitude.

6.3 Contact stiffness simulations

In this section, I present contact stiffness simulations based on the Hertz model [159, 160] for a spherical indenter, and on the Sneddon model for a conical indenter [161] (see Section 2.2.2.1). The goal of these simulations is to inform the choice in cantilever (i.e. in cantilever spring constant k_c) when a rough idea of the sample's modulus (i.e. its order of magnitude) is known. As a first approximation, adhesion is not taken into account in these simulations.

For the Hertz spherical model [159, 160] and the Sneddon conical model [161], the relation between F and d can be expressed as follows (see Section 2.2.2.1):

$$F = \begin{cases} \frac{3}{4}\sqrt{R_I}\tilde{E}d^{3/2}, & \text{for spherical model} \\ \frac{2}{\pi}\tan(\alpha)\,\tilde{E}d^2, & \text{for conical model} \end{cases} \tag{6.1}$$

As explained in Section 2.2.2.1, k_S can be calculated as the derivative of F over d [105, 162] which leads to:

$$k_S = \frac{dF}{dd} = \begin{cases} 2\sqrt{R_I}\tilde{E}d^{1/2}, & \text{for spherical model} \\ \frac{4}{\pi}\tan(\alpha)\,\tilde{E}d, & \text{for conical model} \end{cases} \tag{6.2}$$

In Fig. 6.3, k_S is mapped for a spherical ($R_I = 7\,\text{nm}$) and a conical ($\alpha = 17.5°$) indenter for a sample with $\tilde{E}$ ranging from 1 kPa to 1 GPa, and d from 1 nm to 2.5 µm.

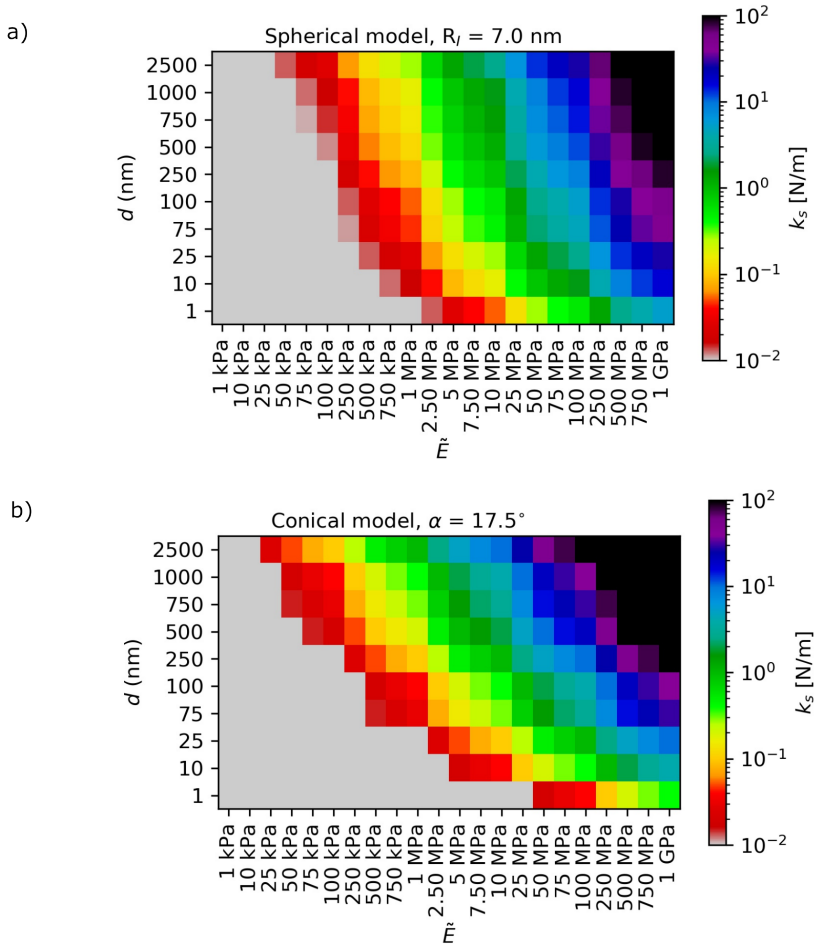


Figure 6.3: Contact stiffness (k_S) simulations for different sample deformations (d) and reduced Young's modulus ($\tilde{E}$) values for (a) a Hertz spherical indenter with radius $R_I = 7\,\text{nm}$, and (b) a Sneddon conical indenter with semi-vertical angle $\alpha = 17.5°$.

Using $\tilde{E}$ instead of E for mapping k_S allows to rescale the map if ν_S is known. In Fig. 6.4, k_S is mapped for spherical indenters with larger radii: $R_I = 2\,\mu\text{m}$ and $25\,\mu\text{m}$.

As explained in Section 2.2.2, for AFM indentation experiments it is recommended to use a cantilever with k_c larger than or comparable to k_S [105]. The comparison of the results in Fig. 6.3 and Fig. 6.4, shows that, for a fixed $\tilde{E}$, as the indenter size increases, k_c of the cantilever used should also increase in order to stay comparable to k_S. It is important to keep in mind that these simulations do not consider adhesion forces. k_S in presence of adhesion forces may be different, since adhesion usually

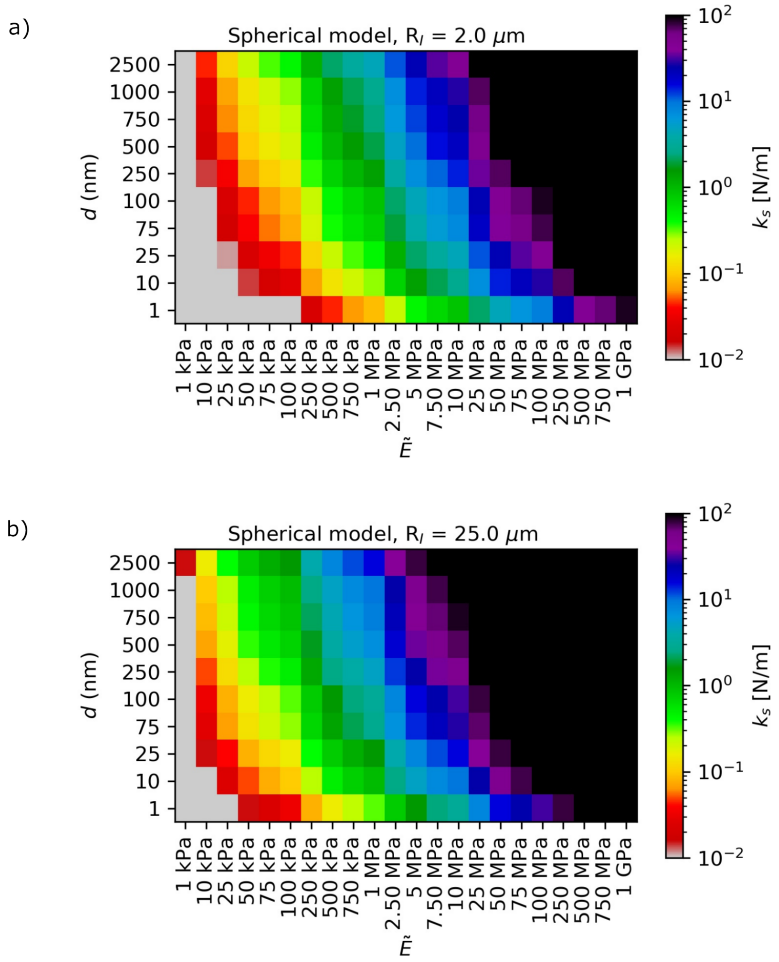


Figure 6.4: Contact stiffness (k_S) simulations for different sample deformations (d) and reduced Young's modulus ($\tilde{E}$) values for Hertz spherical indenters with a radius (R_I) of (a) 2 µm, and (b) 25 µm.

increases a (see Section 2.2.2.2).

6.4 Stress relaxation experiments

In order to perform stress relaxation experiments (see Section 1.2.1), a static deformation was applied to a SBR sample by means of the AFM cantilever (Fig. 6.5 (a)). During the time of the deformation, the sample relaxed as shown in Fig. 6.5 (b).
Three stress relaxation curves were acquired. The static indentation d_0 obtained was around 630 nm for all curves (see Fig. 6.5 (a)). d_0 was not perfectly constant because it was calculated from the cantilever deflection and the Z-piezo position (see Section 2.2.2). d_0 changes almost 5 nm during the first second of the dwell (that corresponds to less than 1 % of the total d_0), as shown in Fig. 6.5 (c). Therefore, dwells were analysed from 1 s onwards (where d_0 was mostly constant). The stress relaxation was fit with the standard linear solid (SLS) model described in Appendix A with Eq. (A.1).
Initial guesses of the parameters for the fit were calculated with Eq. (A.1), using the experimental data (F, d_0) at particular times during the dwell ($t = \infty$, 0, and τ_M) as follows. For $t = \infty$ (in this experiment $t = 60$ s):

$$k_\infty = \frac{F(t=\infty)}{d_0} \tag{6.3}$$

For $t = 0$ (in this experiment $t = 1$ s):

$$k_1 = \frac{F(t=0)}{d_0} - k_\infty \tag{6.4}$$

Next, $t = \tau_M$ (τ_M being the relaxation time of the material, see Appendix A) can be

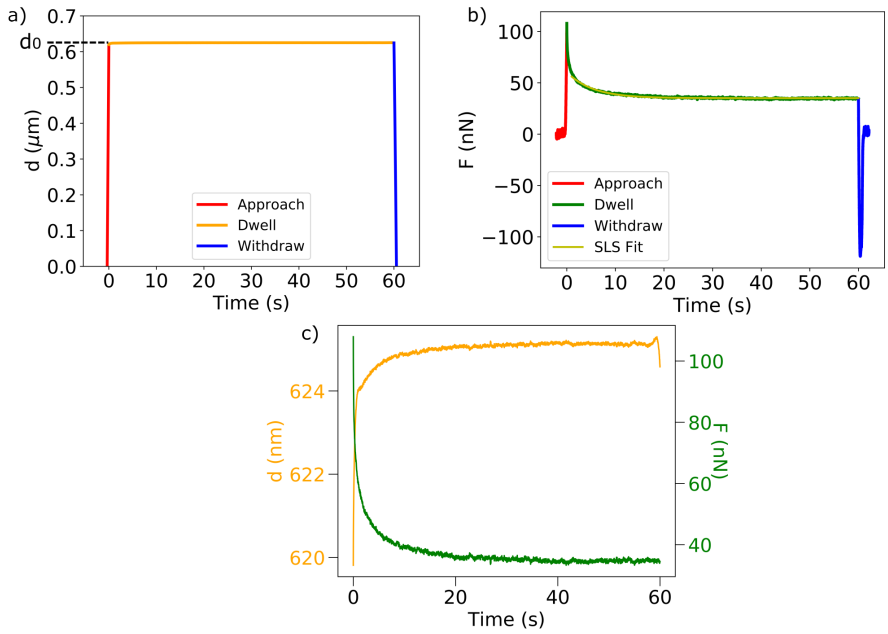


Figure 6.5: Stress relaxation of the SBR sample. Typical stress relaxation of the SBR obtained by keeping the deformation constant. Panel (a) shows indentation (d) during the approach (red line), dwell (orange line), and withdraw (blue line) by the cantilever on the sample. A static indentation (d_0) is applied during the dwell. Panel (b) shows the force (F) during the approach (red line), dwell (green line) and withdraw (blue line) of the cantilever. The yellow line corresponds to a fit of the SLS model to the data. Panel (c) shows d (orange line) and F (green line) during the dwell.

calculated from $F(t = \tau_M)$ as follows:

$$F(t = \tau_M) = d_0(k_\infty + \frac{k_1}{e}) \tag{6.5}$$

Once that τ_M was known, η was calculated as $\eta = k_1\tau_M$. The parameters k_∞, k_1, η, and $\tau_M = \eta/k_1$ obtained from the fit on the three stress relaxation curves were averaged and are reported with their standard deviations in Table 6.1.

The calculated τ_M corresponds to a frequency $f_M = 1/(2\pi\tau_M) \approx 0.03\,\mathrm{Hz}$, which matches the low frequency resonance around 10^{-2}–$10^{-3}\,\mathrm{Hz}$ in $\tan\delta$, E', and E'' evident in the macroscopic DMA data (Fig. 6.2).

k_∞ (N/m)	k_1 (N/m)	η $(N \cdot s/m)$	τ_M (s)
0.054 ± 0.008	0.037 ± 0.005	0.224 ± 0.015	6.158 ± 0.848

Table 6.1: Mean values and standard deviations of the SLS parameters obtained from three stress relaxation curves.

6.5 PT-AFM nano-DMA experiments

In this section, the steps that led to the measurement and calculation of a sample's viscoelastic quantities by means of the PT-AFM nano-DMA experiments are presented. Here, I also demonstrate how to obtain accurate measurements of the viscoelastic quantities of a SBR sample using PT-AFM nano-DMA. The different variables, experimental conditions, and theoretical analysis frameworks that could affect the outcome of the measurement were thoroughly investigated. These factors included: (i) the effect of altering PT excitation by changing the position of the PT-EL on the cantilever (Sections 6.5.1 and 6.5.2), (ii) the effect of the reference signal (Section 6.5.3), (iii) the effect of PT-EL power (Section 6.5.4), (iv) the effect of different PT-EL excitation signal amplitudes (Section 6.5.5), (v) the effect of different indentation depths (Section 6.5.6), (vi) the effect of using different cantilever approach velocities (Section 6.5.7), (vii) the effect of the cantilever stiffness (Section 6.5.8). Furthermore, data obtained via PT-AFM nano-DMA are compared to data obtained via PE-AFM nano-DMA (Section 6.6). An analysis on the contact mechanics models used for the calculation of E^* from k^* is also presented (Section 6.7). Additionally, I compare the mechanical properties of the SBR sample obtained with quasi-static force indentation curves to PT-AFM nano-DMA data (Section 6.8). Lastly, PT-AFM nano-DMA is also compared with multifrequency PT AM-FM AFM (Section 6.9).

The goal of the PT-AFM nano-DMA technique that I have been developing is to measure the viscolastic quantities (i.e. k', k'', $\tan\delta$, E', and E'') of materials over a broad and continuous range of frequencies by means of chirp signals.

Cantilever oscillations can be achieved by modulating a PT-EL focused at the back

of the cantilever. The cantilever's response during the indentation of the sample, and the cantilever's response when the tip is not in contact with the sample (reference signal) are necessary to calculate the viscoelastic properties of the sample (see Section 2.2.3). In particular, the amplitude and the phase signals of the cantilever's responses are needed to calculate k^* and $\tan\delta$ of the material (see Section 2.2.3).
Reference measurements were acquired far away from the sample (see Section 3.3.3.3). Measurements on the sample were acquired in the following way: an initial deformation was applied to the sample with the AFM tip, a few seconds were waited for the stress relaxation of the sample [125], and then the oscillatory signal was applied to the cantilever. The position of the Z-piezo was kept constant by the AFM feedback loop for the whole duration of the chirp signal. Therefore, the oscillatory deformations of the sample were only given by the oscillatory movements of the cantilever.

The typical response of an AC160TSA-R3 cantilever during the interaction with the SBR sample is shown in Fig. 6.6 (a) (red line). The reference measurement (out of contact) is also shown in Fig. 6.6 (a) (black line). The drive signal (i.e. the signal exciting the PT-EL) plotted in the inset is a logarithmic chirp from 1 Hz to 1001 Hz frequency range, with a sweep time of 30 s and a drive amplitude of 1 V. The change in the cantilever's response between the sample and reference measurement is already evident in the time domain (Fig. 6.6 (a)).
For chirp signals with frequencies below 1 kHz, the amplitude and phase of the cantilever oscillations were transformed from the time to frequency domain by means of FFT (see Appendix B for more details). For higher frequencies, a LIA was employed to acquire the data.
The amplitude and phase of the reference and the sample measurements are plotted in the frequency domain in Fig. 6.6 (b,c). Both the amplitude and phase signals dropped with increasing frequency. This behaviour, typical of PT measurements [282], can be explained by the decrease in the exciting PT force due to smaller T changes as fre-

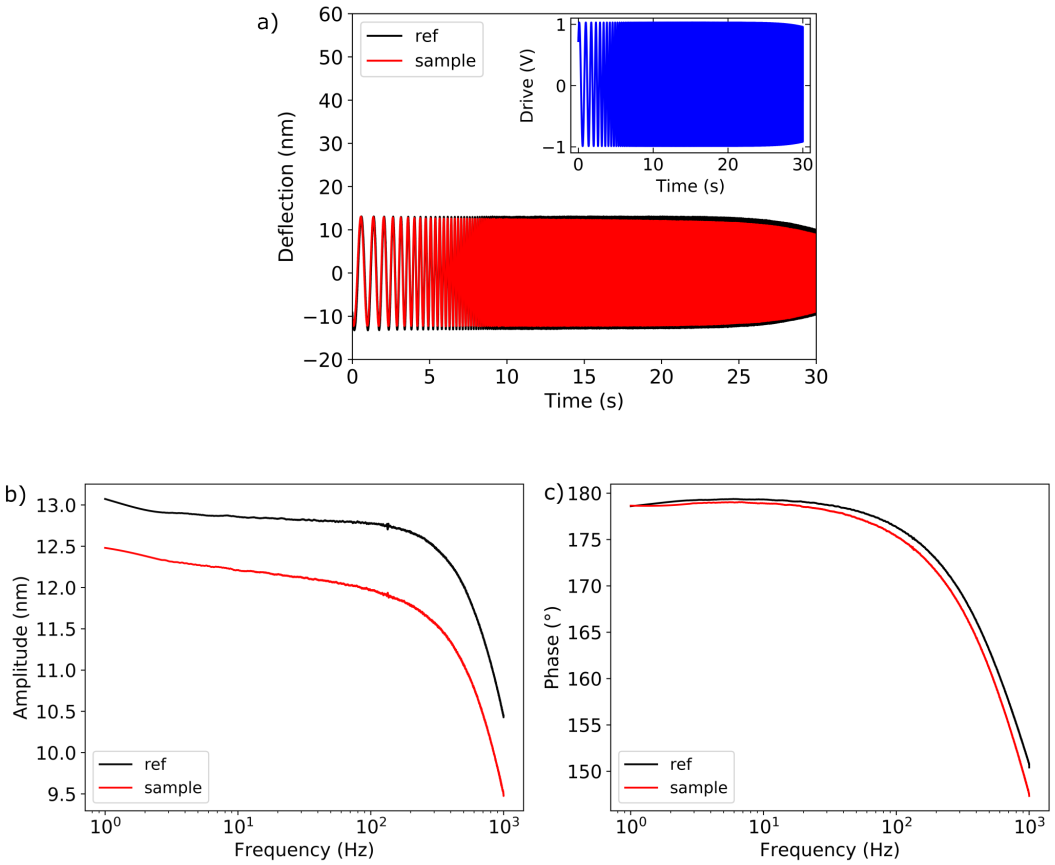


Figure 6.6: Typical response of an AC160TSA-R3 cantilever to a chirped PT excitation. (a) Deflection of the cantilever in contact (red line) and out of contact (black line) with the SBR sample during the PT excitation. The drive signal sent to the PT-EL is plotted in the inset. (b) Amplitude, and (c) phase of the deflection signals from (a) plotted in the frequency domain.

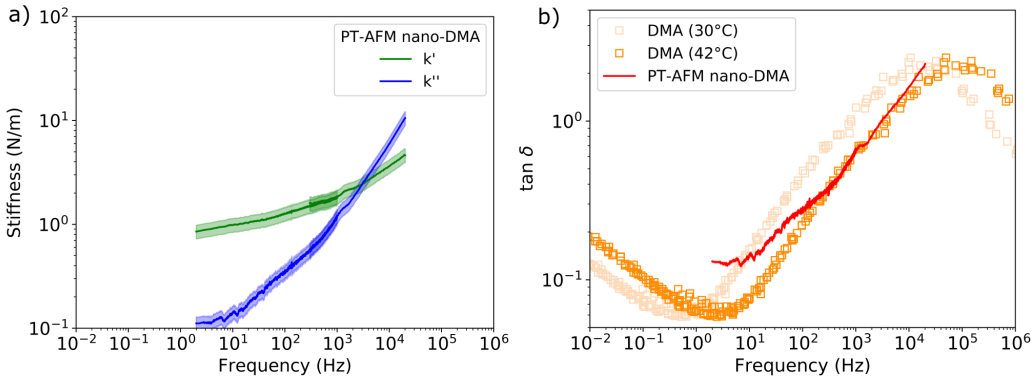


Figure 6.7: Storage stiffness (k'), loss stiffness (k''), and loss tangent ($\tan\delta$) of a SBR sample obtained using the PT-AFM nano-DMA technique. Panel (a) shows k' (green line) and k'' (blue line). Panel (b) shows a comparison of $\tan\delta$ obtained with PT-AFM nano-DMA (red line), and with macroscopic DMA at 30 °C and 42 °C (peach and orange unfilled squares, respectively). Error on the PT-AFM nano-DMA data are shown as shades and are calculated as explained in Section 6.5.2.

quency increases [152]. Phase signals correspond to the phase difference between the PT-EL drive signal and the oscillations of the cantilever. The 180° phase can be explained because the higher the PT-EL power, the more the cantilever gold coating expands bending the cantilever down. The comparison between the amplitude and phase between the reference and the sample signals in the frequency domain in Fig. 6.6 (b,c) shows these differences even more clearly than the time domain (Fig. 6.6 (a)).

As explained in Section 2.2.3, k' and k'' for direct cantilever excitation can be calculated from the amplitude and phase of the sample and reference signals (Eq. (2.28)). $\tan\delta$ can be calculated as the ratio of k'' and k' (see Eq. (2.34)). These viscoelastic quantities are shown in Fig. 6.7. They were calculated using the average of the amplitude and phase of multiple signals for both the reference (6) and the sample (5) measurements. In Fig. 6.7 (a), both k' and k'' increase with increasing frequency. Similarly to Fig. 6.2 (b), the loss component has a steeper increase and becomes larger than the elastic component.

In Fig. 6.7 (b), $\tan\delta$ obtained with the PT-AFM nano-DMA is compared to

macroscopic DMA data. It would be expected that PT-AFM nano-DMA would be comparable with macroscopic DMA data around 30 °C, since the ambient T of the AFM was around 31 °C−33 °C. However, as shown in Fig. 6.7 (b), PT-AFM nano-DMA data are not in agreement with macroscopic DMA data at 30 °C (peach unfilled squares). Instead, PT-AFM nano-DMA data matched very well DMA data at 42 °C (orange unfilled squares). This result suggests that the PT-EL was locally heating the system.

In the low frequency range, a small deviation of $\tan\delta$ obtained with PT-AFM nano-DMA and with macroscopic DMA can be observed in Fig. 6.7 (b). Small differences between local and macroscopic data have already been reported in previous studies [130, 131, 133], although the causes were not clearly elucidated. In some cases, it was proposed that non-linear viscoelastic effects, due sample stiffness changing with frequency which could affect the amplitude of the strain applied, could potentially be a contribution [133]. I exclude this hypothesis for my experiments because, as it is shown in Section 6.5.5, by changing the amplitude of the cantilever oscillations the sample was proved to be in the linear viscoelastic regime. Another hypothesis is the higher relevance of surface effects at the small scale [130], which could be affecting my measurements. Additionally, it is important to consider that data obtained with macroscopic DMA are averages of the mechanical properties of the material, which might therefore hide the contributions to the material properties at the local scale.

The T increase of the sample due to the PT-EL is further discussed throughout the rest of the chapter. Comparison of PT and PE excitation showed differences in the calculated viscoelastic properties of the SBR sample (see Section 6.6). This observation is also consistent with an increase of T due to PT excitation. Additionally, quasi-static force indentation curves with and without the PT-EL focused on the cantilever presented significant difference in the modulus of the sample (see Section 6.7).

6.5.1 Effects of altering the position of the PT excitation laser

In this subsection, I describe the effects of the positioning of the PT-EL on PT-AFM nano-DMA measurements.

Previous studies have reported that the position of the PT-EL on the cantilever alters the amplitude of coated [152, 154, 157, 283, 284] and uncoated [153, 154, 284] cantilever oscillations. Off-resonance studies (with frequencies smaller than 10 % of the cantilever's resonance frequency) highlighted the importance of the PT-EL positioning on the cantilever in order to obtain correct quantification of stiffness of materials [157].

Several different photothermal excitation laser spot (PT-ELS) positions were tested in order to study the effect of PT-ELS position on PT-AFM nano-DMA measurements. PT-ELS positions were quantified by introducing a reference system with its centre in the middle of the cantilever base (see Fig. 6.8 (a)). In this reference system the centre of the reference system is placed in the middle of the cantilever base. x defines the PT-ELS position over the length of the cantilever (L), and y defines the PT-ELS position over the width of the cantilever (W).

The PT-ELS position in these coordinates is expressed as a fraction, x/L and y/W. Nine different PT-ELS positions (combining three different x/L ratios with three different y/W ratios) were tested, as shown in Fig. 6.8 (a-i). The PT-ELS position at $x/L = 1/10$ and $y/W = 0$ (Fig. 6.8 (d)) has been shown to give reliable results for off-resonance mechanical measurements [157]. For this reason, PT-ELS at $x/L = 1/10$ and $y/W = 0$ was used as reference for this study.

The amplitude and the phase signals obtained with the nine different PT-ELS configurations (Fig. 6.8) are plotted in Fig. 6.9 for both the reference and the sample measurements. Both the amplitude and the phase of the cantilever oscillations were affected by the positioning of the PT-ELS. As shown in Fig. 6.9, the amplitude of

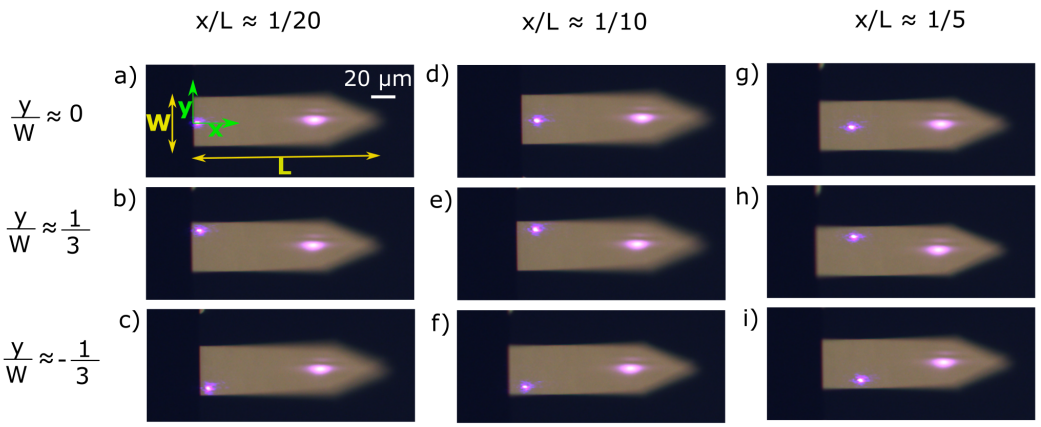


Figure 6.8: PT-ELS positions on the cantilever. (a-i) Different PT-ELS positions on the cantilever. Scale bar 20 µm.

signals measured with PT-ELS at $x/L = 1/5$ is higher compared to that of $x/L = 1/10$ (a similar finding to that of Ramos *et al.* [152] who studied PT-EL positioning on coated cantilevers in liquid). The amplitude calculated for signals measured with PT-ELS at $x/L = 1/20$ is the lowest, and almost half to that measured for $x/L = 1/5$. PT-ELS movement on the y-axis affected the amplitude and the phase of the signals much less than movements on the x-axis. For $x/L = 1/20$ and $x/L = 1/5$, the shift of the PT-ELS towards the edges of the cantilever width seems to slightly increase the amplitude of the measured signals. However, it is unclear whether these effects are due to the movement of the PT-ELS in the y direction, or due to an involuntary shift of the PT-ELS on the x position during the re-positioning of the PT-ELS. It is also worth noting that a non uniform metallic coating of the cantilever could also be affecting the response of the cantilever to the PT excitation.

The reference and the sample of signals from Fig. 6.9 were used to calculate $\tan\delta$ as explained in Section 2.2.3. While $\tan\delta$ calculated from signals measured with PT-ELS at $x/L = 1/20$ and $x/L = 1/10$ overlap very well with each other, $\tan\delta$ calculated from signals measured with PT-ELS at $x/L = 1/5$ is slightly lower.
This result agrees with the finding of Wagner and Killgore [157] on the importance

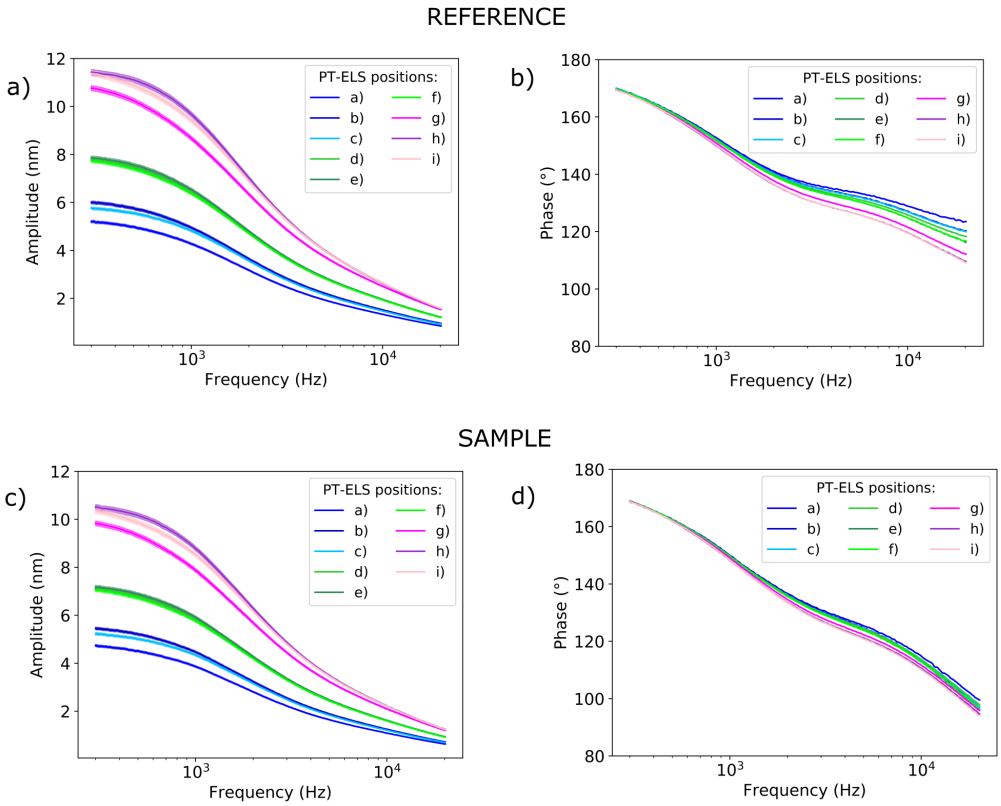


Figure 6.9: Amplitude and phase signals of reference and sample measurements obtained with different PT-ELS positions. Reference (a) amplitude, and (b) phase signals, as well as sample (c) amplitude, and (d) phase signals, obtained from the nine PT-ELS positions shown in Fig. 6.8. Letters in the legends correspond to the positions shown in Fig. 6.8 (a-i). (i.e. "a)" in the legend corresponds to panel (a) in Fig. 6.8).

of the PT-EL positioning in PT off-resonance mechanical characterisation of materials. Wagner and Killgore showed that for off-resonance PT actuation the cantilever vibration shape in contact with the sample depends on the laser position and changes depending on the sample stiffness [157]. Therefore, it is possible that for measurements with PT-ELS at $x/L = 1/5$ the cantilever vibration shape during the contact with the sample could have been different compared to that of the reference signal, thereby leading to miscalculations of the $\tan\delta$ values.

Another possibility could be that the higher proximity of the PT-ELS to the sample for the $x/L = 1/5$ configuration increased the T of the sample more compared to $x/L = 1/20$ and $x/L = 1/10$, therefore shifting $\tan\delta$ to higher T. Further studies may be required for the comprehension of this phenomenon, but its complete understanding is beyond the scope of this research.

Nevertheless, this study restates the importance of PT-ELS positioning for PT-AFM nano-DMA experiments for the quantification of viscoelastic properties, and indicates that positioning the PT-ELS at the base of the cantilever generates more reliable results for PT-AFM nano-DMA experiments. While spots as close to the cantilever base as possible ($x/L = 1/20$) gave good agreement with macroscopic DMA, the higher amplitudes generated by PT-ELS at $x/L = 1/10$ could be helpful, especially at higher frequencies. Therefore, the $x/L = 1/10$ and $y/W = 0$ PT-ELS position seems the best to use for PT-AFM nano-DMA experiments, as this position has been shown to be reliable by the literature [157] and by these experiments.

6.5.2 Effects of PT excitation laser spot displacements during cantilever movements

Here, I study the effects of displacements of the PT-ELS position on the cantilever that might occur during movements of the AFM motors.

As shown in Section 6.5.1, different PT-ELS positions on the cantilever alter the can-

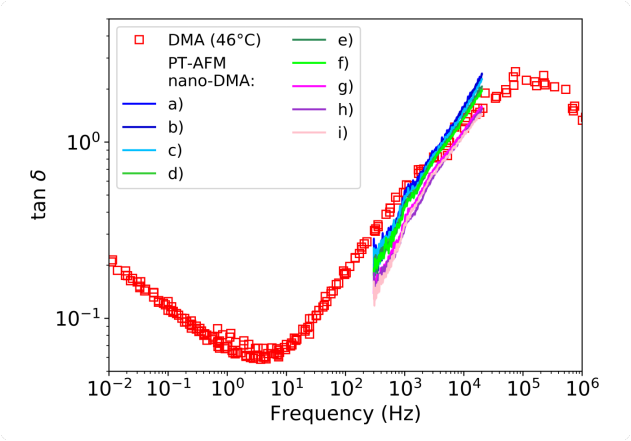


Figure 6.10: Loss tangent ($\tan\delta$) calculated from the signals shown in Fig. 6.10 compared to that of macroscopic DMA data at 46 °C (red unfilled squares). Letters in the legends correspond to the positions shown in Fig. 6.8 (a-i). (i.e. "a)" in the legend corresponds to panel (a) in Fig. 6.8. Error on the PT-AFM nano-DMA data are shown as shades and are calculated as explained in Section 6.5.2.

tilever's response. Therefore, it is possible that differences in the amplitude and phase between the reference and sample could be caused by movements of the PT-ELS position, rather than the tip's interaction with the sample. This systematic error could thereby cause miscalculation of the viscoelastic quantities of the sample. Since such changes in the PT-ELS positions are impossible to avoid, it is necessary to estimate the systematic error of PT-AFM nano-DMA measurements.

To calculate this error for both the reference (R) and sample (S) measurements, several signals for both the reference and the sample were compared. Comparison signals were collected by the following procedure. (1) A reference signal was taken 500 µm above the surface of the sample. (2) The tip was then brought (down) into contact with the sample as usual. (3) The sample signal was acquired. (4) The cantilever was then lifted (up) to 600 µm above the surface, then lowered (down) to 550 µm, and finally (down) to 500 µm. Step (1-4) were repeated five times. Step (4) of this procedure was introduced to avoid backlash of the motors (temporary jerking of the cantilever caused by a reversal in the direction of the motors, in this case by changing from moving down to moving up).

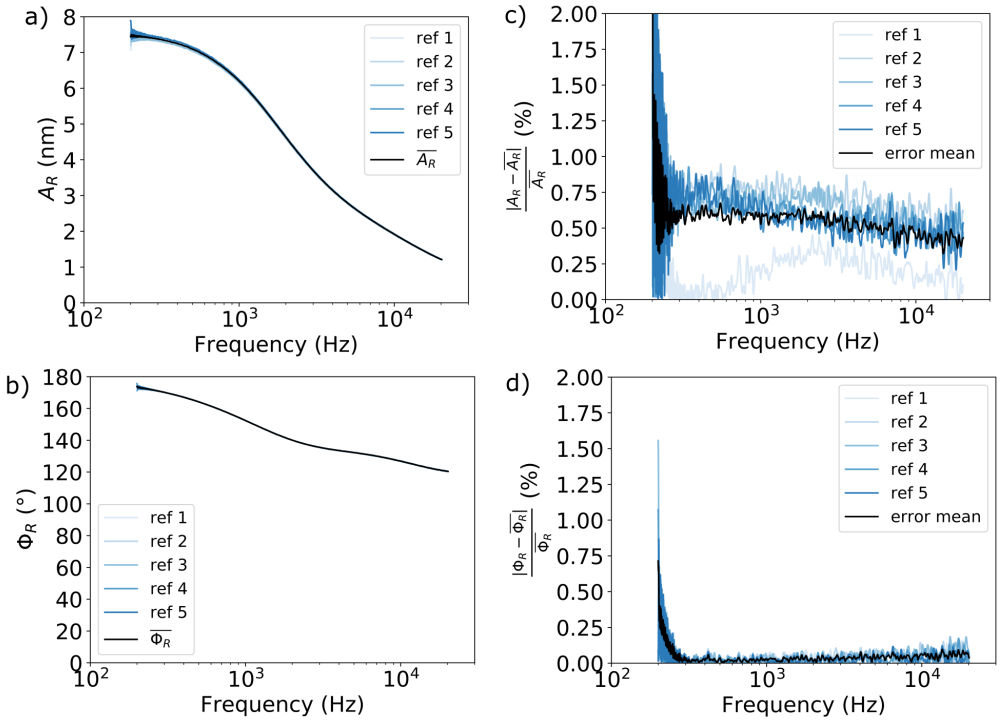


Figure 6.11: Reference measurements from rising and lowering the cantilever multiple times. (a) Amplitude (A_R), and (b) phase (ϕ_R) signals of the reference measurements. The black line corresponds to the mean of the signals ($\bar{A}_R$, $\bar{\phi}_R$). (c,d) Relative errors of the signals in (a,b) calculated with Eq. (6.6). The black line corresponds to the mean relative error.

The amplitude (A) and phase (ϕ) calculated for the reference and the sample measurements are shown in Fig. 6.11 and Fig. 6.12, respectively.

For both reference and sample measurements, the mean amplitude ($\bar{A}_R$ and $\bar{A}_S$, respectively) and the mean phase ($\bar{\phi}_R$ and $\bar{\phi}_S$, respectively) signals were calculated (black lines in Fig. 6.11 (a,c) and Fig. 6.12 (a,c), respectively). The relative error of each signal (X) with respect to the mean ($\bar{X}$), was calculated as:

$$err(\%) = \frac{|X - \bar{X}|}{\bar{X}} \tag{6.6}$$

The relative errors of the amplitude and phase signals for the reference and the sample measurements are shown respectively in Fig. 6.11 (c,d) and Fig. 6.12 (c,d).

For frequencies above 300 Hz, errors in the amplitude signals were less than 1 % of

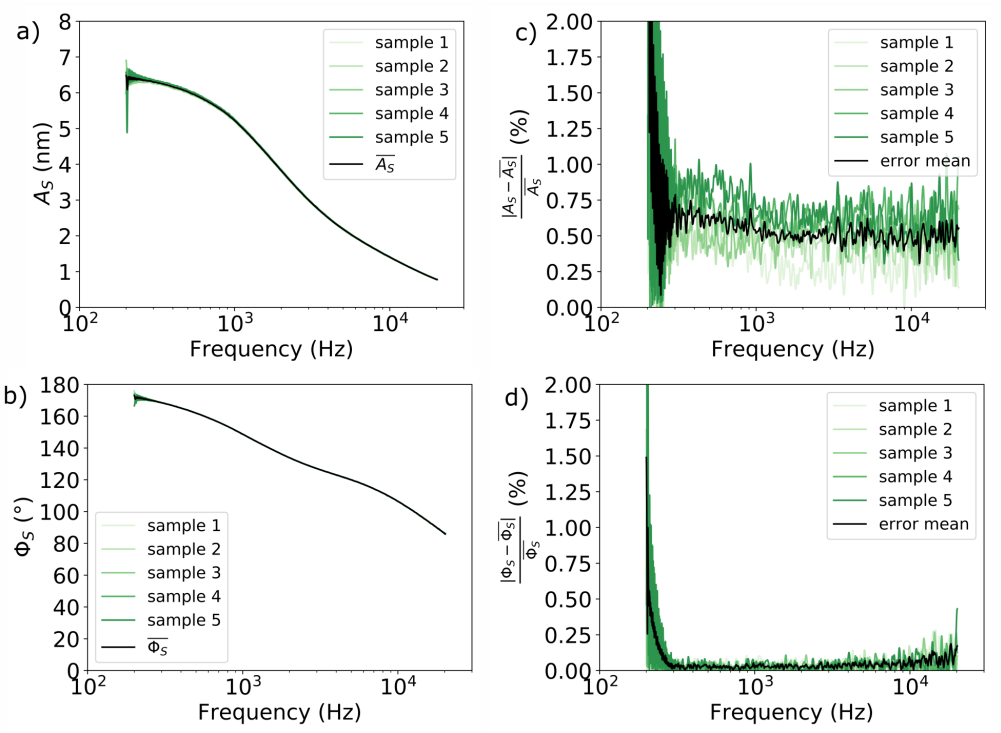


Figure 6.12: Sample measurements from rising and lowering the cantilever multiple times. (a) Amplitude (A_S), and (b) phase (ϕ_S) signals of the sample measurements. The black line corresponds to the mean of the signals ($\bar{A}_S$, $\bar{\phi}_S$). (c,d) Relative errors of the signals in (a,b) calculated with Eq. (6.6). The black line corresponds to the mean relative error.

the mean amplitude, and the errors in the phase signals were well below the 0.25 % of the mean phase. Since the phase signals were highly reproducible, only the amplitude errors were used to calculate the uncertainty of the viscoelastic quantities.

Errors are larger for frequencies below 300 Hz possibly because of FFT chirp lobes at the edges of the frequency range (see Section 2.2.4). This noisy part was removed from all the signals used in this study. In the rest of this thesis, signals obtained with chirp signals with initial frequency 200 Hz and final frequency 20 200 Hz (like the ones used here) were cut, usually at 300 Hz, to remove the chirp lobes. Similarly, signals obtained with other chirp signal frequency ranges were cut to remove the chirp lobes (usually 0.1 Hz to 10.1 Hz chirp signals were cut at 0.2 Hz, and signals obtained with 1 Hz to 1001 Hz chirp signals were cut at 2 Hz).

The uncertainty dy for a given a quantity y that is the product (or ratio) of N x_i that have uncertainties dx_i ($i = 1, ..., N$, with $N \in \mathbb{N}$), can be calculated as follows [285]:

$$\frac{dy}{|y|} = \sqrt{\sum_{i=1}^{N} \left(\frac{dx_i}{x_i}\right)^2} \tag{6.7}$$

The error on k' and k'', calculated with Eq. (2.28), can then be calculated as:

$$\frac{dk}{k^j} = \sqrt{\left(\frac{dk_c}{k_c}\right)^2 + \left(\frac{d\bar{A}}{\bar{A}}\right)^2} \tag{6.8}$$

where j corresponds to $'$ for k' and to $''$ for k''. dk_c/k_c, for k_c measured with the thermal noise method [202] (the case of this thesis), can be estimated as 15 % [286]. For the error on $\bar{A}$, by rounding up the relative error of the amplitude signals to 1 %, $d\bar{A}/\bar{A}$ can be calculated as follows:

$$\begin{aligned} \frac{d\bar{A}}{\bar{A}} &= \sqrt{\left(\frac{dA_R}{A_R}\right)^2 + \left(\frac{dA_S}{A_S}\right)^2} \\ &= \sqrt{0.01^2 + 0.01^2} \approx 1.4\% \end{aligned} \tag{6.9}$$

$\tan\delta$ can be calculated with Eqs. (2.28) and (2.34) for PT-AFM nano-DMA measurements. The uncertainty dy for y defined as a function of x_i ($y = f(x_1, ..., x_N)$), can be calculated as follows [285]:

$$dy = \sqrt{\sum_{i=1}^{N} \left(\frac{\partial f}{\partial x_i}\right)^2 dx_i^2} \tag{6.10}$$

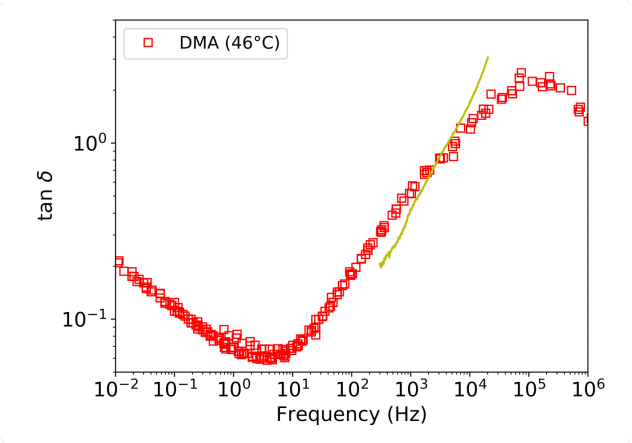


Figure 6.13: Loss tangent ($\tan\delta$) of the SBR measured with DMA at 46 °C (red unfilled squares) and with PT-AFM nano-DMA (yellow line). The green shade is the error calculated with Eq. (6.11) for the PT-AFM nano-DMA measurement.

Therefore, the error on $\tan\delta$ can be calculated as follows:

$$\begin{aligned} d\tan\delta &= \frac{\partial\left(\frac{\bar{A}\sin\Phi}{\bar{A}\cos\Phi-1}\right)}{\partial\bar{A}}d\bar{A} \\ &= -\frac{\tan\delta}{\bar{A}\cos\Phi-1}\frac{d\bar{A}}{\bar{A}} \end{aligned} \tag{6.11}$$

$\tan\delta$ measured with PT-AFM nano-DMA is plotted in Fig. 6.13 with a yellow line; $d\tan\delta$ calculated as described above is also plotted (green shade, almost not visible). Macroscopic DMA data are also shown at 46 °C (red unfilled squares) for comparison. In the rest of this thesis, the errors on k', k'', and $\tan\delta$ are calculated with Eqs. (6.8) and (6.11) for PT-AFM nano-DMA measurements.

6.5.3 Determination of the optimal tip-sample distance for the reference measurement

In this subsection, I compare reference signals measured at different distances between the AFM cantilever and the sample.

In order to do that, reference measurements were acquired at several cantilever-sample

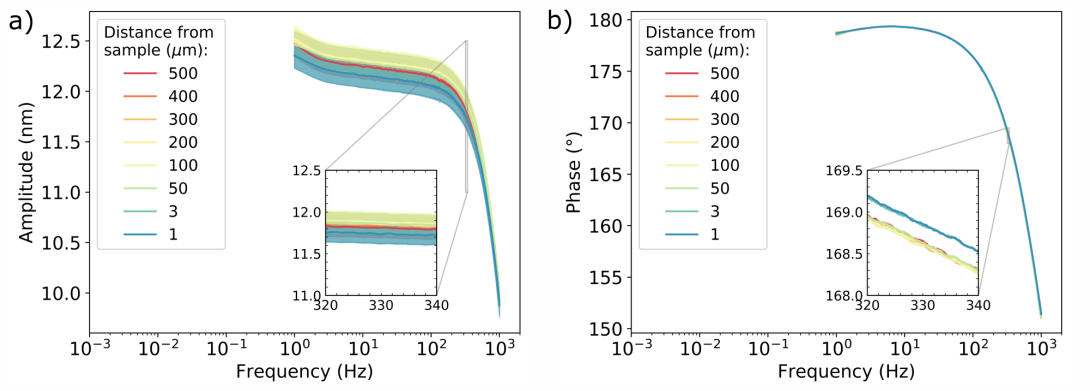


Figure 6.14: Cantilever signal recorded at different distances from the sample. (a) Amplitude and (b) phase of reference signals obtained at different heights above the sample. In the inset a zoomed area of the curves is plotted. Errors are shown as shades and are calculated as explained in Section 6.5.2.

distances: 500 µm, 400 µm, 300 µm, 200 µm, 100 µm, 50 µm, 3 µm and 1 µm. Distances down to 50 µm were obtained by changing the "PreEngage Height" in the Engage panel of the Igor Pro software. The software prevents PreEngage heights less than 50 µm. Therefore, 1 µm and 3 µm distances were obtained by performing a quasi-static force indentation curve on the sample and using a withdraw distance of 1 µm and 3 µm, respectively. For each height, three reference measurements were collected and averaged at each height.

The amplitude and phase of the averaged curves are shown in Fig. 6.14. Reference amplitudes (Fig. 6.14 (a)) were all within the calculated error of one-another, and hence did not vary with reference height. Phase signals are plotted in Fig. 6.14 (b). In the inset, a difference of approximately 0.2° between the phase of reference measurements taken at 1 µm and 3 µm and the others can be noted.

Four measurements were performed on the sample and averaged. The averaged sample signal was used to calculate the $\tan\delta$ for each reference measurement obtained at the different heights. In Fig. 6.15 the so calculated $\tan\delta$ are displayed. It can be observed that there are deviation between $\tan\delta$ calculated from reference signals taken at 1 µm and 3 µm and the others.

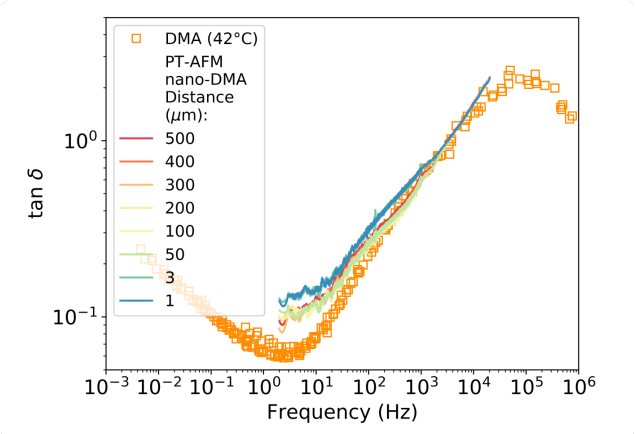


Figure 6.15: Loss tangent calculated from reference signals recorded at different distances from the sample. Comparison between macroscopic DMA loss tangent ($\tan\delta$) at 42 °C (orange unfilled squares) to the PT-AFM nano-DMA obtained $\tan\delta$ calculated with reference signals measured at different distances from the sample.

PT-AFM nano-DMA $\tan\delta$ calculated with reference taken at heights ≥ 50 µm better reproduce the $\tan\delta$ shape obtained with macroscopic DMA at 42 °C. It is possible that the references signals obtained at 1 µm and 3 µm reference heights suffer from the backlash of the motors, which might cause an inadvertent movement of the PT-ELS position, when the tip is withdrawn from the sample during the quasi-static force indentation curves needed to achieve these heights.

This study has shown that height at which reference measurements are taken for PT-AFM nano-DMA has little effect on the value of $\tan\delta$, unless an inadvertent change in laser spot position occurs. For the other experiments in this chapter, I decided to use reference measurements taken at sample-cantilever distances ≥ 500 µm.

6.5.4 Effect of the PT excitation laser power

Here, I compare PT-AFM nano-DMA results obtained with different PT-EL powers. Three different PT-EL powers were used. Different PT-EL powers were achieved by reducing the PT-EL power to 10 % and 30 % of the maximum power (100 %) using some filters, as explained in Section 3.3.3.3. For all the three power percentages, a

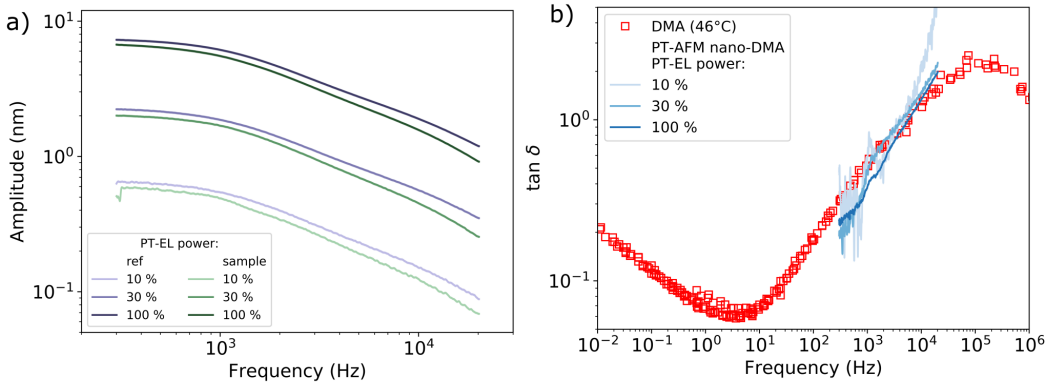


Figure 6.16: Effect of PT-EL power for PT-AFM nano-DMA results. Measurements were taken with the PT-EL at 10 %, 30 % and 100 % of its maximum power. Panel (a) shows cantilever amplitudes for the reference (blue lines) and sample (green lines) measurements. Panel (b) compares PT-AFM nano-DMA loss tangent ($\tan\delta$) calculated from the signals obtained with different power percentages with DMA calculated at 46 °C (red unfilled squares).

drive amplitude of 1 V was used.

The amplitudes recorded for each PT-EL power are shown for both for the reference (blue lines) and the sample (green lines) in Fig. 6.16 (a). The amplitudes obtained with a PT-EL at 10 % and 30 % of its maximum power are very small (below 1 nm and 3 nm, respectively). In Fig. 6.16 (b), $\tan\delta$ calculated for each PT-EL power percentage is shown. $\tan\delta$ with the PT-EL at 10 % and 30 % of its maximum power are very noisy compared to when the PT-EL is at 100 % power. Comparison with macroscopic DMA (red unfilled squares) in Fig. 6.16 (b) shows a slight shift to the left of the PT-AFM nano-DMA $\tan\delta$ for 10 % and 30 % PT-EL powers, most likely because they cause a smaller T increase of the system compared to the PT-EL 100 % power.

This observation highlights the importance of choosing the power of the PT-EL according to the response of the cantilever, in order to have high enough amplitudes during the PT-AFM nano-DMA measurements. This is especially relevant for high frequencies to prevent the amplitude from dropping beneath the noise level.

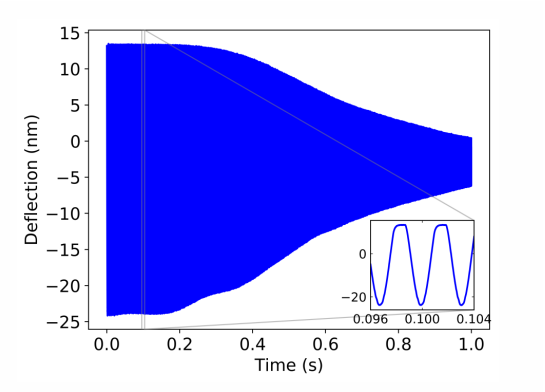


Figure 6.17: Artefacts in the deflection signal caused by failure to be in the PT-EL operating range. The inset shows a zoomed region of the deflection.

6.5.5 Effect of the PT excitation laser drive amplitude

Here, I examine the effect that oscillation amplitude has on the measured viscoelastic properties of the sample.

Different cantilever oscillation amplitudes were obtained by exciting the cantilever with PT drive signals with different AC amplitudes. It was crucial to consider the operating range of the PT-EL. Failure to be in this range caused artefacts on the oscillations in the deflection signal, as shown in Fig. 6.17.

Reference and sample measurements were obtained by using several AC drive amplitudes in the PT-EL operating range (0.1 V, 0.25 V, 0.50 V, 1.00 V and 1.50 V). For each drive amplitude, two curves for both the reference and the sample signals were recorded and averaged. The average amplitude of the reference (A_R) and sample (A_S) are plotted in Fig. 6.18 (a,b), respectively.

Reference and sample amplitudes measured at several frequencies (300 Hz, 1000 Hz, 3000 Hz and 10 000 Hz) show a linear increase with the drive amplitude (see Fig. 6.18 (c,b)). Therefore, an increase in the drive amplitude corresponded to a linear increase in the deflection amplitude of the cantilever.

In Fig. 6.19, A_S is plotted against A_R obtained at the same drive amplitude for 300 Hz, 1000 Hz, 3000 Hz and 10 000 Hz. The linearity of these graphs is an indication

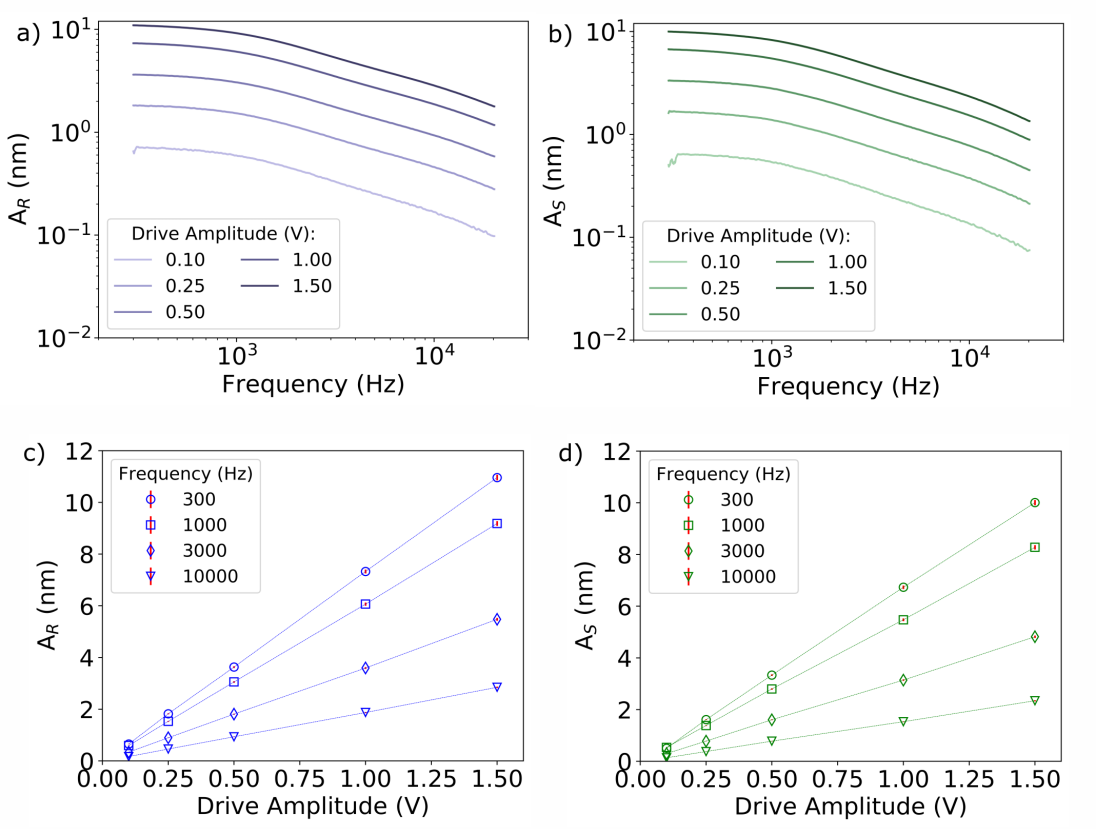


Figure 6.18: Relationship between drive amplitude and the cantilever's response amplitudes. Amplitudes of the (a) reference (A_R), and (b) sample (A_S) measurements obtained with different drive amplitudes. The error was calculated as explained in Section 6.5.2. The relationship between the drive amplitude and (c) A_R, and (d) A_S is also plotted at four discrete frequencies 300 Hz, 1000 Hz, 3000 Hz and 10 000 Hz.

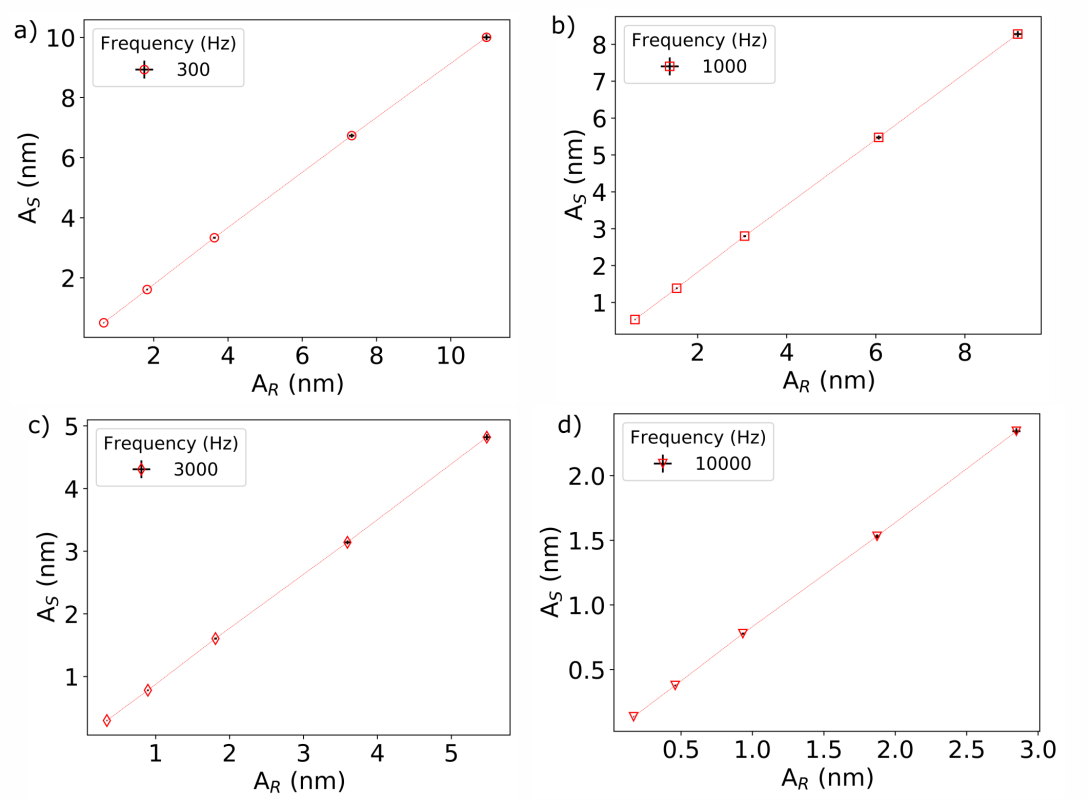


Figure 6.19: Linear relationship between the reference and sample signal amplitudes at several frequencies. Sample signal amplitudes (A_S) versus reference signal amplitudes (A_R) of Fig. 6.18 (a,b) obtained with the same drive amplitude at (a) 300 Hz, (b) 1000 Hz, (c) 3000 Hz, (d) 10 000 Hz.

of being in the linear viscoelastic regime, because the response of the sample to the stimulus applied is linear. That is, increasing the amplitude of the oscillatory force applied to the sample ($\propto A_R$) causes a linear increase in the oscillatory deformation of the sample (A_S). It is important to note that the slopes of lines in Fig. 6.19 (a-d) do not have to be the same at each frequency because the viscoelastic response of the sample is frequency-dependent.

$\tan\delta$ calculated for signals obtained at different drive amplitudes is displayed in Fig. 6.20. As expected from the linearity found in Fig. 6.19, $\tan\delta$ for all the drive amplitudes agree very well with each other, and with macroscopic DMA data at 46 °C. $\tan\delta$ calculated for drive amplitudes below 1 V is noisy, likely because the amplitudes are extremely small (see Fig. 6.18).

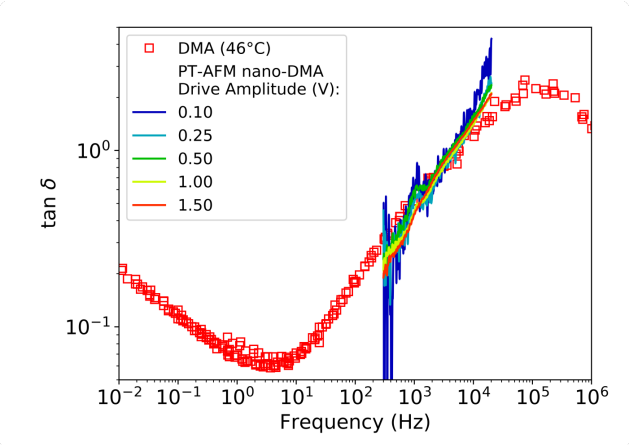


Figure 6.20: Loss tangent calculated from signals obtained with different drive amplitudes. Comparison between the loss tangent ($\tan\delta$) obtained with PT-AFM nano-DMA experiments performed with different drive amplitudes. PT-AFM nano-DMA results are also compared with macroscopic DMA data at 46 °C (red unfilled squares).

This experiment was repeated with an AFM system that possessed a wider PT-EL operating range. Sample measurements obtained with trigger points below 250 nN were used for the analysis. In this case, the DC was 5 V and a range of drive amplitudes from 0.1 V to 2 V was used. A_R and A_S obtained from this test are displayed in Fig. 6.21 (a,b).

Comparison of the results from the two different AFM system (Fig. 6.21 (a,b) and Fig. 6.18 (a,b)) reveals that a wider PT-EL operating range allows a larger variety of cantilever amplitudes. Moreover, for the same drive amplitude of 1 V, the second system has reference amplitude roughly twice that of the first system, indicating that PT-EL power is unique to each AFM system.

Measurements of $\tan\delta$ obtained with the second AFM system are shown in Fig. 6.22 for different drive amplitudes. Again, lower drive amplitudes lead to noisy signals. Interestingly, the curves obtained with this second AFM system agree with DMA measurements at 48 °C, which is 2 °C higher than the first system (cfr. Fig. 6.20). This observation suggests that the higher power of the PT-EL in the second system could result in a greater increase in T than that of the first system. This, in turn,

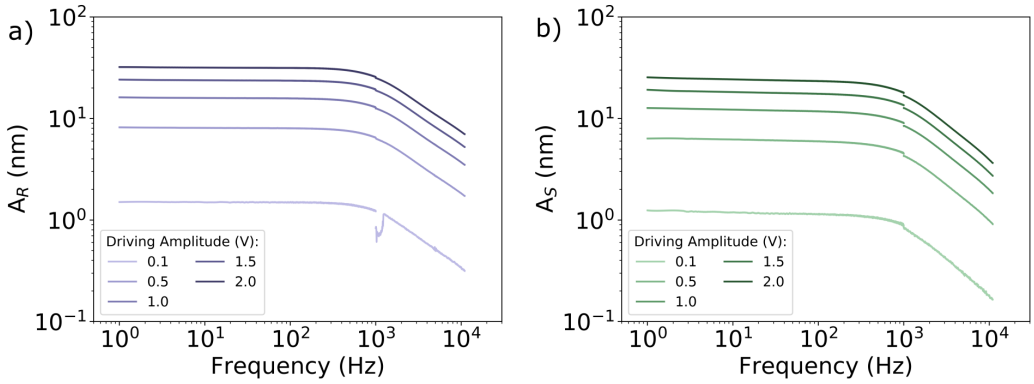


Figure 6.21: Reference and sample signal amplitudes for different drive amplitudes in a second AFM system. Amplitude of (a) reference (A_R), and (b) sample (A_S) signals obtained with different drive amplitudes.

could mean that AFM systems with different PT-EL features might increase the T differently. In order to further test this hypothesis, it would be necessary to repeat this experiment while measuring T in proximity of the cantilever/sample (not known for the experiments reported here).

This study reveals that the PT-AFM nano-DMA measurements done in this chapter were in the linear viscoelastic regime of the SBR sample: an increase of the stimulus applied to the sample resulted in a linear increase of the response of the material.

6.5.6 Effect of the indentation depth

In this section, the effect of the indentation depth on the measured viscoelastic behavior of the SBR was studied by varying the trigger point.

To study the viscoelastic behaviour dependence on the deformation applied to the sample, different force trigger points were used for the measurements: 10 nN, 25 nN, 50 nN, 75 nN, 100 nN, 250 nN, 500 nN and 1000 nN. Five measurements were performed for each trigger point.

The 10 nN, 25 nN, 50 nN, 75 nN, 100 nN, 250 nN, 500 nN and 1000 nN trigger points

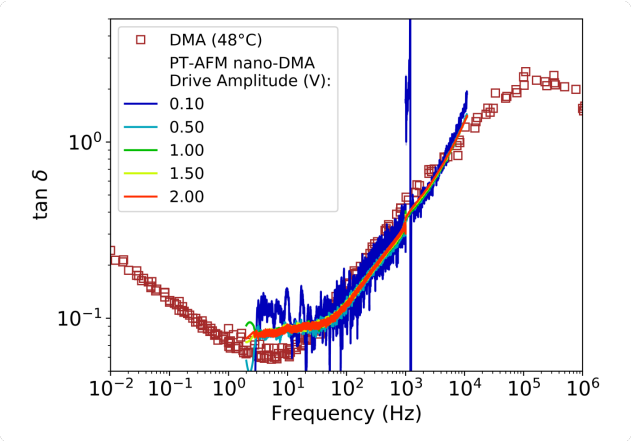


Figure 6.22: Loss tangent calculated from signals obtained with different drive amplitudes in a second AFM system. PT-AFM nano-DMA Loss tangent ($\tan\delta$) obtained at different PT-EL drive amplitudes us compared to macroscopic DMA data calculated at 48 °C (brown unfilled squares).

led to initial indentations (i.e. before the chirp signal was applied) of approximately 106 nm, 118 nm, 143 nm, 191 nm, 362 nm, 555 nm and 884 nm, respectively. The listed indentations are the mean values measured at the last point of the approach curve for five curves taken with each trigger point. Lower trigger points often resulted in a false engage with no sample deformation and have therefore been excluded from the analysis.

The values of k' and k'' for measurements taken at each trigger point were calculated using the theory described in Section 2.2.3, using the average amplitude and phase signals of five curves. As shown in Fig. 6.23, k' and k'' increase for higher trigger points. This observation is unsurprising, since stiffness is an extensive quantity that depends on the contact area (see Section 6.3). However, k' at high frequencies is distorted for higher trigger points. Therefore, it is likely that higher trigger points (higher deformations) led to a non linear viscoelastic behaviour of the sample.

These results suggest that care must be taken in the choice of the trigger point used for PT-AFM nano-DMA to avoid misestimations of the viscoelastic quantities of the sample.

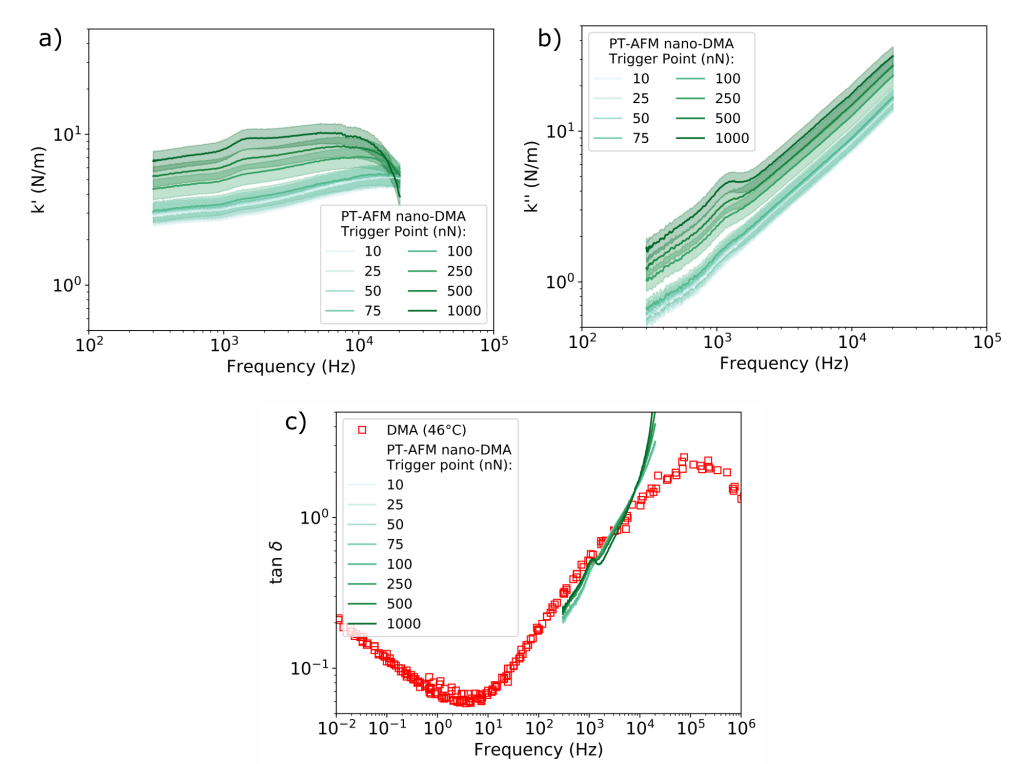


Figure 6.23: Viscoelastic quantities calculated with PT-AFM nano-DMA for different trigger points. (a) Storage stiffness (k'), (b) loss stiffness (k'') and (c) loss tangent ($\tan\delta$) calculated with PT-AFM nano-DMA for several trigger points compared with macroscopic DMA data calculated at 46 °C (red unfilled squares). The errors for the AFM curves are calculated as described in Section 6.5.2 and plotted as shades.

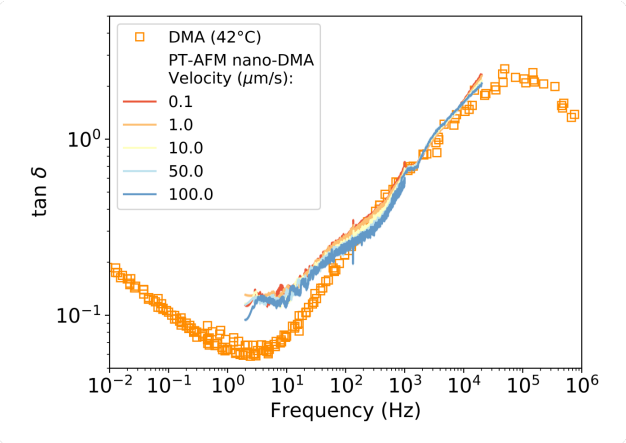


Figure 6.24: Loss tangent ($\tan\delta$) calculated from signals obtained with PT-AFM nano-DMA measurements at different cantilever approach/withdraw velocities. PT-AFM nano-DMA $\tan\delta$ is also compared to macroscopic DMA data at 42 °C (orange unfilled squares). Errors are shown as shades and are calculated as explained in Section 6.5.2.

6.5.7 Effect of the cantilever approach and withdraw velocity

Here, I test the effect the cantilever approach/withdraw velocity on the PT-AFM nano-DMA results.

Five velocities were compared: $0.1\,\mu m\,s^{-1}$, $1.0\,\mu m\,s^{-1}$, $10.0\,\mu m\,s^{-1}$, $50.0\,\mu m\,s^{-1}$ and $100.0\,\mu m\,s^{-1}$. For the $0.1\,\mu m\,s^{-1}$ the approach time was set to 35 s to allow time for the cantilever approach to the sample.

$\tan\delta$ was calculated for the five velocities and compared to macroscopic DMA data. In Fig. 6.24, $\tan\delta$ calculated for the five velocities all overlap very well with macroscopic DMA data at 42 °C. Therefore, approach/withdraw velocity did not affect the PT-AFM nano-DMA measurements of the SBR sample.

6.5.8 Effect of the cantilever: choosing the correct stiffness

In this subsection, I compare viscoelastic quantities measured on a SBR sample with PT-AFM nano-DMA using three different cantilevers.

The choice of cantilevers was based on the analysis presented in Section 6.3, and on

the basis that it is recommended that $k_c > k_S$ for PT cantilever excitation in order to get mechanically meaningful results [157].

Cantilevers with small tip dimensions were chosen in order to obtain nanometre resolution. k_S is on the order of $0.1\,\mathrm{N\,m^{-1}}$ to $1\,\mathrm{N\,m^{-1}}$ for a small indenter, with a sample modulus in the range of 1 MPa to 10 MPa, and a deformation of hundreds of nm, (see Fig. 6.3). Therefore, cantilevers with k_c larger than $1\,\mathrm{N\,m^{-1}}$ can be used for measuring the mechanical properties of the such a sample.

The usage of a cantilever tip with a big radius could be helpful to average over a larger area of the sample. From Fig. 6.4, k_S is on the order of $1\,\mathrm{N\,m^{-1}}$ to $10\,\mathrm{N\,m^{-1}}$ for a tip radius of 2 µm, with a sample modulus in the range of 1 MPa to 10 MPa, and a deformation of hundreds of nm. In this case the cantilever spring constant should than be higher than $10\,\mathrm{N\,m^{-1}}$.

The following cantilevers were therefore used: AC160TSA-R3 (Olympus, nominal spring constant $42\,\mathrm{N\,m^{-1}}$, resonance frequency 300 kHz, tip radius 7 nm, tetrahedral tip shape), AC240TSA-R3 (Olympus, nominal spring constant $2\,\mathrm{N\,m^{-1}}$, resonance frequency 70 kHz, tip radius 7 nm, tetrahedral tip shape), and biosphere$^{\mathrm{TM}}$-NT_B2000_v0010 (Nanootools, nominal spring constant 40 $\mathrm{N\,m^{-1}}$, resonance frequency 330 kHz, tip radius 2 µm, spherical tip shape). Each cantilever was calibrated by indenting a hard substrate to calculate the OLS and then using the thermal noise method to calculate the spring constant [202] (see Section 2.2). The spring constants and resonance frequencies obtained were: $1.13\,\mathrm{N\,m^{-1}}$ and 55 kHz for the AC240TSA-R3, $16.93\,\mathrm{N\,m^{-1}}$ and 267 kHz for the AC160TSA-R3, and $38.92\,\mathrm{N\,m^{-1}}$ and 284 kHz for the biosphere$^{\mathrm{TM}}$-NT_B2000_v0010. The drive amplitude was chosen cantilever-specific in order to have approximately the same reference amplitude for all three cantilevers.

For each cantilever, three measurements of both reference and the sample signals were acquired and averaged. The calculated k', k'' and $\tan\delta$ are shown in Fig. 6.25 (a-c).

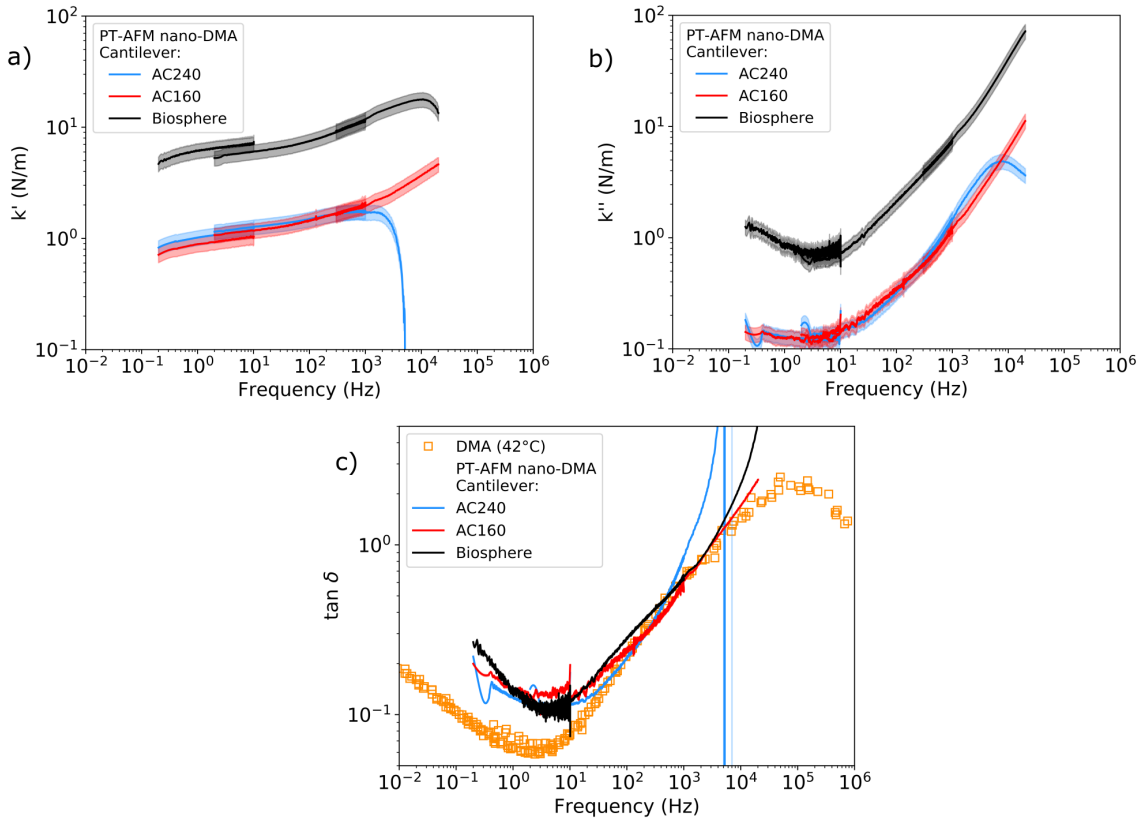


Figure 6.25: Viscoelastic quantities of the SBR sample obtained with different AFM cantilevers. The three cantilevers used were: AC240TSA-R3 (light blue line), AC160TSA-R3 (red line), and biosphere$^{\text{TM}}$-NT B2000 v0010 (black line). Panel (a) shows the storage stiffness (k'), and panel (b) the loss stiffness (k''). Panel (c) shows a comparison of macroscopic DMA $\tan\delta$ at 42 °C (orange unfilled squares) to that of PT-AFM nano-DMA. Errors are shown as shades and are calculated as explained in Section 6.5.2.

The values from the biosphere$^{\text{TM}}$-NT_B2000_v0010 of k' and k'' are higher than the data from the other two cantilevers. This is expected, since stiffness is an extensive quantity and depends on the geometry of the contact (cfr. Section 6.3).

Data from AC160TSA-R3 and AC240TSA-R3 overlap for frequencies up to 1 kHz, after which data obtained with the AC240TSA-R3 start to deviate from the expected values. Indeed, around 1 kHz k' ($\approx 2\,\text{N}\,\text{m}^{-1}$) starts to be higher than k_c of the AC240TSA-R3 ($1.13\,\text{N}\,\text{m}^{-1}$). The same thing happens to the biosphere$^{\text{TM}}$-NT_B2000_v0010 data around 10 kHz, where k' of the SBR ($\approx 20\,\text{N}\,\text{m}^{-1}$), becomes

comparable to k_c ($= 38.92\,\mathrm{N\,m^{-1}}$). This issues does not appear for the AC160TSA-R3, because its k_c ($= 16.93\,\mathrm{N\,m^{-1}}$) is always higher than k' of the SBR in the frequency range studied.

Fig. 6.25 (c) shows very good agreement between the $\tan\delta$ obtained with macroscopic DMA (42 °C) and that obtained from PT-AFM nano-DMA measured with different cantilevers, up to the frequency where k' of the SBR exceed k_c.

This study highlights the importance for PT-AFM nano-DMA of choosing a cantilever with an appropriate spring constant ($k_c > k'$), to not to incur in miscalculations of the sample viscoelastic quantities.

6.6 Direct versus indirect cantilever actuation

In this section, I compare direct and indirect excitation for AFM nano-DMA.

As described in Section 2.2.1, the most common way to excite AFM cantilever is by indirect actuation via piezo actuators. In this section, I compare results obtained with direct actuation by PT excitation to indirect actuation by placing a piezo actuator underneath the sample (PE actuation via sample modulation).

The experiment was structured in the following way:

(i) PE measurements were done first, to prevent PT heating of the cantilever/sample from affecting the PE measurements. Reference measurements were done before sample measurements.

(ii) PT measurements were taken in the same spot on the sample.

(iii) Next, PE measurements with the PT-EL focused on the back of the cantilever (only DC power, the same used for PT measurements) were acquired (PE PT-EL on). Sample signals were taken in the same sample spot as (i) and (ii). Then, for the reference measurements, it was necessary to move the cantilever

to the glass slide, thereby losing the spot of the SBR sample. After taking the PE reference on the glass slide, the cantilever was moved to a second spot on the SBR sample. PE actuation with the PT-EL on was measured on the new spot (PE PT-EL on 2) and compared to the original spot (PE PT-EL on). The $\tan\delta$ signals of the two spots overlapped (data not shown), allowing use of the second spot in the following discussion, as well as comparison of PT vs PE for the new and old spots.

(iv) Lastly, PE measurements were acquired (on the new sample spot) after switching off the PT-EL (PE_2).

The amplitude and the phase of the reference and the sample measurements obtained with both PE (i) and PT (ii) excitations are plotted in Fig. 6.26. The PT phase signals are shifted by 180° for easier comparison with PE data. In Fig. 6.26 (a,b), the PT signals show a smooth behaviour over the entire frequency range studied. However, PT signal values decrease with frequency, as is typical of PT excitation [152, 282]. PT signals, although having a smooth behaviour at low frequency, start to show spurious peaks after 1 kHz, most likely due to resonances of the piezo actuator/AFM system (see Section 2.2.1).

In Fig. 6.27, $\tan\delta$ calculated from measurements in steps (i-iv) are displayed and compared with macroscopic DMA data at 30 °C, 34 °C and 42 °C. For PE data, k' (not shown), k'' (not shown), and $\tan\delta$ were calculated with Eqs. (2.33) and (2.34). The respective uncertainties were obtained with Eqs. (6.7) and (6.10), using the standard deviations of A_{CM} and A_{CS} calculated over the different measured curves.

PE data from step (i) (black line) are in very good agreement with DMA at 30 °C (peach unfilled squares), approximately the ambient T of the AFM. PT data from step (ii) (red line), matches macroscopic DMA data at 42 °C (orange unfilled squares), thereby indicating that the PT-EL was locally heating the system. This also means that the T of the system increased almost immediately when the PT-EL was switched

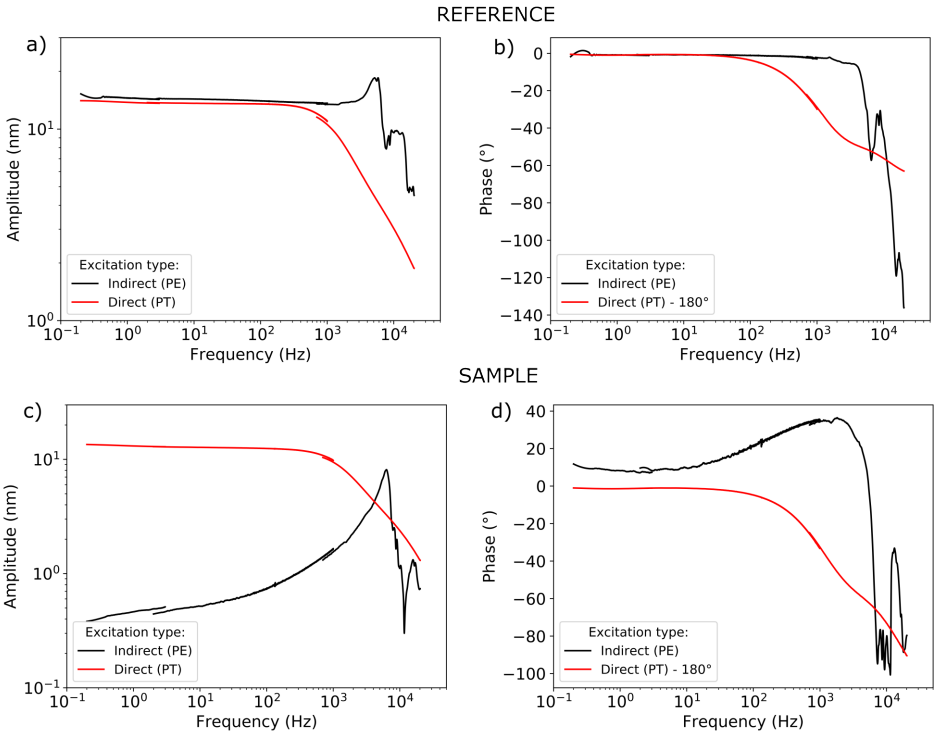


Figure 6.26: Amplitude and phase signals obtained via PT direct actuation (red lines) and PE indirect actuation (black lines). Reference (a) amplitude, and (b) phase signals. Sample (c) amplitude, and (d) phase signals. Phase signals obtained with PT excitation were shifted of 180° to allow easier comparison with PE excitation.

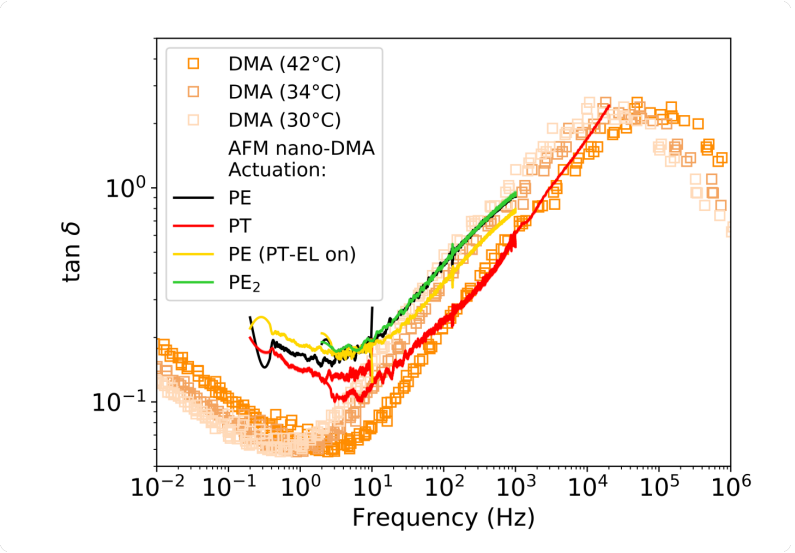


Figure 6.27: Loss tangent calculated for direct and indirect actuation. Loss tangent ($\tan\delta$) calculated from data obtained with the following excitation method: (i) PE (black line), (ii) PT (red line), (iii) PE while the PT-EL was still focused on the cantilever (only DC power) (PE (PT-EL on), yellow line), (iv) PE after switching off the PT-EL (PE_2, green line). The AFM nano-DMA $\tan\delta$ are compared with macroscopic DMA data at 30 °C (peach unfilled squares), 34 °C (light orange unfilled squares), and 42 °C (orange unfilled squares).

on. PE data with the PT-EL focused on the cantilever ((iii), yellow curve) matches macroscopic DMA at the intermediate T of 34 °C, thereby validating the hypothesis that the PT-EL heats the system. PE data obtained after switching the PT-EL off ((iv), green line), are in excellent agreement with PE data from (i) and macroscopic DMA data at 30 °C. This means that the system cooled down almost immediately when the PT-EL was switched off.

It is important to note that $\tan\delta$ was used to compare the T of signals because $\tan\delta$ does not depend on the geometry (i.e. contact model) of the system [23]. Therefore, the use of $\tan\delta$ avoids any possible error introduced by a wrong choice of the contact model.

This study highlights the advantage of exciting the AFM cantilever using PT compared to a PE mechanism. PT actuation avoids the presence of mechanical resonances due to PE actuation that affects the response of the cantilever. Furthermore, the com-

parison between PT and PE has provided another proof to the the hypothesis of the increase in T of the system when the PT-EL is employed. Also, this study indicates that both the heating and the cooling of the system are almost immediate.

6.7 Calculation of the dynamic modulus

Here, E' and E'' are calculated from k' and k'' of the SBR sample measured via AFM nano-DMA by selecting an appropriate contact model to describe the SBR/AFM tip system. For the following calculations, the nominal radii of the cantilevers were used. Addittionally, it was assumed that the sample had $\nu_S = 0.5$, commonly adopted for SBR [131–134].

A typical F versus d curve of a PT-AFM nano-DMA experiment on the SBR sample conducted with an AC160TSA-R3 cantilever is plotted in Fig. 6.28. This curve was obtained with a chirp signal with a 0.1 Hz to 10.1 Hz frequency range.

As explained in Section 2.2.2.2, the JKR model [164] can be applied to calculate parameters such as w and K for indentation experiments with a spherical indenter in the presence of adhesion forces. K and w can be calculated using the *"two-points method"* [168] on some "special points" of the withdraw curve (see Section 2.2.2.2). The point of zero load "0", the point around which the oscillations happens "1", and the point of zero deformation "2" are marked by a filled green circle in Fig. 6.28. In particular, here point "1" was taken as the average force of the oscillatory part of the curve (since this average is the point around which the oscillation occurs).

The theoretical JKR curve [164] can be calculated as explained in Section 2.2.2.2 once K and w are known. The theoretical JKR curve calculated for the experimental curve in Fig. 6.28 is plotted in Fig. 6.28 with a pink dashed line. Similarly, as explained in Section 2.2.2.2, $\tilde{E}$ and w can be obtained for an indenter with a hyperboloidal shape [168] and the theoretical curve can be calculated (Eqs. (2.17) to (2.25), orange dashed

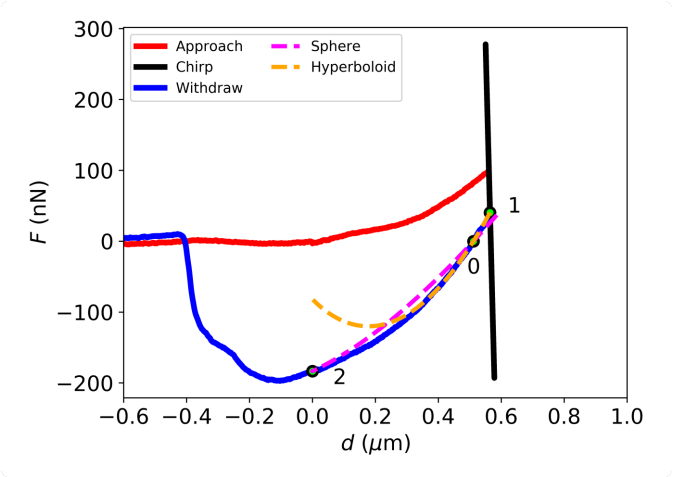


Figure 6.28: Typical force (F) versus indentation (d) curve of a PT-AFM nano-DMA experiment obtained on SBR with an AC160TSA-R3 cantilever, for a chirp frequency range of 0.1 Hz to 10.1 Hz (180 s sweep time). The approach (red line), chirped oscillations (black line), and withdraw (blue line) curves are all shown. Point "1" corresponds to the average of the oscillatory force, point "0" corresponds to the point of zero load, and point "2" corresponds to the point of zero indentation. The dashed lines represent the theoretical curves evaluated from point "1" to point "2" for (i) a JKR sphere (Eqs. (2.7) to (2.11), pink line) (R_I =7 nm), and (ii) a hyperboloid (Eqs. (2.17) to (2.25), orange line) (R_I =7 nm, $\alpha = 17.5°$).

line in Fig. 6.28).

Fig. 6.28 shows that the theoretical curve for the hyperboloidal model with adhesion is in good agreement with the experimental curve between points "0" and "1". Indeed, it is expected that the theoretical curve for the hyperboloidal model works better for higher indentations where the assumption that I used for Eq. (2.16) ($a >> A$) is more likely to be satisfied.

The Tabor parameter μ (Eq. (2.6)) (calculated using the $\tilde{E}$ and w values obtained with the hyperboloidal model, and using an interatomic equilibrium separation z_0 of 0.4 nm) for the curve in Fig. 6.28 is $\mu \approx 184$. This value is much greater than the threshold of 1 ($\mu \approx 184 >> 1$) that corresponds to the JKR regime [166, 167] (see Section 2.2.2.2).

In Fig. 6.29, the F versus d curves of PT-AFM nano-DMA experiments on the SBR sample are plotted for the three chirp frequency ranges used: 0.1 Hz to 10.1 Hz, 1 Hz

to 1001 Hz, and 200 Hz to 20 200 Hz. As explained in Section 3.3.3.3, an appropriate sweep time for each chirp frequency range was used (180 s, 30 s and 1 s, respectively). The approach curve does not seem to be affected by the chirp frequency range used. In the withdraw curve, instead, the point of maximum adhesion (minimum force) is different among the curves depending on the chirp frequency range used. This is likely due to the different amount of time that the AFM tip spent in contact with the sample for each chirp frequency range. This is confirmed by the fact that AFM quasi-static force curves (i.e. no dwell), represented as black lines in Fig. 6.29, have a much smaller adhesion than the PT-AFM nano-DMA curves. Indeed, in AFM quasi-static force curves the tip is in contact with the sample only for the time to reach the trigger point and withdraw. The tip is in contact with the sample for much longer during AFM nano-DMA experiments, with the additional dwell time (waiting time for the material to relax plus chirp sweep time) that is not present in the AFM quasi-static force curves. Additionally, this hypothesis agrees with the findings of Sun and Walker [287] on the adhesion between a cantilever and PDMS, where they found that increasing dwell times lead to increasing adhesion.

Fig. 6.29 shows that the chirp frequency ranges have only a slight effect on the the positions of points "0" and "1". Point "2", instead, strongly depends on the chirp frequency regime. For this reason, F and d measured in points "0", "1", and "2" were calculated for each chirp range as the average of multiple curves taken for each range. These points are important because they allow calculation of a. As described in Section 2.2.2.2, the *"two-points method"* [168] allows calculation of the quantities (e.g. $\tilde{E}$, K, w) needed to estimate a. a in turn is needed to convert k^* into E^*.

E' and E'' calculated with Eq. (2.36) (JKR stiffness) for PT-AFM nano-DMA measurements are plotted in Fig. 6.30 (violet lines). E' and E'' calculated from the signals with different chirp regimes do not overlap with each other, nor with the macroscopic DMA data. Therefore, Eq. (2.36) does not well represent the contact between the

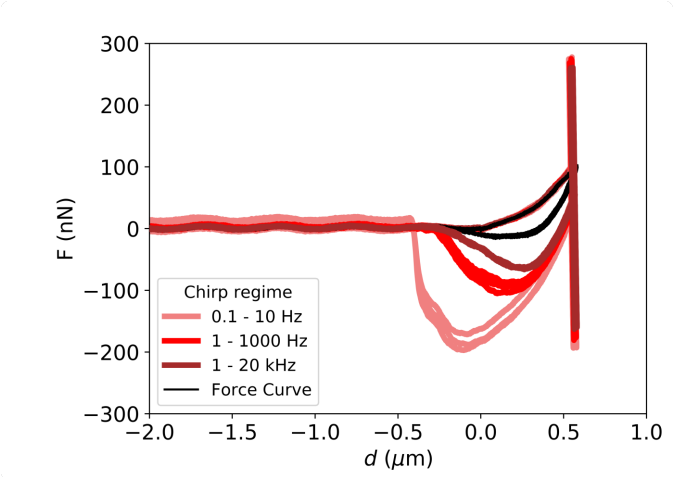


Figure 6.29: Force (F) versus indentation (d) curves of PT-AFM nano-DMA experiments obtained on SBR with different chirps of varying sweep times. Three chirp signals from: 200 Hz to 20 200 Hz with 1 s (dark red), 1 Hz to 1001 Hz with 30 s (red), and 0.1 Hz to 10.1 Hz with 180 s (light red) are plotted. The black line represents quasi-static force indentation curves.

indenter and the sample during the oscillations, leading to misestimation of the components of E^*.

Consequently, E' and E'' were estimated using the flat punch stiffness expressed as $\tilde{E}^* = k^*/(2a)$ [171, 172] (see Section 2.2.3), with $a = a_1$.

Initially, E' and E'' were obtained for a spherical indenter in the presence of adhesion forces (JKR model [164]) calculating a_1 with Eq. (2.7). The so obtained E' and E'' are plotted in Fig. 6.30 with pink lines. E' and E'' calculated with the flat punch stiffness do not present jumps for chirp signals with different frequency regimes. Also, E' and E'' calculated for spherical indenter with the flat punch stiffness are closer to the macroscopic DMA data compared to E' and E'' calculated with the JKR stiffness. However, they still overestimate E' and E''. This means that the flat punch stiffness improved the description of the contact during the oscillations, but the JKR model [164] used to calculate a (Eq. (2.7)) underestimated a_1. The JKR model [164] is an extension of the Hertz model in the presence of adhesion. The Hertz model [159, 160] assumes deformations much smaller than the radius of the spherical indenter.

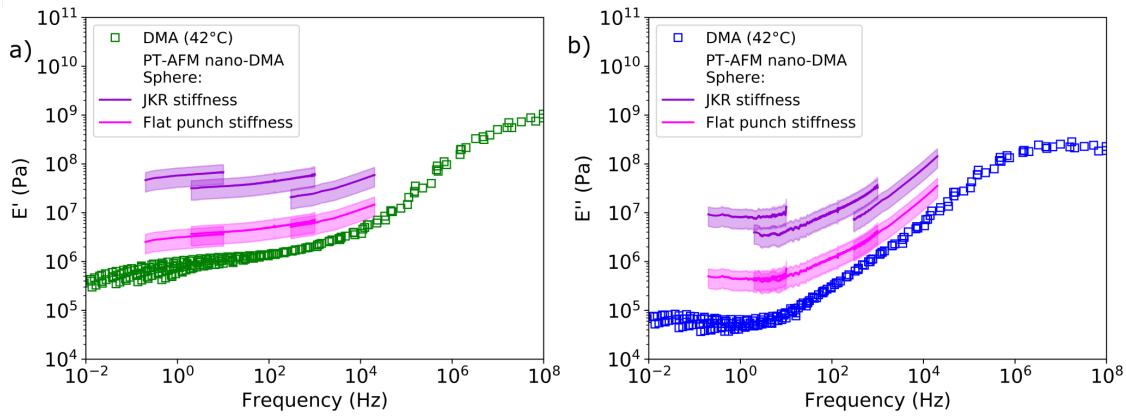


Figure 6.30: PT-AFM nano-DMA storage (E') and loss (E'') moduli calculated for a spherical indenter with JKR and flat punch stiffness. (a) E', and (b) E'' calculated with Eq. (2.36) (purple line), and for the flat punch stiffness ($\tilde{E}^* = k^*/(2a)$, pink line, see Section 2.2.3).

However, that assumption was clearly violated in the AFM nano-DMA here reported (cfr. Figs. 6.28 and 6.29). Additionally, also the approximation of the AC160TSA-R3 tip as a spherical indenter fails with such large indentations.

Then, E' and E'' were obtained by calculating a_1 for a conical indenter ($\alpha = 17.5°$, corresponding to half of the nominal back angle of a AC160TSA-R3 cantilever) in the presence of adhesion using Eq. (2.12) [169, 170] as explained in Section 2.2.2.2. The calculated E' and E'' are still overestimated compared to the macroscopic DMA values, as shown in Fig. 6.31 (cyan line).

Finally, E' and E'' were estimated by calculating a_1 for a hyperboloidal indenter in the presence of adhesion forces [168]. For a hyperboloidal indenter a_1 can be calculated from Eq. (2.23) as explained in Section 2.2.2.2. For these calculations, I used R_I =7 nm and $\alpha = 17.5°$. The so obtained E' and E'' are plotted in Fig. 6.31 with red lines. Fig. 6.31 shows a good agreement between macroscopic DMA data (green and blue unfilled squares) and the PT-AFM nano-DMA data calculated with the hyperboloidal model (flat punch stiffness behaviour).

These results demonstrate that the flat punch stiffness correctly represented the fact

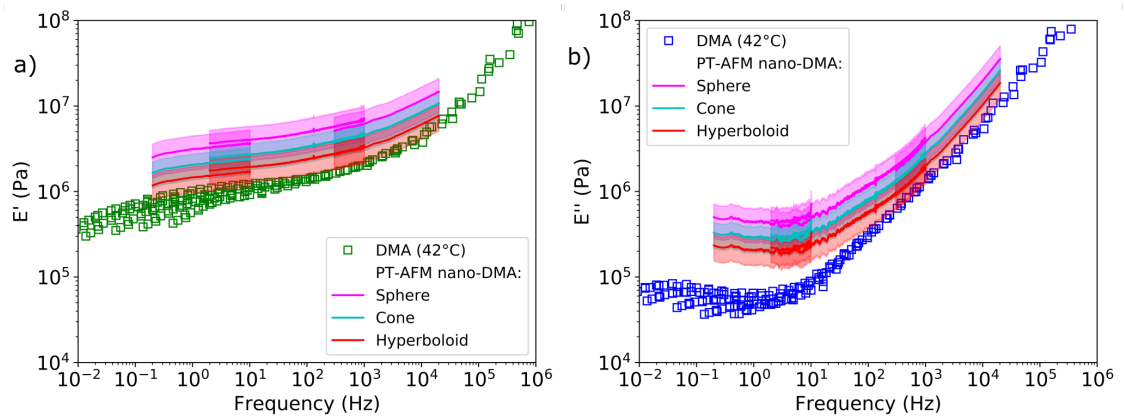


Figure 6.31: Comparison between PT-AFM nano-DMA storage (E') and loss (E'') moduli calculated with spherical, conical, and hyperboloidal contact models with flat punch stiffness. (a) E', and (b) E'' calculated for flat punch stiffness for indenters with a spherical (pink line), conical (cyan line), and hyperboloidal shape (red line) as explained in the text.

that the contact radius is not changing during the oscillations [171, 172]. Additionally, the adoption of the hyperboloidal model in the presence of adhesion better estimated the contact radius a_1 compared to the spherical and conical models.

The uncertainty on the components of the dynamic modulus E^j (j being $'$ or $''$ for the E' and E'', respectively) for the flat punch stiffness is given by (see Appendix G):

$$\frac{dE^j}{E^j} = \sqrt{\left(\frac{dk}{k^j}\right)^2 + \left(\frac{da_1}{a_1}\right)^2}$$

where k^j is the dynamic stiffness component and its error dk is calculated as explained in section Section 6.5.2. The error in the calculation of a_1 was estimated by varying the dimensions of the AFM tip (R_I, α) from the nominal values (see Appendix G). The uncertainty on a_1 was estimated to be 40 % for the spherical model and 30 % for the hyperboloidal model for an AC160TSA-R3 cantilever.

PT-AFM nano-DMA experiments conducted with AC240TSA-R3 and biosphere^{TM}-NT_B2000_v0010 cantilevers had similar behaviours for F versus d curves with increasing chirp sweep time to those of the AC160TSA-R3 (see Fig. 6.32).

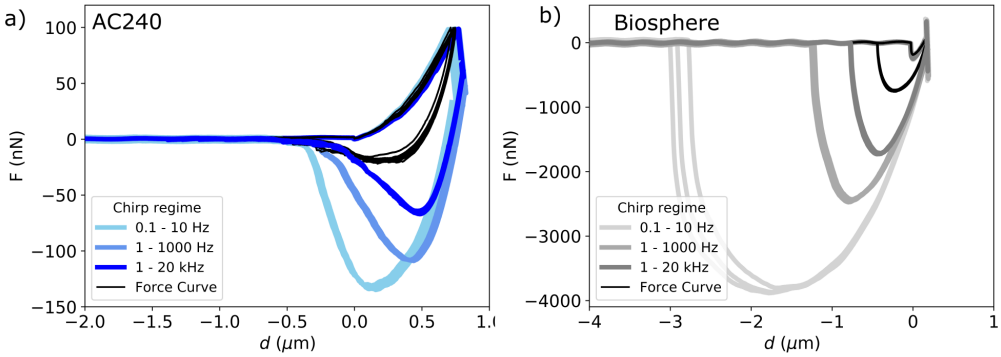


Figure 6.32: Force versus indentation curves of PT-AFM nano-DMA experiments obtained with different cantilevers for different chirp frequency regimes. Force (F)-indentation (d) curves for (a) AC240TSA-R3 (blue shades), and (b) biosphere^{TM}-NT_B2000_v0010 (grey shades), obtained with chirps with increasing sweep times of 1 s for the 200 Hz to 20 200 Hz frequency range (dark shade), 30 s for the 1 Hz to 1001 Hz frequency range (medium shade), and 180 s for the 0.1 Hz to 10.1 Hz frequency range (light shade). Black lines represent quasi-static force indentation curves.

The tip of an AC240TSA-R3 cantilever has the same shape and dimensions as the AC160TSA-R3 tip. E' and E'', and their uncertainties were calculated as above with a flat punch stiffness for a hyperboloidal indenter. The tip of a biosphere^{TM}-NT_B2000_v0010 cantilever has a nominal radius $R_I = 2\,\mu m$, which is much larger than the deformation at which the oscillation occurred ($\approx$175 nm, see Fig. 6.32 (b)). Therefore, for this cantilever, E' and E'' were calculated with the flat punch stiffness for a JKR spherical indenter. Uncertainties were calculated as explained in Appendix G.

The values of E' and E'' obtained with the three different cantilevers (AC160TSA-R3, red lines; AC240TSA-R3, ligh blue lines; biosphere^{TM}-NT_B2000_v0010, black lines; see Section 6.5.8) are plotted in Fig. 6.33. It is worth noting two major observations. First, data from the AC240TSA-R3 are in good agreement with data from AC160TSA-R3 and macroscopic DMA up to the point where the k_c is comparable to k' (cfr. Section 6.5.8). Second, E' and E'' calculated with the biosphere^{TM}-NT_B2000_v0010 are almost two times higher than the other moduli and the DMA

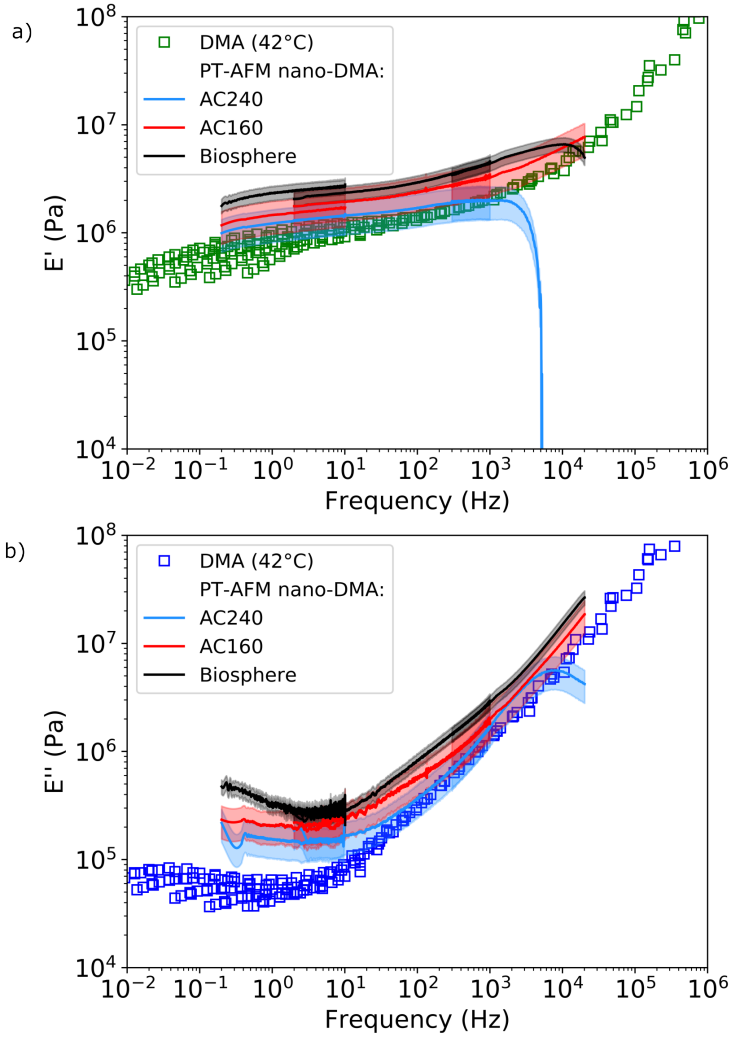


Figure 6.33: Comparison of PT-AFM nano-DMA storage (E') and loss (E'') moduli obtained with different cantilevers. (a) E', and (b) E'', obtained with an AC160TSA-R3 (red lines), an AC240TSA-R3 (ligh blue lines), and a biosphere^{TM}-NT_B2000_v0010 (black lines) are compared with macroscopic DMA data at 42 °C (unfilled squares)

.

data. A similar issue has been reported by Igarashi and co-workers [131] for studies performed with PE-AFM excitation on rubbers. Their AFM measurements of E' and E'' (via PE actuation) were in good agreement with macroscopic DMA data when measured with an AC240 cantilever [131]. However, different cantilevers resulted in different values of E' and E'' (even though they all had the same order of magnitude) [131]. Regardless of these differences, the shape of the moduli here obtained with the biosphere^{TM}-NT_B2000_v0010 reproduce the shape of the macroscopic DMA data.

In Fig. 6.34, the components of E^* obtained with PT excitation (red lines) are compared to those obtained with PE excitation (black lines) (cfr. Section 6.6, steps (i-iii)). The AFM nano-DMA data are compared with E' and E'' data obtained with macroscopic DMA data at 30 °C (lighter unfilled squares), and 42 °C (darker unfilled squares). These DMA T were deduced from $\tan\delta$ (see Section 6.6).

E' and E'' calculated for PE-AFM nano-DMA overlap well with DMA data at 30 °C. PE-AFM nano-DMA data when the PT-EL was kept on, are in between the macroscopic DMA data at 30 °C and 42 °C. PE data taken after switching off the PT-EL (data not shown) overlap with the PE data shown in Fig. 6.34.

Proof that the PT-EL affects the properties of the sample by rising the T, can also be found in Fig. 6.35. Quasi-static force curves were performed with and without the PT-EL focused on the back of the cantilever. In Fig. 6.35, a typical force curve is displayed for curves with the PT-EL on (red curve), and off (black curve), which are clearly different. To quantify this difference, E of the SBR sample was calculated. The approach curves of twenty force curves for each configuration (PT-EL on/off) were fit with the hyperboloidal model [168] without adhesion (by removing the adhesion terms of Eqs. (2.12) and (2.13) from Eqs. (2.17) and (2.18)) from 30 nN to 45 nN. The choice of studying the approach curves is explained in Section 6.8.

The mean value $\bar{E}$ was calculated over the twenty curves for each configuration. $\bar{E}_{PT-ELon}$ =(0.95 ± 0.03) MPa and $\bar{E}_{PT-ELoff}$ =(1.09 ± 0.06) MPa are displayed

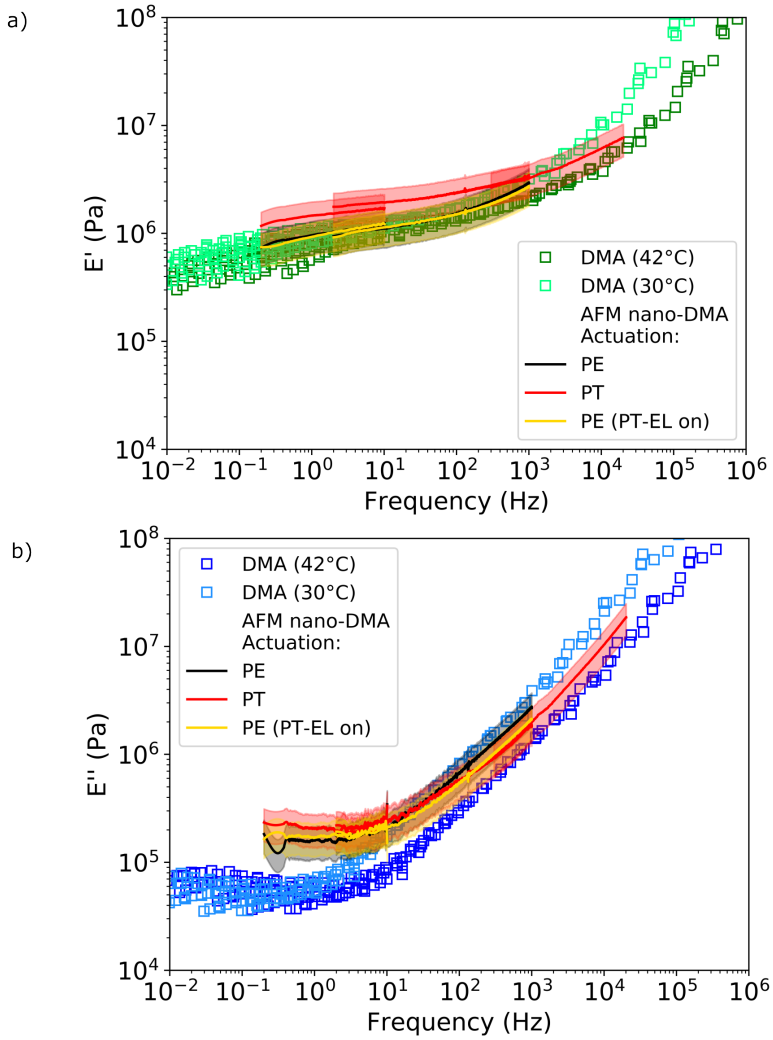


Figure 6.34: Comparison between storage (E') and loss (E'') moduli obtained with PT and PE AFM nano-DMA. (a) E', and (b) E'' obtained with PE (black line), PT (red line), and PE while keeping the PT-EL on (only DC power) (yellow line). AFM nano-DMA data are compared with macroscopic DMA data at 30 °C (lighter unfilled squares), and 42 °C (darker unfilled squares).

.

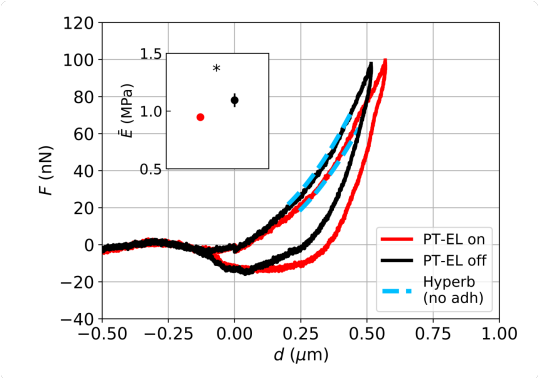


Figure 6.35: Quasi-static force (F) indentation (d) curves obtained with (red curve) and without (black curve) the PT-EL focused on the cantilever. The light blue dashed line represents the theoretical curve for the hyperboloidal model without adhesion calculated with the mean Young's moduli ($\bar{E}$) obtained from ten curves for the two configuration. In the inset, $\bar{E}$ calculated for the two configurations are shown with their standard deviation (PT-EL on, red marker; PT-EL off, black marker). The star indicates that $E_{PT-ELon}$ and $E_{PT-ELoff}$ are significantly different.

within the inset of Fig. 6.35 (PT-EL on, red marker; PT-EL off, black marker). $E_{PT-ELon}$ and $E_{PT-ELoff}$ are significantly different, with a paired t-test p-value of $\approx 10^{-10} << 0.05$.

In Fig. 6.36, E' and E'' obtained for three different approach (and withdraw) velocities are compared. Data are in good agreement with each other and with macroscopic DMA data calculated at 42 °C. Therefore, the contact model chosen was appropriate for the studied system since it eliminated differences between the curves (and thus in the contact radius) originating from different cantilever velocities (see Fig. 6.37 (a)).

6.8 Quasi-static force indentation curves

In this section, I show how AFM quasi-static force indentation curves might not be the appropriate tool to quantify the mechanical properties of viscoelastic materials. Very often, viscoelastic materials are studied with AFM quasi-static force indentation curves, i.e. force curves obtained with a certain indentation velocity and without dwelling on the sample. These force curves are usually fit with contact models that

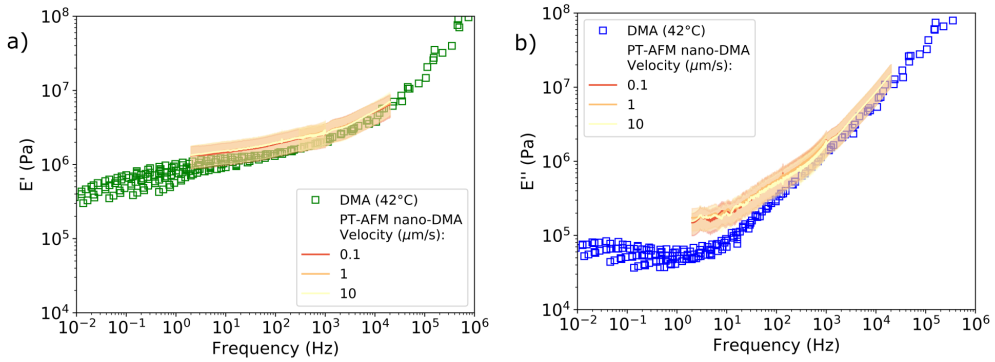


Figure 6.36: Comparison of PT-AFM nano-DMA storage (E') and loss (E'') moduli obtained with different cantilever approach/withdraw velocities. (a) E', and (b) E'' obtained with PT-AFM nano-DMA performed at different cantilever velocities, are compared with macroscopic DMA data at 42 °C (unfilled squares).

.

do not include viscoelasticy.

AFM quasi-static force curves obtained at different cantilever approach (and withdraw) velocities (0.1 µm s^{-1}, 1 µm s^{-1}, 10 µm s^{-1}, 50 µm s^{-1} and 100 µm s^{-1}) on the SBR sample are displayed in Fig. 6.37 (a). The DC power of the PT-EL was kept on during the measurements.

As expected for a viscoelastic material, the curves behave differently with different cantilever approach/withdraw velocities. Curves show more resistance to deformation as the cantilever approach/withdraw velocity increases (i.e. for the same force trigger point of 100 nN the corresponding indentation decreases with increasing velocity). To quantify this behaviour, it is possible to fit the curve and obtain E of the material (see Section 2.2.2). Note that E is a measure of the elasticity of the material, and the models used for its calculation do not consider the viscous behaviour of the sample. Withdraw curves show that there are adhesive interactions between the AFM tip and the sample (Fig. 6.37 (a)). Moreover, these adhesive interactions increase with decreasing cantilever velocity. This is analogous to what observed for AFM nano-DMA experiments performed via chirp signals with different frequency ranges (cfr. Figs. 6.29 and 6.32). Indeed, quasi-static force indentation curves with slower can-

tilever velocity (i.e. that spend more time in contact with the sample) are subjected to higher adhesion forces.

The model for a hyperboloidal indenter [168] without adhesion (i.e. removing the adhesion terms of Eqs. (2.12) and (2.13) from Eqs. (2.17) and (2.18)) was used on the approach curve to calculate E. The hyperboloidal model with adhesion [168] was used to calculate E for the withdraw part of the curve (Eqs. (2.17) and (2.18)).

For the approach curves, E was calculated for ten quasi-static force curves for each velocity by fitting each curve between 30 nN to 45 nN (R_I =7 nm, $\alpha = 17.5°$). The theoretical curves (hyperboloidal model without adhesion) calculated from the measured E are plotted for each velocity in Fig. 6.37 (a) with dashed pink lines, giving a good agreement with the experimental curves. The mean $\bar{E}$ was calculated over the ten curves for each velocity.

For the withdraw curves, the *"two-points method"* [168] was employed by using point "0" and the point at $F = 40$ nN to calculate E for each curve (R_I =7 nm, $\alpha = 17.5°$). The theoretical curve for the hyperboloidal model with adhesion is plotted in Fig. 6.37 (a) with dashed black lines, in good agreement with the experimental data. For each velocity, the mean $\bar{E}$ was calculated over ten force curves.

$\bar{E}$ calculated with the two models are plotted in Fig. 6.37 (b) (hyperboloidal model without adhesion, pink markers; hyperboloidal model with adhesion, black markers). In Fig. 6.37 (b), $\bar{E}$ calculated with the two models are compared with macroscopic DMA at 34 °C (dark green unfilled squares). The corresponding frequency was calculated as the ratio between the approach/withdraw velocity and the total distance travelled by the cantilever (6 µm). For low frequencies, $\bar{E}$ calculated from approach curves of the quasi-static force curves overlap well with macroscopic DMA data. However, $\bar{E}$ diverge from DMA data for higher frequencies. This observation is likely due to the increase of the loss component (E'') with increasing frequency, which is not taken into account in the calculation of $\bar{E}$. Models to study force curves that include

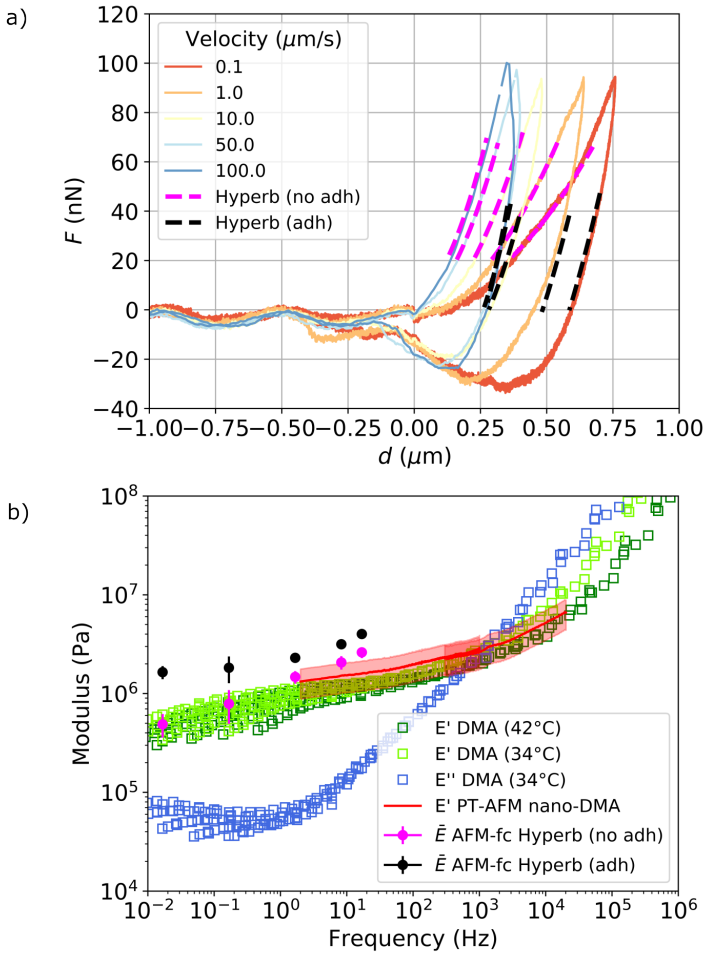


Figure 6.37: Comparison between PT-AFM nano-DMA and quasi-static force indentation curves. (a) Force curves obtained with different cantilever approach (and withdraw) velocities. Dashed lines represent the theoretical curves calculated with the hyperboloidal model with (pink lines) and without (black lines) adhesion forces. (b) Storage modulus (E') measured with PT-AFM nano-DMA (red line) and average Young's modulus ($\bar{E}$) obtained with AFM quasi-static force curves. $\bar{E}$ was calculated with the hyperboloidal model from the approach (pink markers) and the withdraw (black markers) curves (see text). Error bars on $\bar{E}$ correspond to three standard deviations. AFM data are also compared with macroscopic DMA data at 34 °C and 42 °C (E' and loss modulus E'', green and blue unfilled squares, respectively).

viscoelasticity in contact models have been developed [288], but their application is beyond the goal of this research.

$\bar{E}$ calculated with the two models differ at low frequencies, where the adhesion in the withdraw curve is higher. Possibly, the large adhesion is preventing an appropriate estimation of $\bar{E}$. At higher frequencies, where the adhesion in the withdraw curve is smaller, $\bar{E}$ calculated with the two models are closer.

PT-AFM nano-DMA experiments were performed in the same spot on the sample as the quasi-static force curves. PT-AFM nano-DMA E' is displayed in Fig. 6.37 (b) (red lines) and agrees with macroscopic DMA E' at 42 °C (dark green unfilled squares). The choice of the macroscopic DMA T was done following the results of Section 6.6 (see Fig. 6.27), where the predicted T of the system was found to be 34 °C for the PT-EL focused on the cantilever with only DC power applied, and 42 °C for the PT-AFM nano-DMA. $\bar{E}$ calculated from the AFM quasi-static force curves differs from E' calculated for macroscopic DMA and for PT-AFM nano-DMA, especially at high frequencies. For frequencies > 1 Hz, in fact, the macroscopic DMA E'' at 34 °C (light blue unfilled squares) increases, approaching E'. This observation supports the argument that ignoring the viscous properties of the sample can lead to erroneous estimation of the sample's elastic behaviour, especially when the loss component becomes more relevant (i.e. comparable to the elastic component).

This study highlights the importance of considering the viscous component of viscoelastic materials when measuring its mechanical properties. Indeed, when the viscous component (E'') becomes relevant, elastic measurements are not enough to capture the mechanical behaviour of the sample.

6.9 Viscoelastic mapping

In this section, the viscoelastic properties of the SBR measured by the PT-AFM nano-DMA and by the AM-FM AFM technique, mentioned in Section 1.3, are compared. Briefly, in AM-FM AFM the cantilever is simultaneously oscillated at two of its resonance frequencies, usually the first and the second modes [114]. Two feedback loops keep the amplitude of the first mode constant (amplitude modulation) and the frequency of the second mode at resonance (frequency modulation). AM-FM AFM provides information on: the topography of the sample (from the first mode), $\tan\delta$ (from the first mode) by taking the ratio of power dissipated over power stored by the tip-sample system [289, 290], and E' (from the higher mode) by applying contact models (based on the Hertz model) to the amplitude, phase, and frequency of the cantilever oscillations [114, 115]. As mentioned before (see Section 2.2.2), the Hertz contact model does not consider adhesion forces.

In this experiment an AC240TSA-R3 cantilever was driven with PT excitation at its first ($\approx$9.5 kHz) and second ($\approx$57.1 kHz) modes. Fig. 6.38 (a-c) show the height, $\tan\delta$, and E' of the SBR obtained with AM-FM AFM. Both $\tan\delta$ and E' show variations in the calculated viscoelastic properties across the surface of the sample.

The heterogeneity of $\tan\delta$ and E' of the sample in Fig. 6.38 (b,c) could be caused by surface effects, such as sample defects or adhesion forces, to which AM-FM AFM is sensitive [115]. For example, on the bottom right of Fig. 6.38 (b,c), a black spot (corresponding to lower values of $\tan\delta$ and E'), can be related to the feature on the bottom right of Fig. 6.38 (a). This feature is highlighted with a cyan oval in Fig. 6.38 (a-c).

The average value of $\tan\delta$ and E' calculated over fifteen PT AM-FM AFM images and PT-AFM nano-DMA data (obtained with an AC240TSA-R3 cantilever, from Sections 6.5.8 and 6.7) are compared to macroscopic DMA data in Fig. 6.38 (d,e).

$\tan\delta$ in Fig. 6.38 (d) shows a good agreement between PT-AFM nano-DMA and PT

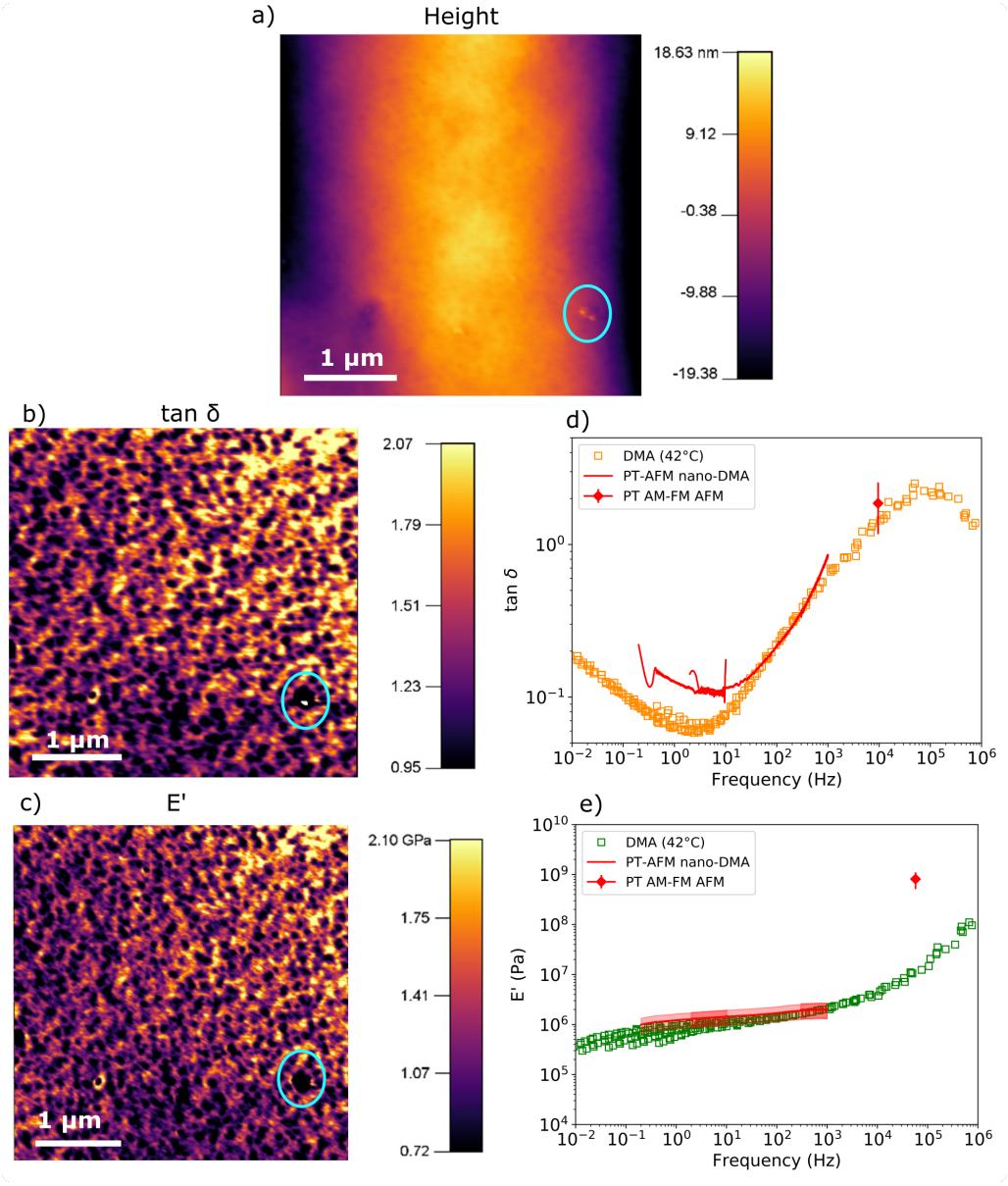


Figure 6.38: PT-AFM nano-DMA, PT AM-FM AFM, and DMA on a SBR sample. PT AM-FM AFM maps of SBR (a) height, (b) loss tangent ($\tan\delta$), and (c) storage modulus (E'). The cyan ovals in (a-c) mark a feature present in the height image in (a) that correspond to low values of $\tan\delta$ and E' in (c,b), respectively. Comparison of (d) $\tan\delta$, and (e) E' obtained with PT-AFM nano-DMA (red), PT AM-FM AFM (red diamond), and macroscopic DMA (42 °C, orange unfilled squares). In (d,e) error bars of the PT AM-FM AFM data correspond to the standard deviation. PT AM-FM AFM images, $\tan\delta$ and E' values were provided by Ms. Adam and printed with her permission.

AM-FM AFM data with macroscopic DMA. The agreement of PT AM-FM AFM data with macroscopic DMA at 42 °C, further supporting my hypothesis that the PT excitation is heating the system.

In terms of E', PT-AFM nano-DMA data agree well with macroscopic DMA data. However, AM-FM AFM data are about one order of magnitude higher than DMA results.

AM-FM AFM indentations are typically very small, which leads to miscalculation and variations of E' in the presence of roughness and adhesion forces [115]. Additionally, the Hertz model used to calculate E' for AM-FM AFM does not consider adhesion [114, 115]. The importance of accounting for adhesion forces on this sample for the calculation of E' has already been shown in Section 6.7 for PT-AFM nano-DMA data. Therefore, the observed overestimation of AM-FM AFM E' might be due to the presence of adhesion forces between the AFM tip and the sample. Adhesion is not involved in the calculation of $\tan\delta$ (see Section 2.2.3 and refs. [289, 290]), which is accurate for AM-FM AFM $\tan\delta$, thereby supporting this hypothesis.

The study highlights the potential of combining PT-AFM nano-DMA and AM-FM AFM, to extend the frequency range of the measurable viscoelastic properties and even to map them.

6.10 Conclusions

PT actuation is an elegant way of exciting the cantilever and avoid spurious resonances typical of indirect actuation by PE excitation. In this work, the combination of PT actuation and chirp signals provided a way to measure the viscoelastic properties of a SBR sample from 0.2 Hz up to 20 kHz in a continuous spectrum.

The comparison between the PT-AFM nano-DMA and macroscopic DMA indicated an increase in T of the system. T increased about 10 °C compared to the ambient

AFM temperature. This T increase was most likely caused by the focusing of the PT-EL on the back of the cantilever. The increase in T was also confirmed by comparison of the SBR viscoelastic properties measured with PT and PE actuation (Section 6.6). The $\tan\delta$ of the sample measured with PE excitation was in good agreement with macroscopic DMA data at 30 °C, indicating that the overall T of the cantilever-sample system was in agreement with the expected T of the instrument. PE measurements obtained while leaving the PT-EL focused on the back of the cantilever with DC power, showed an increase in T to 34 °C, also validating the hypothesis that the PT-EL heats the system. Quasi-static force curves acquired with and without the PT-EL focused on the back of the cantilever exhibited different behaviours (Section 6.7), adding additional evidence to the hypothesis of the PT-EL heating the sample.

This heating of the cantilever-sample system is therefore an important issue to take into account when performing PT-AFM nano-DMA experiments. In this study, the macroscopic DMA results were useful as a "thermometer" for the AFM measurements. Another solution to measure the increase in T could be to use a thermocouple in the proximity of the cantilever/sample or to use cantilevers with integrated thermometers [291, 292].

This research also highlights the importance of k_c for quantitative viscoeastic measurements. Viscoelastic quantities of the sample are incorrect when k_c is smaller than or comparable to k' of the sample ($k_c \leq k'$, see Section 6.5.8).

E^* measured by PT-AFM nano-DMA has been proved to be in good agreement with macroscopic DMA data when calculated from k^* by using the appropriate contact model. Failure to define the right contact model led to misestimation of E' and E'' of the material. The best model to describe the SBR-cantilever system was a flat punch stiffness [171, 172] with one of two mechanical models describing the geometry of the system for the calculation of the contact radius during the oscillations. These models were the hyperboloidal model accounting for adhesion [168]

for AC160TSA-R3 and AC240TSA-R3 cantilevers, and the JKR model [164] for a biosphere^{TM}-NT_B2000_v0010, which led to a quantitatively good match between the PT-AFM nano-DMA (and PE-AFM nano-DMA) and macroscopic DMA data.

Finally, the combination of PT-AFM nano-DMA and AM-FM AFM proved to be promising for mapping and expanding the spectrum of the viscoelastic properties achievable with AFM. Nevertheless, these results suggest that it may be necessary to expand AM-FM AFM to rely on different contact mechanics models in order to account for adhesion and surface effects.

Chapter 7

Conclusions and future work

The physical properties of hydrogels make them useful materials for biomedical applications. Indeed, hydrogels are already being used in applications including wound healing, contact lenses, drug delivery, and tissue engineering [10]. As explained in Chapter 1, the mechanical behaviour of hydrogels is key in determining their application to biomedical problems, as well as the outcome of the application. The goals of this thesis have been (i) the study of the local elasticity of hydrogels with tunable mechanical properties, and (ii) the development of a novel technique that provides a way to quantify a sample's viscoelasticity, more relevant for polymeric materials than elasticity alone.

In this chapter, I summarise the main results of my research and the relevance of these findings to the development of novel materials. I also provide a brief outlook on future experiments that can be performed using the materials and technique studied in this thesis.

7.1 Hydrogels for biomedical applications

The possibility of controlling the mechanical properties of hydrogels, either via external stimuli and/or changing their composition, is a powerful strategy to develop

better materials for biomedical applications.

To better understand how to tune the mechanical properties of hydrogels, Chapters 4 and 5 measured the local elastic properties of hydrogels via AFM quasi-static force indentation curves at the micron scale and quantified using the Hertz contact model. The study of plain chitosan (and PNIPAAm) hydrogels in this thesis (Chapter 4) revealed magneto-mechanical coupling within these hydrogels, and the possibility of tuning the local elastic properties of these hydrogels via the application of B. The effect of B was also tested on the local elastic properties of chitosan composite hydrogels with embedded magnetic nanowires (Section 5.2), which responded to B in a similar manner to plain chitosan hydrogels. The local elastic properties of composite hydrogels based on fullerenes was also researched (Section 5.3). The elastic properties of fullerene-based hydrogels depended on the size of the fullerene used in their synthesis. This result suggests the possibility of tailoring the elastic properties of fullerene-based hydrogels to various biomedical applications by using different fullerene cages in hydrogel synthesis.

7.1.1 Changes in the local elastic properties of chitosan-based hydrogels due to magneto-mechanical coupling

Application of B to plain chitosan hydrogels altered their local $\tilde{E}$ (Chapter 4). This change in $\tilde{E}$ was heterogeneous over the surface of the materials. In other words, there was not a consistent softening/stiffening of the sample in response to B, but a mixture of responses instead. Similar results were found for two other polymeric materials (PNIPAAm hydrogel, and non-porous PDMS elastomer). The heterogeneity in the magneto-mechanical coupling of the plain chitosan hydrogel is attributed to a local distribution of electrical charges within the polymeric matrix that, when displaced during the deformation, can be affected by the presence of B (by Lorentz force), resulting in different mechanical properties. A non homogeneous distribution

of charges can also explain the inhomogeneity of the mechanical response of the materials.

Kelvin force microscopy (KFM), based on the electrostatic interactions between the KFM probe and the sample, could be employed to image the charge concentration on the surfaces of plain chitosan hydrogels studied in this thesis [234, 293, 294]. KFM could thereby provide a clearer understanding of the local charge distribution and the magneto-mechanical coupling observed in the plain chitosan hydrogels studied in this thesis. Once the material's charge distribution is known, the AFM experiments of this thesis could be performed in regions with different charge concentration to test the correlation between charge distribution and magneto-mechanical coupling of the sample.

The observed magneto-mechanical coupling in the chitosan hydrogels studied in this thesis could inspire the design of new smart materials without the incorporation of magnetic nanostructures. Thanks to their magneto-mechanical coupling, a possible application of these materials could be the creation of smart hydrogels for tissue engineering to stimulate cells with the application of B. The ability to avoid incorporating magnetic nanostructures, and further understanding of the natural magneto-mechanical coupling in polymeric materials could improve the fabrication of materials for biomedical applications such as drug delivery, tissue engineering, and biosensors.

The magneto-mechanical behaviour of chitosan composite hydrogels was also analysed by incorporating magnetic nanowires into the polymeric matrix during hydrogel synthesis (Section 5.2). Incorporation of the magnetic nanowires was meant to enhance and homogenise the magneto-mechanical effect observed on plain chitosan hydrogels, especially when the nanowires were oriented during hydrogel synthesis. However, chitosan composites showed nanowire agglomerates. These agglomerates were uniformly aligned in the case of hydrogels with oriented nanowires, but still present in hydrogels without oriented nanowires. Even in chitosan composite hydrogels, alterations of $\tilde{E}$

with B were still heterogeneous. This lack of homogenous response is likely due to the non uniform distribution of the nanowires in the chitosan composite matrices as well as the heterogeneous response of chitosan itself to B.

The magneto-mechanical response of chitosan composite hydrogels could be homogenised by using stronger and more homogeneous magnetic fields during hydrogel synthesis to help avoid the formation of nanowire clusters. Moreover, superparamagnetic nanowires could be employed as the magnetic component of the hydrogel so that no remanent magnetisation would be present after B is removed.

It would also be worth analysing the change of shape, dimension, and pore size of both plain and composite chitosan hydrogels when B is applied (magnetostriction). Although imaging of the samples was not possible with the magnetic AFM set-up used in this thesis, different experimental conditions could potentially allow imaging of the change in sample topology with/without B. If magnetostrictive effects are revealed by such studies, this would increase the usefulness of these materials to applications that include: controlled release of biological factors (such as cells, nutrients, etc.), drug delivery, and construction of artificial tissues (e.g. muscles or artificial membranes). Indeed, besides revealing a magneto-mechanical coupling that could potentially be used to stimulate cells and/or release drugs, both plain and composite chitosan hydrogels showed elastic properties in the range of those of biological tissues and other drug carriers [17, 18, 57, 61, 231]. These properties make the chitosan-based hydrogel studied in this thesis promising materials for both tissue engineering and drug delivery.

7.1.2 Local elastic properties of hydrogels based on C_{60}, C_{84}, and C_{90-92} fullerenes

In this thesis (Section 5.3), the local elastic properties of novel fullerene-based self-assembled supramolecular macroporous hydrogels were analysed. Hydrogel morphol-

ogy, including the pore size, depended on whether C_{60}, C_{84}, or C_{90-92} fullerene cages were used in the hydrogel's synthesis. The elastic properties, quantified by $\overline{\tilde{E}}$, of the hydrogels also depended on the fullerene cage used, and matched the elasticity of biological tissues and other drug carriers [17, 18, 57, 61, 231]. In particular, $\overline{\tilde{E}}$ of C_{60} hydrogel matched that of muscles, while $\overline{\tilde{E}}$ of C_{84} and C_{90-92} hydrogels matched that of bone, suggesting their biomechanical compatibility.

The fullerene-based hydrogels presented and characterised here open the door to a new class of carbon-based materials, with physical properties that can be tailored to the desired application by choosing the most appropriate fullerene cage.

An interesting study would be to test the suitability of these hydrogels as scaffolds for cell culture and tissue engineering. For example, similarly to other studies [61–63], stem cells could be seeded onto or into the different fullerene-based hydrogels (having different $\overline{\tilde{E}}$) and cell viability and differentiation could be analysed.

Additionally, the potential of fullerenes as anticancer drug carriers [278–280] and the high NIR optical absorption of carbon nanomaterials [45–47], could potentially be combined in these hydrogels for chemo-photothermal cancer treatment purposes [45–47]. Conjunct studies on the load, release, and heating effect of these fullerene-based hydrogels could potentially bring a great contribution for the development of new drug delivery materials and anticancer therapies.

7.2 PT-AFM nano-DMA for viscoelastic measurements at the local scale

While the study of elasticity is a starting point for the mechanical characterisation of hydrogels, viscoelasticity is the most appropriate quantity to consider for polymeric materials, as explained in Chapter 1. To help characterise the viscoelastic properties of hydrogels, rather than elastic properties alone, I developed a novel AFM technique

to quantify viscoelasticity at the nano and micro-scale. This novel technique, validated in Chapter 6, uses PT excitation of the AFM cantilever (Section 2.2.1) and chirp signals (Section 2.2.4).

For the first time, to the best of my knowledge, a nano-rheology technique based on the PT excitation of an AFM cantilever has been used to study the viscoelastic properties (k', k'', $\tan\delta$, E', E'') of a polymeric material over a continuous frequency range spanning five orders of magnitude (0.2 Hz to 20 200 Hz). PT chirp signals were used to excite the cantilever and provide this continuous spectrum. The PT-AFM nano-DMA technique was tested on a SBR sample in air.

Theoretical models allowed the calculation of k', k'', and $\tan\delta$ of the SBR sample from the amplitude and phase of the chirped cantilever oscillations. Experiments performed with the PT-AFM nano-DMA technique had several major results.

First, my results show that an increase in temperature (by about 10 °C compared to the AFM ambient temperature) of the sample was caused by the PT excitation of the cantilever. This result was confirmed by comparing PT-AFM nano-DMA to macroscopic DMA data, PT and PE excitation of the AFM cantilever, PT-AFM nano-DMA to PT AM-FM AFM, and with quasi-static force indentation curves obtained with/without the PT-EL on the cantilever.

Second, the importance of cantilever selection for PT-AFM nano-DMA application was highlighted. Indeed, whenever k_c was smaller than k', the calculated viscoelastic quantities incorrectly deviated from the expected behaviour.

Third, the importance of ascertaining the best contact mechanics model to describe the contact between the indenter (AFM tip) and the sample, and the consequent calculation of E' and E'' from k' and k'' was highlighted. A flat punch stiffness behaviour of a hyperboloidal (spherical) indenter subject to adhesion forces was successfully adopted to determine E' and E'' of the SBR sample for experiments performed at the nano- (micro-) scale with AC160TSA-R3 and AC240TSA-R3 (biosphere$^{\text{TM}}$-

NT_B2000_v0010) cantilevers.

Finally, the potential of combining PT-AFM nano-DMA with AM-FM AFM for viscoelasticity mapping and broadening of the viscoelastic spectrum was also demonstrated. Even though the introduction of different contact mechanics models might be needed for the correct determination of E' for AM-FM AFM measurements, the AM-FM AFM $\tan\delta$ was in good agreement with PT-AFM nano-DMA and macroscopic DMA.

Overall, the PT-AFM nano-DMA results were found to be in good agreement with macroscopic DMA and nanoscopic PT AM-FM AFM data, ensuring the reliability of the novel technique that I have developed. Therefore, PT-AFM nano-DMA was proved to provide quantitative information on the viscoelastic properties of materials at the nano and micro-scale over a wide and continuous range of frequencies.

It is important to account for the increase in sample temperature due to PT AFM cantilever excitation when measuring a sample's viscoelastic properties (Section 1.2.2). In order to assess the temperature change of the sample, either another technique should be used as reference (e.g. macroscopic DMA) or a direct measurement is needed. Direct measurements of the temperature of the sample could be performed with thermocouples or thermal cantilevers [291, 292] to better understand PT-EL heating of the system.

AFM nano-DMA technique based on PT excitation allows rheological experiments to be performed in liquid while avoiding the presence of artefacts due to mechanical resonances typical of PE excitation, or perturbations of the experiment by application of magnetic fields needed for magnetically actuated cantilevers (see Section 2.2.1).

The next step in the development of the PT-AFM nano-DMA should be to test the technique in liquid environments, possibly accounting for effects due to the hydrodynamic drag on cantilever movements due to the surrounding liquid [295].

The potential of working in liquid across a large range of frequencies makes PT-AFM

nano-DMA a promising technique for several applications. Some of these applications and preliminary data are proposed below. As previously mentioned in this thesis (see Chapter 1), the mechanical properties of polymeric materials can be tailored by changing their composition or the concentrations of their constituents. Application of PT-AFM nano-DMA on polymeric materials in liquid at the nano and micro-scale could be used to characterise the viscoelastic properties of hydrogels in order to tune them for biomedical applications. An example could be the study of the viscoelastic properties of cells and hydrogels used as substrates for cell culture, before and after cell seeding. Quantifying changes in the viscoelastic properties of cells and hydrogels can not only help with the development of novel scaffold materials, but could also provide important information on how cells respond to and modify the mechanical properties of their environment.

One promising cell culture substrate to probe with PT-AFM nano-DMA is poly(HEMA). Poly(HEMA) is a hydrogel widely used as a material in contact lenses and as a substrate for cell culture [25, 296]. Poly(HEMA) is a promising material for tissue engineering, since cell activities are affected by the concentration of the poly(HEMA) on which the cells are cultured [201].

Poly(HEMA) hydrogels at different concentrations (per unit surface area of the sample: 1.14 mg of poly(HEMA) per cm^2, and 11.4 mg of poly(HEMA) per cm^2) were tested with PT-AFM nano-DMA in liquid. PT-AFM nano-DMA preliminary data on the poly(HEMA) hydrogels at the two different poly(HEMA) concentrations are shown in Fig. 7.1. These results do not account for hydrodynamic drag. However, these results already suggest the possibility of discriminating between hydrogels with different properties. Additionally, the measured $\tan\delta$ are similar to those of poly(HEMA) hydrogels in the literature [297]. Future experiments to study the effect of hydrodynamic drag on the AFM cantilever [295] and to test hydrogels made with more than two concentrations of poly(HEMA), are required to better quantify

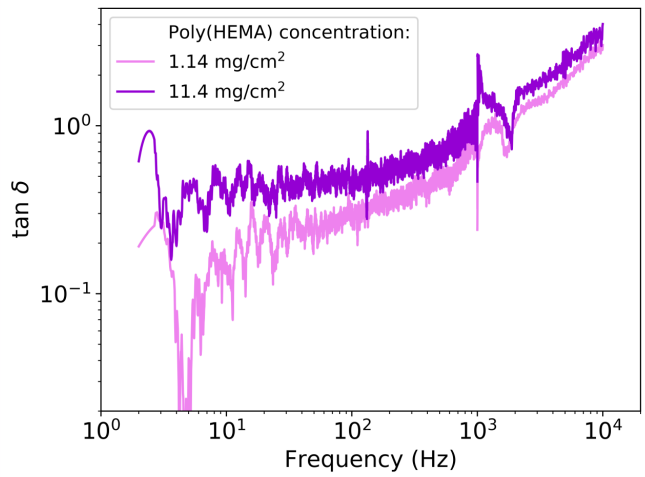


Figure 7.1: Loss tangent ($\tan\delta$) of poly(HEMA) hydrogels measured by PT-AFM nano-DMA. Hydrogels with two different poly(HEMA) concentrations per unit surface area of the sample were tested: 1.14 mg of poly(HEMA) per cm^2 (pink line), and 11.4 mg of poly(HEMA) per cm^2 (purple line).

differences between these hydrogels. Nevertheless, Fig. 7.1 suggests that PT-AFM nano-DMA can be applied in liquid to measure differences in the viscoelastic behaviour of hydrogels with different features.

PT-AFM nano-DMA could also be used in diagnosis to discriminate normal or wild-type cells from mutated and/or diseased cells [122]. Once the viscoelastic behaviour of healthy cells and tissues is known, PT-AFM nano-DMA could be used to detect those that are compromised by disease or injury. PT-AFM nano-DMA measurements of a patient's tissues and cells could be compared to measurements of healthy tissues and cells. If PT-AFM nano-DMA results differ from those of healthy tissues and cells, that would indicate that substantial tissue modification, which often occurs in disease [55–57], has occurred.

Furthermore, given the possibility of changing the environmental temperature of the AFM, the TTS principle could be tested with PT-AFM nano-DMA on polymeric materials, to evaluate how these materials respond to temperature changes at the nano and micro-scale [118, 133, 134].

To conclude, PT-AFM nano-DMA can not only provide insightful contributions to biomedical research by measuring hydrogels and/or biological matter in liquid, but also provides a new way to test heterogeneous systems, theoretical models, and a wide range of materials at small length scales. This technique has the potential to improve polymer physics and material science in general.

7.3 Implications of the findings in this thesis

Hydrogels are useful for biomedical applications and knowing their mechanical properties is important to understanding how they can be best applied in therapies. Once we elucidate the role of the mechanical properties of hydrogels in determining their efficacy in biomedical applications, it will be possible to better-design new biomedical treatments. The work in this thesis revealed the possibility of tuning local elastic properties of chitosan-based hydrogels with external magnetic fields, tuning local elasticity of fullerene-based hydrogels by choosing different fullerene cages, and developed a new technique to quantify hydrogel viscoelasticity.

In the future, treatments may include a form of nano/micro-rheology to diagnose a disease by comparing viscoelastic properties of healthy and unhealthy tissues. Diseased tissues could potentially be surgically removed and replaced with artificial tissues constructed from smart hydrogels, which would allow stimulation and control of cells via remotely manipulable cues (such as external magnetic fields). The work of this thesis contributes to this goal by improving the viscoelastic characterisation of polymeric materials and gaining insight into the mechanics of hydrogels with tunable mechanical properties.

Appendices

A Mechanical models for viscoelastic materials

The viscoelastic behaviour of materials can be theoretically described using springs (Fig. A.1 (a) left) and dashpots (Fig. A.1 (a) right) to represent the elastic and the viscous behaviour, respectively. The spring behaviour can be described by Eq. (1.1), while the dashpot with Eq. (1.2). Combinations of these elements provide different models that can be used to describe the mechanical behaviour of materials [19, 21, 23, 101]. A detailed description of mechanical models, here briefly summarised, can be found in refs. [19, 21, 23, 101]. The two easiest models are based on the arrangement of a spring and a dashpot in series (Maxwell (MW) model) and in parallel (Kelvin-Voigt (KV) model). A three-element model often used to describe viscoelastic solid is the SLS model, which has a MW arm and a spring in parallel (see Fig. A.1 (b)). The solution for the SLS model to stress relaxation is given by:

$$\sigma(t) = \left(E_\infty + E_1 e^{-t/\tau}\right) \epsilon_0 \tag{A.1}$$

where $\tau = \eta/E_1$. Solution of stress relaxation experiments can be written as $\sigma(t) = E(t)\epsilon_0$, where $E(t)$ is called the relaxation modulus. For Eq. (A.1), $E(t) = E_\infty + E_1 e^{-t/\tau}$. The characteristic time of a stress relaxation experiment τ is called the relaxation time.

Mechanical models can also be used to represent dynamic experiments. Given a

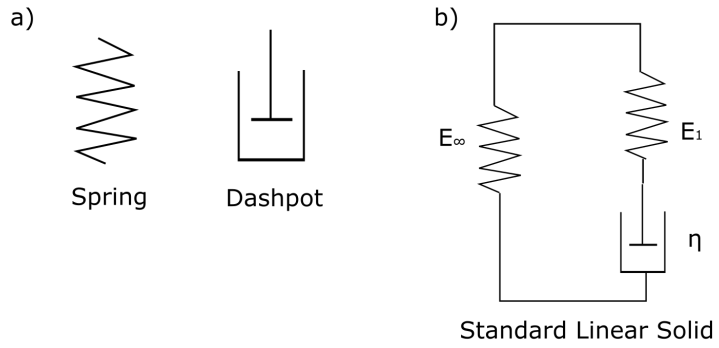


Figure A.1: Mechanical models for viscoelastic materials. (a) Basic elements: elastic spring and viscous dashpot. (b) The SLS model.

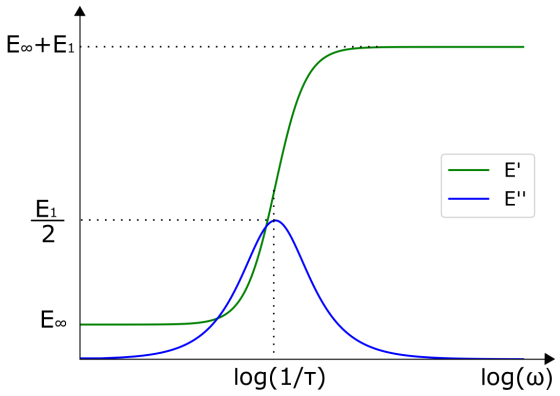


Figure A.2: Storage and loss moduli for the SLS model. Schematic representation of the storage (E') and loss (E'') moduli calculated with the SLS model for a dynamic experiment.

periodic strain of the form $\epsilon = \epsilon_0 e^{i\omega t}$, the solution can be written in terms of E^*. For the SLS model, the calculation of the components of E^* leads to:

$$E' = E_\infty + E_1 \frac{\omega^2\tau^2}{1+\omega^2\tau^2} \tag{A.2}$$

$$E'' = E_1 \frac{\omega\tau}{1+\omega^2\tau^2} \tag{A.3}$$

This system has a resonance for $\omega = 1/\tau$ and the behaviour of E' and E'' is schematically represented in Fig. A.2.

In reality, as it is discussed in Section 1.2.2, polymers have several characteristic times.

More complicated mechanical models, such as the generalised SLS model (i.e. a spring and a certain number of MW arms in series) where every arm takes into account a different characteristic time $\tau_i = \eta_i/E_i$, can be employed to describe materials with multiple characteristic times (see Section 1.2.2).

B Lock-in and time signals

As explained in Section 2.2, the deflection of the cantilever is measured using a detection laser reflected from the back of the cantilever to a PSD. The raw deflection signal is measured in Volts. For the AFM nano-DMA, this deflection signal can be used in two ways. The first way is to save the deflection signal and the drive signal in the time domain, apply FFT and compare the two in the frequency domain. I call this first method "TS", from time signal. The second way is to use a LIA (accessible within the Cypher AFM and used in this thesis), where amplitude and phase of the oscillations are obtained directly in the frequency domain. I call this second method "lock-in (LI)". The working principle of a LIA can be found in refs. [298, 299].

The difference between these two methods is that the signal has to pass through different LPF and high-pass filter (HPF) within the Cypher AFM. These filters can distort the signals, and it is therefore useful to observe both the LI and TS in order to account for filter effects.

For the TS method, the deflection signal was transformed from the time domain to the frequency domain by FFT. FFT calculations were done using the NumPy library [187] in Python [181]. The FFT of the cantilever's oscillations was normalised by the FFT of the drive signal as follows:

$$\begin{aligned} \frac{FFT(defl)}{FFT(drive)} &= \frac{A_{defl}e^{i\phi_{defl}}}{A_{drive}e^{i\phi_{drive}}} \\ &= \frac{A_{defl}}{A_{drive}}\ e^{i(\phi_{defl}-\phi_{drive})} \end{aligned} \tag{B.1}$$

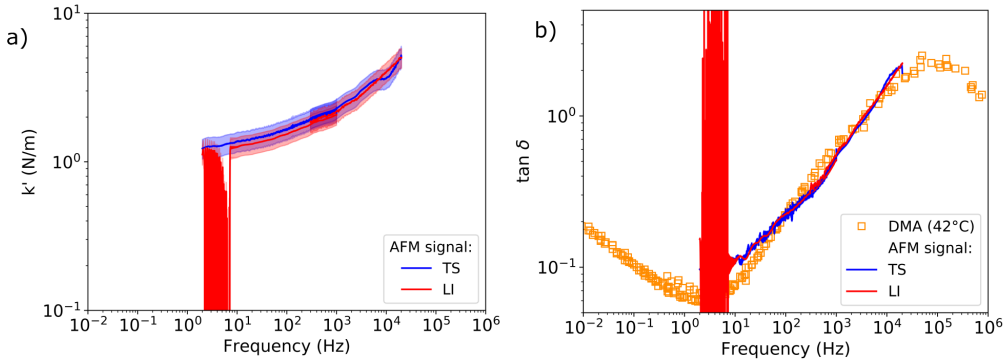


Figure B.1: Comparison between PT-AFM nano-DMA signals obtained with TS and LI. (a) Storage stiffness (k'), and (b) loss tangent ($\tan\delta$) of the SBR sample calculated with TS (blue line) and LI (red line). In (b) the PT-AFM nano-DMA data are compared with macroscopic DMA data at 42 °C (orange unfilled squares).

where A and ϕ are the FFT amplitude and phase signals of the deflection and the drive signal. Eq. (B.1) is then smoothed using the Savitzky-Golay filter (using the SciPy library [191] in Python [181]). Finally, Eq. (B.1) is multiplied by the zero-to-peak amplitude of the drive signal (A_D), and by the OLS^{-1} (see Section 2.2) in order to obtain the amplitude in metres.

To decide whether to use TS and/or LI for data acquisition for AFM nano-DMA measurements I compared data obtained with both methods in different frequency ranges. k' and $\tan\delta$ obtained with the LI (red curve) and the TS (blue curve) for PT-AFM nano-DMA measurements are compared in Fig. B.1. The TS data is much smoother than the LI for frequency less than 10 Hz. Therefore, TS is better for low frequencies. However, TS data is distorted for frequency above 10 kHz, possibly due to a filter in the electronics used by the TS. For these reasons, in this thesis, I decided to use TS for frequencies below 1 kHz and LI data for frequencies above 1 kHz.

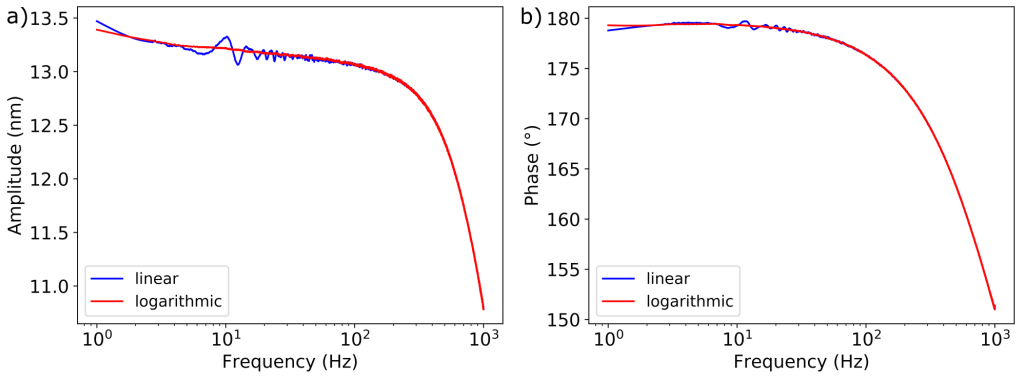


Figure C.1: Comparison between the response of a cantilever from a linear and a logarithmic chirp drive signals for PT excitation. (a) Amplitude, and (b) phase of a reference signal obtained with a linear (blue line) and a logarithmic (red line) chirp.

C Linear versus logarithmic chirp signals

As explained in Section 2.2.4, the instantaneous frequency of chirp signals can have different time dependences. The amplitude and phase of a typical PT-AFM nano-DMA reference measurement obtained with a linear and a logarithmic chirp are compared in Fig. C.1. The linear chirp has fringes in the amplitude and phase signals at low frequencies which are not present in the logarithmic chirp signals. Therefore, logarithmic chirps were used as excitation signals in this study.

D Control of the effect of an applied magnetic field on AFM measurements

The approach curves of the cantilever towards a glass sample at $10\,\mu m\,s^{-1}$ with (red line) and without (black line) the presence of B are presented in Fig. D.1. No significant difference can be seen between the curves with/without B in ultrapure water (Fig. D.1 (a)), nor in PBS (Fig. D.1 (b)). Therefore, the presence of B did not introduce systematic error in the AFM measurements. Similar results were obtained for $25\,\mu m\,s^{-1}$ and $50\,\mu m\,s^{-1}$ approach velocities (not shown).

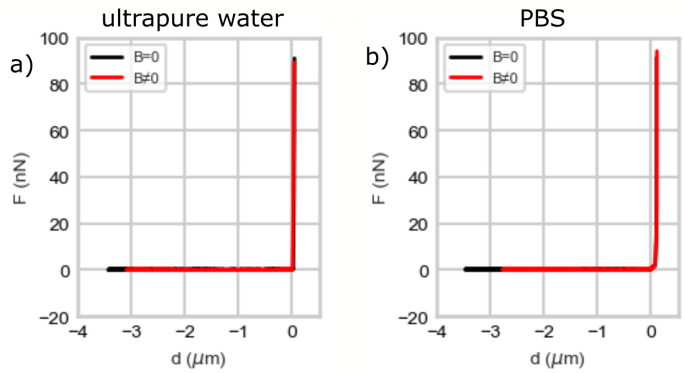


Figure D.1: Effects of an external magnetic field (B) on an AFM cantilever. cantilever approach to the glass sample in presence (red line) and in absence (black line) of B at $10\,\mu m\,s^{-1}$ in (a) ultrapure water, and (b) PBS.

E Heterogeneity in the effect of an applied magnetic field on plain polymeric materials

$\tilde{E}_B$ for $B = 0$, $B \neq 0$, and $B = 0(II)$ are plotted for several positions obtained on plain chitosan (Fig. 4.6), PNIPAAm (Fig. E.1), and PDMS (Fig. E.2) samples. $\tilde{E}_B$ are plotted for measurements obtained both in ultrapure water and PBS, for AFM cantilever approach velocities of $10\,\mu m\,s^{-1}$, $25\,\mu m\,s^{-1}$ and $50\,\mu m\,s^{-1}$. For each velocity, positions where $\tilde{\bar{E}}_B$ was much larger (three times higher or more) than the average $\tilde{E}$ calculated over all the measured positions were assumed to be outliers, and therefore were discarded for the analysis. In these plots, red asterisks mark position where Eq. (4.1) (a-d) are satisfied.

Similarly to chitosan hydrogels, for both the PNIPAAm and PDMS samples, there are several positions where all the conditions in Eq. (4.1) are satisfied, in both ultrapure water and PBS (see Figs. E.1 and E.2). This indicates a significant change in $\tilde{E}$ with/without B. This effect is attributed to the displacement of electrical charges localised within the polymeric matrices (see Chapter 4).

The heterogeneity in the stiffening/softening of the samples with B (see Figs. E.1, E.2 and 4.6) could be due to an inhomogeneous distribution of electrical charges within

the polymeric materials. Moreover, it is also another proof (together with the results obtained for glass in Appendix D) that there is no systematic error due to the effect of B on the AFM.

To compare the effect of the velocity of the deformation on the change in $\bar{\tilde{E}}$ in the presence of B, the absolute value of the difference between $\bar{\tilde{E}}_{B\neq 0}$ and the average between $\bar{\tilde{E}}_{B=0}$ and $\bar{\tilde{E}}_{B=0(II)}$ ($|\Delta\bar{\tilde{E}}|$) was calculated. $|\Delta\bar{\tilde{E}}|$ was calculated for the three polymeric materials for the positions where the conditions in Eq. (4.1) (a-d) were satisfied for all three approach velocities: $10\,\mu m\,s^{-1}$, $25\,\mu m\,s^{-1}$ and $50\,\mu m\,s^{-1}$ (cfr. Figs. E.1, E.2 and 4.6). $|\Delta\bar{\tilde{E}}|$ results are shown in Fig. E.3 for the chitosan and PNIPAAm hydrogels and in Fig. E.4 for the PDMS sample. No clear trend is observable in $|\Delta\bar{\tilde{E}}|$ with respect to approach velocity.

To study the global elastic behaviour ($\overline{\bar{\tilde{E}}}$) of the three polymeric materials, the average of $\bar{\tilde{E}}$ over all the positions that satisfied the conditions in Eq. (4.1) (a,b) was calculated. For each position, $\overline{\bar{\tilde{E}}}_{B=0}$ was calculated by averaging $\bar{\tilde{E}}_{B=0}$ and $\bar{\tilde{E}}_{B=0(II)}$, for each velocity. Results are shown in Fig. E.5 (red for $B \neq 0$, black for $B = 0$) for the three polymeric materials, in ultrapure water and PBS, for a cantilever approach velocity of $10\,\mu m\,s^{-1}$. For all the three samples, there was no significant change in $\overline{\tilde{E}}$ with/without B. Similar results were obtained at $25\,\mu m\,s^{-1}$ and $50\,\mu m\,s^{-1}$ (not shown).

$\overline{\tilde{E}}$ of the polymeric materials slightly decreased when measured in PBS, compared to ultrapure water. While differences in swelling could explain this observation for the hydrogels [300], swelling is unlikely for the non-porous PDMS elastomer. One possible explanation for this observation is that the ions present in PBS (but absent in the ultrapure water) alter the distribution of the localised electrical charges hypothesised to be on the surface of the polymeric materials here studied (cfr. Chapter 4). It is possible that the alteration of the localised charges due to the presence of the PBS ions might, in turn, change the mechanical properties of the polymeric materials.

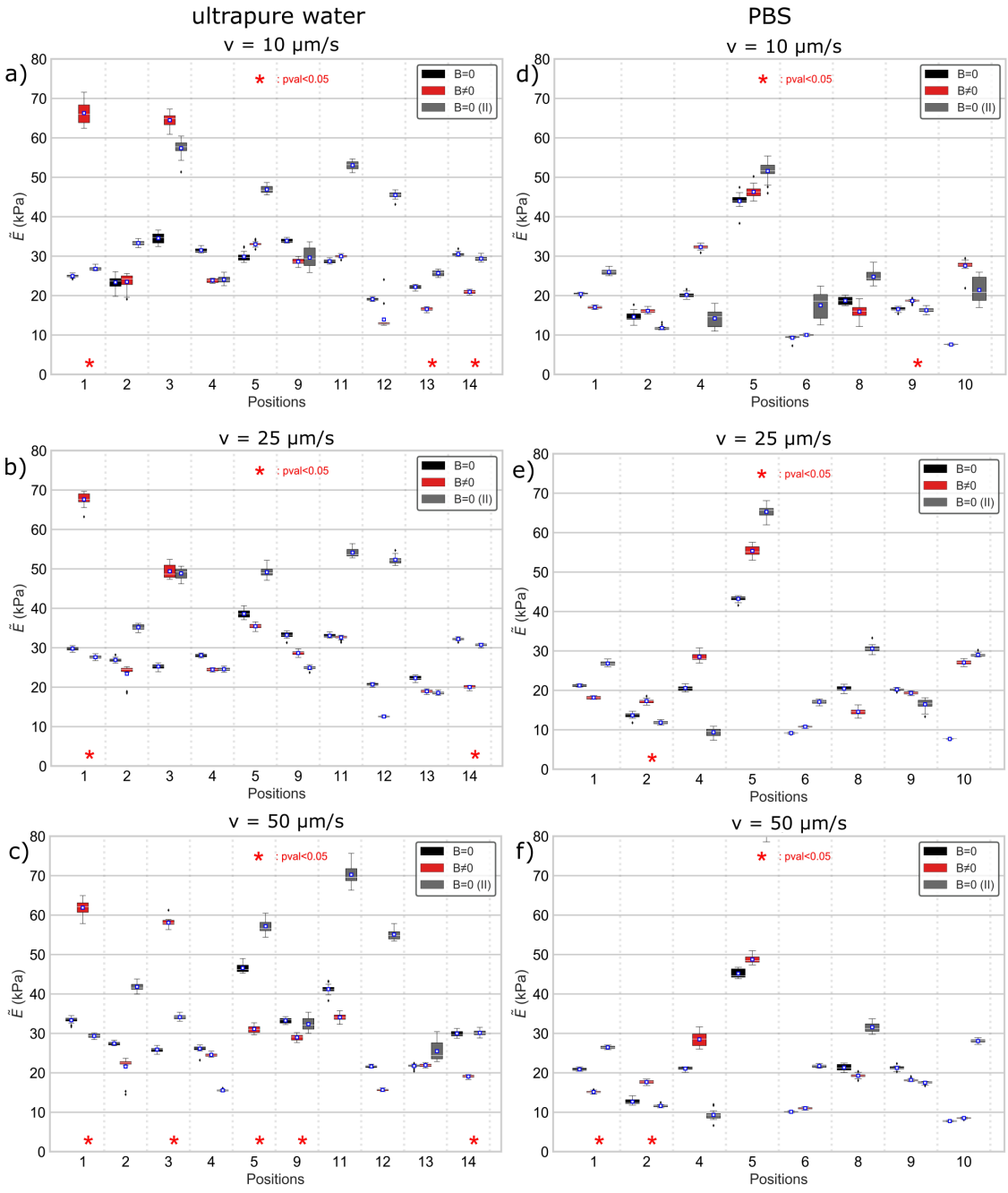


Figure E.1: Distribution of change in reduced Young modulus ($\tilde{E}$) with an external magnetic field (B) for a PNIPAAm hydrogel: $\tilde{E}$ calculated in several positions on PNIPAAm hydrogel in ultrapure water from indentations at (a) $10\,\mu m\,s^{-1}$, (b) $25\,\mu m\,s^{-1}$, and (c) $50\,\mu m\,s^{-1}$, and in PBS at (d) $10\,\mu m\,s^{-1}$, (e) $25\,\mu m\,s^{-1}$, and (f) $50\,\mu m\,s^{-1}$ cantilever approach velocities.

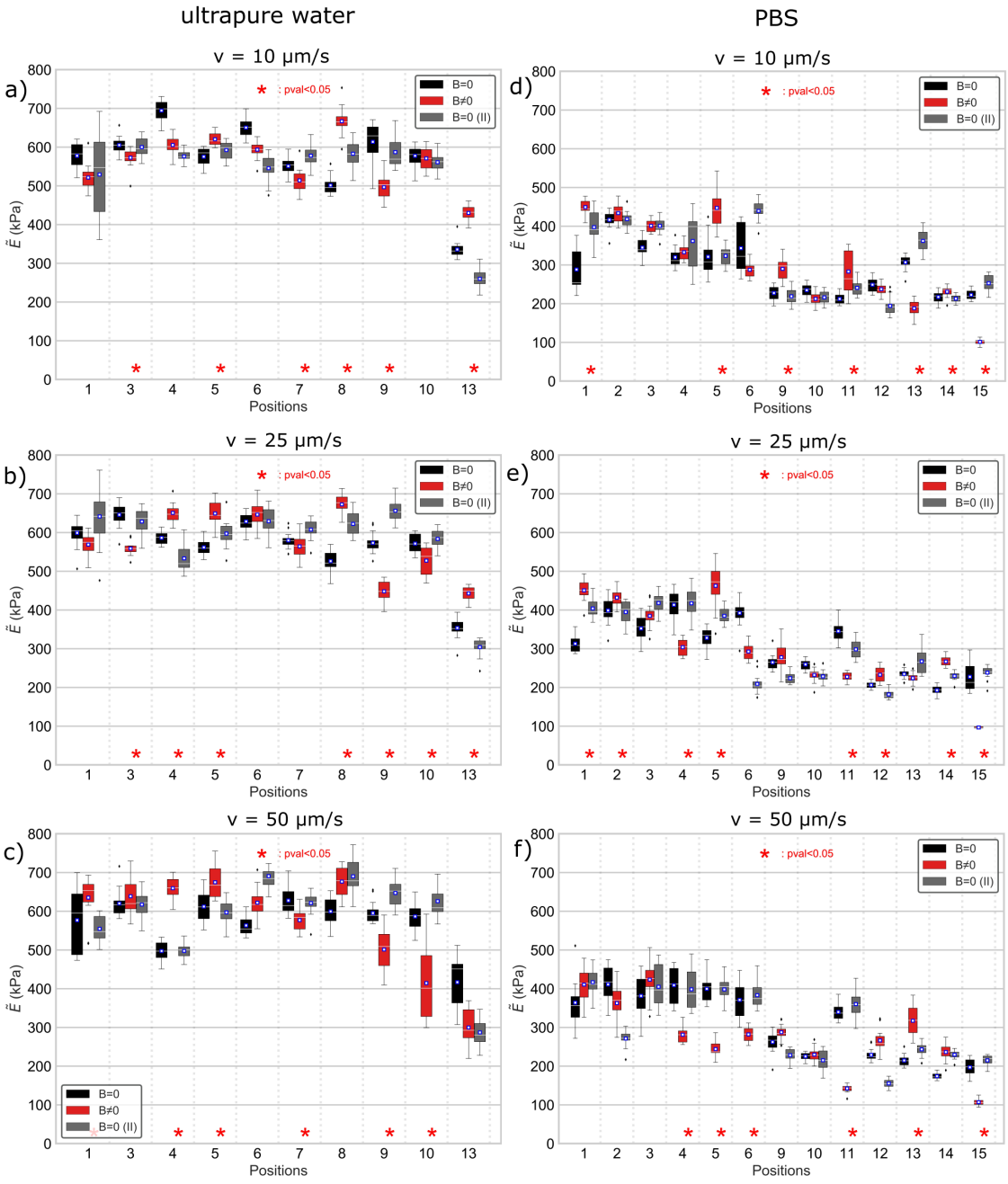


Figure E.2: Distribution of change in reduced Young modulus ($\tilde{E}$) with an external magnetic field (B) for a PDMS elastomer: $\tilde{E}$ calculated in several positions on PDMS elastomer in ultrapure water from indentations at (a) $10\,\mu m\,s^{-1}$, (b) $25\,\mu m\,s^{-1}$, and (c) $50\,\mu m\,s^{-1}$, and in PBS at (d) $10\,\mu m\,s^{-1}$, (e) $25\,\mu m\,s^{-1}$, and (f) $50\,\mu m\,s^{-1}$ cantilever approach velocities.

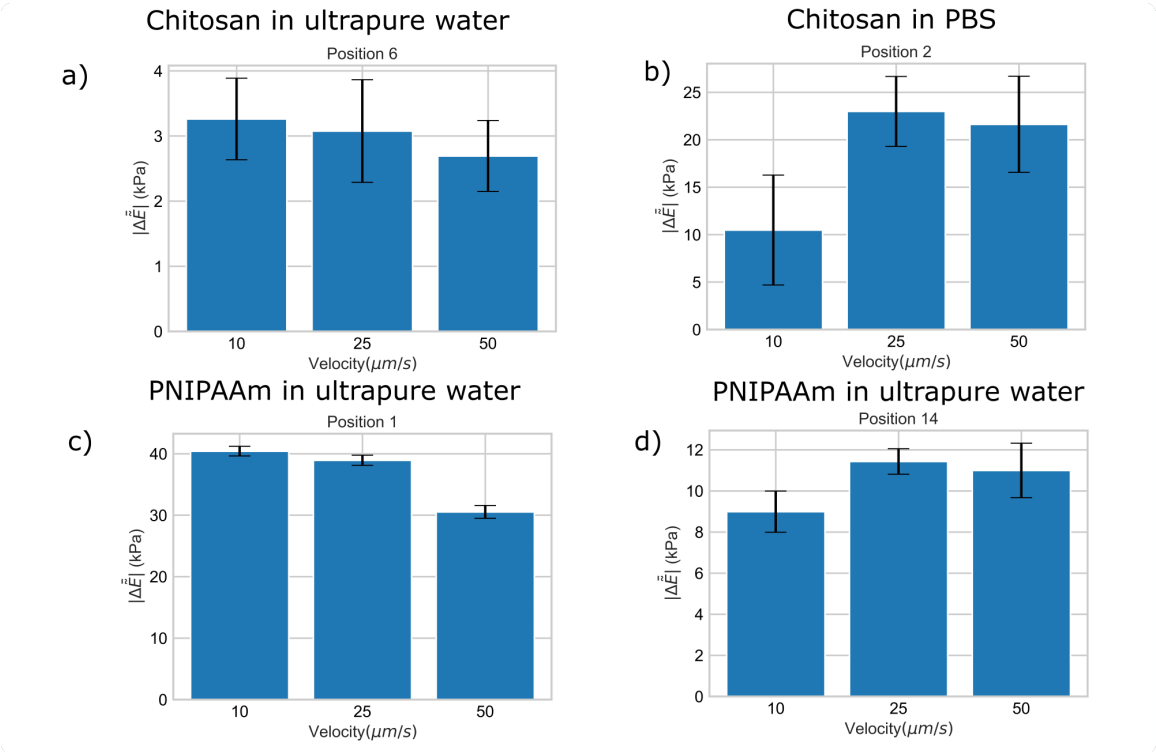


Figure E.3: Changes in $|\Delta\tilde{\tilde{E}}|$ for chitosan and PNIPAAm hydrogels for $10\,\mu m\,s^{-1}$, $25\,\mu m\,s^{-1}$ and $50\,\mu m\,s^{-1}$ cantilever approach velocities. Changes in $|\Delta\tilde{\tilde{E}}|$ are shown for chitosan in (a) ultrapure water, and (b) PBS. Changes in $|\Delta\tilde{\tilde{E}}|$ are shown for PNIPAAm in (a,b) ultrapure water at different positions on the hydrogel. Error bars correspond to the standard deviation.

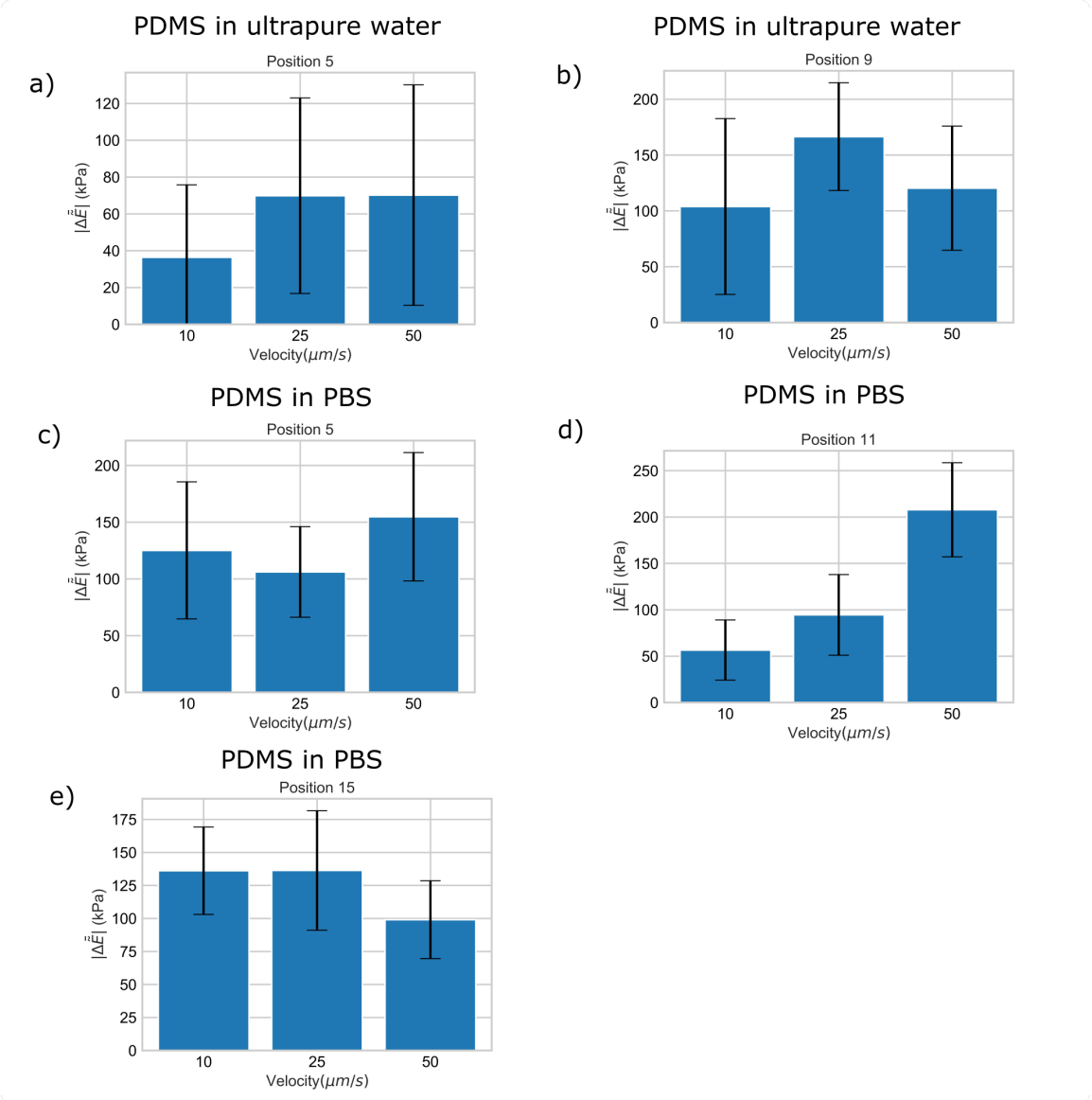


Figure E.4: Changes in $|\Delta\tilde{\bar{E}}|$ for PDMS in (a,b) ultrapure water and (c-e) PBS for $10\,\mu m\,s^{-1}$, $25\,\mu m\,s^{-1}$ and $50\,\mu m\,s^{-1}$ cantilever approach velocities. Error bars correspond to the standard deviation.

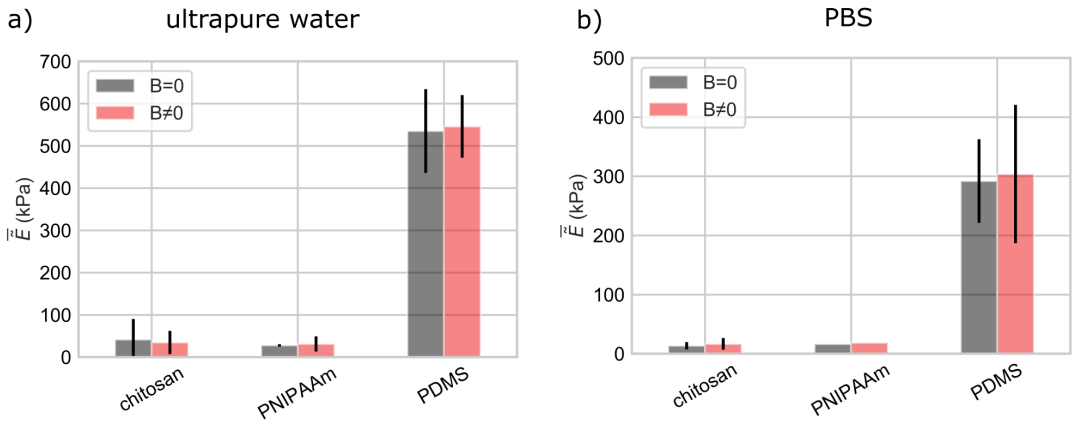


Figure E.5: Average reduced Young's modulus ($\overline{\tilde{E}}$) over all the tested positions that satisfied the conditions in Eq. (4.1) (a,b) calculated independently for chitosan, PNIPAAm, and PDMS samples. $\overline{\tilde{E}}_B$ (black, $B = 0$; red $B \neq 0$) calculated for measurements obtained at $10\,\mu\mathrm{m\,s}^{-1}$ in (a) ultrapure water, and (b) PBS. Error bars correspond to the standard deviation.

Further studies are required to test this hypothesis, which is however beyond the scope of this research.

F Heterogeneity in the effect of an applied magnetic field on chitosan composite hydrogels with Fe_3O_4 nanowires

Several positions on the surface of the chitosan composite hydrogels were tested. Fig. F.1 shows boxplots of $\tilde{E}$ calculated from indentations at different positions on chitosan composite hydrogels in the presence ($B \neq 0$, red) and absence ($B = 0$, black) of B. Results are displayed for composite hydrogels with (a) horizontally aligned and (b) randomly oriented Fe_3O_4 nanowires. The value of $\tilde{E}$ changed significantly when B was applied (i.e. p value of paired t-test between $\tilde{E}_{B=0}$ and $\tilde{E}_{B\neq0}$ smaller than 0.05). Positions where $\tilde{E}$ changed significantly when B are marked in Fig. F.1 with red asterisks. This change did not present a specific trend (i.e. softening or stiffening)

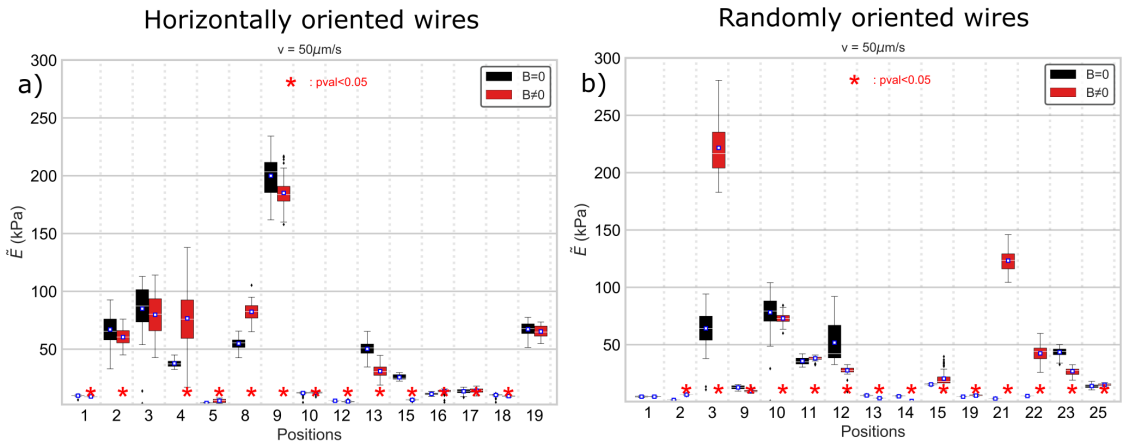


Figure F.1: Distribution of change in the reduced Young modulus ($\tilde{E}$) with external magnetic field (B) at different positions on chitosan composites: $\tilde{E}$ was calculated at several positions from indentations in PBS, on chitosan composites with (a) horizontally, and (b) randomly oriented Fe_3O_4 nanowires. The indentation velocity was $50\,\mu m\,s^{-1}$.

but varied for each position. For example, in the chitosan hydrogel with horizontally oriented wires (Fig. F.1 (a)) the presence of B sometimes caused an increase in $\tilde{E}$ (e.g. positions 4 and 8), and other times a decrease (e.g. positions 13 and 15). The same behaviour was found in the chitosan hydrogel with randomly oriented wires (Fig. F.1 (b)). These results are similar to those of plain chitosan hydrogels (see Chapter 4).

G Error calculation for the dynamic modulus

As discussed in Section 2.2.3, in some cases it is possible to use the flat punch stiffness $\tilde{E}^* = k^*/(2a)$ to describe the contact with viscoelastic adhesive samples [171, 172]. E' and E'' can then be calculated, similarly to Eq. (2.35), as follows:

$$E^j = \frac{1-\nu_S^2}{2a_1} k^j$$

where j indicates the storage ($'$) or the loss ($''$) component. a_1 is the contact radius during the oscillations that can be calculated using the contact models for adhesive

contacts described in Section 2.2.2.2. Uncertainties in E^j can be calculated as (cfr. Eq. (6.7)):

$$\frac{dE^j}{E^j} = \sqrt{\left(\frac{dk}{k^j}\right)^2 + \left(\frac{da_1}{a_1}\right)^2}$$

where the error in k is calculated as explained in section Section 6.5.2. The uncertainty in a_1 (da_1) is given by two contributions. The first factor da^{curve} is the error in the quantities of the curve used to calculate a_1 (i.e. variation in F and d in the "special points" (see Sections 2.2.2.2 and 6.7 and Fig. 6.28)). The second factor is the error in the indenter's geometrical parameters (da^{tip}). It is then possible to write:

$$da = da^{curve} + da^{tip}$$

da_1^{curve} can be calculated as the standard deviation of a_1 calculated over several curves. The uncertainty resulting from variations in the tip geometry (R_I, α) compared to the nominal values given by the manufacturer can be estimated by calculating how much a_1 changes by varying the tip geometry. For the following calculations, I used a typical PT-AFM nano-DMA curve with a chirp frequency range of 1 Hz to 1001 Hz, obtained on the SBR sample with the cantilever in question.

a_1 for an AC160TSA-R3 cantilever was calculated with the JKR model [164] (see Section 2.2.2.2) and plotted for its nominal radius ($R_I = 7\,\text{nm}$), and for larger radii ($R_I = 10\,\text{nm}$ and $14\,\text{nm}$) in Fig. G.1 (a) to study the effect of a blunted tip. a_1 is plotted with the standard deviation obtained averaging several curves (da_1^{curve}).

In the case of a highly blunted tip (radius is doubled compared to the nominal), the error is $da_1^{tip} = |a_1^{R=7nm} - a_1^{R=14nm}|$. This corresponds to $da_1^{tip}/a_1 \approx 40\,\% >> da_1^{curve}/a_1$, thereby resulting in $da_1/a_1 \approx da_1^{tip}/a_1 \approx 40\,\%$.

In Fig. G.1 (b), a_1 was calculated for an AC160TSA-R3 with the hyperboloidal model with adhesion [168] (see Section 2.2.2.2) using the cantilever's nominal radius ($R_I = 7\,\text{nm}$) and semi-vertical angle ($\alpha = 17.5°$, taken as the half of the tip nominal back

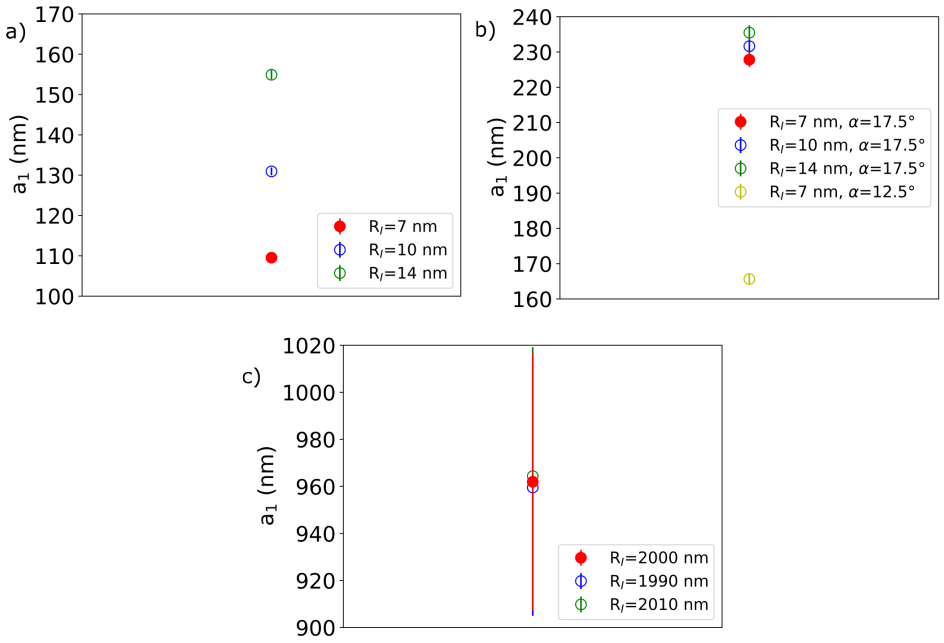


Figure G.1: Contact radius calculated at the special point "1" for different tip dimensions. (a) Contact radius calculated with the JKR model for a spherical indenter of different radii (R_I) (nominal $R_I = 7\,\text{nm}$). (b) Contact radius calculated with the hyperboloidal model with adhesion for different radii and semi-vertical angles (α) (nominal $R_I = 7\,\text{nm}$, $\alpha = 17.5°$). (c) Contact radius calculated with the JKR model for a spherical indenter of different R_I (nominal $R_I = 2\,\mu\text{m}$).

angle). a_1 was also calculated for larger tip radii ($R_I = 10\,\text{nm}$ and $14\,\text{nm}$), and a smaller semi-vertical angle ($\alpha = 12.5°$, taken as the half of the average of the tip nominal back and side angles). The larger contribution is given by the change in the angle and leads to a relative error of $da_1^{tip}/a_1 \approx 30\,\%>> da_1^{curve}/a_1$, resulting in $da_1/a_1 \approx da_1^{tip}/a_1 \approx 30\,\%$.

a_1 for a biosphere$^{\text{TM}}$-NT_B2000_v0010 cantilever was calculated with the JKR model [164] (see Section 2.2.2.2) and plotted for its nominal radius ($R_I = 2\,\mu\text{m}$) in Fig. G.1 (c). In this case, the nominal error of the radius ($\pm\ 10\,\text{nm}$) was used to calculate the variation in a_1 (blue and green unfilled circles). In this case, $da_1^{tip}/a_1 \approx 0.25\,\%<< da_1^{curve}/a_1$, which results in $da_1/a_1 \approx da_1^{curve}/a_1$.

Bibliography

1. Silvestre, C. *et al.* Food packaging based on polymer nanomaterials. *Progress in polymer science* **36,** 1766–1782 (2011).

2. Naskar, A. K. *et al.* Polymer matrix nanocomposites for automotive structural components. *Nature nanotechnology* **11,** 1026–1030 (2016).

3. Fraleoni-Morgera, A. & Chhikara, M. Polymer-based nano-composites for thermal insulation. *Advanced engineering materials* **21,** 1801162 (2019).

4. Wang, G. N. *et al.* Stretchable polymer semiconductors for plastic electronics. *Advanced electronic materials* **4,** 1700429 (2018).

5. Ratner, B. D. *et al. Biomaterials science: an introduction to materials in medicine* (Elsevier, 2004).

6. Seliktar, D. Designing cell-compatible hydrogels for biomedical applications. *Science* **336,** 1124–1128 (2012).

7. Hoffman, A. S. Hydrogels for biomedical applications. *Advanced drug delivery reviews* **64,** 18–23 (2012).

8. Caló, E. & Khutoryanskiy, V. V. Biomedical applications of hydrogels: a review of patents and commercial products. *European polymer journal* **65,** 252–267 (2015).

9. Peppas, N. A. *et al.* Hydrogels in pharmaceutical formulations. *European journal of pharmaceutics and biopharmaceutics* **50,** 27–46 (2000).

10. Cascone, S. & Lamberti, G. Hydrogel-based commercial products for biomedical applications: A review. *International journal of pharmaceutics* **573,** 118803 (2020).

11. Mogoşanu, G. D. & Grumezescu, A. M. Natural and synthetic polymers for wounds and burns dressing. *International journal of pharmaceutics* **463,** 127–136 (2014).

12. Liechty, W. B. *et al.* Polymers for drug delivery systems. *Annual review of chemical and biomolecular engineering* **1,** 149–173 (2010).

13. Jagur-Grodzinski, J. Polymers for tissue engineering, medical devices, and regenerative medicine. Concise general review of recent studies. *Polymers for advanced technologies* **17,** 395–418 (2006).

14. Guo, S. *et al.* Applications of polymer-based nanoparticles in vaccine field. *Nanotechnology reviews* **8,** 143–155 (2019).

15. Bobbala, S. & Hook, S. Vaccine implants: current status and recent advancements. *Emerging topics in life sciences* **4,** 601–612 (2020).

16. Jagur-Grodzinski, J. Biomedical application of functional polymers. *Reactive & functional polymers* **39,** 99–138 (1999).

17. Rehfeldt, F. *et al.* Cell responses to the mechanochemical microenvironment — implications for regenerative medicine and drug delivery. *Advanced drug delivery reviews* **59,** 1329–1339 (2007).

18. Anselmo, A. C. & Mitragotri, S. Impact of particle elasticity on particle-based drug delivery systems. *Advanced drug delivery reviews* **108,** 51–67 (2017).

19. Ferry, J. D. *Viscoelastic properties of polymers* (John Wiley & Sons, 1980).

20. Rubinstein, M. & Colby, R. H. *Polymer physics* (Oxford University Press, 2003).

21. Sperling, L. H. *Introduction to physical polymer science* (John Wiley & Sons, 2005).

22. Doi, M. *Soft matter physics* (Oxford University Press, 2013).

23. Menard, K. P. *Dynamic mechanical analysis: a practical introduction* (CRC Press, Boca Raton, FL, 2008).

24. Tipnis, N. P. & Burgess, D. J. Sterilization of implantable polymer-based medical devices: A review. *International journal of pharmaceutics* **544,** 455–460 (2018).

25. Musgrave, C. S. A. & Fang, F. Contact lens materials: a materials science perspective. *Materials* **12,** 261 (2019).

26. Tokarev, I. & Minko, S. Stimuli-responsive hydrogel thin films. *Soft matter* **5,** 511–524 (2009).

27. Stuart, M. A. C. *et al.* Emerging applications of stimuli-responsive polymer materials. *Nature materials* **9,** 101–113 (2010).

28. Molina, M. *et al.* Stimuli-responsive nanogel composites and their application in nanomedicine. *Chemical society reviews* **44,** 6161–6186 (2015).

29. Thévenot, J. *et al.* Magnetic responsive polymer composite materials. *Chemical society reviews* **42,** 7099–7116 (2013).

30. Wei, M. *et al.* Stimuli-responsive polymers and their applications. *Polymer chemistry* **8,** 127–143 (2017).

31. Mirvakili, S. M. & Hunter, I. W. Artificial muscles: mechanisms, applications, and challenges. *Advanced materials* **30,** 1704407 (2018).

32. Palagi, S. & Fischer, P. Bioinspired microrobots. *Nature reviews materials* **3,** 113 (2018).

33. Toma, M. *et al.* Active control of SPR by thermoresponsive hydrogels for biosensor applications. *The journal of physical chemistry C* **117,** 11705–11712 (2013).

34. Li, X. & Serpe, M. J. Understanding the shape memory behavior of self-bending materials and their use as sensors. *Advanced functional materials* **26,** 3282–3290 (2016).

35. Hoare, T. *et al.* Magnetically triggered nanocomposite membranes: a versatile platform for triggered drug release. *Nano letters* **11,** 1395–1400 (2011).

36. Bawa, P. *et al.* Stimuli-responsive polymers and their applications in drug delivery. *Biomedical materials* **4,** 22001 (2009).

37. Malafaya, P. B. *et al.* Natural–origin polymers as carriers and scaffolds for biomolecules and cell delivery in tissue engineering applications. *Advanced drug delivery reviews* **59,** 207–233 (2007).

38. Van Vlierberghe, S. *et al.* Biopolymer-based hydrogels as scaffolds for tissue engineering applications: a review. *Biomacromolecules* **12,** 1387–1408 (2011).

39. Pina, S. *et al.* Natural-based nanocomposites for bone tissue engineering and regenerative medicine: A review. *Advanced materials* **27,** 1143–1169 (2015).

40. Li, J. & Mooney, D. J. Designing hydrogels for controlled drug delivery. *Nature reviews materials* **1,** 1–17 (2016).

41. Lee, K. Y. & Mooney, D. J. Hydrogels for tissue engineering. *Chemical reviews* **101,** 1869–1880 (2001).

42. Tibbitt, M. W. *et al.* Emerging frontiers in drug delivery. *Journal of the american chemical society* **138,** 704–717 (2016).

43. Schmaljohann, D. Thermo-and pH-responsive polymers in drug delivery. *Advanced drug delivery reviews* **58,** 1655–1670 (2006).

44. Kocak, G. *et al.* pH-Responsive polymers. *Polymer chemistry* **8,** 144–176 (2017).

45. Zhou, M. *et al.* Doxorubicin-loaded single wall nanotube thermo-sensitive hydrogel for gastric cancer chemo-photothermal therapy. *Advanced functional materials* **25,** 4730–4739 (2015).

46. Xu, G. *et al.* Functionalized mesoporous carbon nanoparticles for targeted chemo-photothermal therapy of cancer cells under near-infrared irradiation. *RSC advances* **4,** 33986–33997 (2014).

47. Zhao, Q. *et al.* Mesoporous carbon nanomaterials in drug delivery and biomedical application. *Drug delivery* **24,** 94–107 (2017).

48. Anselmo, A. C. *et al.* Elasticity of nanoparticles influences their blood circulation, phagocytosis, endocytosis, and targeting. *ACS nano* **9,** 3169–3177 (2015).

49. Guo, P. *et al.* Nanoparticle elasticity directs tumor uptake. *Nature communications* **9,** 1–9 (2018).

50. Drury, J. L. & Mooney, D. J. Hydrogels for tissue engineering: scaffold design variables and applications. *Biomaterials* **24,** 4337–4351 (2003).

51. Griffith, L. G. & Swartz, M. A. Capturing complex 3D tissue physiology in vitro. *Nature reviews molecular cell biology* **7,** 211–224 (2006).

52. Frantz, C. *et al.* The extracellular matrix at a glance. *Journal of cell science* **123,** 4195–4200 (2010).

53. Alberts, B. *Molecular biology of the cell* (Garland Science, New York, New York, 2015).

54. Rozario, T. & DeSimone, D. W. The extracellular matrix in development and morphogenesis: a dynamic view. *Developmental biology* **341,** 126–140 (2010).

55. Bonnans, C. *et al.* Remodelling the extracellular matrix in development and disease. *Nature reviews molecular cell biology* **15,** 786–801 (2014).

56. Humphrey, J. D. *et al.* Mechanotransduction and extracellular matrix homeostasis. *Nature reviews molecular cell biology* **15,** 802 (2014).

57. Butcher, D. T. *et al.* A tense situation: forcing tumour progression. *Nature reviews cancer* **9,** 108–122 (2009).

58. Wang, H.-B. *et al.* Substrate flexibility regulates growth and apoptosis of normal but not transformed cells. *American journal of physiology-cell physiology* **279,** C1345–C1350 (2000).

59. Lo, C.-M. *et al.* Cell movement is guided by the rigidity of the substrate. *Biophysical journal* **79,** 144–152 (2000).

60. Charras, G. & Sahai, E. Physical influences of the extracellular environment on cell migration. *Nature reviews molecular cell biology* **15,** 813 (2014).

61. Engler, A. J. *et al.* Matrix elasticity directs stem cell lineage specification. *Cell* **126,** 677–689 (2006).

62. Huebsch, N. *et al.* Harnessing traction-mediated manipulation of the cell/matrix interface to control stem-cell fate. *Nature materials* **9,** 518–526 (2010).

63. Freeman, F. E. & Kelly, D. J. Tuning alginate bioink stiffness and composition for controlled growth factor delivery and to spatially direct MSC fate within bioprinted tissues. *Scientific reports* **7,** 1–12 (2017).

64. Ikada, Y. Challenges in tissue engineering. *Journal of the royal society interface* **3,** 589–601 (2006).

65. Howard, D. *et al.* Tissue engineering: strategies, stem cells and scaffolds. *Journal of anatomy* **213,** 66–72 (2008).

66. Utech, S. & Boccaccini, A. R. A review of hydrogel-based composites for biomedical applications: enhancement of hydrogel properties by addition of rigid inorganic fillers. *Journal of materials science* **51,** 271–310 (2016).

67. Shin, S. R. *et al.* Carbon-nanotube-embedded hydrogel sheets for engineering cardiac constructs and bioactuators. *ACS Nano* **7,** 2369–2380 (2013).

68. Marchesan, S. *et al.* Nanomaterials for stimulating nerve growth. *Science* **356,** 1010 –1011 (2017).

69. Eslahi, N. *et al.* Smart polymeric hydrogels for cartilage tissue engineering: a review on the chemistry and biological functions. *Biomacromolecules* **17,** 3441–3463 (2016).

70. Sapir-Lekhovitser, Y. *et al.* Magnetically actuated tissue engineered scaffold: insights into mechanism of physical stimulation. *Nanoscale* **8,** 3386–3399 (2016).

71. Santos, L. J. *et al.* Harnessing magnetic-mechano actuation in regenerative medicine and tissue engineering. *Trends in biotechnology* **33,** 471–479 (2015).

72. Meng, J. *et al.* Super-paramagnetic responsive nanofibrous scaffolds under static magnetic field enhance osteogenesis for bone repair in vivo. *Scientific reports* **3,** 1–7 (2013).

73. Matos, A. M. *et al.* Remote triggering of TGF-β/Smad2/3 signaling in human adipose stem cells laden on magnetic scaffolds synergistically promotes tenogenic commitment. *Acta biomaterialia* **113,** 488–500 (2020).

74. Kumar, C. S. S. R. & Mohammad, F. Magnetic nanomaterials for hyperthermia-based therapy and controlled drug delivery. *Advanced drug delivery reviews* **63,** 789–808 (2011).

75. Sun, C. *et al.* Magnetic nanoparticles in MR imaging and drug delivery. *Advanced drug delivery reviews* **60,** 1252–1265 (2008).

76. Arruebo, M. *et al.* Magnetic nanoparticles for drug delivery. *Nano today* **2,** 22–32 (2007).

77. Li, Y. *et al.* Magnetic hydrogels and their potential biomedical applications. *Advanced functional materials* **23,** 660–672 (2013).

78. Shi, W. *et al.* Imparting functionality to the hydrogel by magnetic-field-induced nano-assembly and macro-response. *ACS applied materials & interfaces* **12,** 5177–5194 (2020).

79. Reddy, L. H. *et al.* Magnetic nanoparticles: design and characterization, toxicity and biocompatibility, pharmaceutical and biomedical applications. *Chemical reviews* **112,** 5818–5878 (2012).

80. Wen, J. H. *et al.* Interplay of matrix stiffness and protein tethering in stem cell differentiation. *Nature materials* **13,** 979–987 (2014).

81. Darnell, M. *et al.* RNA-seq reveals diverse effects of substrate stiffness on mesenchymal stem cells. *Biomaterials* **181,** 182–188 (2018).

82. Chaudhuri, O. Viscoelastic hydrogels for 3D cell culture. *Biomaterials science* **5,** 1480–1490 (2017).

83. Huang, D. *et al.* Viscoelasticity in natural tissues and engineered scaffolds for tissue reconstruction. *Acta biomaterialia* **97,** 74–92 (2019).

84. Chaudhuri, O. *et al.* Effects of extracellular matrix viscoelasticity on cellular behaviour. *Nature* **584,** 535–546 (2020).

85. Secrier, M. & Schneider, R. Visualizing time-related data in biology, a review. *Briefings in bioinformatics* **15,** 771–782 (2014).

86. Shamir, M. *et al.* SnapShot: timescales in cell biology. *Cell* **164,** 1302 (2016).

87. Lee, R. M. & Losert, W. *Dynamics phenotyping across length and time scales in collective cell migration* in *Seminars in cell & developmental biology* **93** (Elsevier, 2019), 69–76.

88. Parsons, J. T. *et al.* Cell adhesion: integrating cytoskeletal dynamics and cellular tension. *Nature reviews Molecular cell biology* **11,** 633–643 (2010).

89. Jünger, F. & Rohrbach, A. Strong cytoskeleton activity on millisecond timescales upon particle binding revealed by ROCS microscopy. *Cytoskeleton* **75,** 410–424 (2018).

90. Hoffman, B. D. *et al.* Dynamic molecular processes mediate cellular mechanotransduction. *Nature* **475,** 316–323 (2011).

91. Block, M. R. *et al.* Podosome-type adhesions and focal adhesions, so alike yet so different. *European journal of cell biology* **87,** 491–506 (2008).

92. Labernadie, A. *et al.* Protrusion force microscopy reveals oscillatory force generation and mechanosensing activity of human macrophage podosomes. *Nature communications* **5,** 1–10 (2014).

93. Chaudhuri, O. *et al.* Hydrogels with tunable stress relaxation regulate stem cell fate and activity. *Nature materials* **15,** 326–334 (2016).

94. Lee, K. Y. & Mooney, D. J. Alginate: properties and biomedical applications. *Progress in polymer science* **37,** 106–126 (2012).

95. Cameron, A. R. *et al.* The influence of substrate creep on mesenchymal stem cell behaviour and phenotype. *Biomaterials* **32,** 5979–5993 (2011).

96. Chaudhuri, O. *et al.* Substrate stress relaxation regulates cell spreading. *Nature communications* **6,** 1–7 (2015).

97. Lou, J. *et al.* Stress relaxing hyaluronic acid-collagen hydrogels promote cell spreading, fiber remodeling, and focal adhesion formation in 3D cell culture. *Biomaterials* **154,** 213–222 (2018).

98. Charrier, E. E. *et al.* Control of cell morphology and differentiation by substrates with independently tunable elasticity and viscous dissipation. *Nature communications* **9,** 449 (2018).

99. Beroz, F. *et al.* Physical limits to biomechanical sensing in disordered fibre networks. *Nature communications* **8,** 16096 (2017).

100. Oyen, M. L. Mechanical characterisation of hydrogel materials. *International materials reviews* **59,** 44–59 (2014).

101. Roylance, D. Engineering viscoelasticity. *Department of materials science and engineering–Massachusetts institute of technology, Cambridge, MA 02139,* 1–37 (2001).

102. Waigh, T. A. Microrheology of complex fluids. *Reports on progress in physics* **68,** 685 (2005).

103. Liu, W. & Wu, C. Rheological study of soft matters: a review of microrheology and microrheometers. *Macromolecular chemistry and physics* **219,** 1700307 (2018).

104. Efremov, Y. M. *et al.* Measuring viscoelasticity of soft biological samples using atomic force microscopy. *Soft matter* **16,** 64–81 (2020).

105. Butt, H.-J. *et al.* Force measurements with the atomic force microscope: technique, interpretation and applications. *Surface science reports* **59,** 1–152 (2005).

106. Yuya, P. A. *et al.* Contact-resonance atomic force microscopy for viscoelasticity. *Journal of applied physics* **104,** 74916 (2008).

107. Yuya, P. A. *et al.* Relationship between Q-factor and sample damping for contact resonance atomic force microscope measurement of viscoelastic properties. *Journal of applied physics* **109,** 113528 (2011).

108. Gannepalli, A. *et al.* Mapping nanoscale elasticity and dissipation using dual frequency contact resonance AFM. *Nanotechnology* **22,** 355705 (2011).

109. Killgore, J. P. *et al.* Viscoelastic property mapping with contact resonance force microscopy. *Langmuir* **27,** 13983–13987 (2011).

110. Yablon, D. G. *et al.* Quantitative viscoelastic mapping of polyolefin blends with contact resonance atomic force microscopy. *Macromolecules* **45,** 4363–4370 (2012).

111. García, R. *Amplitude modulation atomic force microscopy* (John Wiley & Sons, 2011).

112. Garcia, R. & Herruzo, E. T. The emergence of multifrequency force microscopy. *Nature nanotechnology* **7,** 217–226 (2012).

113. Garcia, R. & Proksch, R. Nanomechanical mapping of soft matter by bimodal force microscopy. *European polymer journal* **49,** 1897–1906 (2013).

114. Labuda, A. *et al.* Generalized Hertz model for bimodal nanomechanical mapping. *Beilstein journal of nanotechnology* **7,** 970–982 (2016).

115. Kocun, M. *et al.* Fast, high resolution, and wide modulus range nanomechanical mapping with bimodal tapping mode. *ACS nano* **11,** 10097–10105 (2017).

116. Al-Rekabi, Z. & Contera, S. Multifrequency AFM reveals lipid membrane mechanical properties and the effect of cholesterol in modulating viscoelasticity. *Proceedings of the national academy of sciences* **115,** 2658–2663 (2018).

117. Kolluru, P. V. *et al.* AFM-based dynamic scanning indentation (DSI) method for fast, high-resolution spatial mapping of local viscoelastic properties in soft materials. *Macromolecules* **51,** 8964–8978 (2018).

118. Pittenger, B. *et al.* Nanoscale DMA with the atomic force microscope: A new method for measuring viscoelastic properties of nanostructured polymer materials. *JOM* **71,** 3390–3398 (2019).

119. Mahaffy, R. E. *et al.* Scanning probe-based frequency-dependent microrheology of polymer gels and biological cells. *Physical review letters* **85,** 880 (2000).

120. Alcaraz, J. *et al.* Microrheology of human lung epithelial cells measured by atomic force microscopy. *Biophysical journal* **84,** 2071–2079 (2003).

121. Mahaffy, R. E. *et al.* Quantitative analysis of the viscoelastic properties of thin regions of fibroblasts using atomic force microscopy. *Biophysical journal* **86,** 1777–1793 (2004).

122. Rigato, A. *et al.* High-frequency microrheology reveals cytoskeleton dynamics in living cells. *Nature physics* **13,** 771–775 (2017).

123. Schächtele, M. *et al.* Resonance compensating chirp mode for mapping the rheology of live cells by high-speed atomic force microscopy. *Applied physics letters* **113** (2018).

124. Lherbette, M. *et al.* Atomic force microscopy micro-rheology reveals large structural inhomogeneities in single cell-nuclei. *Scientific reports* **7,** 8116 (2017).

125. Nia, H. T. *et al.* Poroelasticity of cartilage at the nanoscale. *Biophysical journal* **101,** 2304–2313 (2011).

126. Nia, H. T. *et al.* High-bandwidth AFM-based rheology reveals that cartilage is most sensitive to high loading rates at early stages of impairment. *Biophysical journal* **104,** 1529–1537 (2013).

127. Nia, H. T. *et al.* High-bandwidth AFM-based rheology is a sensitive indicator of early cartilage aggrecan degradation relevant to mouse models of osteoarthritis. *Journal of biomechanics* **48,** 162–165 (2015).

128. Nia, H. T. *et al.* Aggrecan nanoscale solid–fluid interactions are a primary determinant of cartilage dynamic mechanical properties. *ACS nano* **9,** 2614–2625 (2015).

129. Azadi, M. *et al.* Wide bandwidth nanomechanical assessment of murine cartilage reveals protection of aggrecan knock-in mice from joint-overuse. *Journal of biomechanics* **49,** 1634–1640 (2016).

130. Nalam, P. C. *et al.* Nano-rheology of hydrogels using direct drive force modulation atomic force microscopy. *Soft matter* **11,** 8165–8178 (2015).

131. Igarashi, T. *et al.* Nanorheological mapping of rubbers by atomic force microscopy. *Macromolecules* **46,** 1916–1922 (2013).

132. Nguyen, H. K. *et al.* Viscoelasticity of inhomogeneous polymers characterized by loss tangent measurements using atomic force microscopy. *Macromolecules* **47,** 7971–7977 (2014).

133. Arai, M. *et al.* Viscoelastic maps obtained by nanorheological atomic force microscopy with two different driving systems. *Japanese journal of applied physics* **57,** 08NB08 (2018).

134. Ueda, E. *et al.* Dynamic moduli mapping of silica-filled styrene–butadiene rubber vulcanizate by nanorheological atomic force microscopy. *Macromolecules* **52,** 311–319 (2019).

135. Schäffer, T. E. *et al.* Studies of vibrating atomic force microscope cantilevers in liquid. *Journal of applied physics* **80,** 3622–3627 (1996).

136. Rabe, U. *et al.* Influence of the cantilever holder on the vibrations of AFM cantilevers. *Nanotechnology* **18,** 44008 (2006).

137. Labuda, A. *et al.* Photothermal excitation for improved cantilever drive performance in tapping mode atomic force microscopy. *Microscopy and analysis* **28,** 21–25 (2014).

138. Rebêlo, L. M. *et al.* Microrheology of cells with magnetic force modulation atomic force microscopy. *Soft matter* **10,** 2141–2149 (2014).

139. Jayakumar, R. *et al.* Biomedical applications of chitin and chitosan based nanomaterials—A short review. *Carbohydrate polymers* **82,** 227–232 (2010).

140. Anitha, A. *et al.* Chitin and chitosan in selected biomedical applications. *Progress in polymer science* **39,** 1644–1667 (2014).

141. Fowler, P. W. & Manolopoulos, D. E. *An atlas of fullerenes* (Clarendon Press, Oxford, 1995).

142. Binnig, G. *et al.* Atomic force microscope. *Physical review letters* **56,** 930 (1986).

143. Haugstad, G. *Atomic force microscopy: understanding basic modes and advanced applications* (John Wiley & Sons, 2012).

144. Garcıa, R. & Perez, R. Dynamic atomic force microscopy methods. *Surface science reports* **47,** 197–301 (2002).

145. Lindsay, S. M. *et al.* Scanning tunneling microscopy and atomic force microscopy studies of biomaterials at a liquid–solid interface. *Journal of vacuum science & technology A* **11,** 808–815 (1993).

146. Florin, E. *et al.* Atomic force microscope with magnetic force modulation. *Review of scientific instruments* **65,** 639–643 (1994).

147. Cleveland, J. P. PhD thesis (University of California, Santa Barbara, 1995).

148. Han, W. *et al.* A magnetically driven oscillating probe microscope for operation in liquids. *Applied physics letters* **69,** 4111–4113 (1996).

149. Umeda, N. *et al.* Scanning attractive force microscope using photothermal vibration. *Journal of vacuum science & technology B: microelectronics and nanometer structures* **9,** 1318–1322 (1991).

150. Marti, O. *et al.* Mechanical and thermal effects of laser irradiation on force microscope cantilevers. *Ultramicroscopy* **42-44,** 345–350 (1992).

151. Ratcliff, G. C. *et al.* Photothermal modulation for oscillating mode atomic force microscopy in solution. *Applied physics letters* **72,** 1911–1913 (1998).

152. Ramos, D. *et al.* Photothermal excitation of microcantilevers in liquids. *Journal of applied physics* **99,** 124904 (2006).

153. Nishida, S. *et al.* Photothermal excitation of a single-crystalline silicon cantilever for higher vibration modes in liquid. *Journal of vacuum science & technology B: microelectronics and nanometer structures processing, measurement, and phenomena* **27,** 964–968 (2009).

154. Kiracofe, D. *et al.* High efficiency laser photothermal excitation of microcantilever vibrations in air and liquids. *Review of scientific instruments* **82,** 13702 (2011).

155. Penedo, M. *et al.* Enhanced efficiency in the excitation of higher modes for atomic force microscopy and mechanical sensors operated in liquids. *Applied physics letters* **105,** 173102 (2014).

156. Kocun, M. *et al.* Contact resonance atomic force microscopy imaging in air and water using photothermal excitation. *Review of scientific instruments* **86,** 83706 (2015).

157. Wagner, R. & Killgore, J. P. Photothermally excited force modulation microscopy for broadband nanomechanical property measurements. *Applied physics letters* **107,** 203111 (2015).

158. Nievergelt, A. P. *et al.* Photothermal off-resonance tapping for rapid and gentle atomic force imaging of live cells. *International journal of molecular sciences* **19** (2018).

159. Hertz, H. Ueber die Berührung fester elastischer Körper. *Journal für die reine und angewandte Mathematik* **92,** 156–171 (1882).

160. Landau, L. D. & Lifshitz, E. M. *Course of Theoretical Physics Vol 7: Theory and Elasticity* (Pergamon Press, 1959).

161. Sneddon, I. N. The relation between load and penetration in the axisymmetric Boussinesq problem for a punch of arbitrary profile. *International journal of engineering science* **3,** 47–57 (1965).

162. Oliver, W. C. & Pharr, G. M. An improved technique for determining hardness and elastic modulus using load and displacement sensing indentation experiments. *Journal of materials research* **7,** 1564–1583 (1992).

163. Derjaguin, B. V. *et al.* Effect of contact deformations on the adhesion of particles. *Journal of colloid and interface science* **53,** 314–326 (1975).

164. Johnson, K. L. *et al.* Surface energy and the contact of elastic solids. *Proceedings of the royal society of London. Series A, mathematical and physical sciences* **324,** 301–313 (1971).

165. Tabor, D. Surface Forces and Surface Interactions. *Journal of colloid and interface science* **58,** 2–13 (1977).

166. Muller, V. M. *et al.* On the influence of molecular forces on the deformation of an elastic sphere and its sticking to a rigid plane. *Journal of colloid and interface science* **77,** 91–101 (1980).

167. Maugis, D. Adhesion of spheres: The JKR-DMT transition using a dugdale model. *Journal of colloid and interface science* **150,** 243–269 (1992).

168. Sun, Y. *et al.* Using the adhesive interaction between atomic force microscopy tips and polymer surfaces to measure the elastic modulus of compliant samples. *Langmuir* **20,** 5837–5845 (2004).

169. Popov, V. L. *et al. Handbook of contact mechanics* (Springer, 2019).

170. Maugis, D. & Barquins, M. Adhesive contact of a conical punch on an elastic half-space. *Journal de physique lettres* **42,** 95–97 (1981).

171. Wahl, K. J. *et al.* Oscillating adhesive contacts between micron-scale tips and compliant polymers. *Journal of colloid and interface science* **296,** 178–188 (2006).

172. Greenwood, J. A. & Johnson, K. L. Oscillatory loading of a viscoelastic adhesive contact. *Journal of colloid and interface science* **296,** 284–291 (2006).

173. Han, B. *et al.* AFM-Nanomechanical test: an interdisciplinary tool that links the understanding of cartilage and meniscus biomechanics, osteoarthritis degeneration, and tissue engineering. *ACS biomaterials science & engineering* **3,** 2033–2049 (2017).

174. Klauder, J. R. *et al.* The theory and design of chirp radars. *Bell system technical journal* **39,** 745–808 (1960).

175. Cook, C. E. & Paolillo, J. A pulse compression predistortion function for efficient sidelobe reduction in a high-power radar. *Proceedings of the IEEE* **52,** 377–389 (1964).

176. Paavle, T. *et al. Short-time chirp excitations for using in wideband characterization of objects: an overview* in *2010 12th biennial baltic electronics conference* (IEEE, 2010), 253–256.

177. Egerton, R. F. *Physical principles of electron microscopy* (Springer, 2005).

178. Goldstein, J. I. *et al. Scanning electron microscopy and X-ray microanalysis* (Springer, 2017).

179. Foner, S. Versatile and sensitive vibrating-sample magnetometer. *Review of scientific instruments* **30,** 548–557 (1959).

180. Zieba, A. & Foner, S. Detection coil, sensitivity function, and sample geometry effects for vibrating sample magnetometers. *Review of scientific instruments* **53,** 1344–1354 (1982).

181. `https://www.python.org/`.

182. `https://docs.python.org/3/library/csv.html`.

183. `https://github.com/jcbs/ForceMetric`.

184. `https://docs.python.org/3/library/glob.html`.

185. `https://docs.python.org/3/library/io.html`.

186. `https://matplotlib.org/stable/index.html`.

187. `https://numpy.org/`.

188. `https://docs.python.org/3/library/os.html`.

189. `https://pandas.pydata.org/`.

190. `https://python-pillow.org/`.

191. `https://numpy.org/`.

192. `https://seaborn.pydata.org/`.

193. `https://github.com/cfobel/si-prefix`.

194. `https://www.sympy.org/en/index.html`.

195. Dimida, S. *et al.* Effects of genipin concentration on cross-linked chitosan scaffolds for bone tissue engineering: structural characterization and evidence of biocompatibility features. *International journal of polymer science* **2017** (2017).

196. Bonilla Brunner, I. A. *Remotely actuated polymeric nanocomposites for biomedical applications* PhD thesis (University of Oxford, 2018).

197. Bonilla Brunner, I. A. *et al.* Polymeric microellipsoids with programmed magnetic anisotropy for controlled rotation using low (≈10 mT) magnetic fields. *Applied materials today* **18,** 100511 (2020).

198. Petrov, P. *et al.* UV-assisted synthesis of super-macroporous polymer hydrogels. *Polymer* **50,** 1118–1123 (2009).

199. Al-Rekabi, Z. *et al.* Activation of the IGF1 pathway mediates changes in cellular contractility and motility in single-suture craniosynostosis. *Journal of cell science* **129,** 483–491 (2016).

200. Rašović, I. *Water-Soluble Fullerenes & Molecular Machines: Supramolecular Approaches to Nanomedicine* PhD thesis (University of Oxford, 2019).

201. Folkman, J. & Moscona, A. Role of cell shape in growth control. *Nature* **273,** 345 (1978).

202. Hutter, J. L. & Bechhoefer, J. Calibration of atomic-force microscope tips. *Review of scientific instruments* **64,** 1868–1873 (1993).

203. Seifert, J. *In vivo dynamic AFM mapping of viscoelastic properties of the primary plant cell wall* PhD thesis (University of Oxford, 2018).

204. Chui, C.-Y. *et al.* Atomic force microscopy-indentation demonstrates that alginate beads are mechanically stable under cell culture conditions. *Journal of the mechanical behavior of biomedical materials* **93,** 61–69 (2019).

205. Jokinen, V. *et al.* Oxygen and nitrogen plasma hydrophilization and hydrophobic recovery of polymers. *Biomicrofluidics* **6,** 16501 (2012).

206. Wang, C. X. *et al.* High-speed compression of single alginate microspheres. *Chemical engineering science* **60,** 6649–6657 (2005).

207. Shamos, M. H. & Lavine, L. S. Piezoelectricity as a fundamental property of biological tissues. *Nature* **213,** 267–269 (1967).

208. Athenstaedt, H. Pyroelectric and piezoelectric properties of vertebrates. *Annals of the New York academy of sciences* **238,** 68–94 (1974).

209. Fukada, E. History and recent progress in piezoelectric polymers. *IEEE Transactions on ultrasonics, ferroelectrics, and frequency control* **47,** 1277–1290 (2000).

210. Ribeiro, C. *et al.* Piezoelectric polymers as biomaterials for tissue engineering applications. *Colloids and surfaces B: biointerfaces* **136,** 46–55 (2015).

211. Chen-Glasser, M. *et al.* Piezoelectric materials for medical applications. *Piezoelectricity-organic and inorganic materials and applications,* 125–145 (2018).

212. Rinaudo, M. Chitin and chitosan: properties and applications. *Progress in polymer science* **31,** 603–632 (2006).

213. Ravi Kumar, M. N. V. A review of chitin and chitosan applications. *Reactive and functional polymers* **46,** 1–27 (2000).

214. Croisier, F. & Jérôme, C. Chitosan-based biomaterials for tissue engineering. *European polymer journal* **49,** 780–792 (2013).

215. Aranaz, I. *et al.* Cosmetics and cosmeceutical applications of chitin, chitosan and their derivatives. *Polymers* **10,** 213 (2018).

216. Desbrières, J. & Guibal, E. Chitosan for wastewater treatment. *Polymer international* **67,** 7–14 (2018).

217. Dai, T. *et al.* Chitosan preparations for wounds and burns: antimicrobial and wound-healing effects. *Expert review of anti-infective therapy* **9,** 857–879 (2011).

218. Bhattarai, N. *et al.* Chitosan-based hydrogels for controlled, localized drug delivery. *Advanced drug delivery reviews* **62,** 83–99 (2010).

219. Silva, C. C. *et al.* On the piezoelectricity of collagen–chitosan films. *Physical chemistry chemical physics* **3,** 4154–4157 (2001).

220. Hänninen, A. *et al.* Piezoelectric sensitivity of a layered film of chitosan and cellulose nanocrystals. *Procedia engineering* **168,** 1176–1179 (2016).

221. Praveen, E. *et al.* Investigations on the existence of piezoelectric property of a bio-polymer–chitosan and its application in vibration sensors. *RSC advances* **7,** 35490–35495 (2017).

222. Grahl, T. & Märkl, H. Killing of microorganisms by pulsed electric fields. *Applied microbiology and biotechnology* **45,** 148–157 (1996).

223. Erb, R. M. *et al.* Actuating soft matter with magnetic torque. *Advanced functional materials* **26,** 3859–3880 (2016).

224. Berger, J. *et al.* Structure and interactions in covalently and ionically crosslinked chitosan hydrogels for biomedical applications. *European journal of pharmaceutics and biopharmaceutics* **57,** 19–34 (2004).

225. Muzzarelli, R. A. A. Genipin-crosslinked chitosan hydrogels as biomedical and pharmaceutical aids. *Carbohydrate polymers* **77,** 1–9 (2009).

226. Makhlouf, A. S. H. & Aliofkhazraei, M. *Handbook of materials failure analysis with case studies from the oil and gas industry* (Butterworth-Heinemann, 2015).

227. Baskar, D. *et al.* Mineralization of pristine chitosan film through biomimetic process. *International journal of biological macromolecules* **49,** 385–389 (2011).

228. Lanzalaco, S. & Armelin, E. Poly (n-isopropylacrylamide) and copolymers: a review on recent progresses in biomedical applications. *Gels* **3,** 36 (2017).

229. Wang, J.-J. *et al.* Piezoelectric polydimethylsiloxane films for MEMS transducers. *Journal of micromechanics and microengineering* **22,** 15013 (2011).

230. Zhang, Y. *et al.* Ferroelectret materials and devices for energy harvesting applications. *Nano energy* **57,** 118–140 (2019).

231. Levental, I. *et al.* Soft biological materials and their impact on cell function. *Soft matter* **3,** 299–306 (2007).

232. Subramanian, A. & Lin, H. Crosslinked chitosan: its physical properties and the effects of matrix stiffness on chondrocyte cell morphology and proliferation. *Journal of biomedical materials research part A* **75,** 742–753 (2005).

233. Landau, L. D. *et al. Electrodynamics of continuous media* (Pergamon, Oxford, 1984).

234. Galembeck, A. *et al.* Scanning electric potential microscopy imaging of polymers: electrical charge distribution in dielectrics. *Polymer* **42,** 4845–4851 (2001).

235. Hedayatnasab, Z. *et al.* Review on magnetic nanoparticles for magnetic nanofluid hyperthermia application. *Materials & design* **123,** 174–196 (2017).

236. Cardoso, V. F. *et al.* Advances in magnetic nanoparticles for biomedical applications. *Advanced healthcare materials* **7,** 1700845 (2018).

237. Li, X. *et al.* Current investigations into magnetic nanoparticles for biomedical applications. *Journal of biomedical materials Research Part A* **104,** 1285–1296 (2016).

238. Colombo, M. *et al.* Biological applications of magnetic nanoparticles. *Chemical society reviews* **41,** 4306–4334 (2012).

239. Pankhurst, Q. A. *et al.* Progress in applications of magnetic nanoparticles in biomedicine. *Journal of physics D: applied physics* **42,** 224001 (2009).

240. Haun, J. B. *et al.* Magnetic nanoparticle biosensors. *WIREs nanomedicine and nanobiotechnology* **2,** 291–304 (2010).

241. Lin, W.-S. *et al.* Shape effects of iron nanowires on hyperthermia treatment. *Journal of nanomaterials* **2013** (2013).

242. Yassine, O. *et al.* Highly efficient thermoresponsive nanocomposite for controlled release applications. *Scientific reports* **6,** 28539 (2016).

243. Hultgren, A. *et al.* Cell manipulation using magnetic nanowires. *Journal of applied physics* **93,** 7554–7556 (2003).

244. Contreras, M. F. *et al.* Non-chemotoxic induction of cancer cell death using magnetic nanowires. *International journal of nanomedicine* **10,** 2141–2153 (2015).

245. Fung, A. O. *et al.* Induction of cell death by magnetic actuation of nickel nanowires internalized by fibroblasts. *The journal of physical chemistry C* **112,** 15085–15088 (2008).

246. Bidan, C. M. *et al.* Magneto-active substrates for local mechanical stimulation of living cells. *Scientific reports* **8,** 1–13 (2018).

247. Laurent, S. *et al.* Magnetic fluid hyperthermia: Focus on superparamagnetic iron oxide nanoparticles. *Advances in colloid and interface science* **166,** 8–23 (2011).

248. Estelrich, J. *et al.* Iron oxide nanoparticles for magnetically-guided and magnetically-responsive drug delivery. *International journal of molecular sciences* **16,** 8070–8101 (2015).

249. Lee, N. *et al.* Iron oxide based nanoparticles for multimodal imaging and magnetoresponsive therapy. *Chemical reviews* **115,** 10637–10689 (2015).

250. Liu, G. *et al.* Applications and potential toxicity of magnetic iron oxide nanoparticles. *Small* **9,** 1533–1545 (2013).

251. Kumari, S. & Singh, R. P. Glycolic acid-g-chitosan–Pt–Fe3O4 nanoparticles nanohybrid scaffold for tissue engineering and drug delivery. *International journal of biological macromolecules* **51,** 76–82 (2012).

252. Heidari, F. *et al.* In situ preparation of iron oxide nanoparticles in natural hydroxyapatite/chitosan matrix for bone tissue engineering application. *Ceramics international* **41,** 3094–3100 (2015).

253. Zhang, L. & Zhang, Y. Fabrication and magnetic properties of Fe3O4 nanowire arrays in different diameters. *Journal of magnetism and magnetic materials* **321,** L15–L20 (2009).

254. Han, R. *et al.* 1D magnetic materials of Fe3O4 and Fe with high performance of microwave absorption fabricated by electrospinning method. *Scientific reports* **4,** 7493 (2014).

255. Facchi, D. P. *et al.* New magnetic chitosan/alginate/Fe3O4@ SiO2 hydrogel composites applied for removal of Pb (II) ions from aqueous systems. *Chemical engineering journal* **337,** 595–608 (2018).

256. Cha, J. M. *et al.* Time-dependent modulation of alignment and differentiation of smooth muscle cells seeded on a porous substrate undergoing cyclic mechanical strain. *Artificial organs* **30,** 250–258 (2006).

257. Eivazzadeh-Keihan, R. *et al.* Carbon based nanomaterials for tissue engineering of bone: Building new bone on small black scaffolds: A review. *Journal of advanced research* **18,** 185–201 (2019).

258. Wang, H. *et al.* Carbon-based hybrid nanogels: a synergistic nanoplatform for combined biosensing, bioimaging, and responsive drug delivery. *Chemical society reviews* **47,** 4198–4232 (2018).

259. Al-Jumaili, A. *et al.* Review on the antimicrobial properties of carbon nanostructures. *Materials* **10,** 1066 (2017).

260. Liu, W. & Speranza, G. Functionalization of carbon nanomaterials for biomedical applications. *C—Journal of carbon research* **5,** 72 (2019).

261. Bardhan, N. M. 30 years of advances in functionalization of carbon nanomaterials for biomedical applications: a practical review. *Journal of materials research* **32,** 107–127 (2017).

262. Mendes, R. G. *et al.* Carbon nanostructures as multi-functional drug delivery platforms. *Journal of materials chemistry B* **1,** 401–428 (2013).

263. Dong, R. *et al.* Supramolecular hydrogels: synthesis, properties and their biomedical applications. *Biomaterials science* **3,** 937–954 (2015).

264. Iglesias, D. *et al.* Oxidized nanocarbons-tripeptide supramolecular hydrogels: shape matters! *ACS Nano* **12,** 5530–5538 (2018).

265. Popov, A. A. *et al.* Endohedral fullerenes. *Chemical reviews* **113,** 5989–6113 (2013).

266. Montellano, A. *et al.* Fullerene C60 as a multifunctional system for drug and gene delivery. *Nanoscale* **3,** 4035–4041 (2011).

267. Partha, R. & Conyers, J. L. Biomedical applications of functionalized fullerene-based nanomaterials. *International journal of nanomedicine* **4,** 261 (2009).

268. Rašović, I. Water-soluble fullerenes for medical applications. *Materials science and technology* **33,** 777–794 (2017).

269. Castro, E. *et al.* Fullerenes in biology and medicine. *Journal of materials chemistry B* **5,** 6523–6535 (2017).

270. Goodarzi, S. *et al.* Fullerene: biomedical engineers get to revisit an old friend. *Materials today* **20,** 460–480 (2017).

271. Diederich, F. & Whetten, R. L. Beyond C60: the higher fullerenes. *Accounts of chemical research* **25,** 119–126 (1992).

272. Haino, T. *et al.* Supramolecular nano networks formed by molecular-recognition-directed self-assembly of ditopic calix[5]arene and dumbbell [60]fullerene. *Journal of the American chemical society* **127,** 8936–8937 (2005).

273. Sathish, M. *et al.* Nanoporous Fullerene Nanowhiskers. *Chemistry of materials* **19,** 2398–2400 (2007).

274. Gavat, O. *et al.* 3D supramolecular self-assembly of [60]fullerene hexaadducts decorated with triarylamine molecules. *Chemical communications* **54,** 7657–7660 (2018).

275. Bedrov, D. *et al.* Molecular dynamics simulation study of the role of evenly spaced poly(ethylene oxide) tethers on the aggregation of C60 fullerenes in water. *Langmuir* **21,** 5251–5255 (2005).

276. Hooper, J. B. *et al.* Supramolecular self-organization in PEO-modified C60 fullerenewater solutions: influence of polymer molecular weight and nanoparticle concentration. *Langmuir* **24,** 4550–4557 (2008).

277. Sabirov, D. S. *et al.* Isomers of the C84 fullerene: A theoretical consideration within energetic, structural, and topological approaches. *Fullerenes, nanotubes and carbon nanostructures* **26,** 100–110 (2018).

278. Partha, R. *et al.* Buckysomes: fullerene-based nanocarriers for hydrophobic molecule delivery. *ACS nano* **2,** 1950–1958 (2008).

279. Chaudhuri, P. *et al.* Fullerenol-cytotoxic conjugates for cancer chemotherapy. *ACS nano* **3,** 2505–2514 (2009).

280. Liu, J.-H. *et al.* Fullerene-conjugated doxorubicin in cells. *ACS applied materials & interfaces* **2,** 1384–1389 (2010).

281. Mancke, R. G. & Ferry, J. D. Dynamic mechanical properties of cross-linked rubbers. IV. dicumyl peroxide vulcanizates of styrene-butadiene rubber. *Transactions of the society of rheology* **12,** 335–350 (1968).

282. Yamashita, H. *et al.* Tip-sample distance control using photothermal actuation of a small cantilever for high-speed atomic force microscopy. *Review of scientific instruments* **78,** 83702 (2007).

283. Pini, V. *et al.* Dynamical characterization of vibrating AFM cantilevers forced by photothermal excitation. *Physical review B* **81,** 54302 (2010).

284. Vassalli, M. *et al.* Role of the driving laser position on atomic force microscopy cantilevers excited by photothermal and radiation pressure effects. *Applied physics letters* **97,** 143105 (2010).

285. Farrance, I. & Frenkel, R. Uncertainty of measurement: a review of the rules for calculating uncertainty components through functional relationships. *The clinical biochemist reviews* **33,** 49 (2012).

286. Clifford, C. A. & Seah, M. P. The determination of atomic force microscope cantilever spring constants via dimensional methods for nanomechanical analysis. *Nanotechnology* **16,** 1666 (2005).

287. Sun, Y. & Walker, G. C. Viscoelastic response of poly(dimethylsiloxane) in the adhesive interaction with AFM tips. *Langmuir* **21,** 8694–8702 (2005).

288. Lin, Y. & Hui, C. Y. Mechanics of contact and adhesion between viscoelastic spheres: An analysis of hysteresis during loading and unloading. *Journal of polymer science part B: polymer physics* **40,** 772–793 (2002).

289. Proksch, R. & Yablon, D. G. Loss tangent imaging: Theory and simulations of repulsive-mode tapping atomic force microscopy. *Applied physics letters* **100,** 73106 (2012).

290. Proksch, R. *et al.* Practical loss tangent imaging with amplitude-modulated atomic force microscopy. *Journal of applied physics* **119,** 134901 (2016).

291. King, W. P. *et al.* Heated atomic force microscope cantilevers and their applications. *Annual review of heat transfer* **16** (2013).

292. Shekhawat, G. S. *et al.* Micromachined chip scale thermal sensor for thermal imaging. *ACS nano* **12,** 1760–1767 (2018).

293. Nonnenmacher, M. *et al.* Kelvin probe force microscopy. *Applied physics letters* **58,** 2921–2923 (1991).

294. Rezende, C. A. *et al.* Detection of charge distributions in insulator surfaces. *Journal of physics: condensed matter* **21,** 263002 (2009).

295. Alcaraz, J. *et al.* Correction of microrheological measurements of soft samples with atomic force microscopy for the hydrodynamic drag on the cantilever. *Langmuir* **18,** 716–721 (2002).

296. Montheard, J.-P. *et al.* 2-hydroxyethyl methacrylate (HEMA): chemical properties and applications in biomedical fields. *Journal of macromolecular science, part C: polymer reviews* **32,** 1–34 (1992).

297. Karpushkin, E. *et al.* Rheological properties of homogeneous and heterogeneous poly (2-hydroxyethyl methacrylate) hydrogels. *Polymer international* **61,** 328–336 (2012).

298. Meade, M. L. *Lock-in amplifiers: principles and applications IEE Electrical Measurement Series 1* **1** (London: P. Peregrinus, 1983).

299. DeVore, S. *et al.* Improving student understanding of lock-in amplifiers. *American journal of physics* **84,** 52–56 (2016).

300. Yao, K. D. *et al.* In situ atomic force microscopy measurement of the dynamic variation in the elastic modulus of swollen chitosan/gelatin hybrid polymer network gels in media of different pH. *Polymer international* **48,** 794–798 (1999).